# Dynamics of a Flexible Extendible Beam

by

Marinos Costa Stylianou
B.A.Sc., University of Toronto, 1982
M.A.Sc., University of Toronto, 1985

A Dissertation Submitted in Partial Fulfillment of the
Requirements for the Degree of

DOCTOR OF PHILOSOPHY

in the Department of Mechanical Engineering

We accept this dissertation as conforming
to the required standard

Dr. B. Tabarrok, Supervisor (Mechanical Engineering)

Dr. A. Doige, Department Member (Mechanical Engineering)

Dr. S. Dost, Department Member (Mechanical Engineering)

Dr. D. Hoffman, Outside Member (Computer Science)

Dr. D.B. Cherchas, External Examiner (Mechanical Engineering,
University of British Columbia)



University of Victoria

Supervisor: Dr. B. Tabarrok

## ABSTRACT

Axially-moving materials arise in problems associated with spacecraft antennas, pipes conveying fluid and telescopic robotic manipulators. Flexible extendible beams are a special class of axially-moving materials, in which the axially-moving material is modelled as a slender beam and the mechanism of elastic deformation is transverse bending.

Hamilton's principle is used to derive the governing differential equation of motion and system invariant properties of a flexible extendible beam protruding from a rigid wall with prescribed extrusion profile. The mass of the system is not constant and the general analytical solution to the equation of motion is not known. In this study, numerical solutions are obtained using finite-element analysis. However, instead of following the obvious (but cumbersome) approach of using fixed-size elements and increasing their number, in a stepwise fashion, as mass elements enter the domain of interest, a more elegant approach is followed wherein the number of elements is fixed, while the sizes of the elements change with time. To this end, a variable-domain beam finite element whose size is a prescribed function of time is formulated.

The accuracy of this variable-domain beam element is demonstrated through the time-integration of equations of motion using various extrusion profiles. Additional verification is performed by the evaluation of the system's invariant quantities, comparison with a special analytical solution, and the dynamic stability analysis of pipes conveying fluid. The effects of wall flexibility, tip mass, and high-frequency axial-motion perturbations to the transverse response of the flexible extendible beam are also examined. In order to gain a deeper insight into the mechanics of this system, the dynamic stability characteristics of the flexible extendible beam are also investigated using various extrusion profiles. The effects of physical damping, tip mass, tip support and wall flexibility on the stability characteristics of this system are examined.

The power and versatility of this finite-element formulation is demonstrated in a simulation of an extruding flexible extendible beam which carries a tip mass and protrudes from a flexible envelope beam which imparts three-dimensional rigid-body rotations to the system.

Examiners:

Dr. B. Tabarrok, Supervisor (Mechanical Engineering)

Dr. A. Doige, Department Member (Mechanical Engineering)

Dr. S. Dost, Department Member (Mechanical Engineering)

Dr. D. Hoffman, Outside Member (Computer Science)

Dr. D.B. Cherchas, External Examiner (Mechanical Engineering,
University of British Columbia)

# Table of Contents

# List of Tables

# List of Figures

# Nomenclature

| | |
|---|---|
| $a$ | constant acceleration of beam extrusion/retraction |
| $A$ | beam cross sectional area |
| $[a_i]$ | element invariant matrices (Appendix E) |
| $[A_i]$ | system invariant matrices (Eq. (4.6)) |
| $\{b_i\}$ | element invariant vectors (Appendix E) |
| $[c_1]$ | element dynamic damping matrix (Eq. (3.24), (6.57)) |
| $[c_2]$ | element dynamic damping matrix (Eq. (3.25), (6.57)) |
| $[c_3]$ | element dynamic damping matrix (Eq. (6.57)) |
| $[c_{eq}]$, $[C_{eq}]$ | element and system equivalent damping matrix (Eqs. (3.30), (5.26), (6.60)) |
| $d_t$ | location of beam's tip with respect to ECS (Fig. (3.1), Eq. (3.5)) |
| $E$ | Young's modulus |
| $E(t)$ | total energy (Eqs. (2.58), (4.5)) |
| $H_{II}$, $H_{IX}$, $H_{XI}$, $H_{XX}$ | components of the Hamiltonian vectors (Eqs. (2.23), (2.37)) |
| $I = I_z$, $I_y$ | second moment of area |

| | |
|---|---|
| $[k]$ | element stiffness matrix (Eq. (3.21), (6.47)) |
| $[k_1]$ | element dynamic stiffness matrix (Eq. (3.22), (6.57)) |
| $[k_2]$ | element axial effects matrix (Eq. (3.23), (6.52)) |
| $[k_3]$ | element dynamic stiffness matrix (Eq. (6.57)) |
| $[k_4]$ | element axial effects matrix (Eq. (6.53)) |
| $[k_5]$ | element axial effects matrix (Eq. (6.54)) |
| $[k_6]$ | element dynamic stiffness matrix (Eq. (6.57)) |
| $[k_7]$ | element dynamic stiffness matrix (Eq. (6.57)) |
| $[k_8]$ | element dynamic stiffness matrix (Eq. (6.57)) |
| $[k_{eq}]$, $[K_{eq}]$ | element and system equivalent stiffness matrix (Eqs. (3.31), (5.27), (6.60)) |
| $l(t)$ | element length (Fig. (3.1)) |
| $L(t)$ | length of protruding part of beam (Figs. (3.1), (4.20), (5.6), (6.12)) |
| $L_B$ | total length of beam (Fig. (3.1)) |
| $L_E$ | length of envelope beam (Figs. (4.20), (5.6), (6.12)) |
| $L_i$ | location of ECS with respect to SCS (Fig. (3.1)) |
| $L_o$ | initial length of protruding part of beam |
| $L_P$ | length of pipe (Fig. (5.25)) |
| $\mathcal{L}$ | system Lagrangian density function |
| $\hat{\mathcal{L}}$ | system Lagrangian |
| $\mathcal{L}_i$ | element Lagrangian |
| $\hat{m}$ | translational inertia of lumped mass |

| | |
|---|---|
| $[m]$, $[M]$ | element and system consistent mass matrix (Eqs. (3.20), (6.57)) |
| $n_t$, $n_x$ | components of outward-normal unit-vector (Fig. (2.2)) |
| $[N] = [N]_y, [N]_z$ | shape-functions vectors in $xy$ and $xz$ planes |
| $[\aleph]$ | spatial shape-functions vector |
| $\hat{P}_t$, $\hat{P}_x$ | modified generalised momenta (Eqs. (2.15), (2.25)) |
| $\{r_r\}$, $\{r_e\}$ | position vectors (Eq. (6.11)) |
| $\{r_1\}$, $\{r_2\}$ | element dynamic load vectors (Eq. (6.57)) |
| $R_{tt}$, $R_{tX}$, $R_{Xt}$, $R_{XX}$ | hypermomenta (Eqs. (2.16), (2.25)) |
| $S$ | bounding curve (Fig. (2.2)) |
| $\{S_i\}$ | similarity mode vector (Figs. (4.14), (4.15)) |
| $t$ | time |
| $T^*$ | total complementary kinetic energy of system (Eq. (6.17)) |
| $T_b^*$ | complementary kinetic energy of beam (Eq. (6.18)) |
| $T_m^*$ | complementary kinetic energy of tip mass (Eq. (6.34)) |
| $[T_1]$, $[T_2]$ | equivalent-flow tip force matrices (Appendix G) |
| $U_i$ | non-dimensional velocity of beam extrusion/retraction and of fluid flow in pipes (Eq. (5.12), (5.25)) |
| $v$ | constant velocity of beam extrusion/retraction |
| $V_s$ | flexural strain energy (Eq. (6.45)) |
| $V_l$ | energy due to longitudinal loads (Eq. (6.48)) |
| $\{V\}$, $\{V_{tip}\}$ | velocity vector (Eqs. (6.16), (6.35)) |
| $x$ | position along the element with respect to ECS (Fig. (3.2)) |

| | |
|---|---|
| $X$ | position along the beam with respect to SCS (Fig. (3.2)) |
| $\{\chi\}$ | element spatial nodal-variables vector (Eq. (6.6)) |
| $\{\chi\}$ | system spatial nodal-variables vector |
| $y(t,x)$ | transverse displacement of element in ECS (Fig. (3.2)) |
| $Y(t,X)$ | transverse displacement of beam in SCS (Fig. (3.2)) |
| $y_1, y_2$ | element nodal deflections in $xy$-plane (Eq. (3.9)) |
| $\{y\}$ | element nodal-variables vector in $xy$-plane (Eq. (3.17)) |
| $\{Y\}$ | system nodal-variables vector in $XY$-plane |
| $\{z\}$ | element nodal-variables vector in $xz$-plane (Eq. (6.4)) |
| $z_1, z_2$ | element nodal deflections in $xz$-plane (Eq. (6.5)) |
| $[\ ]_b$ | beam contributions to element matrices (Eqs. (6.23) to (6.31))) |
| $\{\ \}_b$ | beam contributions to element loads (Eqs. (6.32), (6.33)) |
| $[\ ]_m$ | tip mass contributions to element matrices (Eqs. (6.37) to (6.42)) |
| $\{\ \}_m$ | tip mass contributions to element loads (Eqs. (6.43), (6.44)) |
| $\alpha_c, \beta_c$ | proportional-damping coefficients (Eq (4.2)) |
| $\beta$ | inertia ratio for pipes (Eq. (5.25)) |
| $\varepsilon$ | a perturbation parameter (Eq. (4.16)) |
| $\eta$ | a similarity parameter (Eq. (4.9)) |
| $\lambda_i$ | eigenvalues (Eq. (5.7)) |
| $\xi_i$ | modal damping coefficients (Eq. (5.8)) |
| $\rho$ | material density |
| $\tau$ | period of oscillations |

| | |
|---|---|
| $\Theta_1, \Theta_2$ | nodal slopes in $xy$-plane (Eq. (3.9)) |
| $\Phi_1, \Phi_2$ | nodal slopes in $xy$-plane (Eq. (6.5)) |
| $\omega$ | circular frequency |
| $\{\omega_r\}, \{\omega_e\}$ | rotational-velocity vectors (Eqs. (6.13)) |
| $\Omega$ | region (Fig. (2.2)) |

## Acronyms

| | |
|---|---|
| ECS | Element Coordinate System |
| LHS, RHS | Left- and Right-Hand Side |
| SCS | System Coordinate System |

## Operators

| | |
|---|---|
| $\delta$ | variational operator |
| $\frac{d}{dt}$ | total time derivative |
| $\left[\frac{\partial}{\partial x}\right]$ , $\left[\frac{\partial}{\partial t}\right]$ | total differentiation as defined in Section 2.2.1 |
| $_{,x}$ , $_{,t}$ | partial differentiation with respect to $x$ and $t$ |
| $\frac{\partial}{\partial x}$ , $\frac{\partial}{\partial t}$ | partial differentiation with respect to $x$ and $t$ |
| $'$ , $^{\circ}$ | partial differentiation with respect to $x$ and $t$ |

ACKNOWLEDGEMENTS

I thank my supervisor, Professor B. Tabarrok, for his guidance, encouragement, and moral support during the course of this research. The financial assistance received from Professor B. Tabarrok (through the Natural Sciences and Engineering Research Council of Canada and Science Council of British Columbia) and the University of Victoria is gratefully acknowledged. I also thank Dr. C. Konzelman for his numerous useful suggestions.

My gratitude also goes to my family whose sacrifices made it possible for me to pursue a career in engineering.

To Judith.
For her love and patience.

# Chapter 1

# Introduction

## 1.1 Problem Description and History

The subject of this investigation is the dynamics of a flexible extendible beam. To put this subject into perspective, Fig. (1.1) shows a particular physical system involving a flexible extendible beam. This particular system is comprised of a beam protruding from a stationary rigid wall. The tip of the beam may support a tip mass as shown. Note in particular that the length of the protruding part is a prescribed function of time.

The flexible extendible beam problem falls under the broad topic of axially-moving solid continua. Axially-moving materials arise in problems associated with cable tramways, spacecraft antennas, band saws, magnetic tape drives, belts, and chains. Since these systems have one large dimension (along the axis of motion) and two smaller ones, they are usually analysed as one-dimensional string or beam problems. In some applications, however, account must be taken of a second large dimension. For instance, the deployment of solar arrays in space applications requires modelling the array as a moving membrane or plate. A recent survey of these problems is given by Wicker and Mote (1988).

A related problem is that of pipes conveying fluid. Literature on pipes conveying fluids is very extensive and an excellent survey of these problems is given by Païdoussis and Workman (1991). From a materials perspective, these problems fall within the domain of solid mechanics, although the flow aspect of these problems gives them a flavour of fluid mechanics. For instance, in the motion of a computer tape between two reels, it is not practical to follow the individual particles of tape in time, since some tape particles leave (while others enter) the domain of interest. One must then use the Eulerian *window* over the domain of interest. If the tracking of particles is relinquished, then conservation of mass will not be automatically satisfied. That is, new mass elements enter the domain and, depending on the boundary conditions, some mass elements may leave the domain, with the result that the mass in the domain may change with time. In these problems, the rate at which mass elements enter and leave the domain is prescribed.

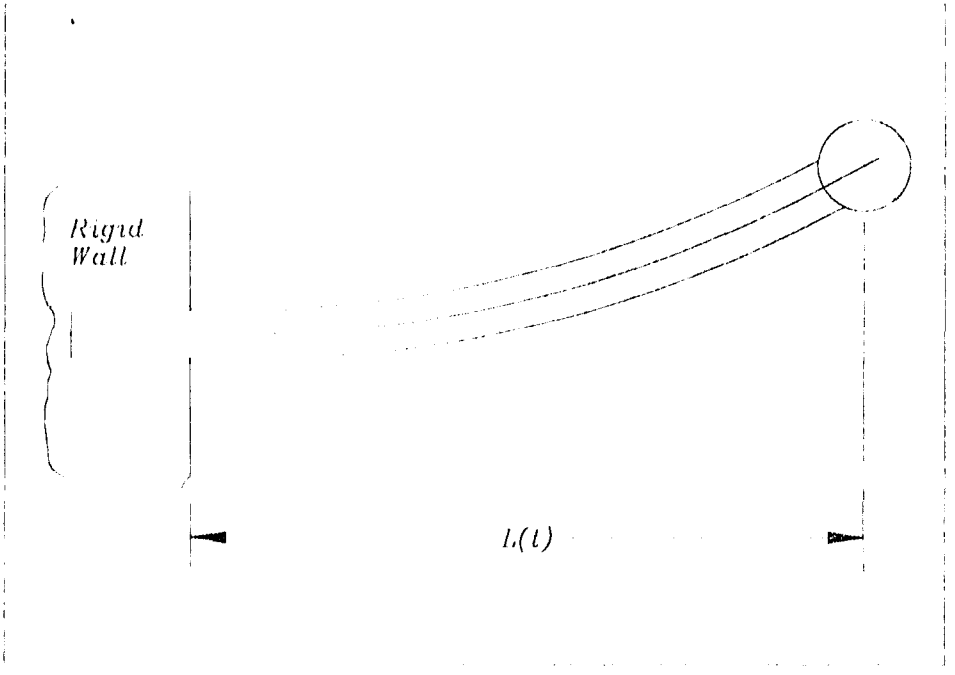


Figure 1.1: A flexible extendible beam.

Most investigations of axially-moving beams deal with beams supported at two points, and it is the transverse motion of the beam within the span that is of interest (Wicker and Mote (1988)). If the beam is assumed to be axially rigid, then under these condi-

tions, the mass of the system within the domain of interest is conserved for small-amplitude motion. For the problem of the flexible extendible beam in Fig. (1.1), mass is not conserved, as new mass elements enter the domain of interest (the protruding part of the beam).

A derivation of the non-linear, coupled longitudinal and transverse equations of motion of the flexible extendible beam has been provided by Tabarrok, Leech, and Kim (1974) through Newton's Second Law. After linearisation, a similarity solution was obtained. In addition, it was shown that for a constant axial velocity, oscillatory motions dominate the response during the initial stage of deployment and that, at least within linear theory, the transverse deflection becomes unbounded with time. Their findings were confirmed by simulations using the assumed-modes technique. The assumed-modes technique was also employed in an investigation by Cherchas and Gossain (1974) of the dynamics of a large flexible solar array as it deploys from a spinning spacecraft. Several investigators have also examined the stability of beams under harmonic longitudinal motion for beams of constant length (Elmaraghy and Tabarrok, (1975)) and variable length (Zajaczkowski and Lipinski (1979), Zajaczkowski and Yamada (1980)). Regions of stability and instability in the excitation-amplitude and frequency parameter space were identified. Although such excitation does not occur in most band-and-wheel systems, many robotic and mechanism components execute periodic axial motions.

Recently, flexible extendible beams have gained prominence due to new applications in the area of robotics, specifically in the modeling of flexible links traveling through prismatic joints. Wang and Wei (1987) use a modified Galerkin method to solve the equation of motion of an axially-moving beam. However, their derivation of the governing equation through Newton's Second Law leaves out certain terms and leads to an incorrect expression for the total energy of the system. Yuh and Young (1991) use the assumed-modes method and compare their simulation results to those obtained through experiments. However, their simulation results for cases involving rigid-body angular accelerations are not plausible on physical grounds, and are in disagreement with results obtained in this study. Buffinton (1992) also uses the assumed-modes technique to model the moving beam as an unconstrained body, and treats the beam's finite number of supports as kinematical constraints. Kim and Gibson (1991) use the finite-element approach to model a sliding flexible link. However, the derivation of the

complementary kinetic energy of the sliding flexible link, outlined by Kim (1988), also leaves out certain terms.

## 1.2 Objectives

Researchers have successfully used global methods, such as the assumed-modes method, to obtain solutions for the axially-moving beam protruding from a rigid wall. The purpose of this study is to investigate the dynamics of the flexible extendible beam under more general configurations. In particular, we investigate the effects of the following factors on the dynamic response and stability characteristics of the flexible extendible beam:

1. Change of tip support.
2. Addition of a tip mass.
3. Wall flexibility

In the case of the assumed-modes approach, different sets of mode-functions must be used depending on the tip supports. Moreover, in the case of more complicated configurations, mode-functions may not be available in closed form, making it necessary to numerically generate them and then to numerically differentiate them to obtain their derivatives, resulting in considerable deterioration of accuracy. In the case where the wall is not rigid, methods such as the assumed-modes method generally lose accuracy if the dynamic stiffness of the wall and the flexible extendible beam are of the same magnitude. The capability to model such configurations is critical in this work if the dynamics of flexible links traveling through flexible prismatic joints are to be accurately modelled.

In the present study, we use the finite-element method and take advantage of the greater flexibility of this versatile approach. Finite-element formulations are normally carried out for fixed-size domains. However, in this study, we develop elements with time-varying domains. In this case the number of elements used to model the extendible beam remains fixed, but their sizes change in a prescribed fashion.

## 1.3 Thesis Organisation

In Chapter 2, the equation of motion and the consistent boundary conditions for the flexible extendible beam are derived through application of Hamilton's principle. Then, by considering a second-order functional with two independent variables, we examine the notion of conserved quantities in a general way. Next, we examine the extremum conditions of the problem at hand in search of its specific conserved quantities.

The equation of motion of the flexible extendible beam is reasonably complex and does not admit a closed-form solution. Accordingly, in Chapter 3 we derive the governing equations of motion through finite-element discretization with a variable-domain beam element. This element accounts for the coupling of axial and transverse effects and changes length in a prescribed fashion so that a fixed number of elements can be used to model the flexible extendible beam.

In Chapter 4, we integrate the finite-element equations in time. We first consider simple configurations for which results are available in the literature through either special closed-form solutions, simulations, and/or experiments. The adequacy of the finite-element models and the accuracy of the solution procedure are further tested by computing the invariant quantities derived in Chapter 2. The generality of the variable-domain element is demonstrated in examples which are not readily analysed by the assumed-modes approach. For instance, we examine the case of the addition of a tip mass and the case of a flexible link moving through a flexible prismatic joint under the influence of a transverse acceleration field. Finally, we look at how high-frequency axial-motion perturbations can be used to suppress transverse oscillations of flexible extendible beams.

Chapter 5 is devoted to the stability analysis of the flexible extendible beam. We begin with a description of the stability analysis procedure used. Next, we define a non-dimensional system-characteristic parameter with respect to which the stability analysis results are reported. Then, starting from the simplest case of the flexible extendible beam protruding from a rigid wall, we examine the effect of changes of some of its pertinent parameters, such as the axial-motion profile, physical damping, mass distribution, tip support, wall rigidity, etc. The similarity solution obtained by Tabarrok et

al. (1974) is used in this chapter for purposes of comparison with the finite-element results. Finally, we demonstrate the versatility of the variable-domain beam element by analysing the stability of the related problem of pipes conveying fluid and compare our results to those found by Païdoussis (1966, 1974, 1975, 1991).

In Chapter 6, we derive the governing equations of motion for a spatial flexible extendible beam carrying a tip mass. Various planar simulations are performed (without a tip mass), and results obtained are compared to those found by Gaultier (1990), and Yuh and Young (1991). In our last example, we perform a simulation of a flexible extendible beam (with a tip mass) partly nested in a flexible envelope beam and undergoing a spatial rigid body motion.

Finally, in Chapter 7 we summarise our work and suggest areas for future research.

## 1.4 Synopsis

The dynamical system of a flexible extendible beam is considered in this dissertation. The dynamic response of the system in the configuration shown in Fig. (1.1), where the wall is rigid and the beam is of uniform mass distribution (without the tip mass), has been the subject of previous investigations. In this study, we extend this investigation and we develop a spatial variable-domain beam element that enables us to study the dynamic and stability characteristics of this configuration as well as of more complicated configurations. Our modeling and solution procedures are presented and tested by comparing our results to:

1. Experimental and simulation results for the dynamic response of flexible extendible beams obtained by Yuh and Young (1991).

2. Experimental and simulation results for the stability analysis of pipes conveying fluid by Païdoussis (1966, 1974, 1975, 1991).

3. The similarity solution for the flexible extendible beam obtained by Tabarrok et al. (1974).

Further testing was performed by the evaluation of certain invariant quantities inherent in the system.

A substantial part of this work involved the development of a special-purpose finite element program for the simulation of spatial flexible extendible beam problems. A detailed description of our software development approach, based on principles of software engineering, is beyond the scope of this work. However, a brief outline of this approach may be found in Appendix H.

# Chapter 2

# Derivation of the Differential Equations and the System Invariant Properties

A flexible extendible beam is depicted in Fig. (2.1). The system is comprised of a beam protruding from a rigid wall, where the length of the protruding part is a prescribed function of time. Such axial motion may be brought about by an applied root force or through application of a uniform acceleration field, such as gravity. Both of these cases are of interest and will be investigated. In this chapter, we derive the equation of motion for the flexible extendible beam through Hamilton's principle. In addition, we examine the notion of conserved quantities for this mechanical system.

## 2.1 Hamilton's Principle

Hamilton's principle requires that

$$\delta \int_{t_1}^{t_2} \hat{\mathcal{L}}\, dt = 0, \tag{2.1}$$

were $\hat{L}$ is the Lagrangian. For the flexible extendible beam the Lagrangian may be expressed as (Tabarrok et al. (1974))

$$\hat{L} = \int_{L(t)-L_B}^{L(t)} \left[ \frac{1}{2}\rho A \left(Y_t + X_t Y_X\right)^2 - \frac{1}{2} EI Y_{XX}^2 + \frac{1}{2}\rho A \left(L - X\right) \dot{L} Y_X^2 \right] dX + \frac{1}{2}\rho A L_B \dot{L}^2, \tag{2.2}$$

where $\rho A$ is the material density per unit length, $EI$ is the flexural rigidity, $L_B$ is the total length of the beam, $L(t)$ is the instantaneous length of the protruding part of the beam (a given function of time), and $Y(t,X)$ is the transverse displacement of the beam as a function of time $t$ and position $X$ (Fig. (2.1)). Partial derivatives of $Y$ with respect to $t$ and $X$ are denoted by corresponding subscripts on $Y$. Likewise, the time rate of change of position $X$ of points along the beam is denoted by $X_t$, which equal $\dot{L}$ for the axially rigid beam considered here.

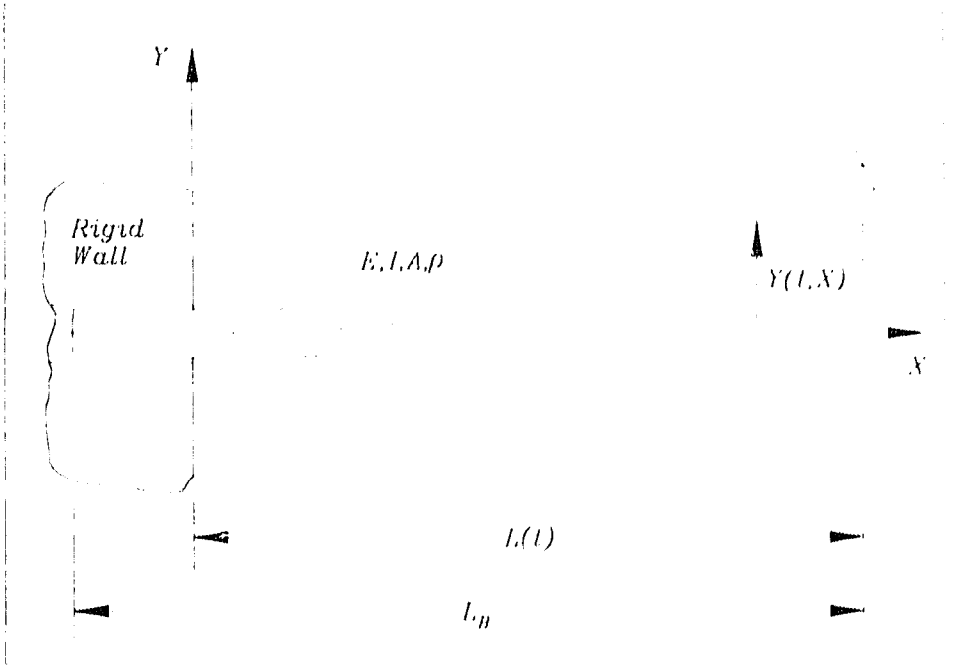


Figure 2.1: The flexible extendible beam.

The four terms in the Lagrangian correspond (in order) to the transverse complementary kinetic energy, the potential (strain) energy, the potential energy of the axial load

(due to possible axial acceleration), and the complementary longitudinal kinetic energy (a prescribed quantity). It is important to note that the term accounting for the potential energy of the axial load is relevant only for the case where the axial motion of the beam is due to a root-applied force; in the case where the beam's axial motion is caused by a uniform acceleration field, such as gravity, there will be no axial force in the beam and this term will not appear in the Lagrangian. Since time appears explicitly in the expression for the Lagrangian, the flexible extendible beam is a rheonomous system.

To ensure that the variation between $t_1$ and $t_2$ in Eq. (2.1) applies for the same aggregate in the continuum, an arbitrarily large length of beam $L_B$ is considered, so that

$$L_B > L(t) \qquad \text{for} \qquad t_2 > t > t_1. \tag{2.3}$$

Since $L(t) - L_B < 0$, and since $Y(t,X)$ and all its derivatives are prescribed for $x < 0$ (corresponding to the part of the beam enveloped within the rigid wall in Fig. (2.1)), then the variation of the Lagrangian $\hat{L}$ vanishes for $x < 0$. In addition, since $\dot{L}$ is prescribed, the variation of the last term in Eq. (2.2) vanishes as well. Consequently, the variational statement becomes

$$\delta \int_{t_1}^{t_2} \int_{0}^{L(t)} \left[ \frac{1}{2}\rho A \left(Y_t + X_t Y_X\right)^2 - \frac{1}{2} EI Y_{XX}^2 + \frac{1}{2}\rho A (L-X) \ddot{L} Y_X^2 \right] dX dt = 0. \tag{2.4}$$

Carrying out the indicated variation of $Y(t,X)$ (details are given in the second part of Appendix A) one obtains:

in the domain $(0 \le X \le L(t), \qquad t > 0)$

$$\rho A \left(Y_{tt} + 2\dot{L} Y_{tX} + \dot{L}^2 Y_{XX} + \ddot{L} Y_X\right) + EI Y_{XXXX} + \rho A a \left[ (L-X) Y_X \right]_X = 0, \tag{2.5}$$

at the boundaries

$$\begin{aligned} \left[ \rho A a (L-X) Y_X + EI Y_{XXX} \right] \delta Y &= 0, \qquad \text{at} \quad X = 0 \quad \text{and} \quad X = L, \\ \left[ EI Y_{XX} \right] \delta Y_X &= 0, \qquad \text{at} \quad X = 0 \quad \text{and} \quad X = L, \end{aligned} \tag{2.6}$$

where we have introduced a new variable $a$ according to the cause of the axial motion such that

$$\begin{aligned} a &= \ddot{L} \qquad \text{for extrusion/retraction due to a root-applied force,} \\ a &= 0 \qquad \text{for extrusion/retraction due to a uniform acceleration field.} \end{aligned} \tag{2.7}$$

Equation (2.5) expresses the dynamic equilibrium for the flexible extendible beam of Fig. (2.1). The differential operator is non-autonomous and does not admit a general closed-form solution. The non-autonomy arises from the time-dependent coefficients in the differential equation. Equations (2.6) provide the consistent boundary conditions for this system. Specifically, the first one indicates that at the ends of the protruding part of the beam either

$$\delta Y = 0, \qquad \text{i.e. deflection is prescribed,}$$

or (2.8)

$$\rho A a\,(L - X)\,Y_X + EIY_{XXX} = 0, \qquad \text{i.e. shear force vanishes.}$$

Likewise, the second boundary condition indicates that at the ends of the protruding beam either

$$\delta Y_X = 0, \qquad \text{i.e. slope is prescribed,}$$

or (2.9)

$$EIY_{XX} = 0, \qquad \text{i.e. bending moment vanishes.}$$

The mechanical system of Fig. (2.1) requires the following kinematic and force boundary conditions:

at the root (i.e. at $X = 0$)

$$Y = Y_X = 0, \tag{2.10}$$

and at the tip (i.e. at $X = L(t)$)

$$Y_{XX} = Y_{XXX} = 0. \tag{2.11}$$

There is no known general analytical solution to Eq. (2.5). However, Tabarrok et al. (1974) obtained a similarity solution for a special case of the flexible extendible beam problem. This similarity solution will be discussed and used in subsequent sections for verification purposes.

## 2.2 A Note on Conserved Quantities

Conservation laws play an important role in mechanics. The best known of these are the conservations of mass, energy and momentum. In the flexible extendible beam it is evident that the length of the protruding beam changes with time and hence mass is not conserved. Likewise we can surmise that since the elements of mass bring (or take) with them certain amounts of kinetic energy, the total energy in the domain of interest will not be conserved. Nevertheless, it is worth enquiring if there are other quantities in the system that are conserved in time. One may equally look for quantities which do not change with position. Such invariant quantities are not self-evident in this system and by identifying them one can shed new light on the underlying structure of the governing equations for the system. Given that the problem is governed by a variational statement, it makes sense to examine the extremum conditions of the problem in search of conserved quantities.

### 2.2.1 Conserved Quantities in Second-Order Functionals with two Independent Variables

The classical statement of conservation of energy, namely *(T+V) = constant,* is normally derived from a functional with first-order derivatives in time. For the flexible extendible beam problem we have seen that the pertinent functional includes higher-order derivatives. To examine this case, consider the following general functional

$$\delta \int_{\Omega} \mathcal{L}(t, X, Y, Y_t, Y_X, Y_{tX}, Y_{Xt}, Y_{tt}, Y_{XX})\, dt dX = 0. \tag{2.12}$$

The extremising function $Y(t,X)$ is governed (details are given in Appendix A):

in the domain $\Omega$ by the Euler-Lagrange equation of this functional

$$\begin{aligned} &\frac{\partial \mathcal{L}}{\partial Y} - \left[\frac{\partial}{\partial t}\right]\left(\frac{\partial \mathcal{L}}{\partial Y_t}\right) - \left[\frac{\partial}{\partial X}\right]\left(\frac{\partial \mathcal{L}}{\partial Y_X}\right) + \left[\frac{\partial^2}{\partial t^2}\right]\left(\frac{\partial \mathcal{L}}{\partial Y_{tt}}\right) + \\ &\left[\frac{\partial^2}{\partial X^2}\right]\left(\frac{\partial \mathcal{L}}{\partial Y_{XX}}\right) + 2\left[\frac{\partial^2}{\partial t \partial X}\right]\left(\frac{\partial \mathcal{L}}{\partial Y_{tX}}\right) = 0, \end{aligned} \tag{2.13}$$

and along the boundary $S$ by

$$\left[\left(\frac{\partial \mathcal{L}}{\partial Y_t}-\left[\frac{\partial}{\partial t}\right]\frac{\partial \mathcal{L}}{\partial Y_{tt}}-\left[\frac{\partial}{\partial X}\right]\frac{\partial \mathcal{L}}{\partial Y_{tX}}\right) n_t + \left(\frac{\partial \mathcal{L}}{\partial Y_X}-\left[\frac{\partial}{\partial t}\right]\frac{\partial \mathcal{L}}{\partial Y_{Xt}}-\left[\frac{\partial}{\partial X}\right]\frac{\partial \mathcal{L}}{\partial Y_{XX}}\right) n_X\right]\delta Y = 0, \tag{2.14}$$

$$\left(\frac{\partial \mathcal{L}}{\partial Y_{tt}} n_t+\frac{\partial \mathcal{L}}{\partial Y_{tX}} n_X\right)\delta Y_t = 0, \qquad \left(\frac{\partial \mathcal{L}}{\partial Y_{Xt}} n_t+\frac{\partial \mathcal{L}}{\partial Y_{XX}} n_X\right)\delta Y_X = 0,$$

where $\lfloor n_t \quad n_x \rfloor$ is the outward-normal unit-vector to the bounding curve $S$ of the region $\Omega$ shown in Fig. (2.2). At this juncture it is worth underscoring the meaning of various differential operators. The operators $\partial/\partial Y$, $\partial/\partial Y_X$, and $\partial/\partial Y_t$ are partial derivatives, that is, for these operations all variables, save those with respect to which the differentiation is being performed, are held fixed. On the other hand, the operators $\partial/\partial t$ and $\partial/\partial X$ are, for all intents and purposes, total derivatives except that for the former $X$ is held fixed and for the latter $t$ is fixed. To maintain clarity in the meaning of these operators we enclose them in brackets $\lfloor \ \rfloor$ whenever a total derivative, in the sense just mentioned, is meant.

If we now define some modified generalised momenta as[1]

$$\begin{aligned}\hat{P}_t &= \frac{\partial \mathcal{L}}{\partial Y_t}-\left[\frac{\partial}{\partial t}\right]R_{tt}-\left[\frac{\partial}{\partial X}\right]R_{tX},\\ \hat{P}_X &= \frac{\partial \mathcal{L}}{\partial Y_X}-\left[\frac{\partial}{\partial t}\right]R_{Xt}-\left[\frac{\partial}{\partial X}\right]R_{XX},\end{aligned} \tag{2.15}$$

where

$$\begin{aligned}R_{tt} &= \frac{\partial \mathcal{L}}{\partial Y_{tt}}, \qquad & R_{tX} &= \frac{\partial \mathcal{L}}{\partial Y_{tX}},\\ R_{Xt} &= \frac{\partial \mathcal{L}}{\partial Y_{Xt}}, \qquad & R_{XX} &= \frac{\partial \mathcal{L}}{\partial Y_{XX}},\end{aligned} \tag{2.16}$$

and will be referred to as the hypermomenta, the Euler-Lagrange equation (Eq. (2.13) may be written as

1. Subscripts on $\hat{P}$ and $R$ do not indicate differentiation.

$$\left[\left[\frac{\partial}{\partial t}\right] \quad \left[\frac{\partial}{\partial X}\right]\right]\begin{bmatrix}\hat{P}_t \\ \hat{P}_X\end{bmatrix} = \frac{\partial \mathcal{L}}{\partial Y}, \qquad \text{in } \Omega. \tag{2.17}$$

Evidently, when $Y$ does not appear in the expression for the Lagrangian density function $\mathcal{L}$, then the notion of *conservation of momentum* takes the form

$$\left[\left[\frac{\partial}{\partial t}\right] \quad \left[\frac{\partial}{\partial X}\right]\right]\begin{bmatrix}\hat{P}_t \\ \hat{P}_X\end{bmatrix} = 0, \qquad \text{in } \Omega. \tag{2.18}$$

It is interesting to see that in this case the conservation of momentum corresponds to the modified momentum vector $\lfloor \hat{P}_t \quad \hat{P}_X \rfloor$ being divergence-free. To develop the conservation equations for the cases when $t$ and/or $X$ are absent (explicitly) from the Lagrangian density function, let us determine the total derivatives (as defined earlier) of $\mathcal{L}$ with respect to $t$ and $X$. Thus we write

$$\begin{aligned}\left[\frac{\partial}{\partial t}\right]\mathcal{L} &= \frac{\partial \mathcal{L}}{\partial t} + \frac{\partial \mathcal{L}}{\partial Y}Y_t + \frac{\partial \mathcal{L}}{\partial Y_t}Y_{tt} + \frac{\partial \mathcal{L}}{\partial Y_{tt}}Y_{ttt} + \frac{\partial \mathcal{L}}{\partial Y_X}Y_{Xt} + \frac{\partial \mathcal{L}}{\partial Y_{XX}}Y_{XXt}\ , \\ \left[\frac{\partial}{\partial X}\right]\mathcal{L} &= \frac{\partial \mathcal{L}}{\partial X} + \frac{\partial \mathcal{L}}{\partial Y}Y_X + \frac{\partial \mathcal{L}}{\partial Y_t}Y_{tX} + \frac{\partial \mathcal{L}}{\partial Y_{tt}}Y_{ttX} + \frac{\partial \mathcal{L}}{\partial Y_X}Y_{XX} + \frac{\partial \mathcal{L}}{\partial Y_{XX}}Y_{XXX}\ .\end{aligned} \tag{2.19}$$

Now, solving for $\frac{\partial \mathcal{L}}{\partial Y}Y_t$ in Eq. (2.13) and using it in the first of Eqs. (2.19), we may write the following

$$\begin{aligned}&\left[\frac{\partial}{\partial t}\right](-\mathcal{L} + \hat{P}_t Y_t + R_{tt}Y_{tt} + R_{tX}Y_{tX}) + \\ &\qquad \left[\frac{\partial}{\partial X}\right](\hat{P}_X Y_t + R_{Xt}Y_{tt} + R_{XX}Y_{tX}) = -\frac{\partial \mathcal{L}}{\partial t}.\end{aligned} \tag{2.20}$$

Similarly, solving for $\frac{\partial \mathcal{L}}{\partial Y}Y_X$ in Eq. (2.13) and using it in the second of Eqs. (2.19) we can derive the following equation

$$\begin{aligned}&\left[\frac{\partial}{\partial t}\right](\hat{P}_t Y_X + R_{tt}Y_{Xt} + R_{tX}Y_{XX}) + \\ &\qquad \left[\frac{\partial}{\partial X}\right](-\mathcal{L} + \hat{P}_X Y_X + R_{Xt}Y_{Xt} + R_{XX}Y_{XX}) = -\frac{\partial \mathcal{L}}{\partial X}.\end{aligned} \tag{2.21}$$

Equations (2.20) and (2.21) suggest a generalisation of the Hamiltonian function. To this end we write these equations as[1]

$$\begin{bmatrix}\left[\frac{\partial}{\partial t}\right] & \left[\frac{\partial}{\partial X}\right]\end{bmatrix}\begin{bmatrix}H_{tt} & H_{tX}\\ H_{Xt} & H_{XX}\end{bmatrix} = -\begin{bmatrix}\frac{\partial \mathcal{L}}{\partial t} & \frac{\partial \mathcal{L}}{\partial X}\end{bmatrix}, \qquad \text{in } \Omega, \tag{2.22}$$

where we define

$$\begin{aligned} H_{tt} &= -\mathcal{L} + \hat{P}_t Y_t + R_{tt} Y_{tt} + R_{tX} Y_{tX}, & H_{tX} &= \hat{P}_t Y_X + R_{tt} Y_{Xt} + R_{tX} Y_{XX}, \\ H_{Xt} &= \hat{P}_X Y_t + R_{Xt} Y_{tt} + R_{XX} Y_{tX}, & H_{XX} &= -\mathcal{L} + \hat{P}_X Y_X + R_{Xt} Y_{Xt} + R_{XX} Y_{XX}. \end{aligned} \tag{2.23}$$

Here we see that the absence of $t$ and $X$ from the Lagrangian density function $\mathcal{L}$ leads to the Hamiltonian vectors $\lfloor H_{tt} \quad H_{Xt} \rfloor$ and $\lfloor H_{tX} \quad H_{XX} \rfloor$, respectively, being divergence-free.

### 2.2.2 The Flexible Extendible Beam

For purposes of using the general results derived in the last section, let us express the functional variation for the flexible extendible beam under a uniform acceleration field as (see Eq. (2.4))

$$\delta \int_{\Omega} \left( \frac{\rho A}{2} \left( Y_t^2 + 2\dot{L} Y_t Y_X + \dot{L}^2 Y_X^2 \right) - \frac{EI}{2} Y_{XX}^2 \right) d\Omega = 0. \tag{2.24}$$

where we have indicated the $(t,X)$ domain by $\Omega$. In this case, the hypermomenta (2.16) and modified momenta (2.15) are given by

$$\begin{aligned} R_{tt} &= 0, & R_{tX} &= 0, \\ R_{Xt} &= 0, & R_{XX} &= -EIY_{XX}, \\ \hat{P}_t &= \rho A \left( Y_t + \dot{L} Y_X \right), & \hat{P}_X &= \rho A \dot{L} \left( Y_t + \dot{L} Y_X \right) + EIY_{XXX}. \end{aligned} \tag{2.25}$$

Upon substituting $\hat{P}_t$ and $\hat{P}_X$ in the Euler-Lagrange equation (Eq. (2.17)) the governing equation becomes

1. Subscripts on $H$ do not indicate differentiation.

$$\rho A\,(Y_{tt} + 2\dot{L}Y_{tX} + \dot{L}^2 Y_{XX} + \ddot{L}Y_X) + EIY_{XXXX} = 0, \tag{2.26}$$

which agrees with Eq. (2.5) for the case of a uniform acceleration field (i.e. $a = 0$ in Eq. (2.5)).

For the flexible extendible beam, $Y$ is absent from $\mathcal{L}$ (Eq. (2.24)), hence, the modified momentum vector is divergence-free. That is, from Eq. (2.18)

$$\begin{bmatrix} \left[\frac{\partial}{\partial t}\right] & \left[\frac{\partial}{\partial X}\right] \end{bmatrix} \begin{bmatrix} \hat{P}_t \\ \hat{P}_X \end{bmatrix} = 0, \qquad \text{in } \Omega. \tag{2.27}$$

Let us examine the consequence of the modified momentum vector being divergence-free. From Green's theorem we have that

$$\int_{\Omega} \begin{bmatrix} \left[\frac{\partial}{\partial t}\right] & \left[\frac{\partial}{\partial X}\right] \end{bmatrix} \begin{bmatrix} \hat{P}_t \\ \hat{P}_X \end{bmatrix} d\Omega = \oint_S \begin{bmatrix} n_t & n_X \end{bmatrix} \begin{bmatrix} \hat{P}_t \\ \hat{P}_X \end{bmatrix} dS = 0, \tag{2.28}$$

where $\lfloor n_t \quad n_X \rfloor$ is the outward-normal unit-vector to the bounding curve $S$ of the region $\Omega$ shown in Fig. (2.2). Before expanding the terms in the line integral we need to evaluate the outward-normal unit-vectors from the region $\Omega$. For three of its sides the outward-normal unit-vectors are self-evident. An outward normal-vector (Fig. (2.2)) at any point along the curved side may be expressed as $\lfloor -\dot{L} \quad 1 \rfloor$ where $\dot{L}$ is the slope of the curve. Therefore, the outward-normal unit-vector on this side may be expressed as

$$\begin{bmatrix} -\dot{L} \\ 1 \end{bmatrix} \cdot \frac{1}{\sqrt{1 + \dot{L}^2}}. \tag{2.29}$$

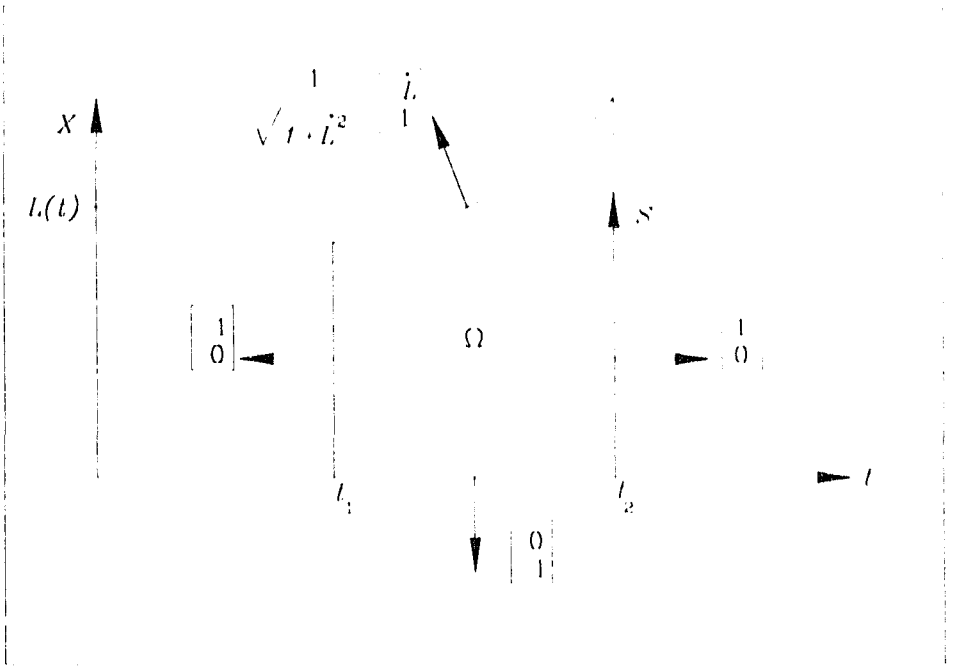


Figure 2.2: Configuration space of the flexible extendible beam.

Now, expanding the line integral of Eq. (2.28) we see that the divergence-free modified-momentum vector implies that

$$\int_0^{L(t_2)} \hat{P}_t\, dX\Big|_{t=t_2} + \int_{t_2}^{t_1} \left(\frac{1}{\sqrt{(1+\dot{L}^2)}}\right)(-\dot{L}\hat{P}_t + \hat{P}_X)\,(\sqrt{(1+\dot{L}^2)})\,(-dt)\Big|_{X=L(t)} + \int_{L(t_1)}^{0} (-\hat{P}_t)\,(-dX)\Big|_{t=t_1} + \int_{t_1}^{t_2} (-\hat{P}_X)\,dt\Big|_{X=0} = 0. \tag{2.30}$$

The term $\sqrt{(1+\dot{L}^2)}$ appears in the calculation of the outward-normal unit-vector of the curved edge *and* in the Jacobian of the transformation from the straight line $t$ to the curved line $L(t)$ and therefore conveniently cancels out.

Now, considering an infinitesimal change in $t$, namely letting

$$t_1 = t \qquad \text{and} \qquad t_2 = t + \Delta t, \tag{2.31}$$

Eq. (2.30) may be written as follows

$$\frac{d}{dt}\left[\int_0^{L(t)} \hat{P}_t\, dX\right] = \hat{P}_X\big|_{X=0} - \left(-\dot{L}\hat{P}_t + \hat{P}_X\right)\big|_{X=L(t)}, \tag{2.32}$$

which, upon substitution of the generalised momenta from Eqs. (2.25) becomes

$$\begin{aligned}\frac{d}{dt}\left[\int_0^{L(t)} \rho A\{Y_t + \dot{L}Y_X\}\, dX\right] &= \left(\rho A\dot{L}\{Y_t + \dot{L}Y_X\} + EIY_{XXX}\right)\big|_{X=0} - \\ &\left(-\rho A\dot{L}\{Y_t + \dot{L}Y_X\} + \rho A\dot{L}\{Y_t + \dot{L}Y_X\} + EIY_{XXX}\right)\big|_{X=L(t)}.\end{aligned} \tag{2.33}$$

Upon making use of the following boundary conditions

$$\begin{aligned} Y_t = Y_X = 0, \qquad &\text{at} \qquad X = 0, \\ Y_{XX} = Y_{XXX} = 0, \qquad &\text{at} \qquad X = L(t), \end{aligned} \tag{2.34}$$

and simplifying, Eq. (2.33) becomes

$$\frac{d}{dt}\left[\int_0^{L(t)} \rho A\{Y_t + \dot{L}Y_X\}\, dX\right] = \left(EIY_{XXX}\right)\big|_{X=0} \ . \tag{2.35}$$

Noting that the expression in braces { } corresponds to the transverse velocity of points along the beam, the above equation states that the rate of change of transverse momentum is equal to the shear force at the base of the protruding part of the beam.

Recall that since time appears explicitly in $\mathcal{L}$ through the prescribed function $L(t)$, the Hamiltonian vector $\lfloor H_t \qquad H_{X_t} \rfloor$ is not divergence-free. That is, from Eq. (2.22)

$$\left[\left[\frac{\partial}{\partial t}\right] \quad \left[\frac{\partial}{\partial X}\right]\right]\begin{bmatrix} H_t \\ H_{X_t} \end{bmatrix} = -\rho A\ddot{L}\left[\left(Y_t + \dot{L}Y_X\right) Y_X\right], \tag{2.36}$$

where the modified Hamiltonian vector components from Eq. (2.23) become

$$
\begin{aligned}
H_{tt} &= \frac{\rho A}{2}\left(Y_t^2 - \dot{L}^2 Y_X^2\right) + \frac{EI}{2} Y_{XX}^2 \ , \\
H_{tX} &= \rho A \left(Y_t + \dot{L} Y_X\right) Y_X \ , \\
H_{Xt} &= \rho A \dot{L} \left(Y_t + \dot{L} Y_X\right) Y_t + EI Y_{XXX} Y_t - EI Y_{XX} Y_{tX} \ , \\
H_{XX} &= \frac{\rho A}{2}\left(\dot{L}^2 Y_X^2 - Y_t^2\right) - \frac{EI}{2} Y_{XX}^2 + EI Y_{XXX} Y_X \ .
\end{aligned}
\tag{2.37}
$$

In the case of the flexible extendible beam, $R_{tt}$ and $R_{tX}$ vanish in Eqs. (2.23), hence, $H_{tt}$ corresponds to the classical definition of the Hamiltonian. Using Green's theorem in the region $\Omega$, with the bounding curve $S$, and the outward-normal unit-vectors as shown in Fig. (2.2), we see that the modified Hamiltonian vector $\left| H_{tt} \quad H_{tX} \right|$ implies that

$$
\begin{aligned}
&\int_0^{L(t_2)} H_{tt}\, dX\Big|_{t=t_2} + \int_{t_2}^{t_1} \left( \frac{1}{\sqrt{(1+\dot{L}^2)}} \right) \left(-\dot{L} H_{tt} + H_{Xt}\right) \left(-\sqrt{(1+\dot{L}^2)}\right) dt \Bigg|_{X \quad L(t)} + \\
&\int_{L(t_1)}^{0} \left(-H_{tt}\right) \left(-dX\right)\Big|_{t=t_1} + \int_{t_1}^{t_2} \left(-H_{Xt}\right) dt\Big|_{X=0} = \int_{\Omega} -\rho A \ddot{L} \left| \left(Y_t + \dot{L} Y_X\right) Y_X \right| d\Omega .
\end{aligned}
\tag{2.38}
$$

Following the same procedure as that employed with the modified momentum vector, we may express Eq. (2.38) as

$$
\begin{aligned}
\frac{d}{dt}\left[ \int_0^{L(t)} H_{tt}\ dX \right] &= \left(H_{Xt}\right)\Big|_{X=0} - \left(-\dot{L} H_{tt} + H_{Xt}\right)\Big|_{X \quad L(t)} - \\
&\int_{\Omega} \rho A \ddot{L} \left| \left(Y_t + \dot{L} Y_X\right) Y_X \right| d\Omega .
\end{aligned}
\tag{2.39}
$$

We will now examine the above expression in the context of different forms of the given function $L(t)$. If the length of the beam is constant ($\dot{L}(t) = \ddot{L}(t) = 0$), then from Eqs. (2.34) and (2.37) above expression becomes

$$
\frac{d}{dt}\left[ \int_0^{L} \left( \frac{EI}{2} Y_{XX}^2 + \frac{\rho A}{2} Y_t^2 \right) dX \right] = 0 .
\tag{2.40}
$$

Thus in this special case the total energy is conserved. If, on the other hand, the beam is moving axially at a constant velocity ($\dot{L}(t) = v$ and $\ddot{L}(t) = 0$), Eq. (2.39) becomes a statement of evolution of the modified Hamiltonian-component $H_{tt}$ in time, namely

$$\frac{d}{dt}\left[\int_0^{L(t)} H_{tt}\, dX\right] = -\dot{L}\left[\frac{\rho A}{2}\{Y_t + vY_X\}^2\right]\Big|_{X=L(t)}. \tag{2.41}$$

The expression in brackets on the right-hand side will be recognised as the complementary kinetic energy per unit length. Since this is a positive-definite term, one can see that changes in $H_{tt}$ are governed by the sign of $\dot{L}$. That is, if the beam is extruding (i.e. $\dot{L}$ is positive) $H_{tt}$ decreases, whereas if the beam is retracting (i.e. $\dot{L}$ is negative) $H_{tt}$ increases.

Finally, for the general case where neither $\dot{L}$, nor $\ddot{L}$ are equal to zero, Eq. (2.39) becomes

$$\frac{d}{dt}\left[\int_0^{L(t)} H_{tt}\, dX\right] = -\dot{L}\left[\frac{\rho A}{2}\{Y_t + \dot{L}Y_X\}^2\right]\Big|_{X=L(t)} - \int_\Omega \rho A\ddot{L}\left[(Y_t + \dot{L}Y_X)\, Y_X\right] d\Omega. \tag{2.42}$$

Another invariant result is obtained by noting that $X$ is absent (explicitly) from $\mathcal{L}$. Hence the modified Hamiltonian vector $\lfloor H_{tX} \quad H_{XX} \rfloor$ is divergence-free. That is, from Eq. (2.22)

$$\left[\left[\frac{\partial}{\partial t}\right] \quad \left[\frac{\partial}{\partial X}\right]\right]\begin{bmatrix} H_{tX} \\ H_{XX} \end{bmatrix} = 0. \tag{2.43}$$

Once again, using Green's theorem, we can assert that the divergence-free modified Hamiltonian vector $\lfloor H_{tX} \quad H_{XX} \rfloor$ implies that

$$\int_0^{L(t_2)} H_{tX}\,dX\big|_{t=t_2} + \int_{t_2}^{t_1}\left(\frac{1}{\sqrt{(1+\dot{L}^2)}}\right)(-\dot{L}H_{tX}+H_{XX})\,(-\sqrt{(1+\dot{L}^2)})\,dt\Big|_{X\ L(t)} + \int_{L(t_1)}^{0}(-H_{tX})\,(-dX)\big|_{t=t_1} + \int_{t_1}^{t_2}(-H_{XX})\,dt\big|_{X=0} = 0. \tag{2.44}$$

Following the same procedure as that employed with the modified momentum vector, we may express Eq. (2.44) as

$$\frac{d}{dt}\left[\int_0^{L(t)} H_{tX}\ dX\right] = (H_{XX})\big|_{X=0} - (-\dot{L}H_{tX}+H_{XX})\big|_{X\ L(t)}, \tag{2.45}$$

which, upon substitution of Eqs. (2.34) and (2.37), becomes

$$\frac{d}{dt}\left[\int_0^{L(t)} \rho A\,\{Y_t+\dot{L}Y_X\}\,Y_X\ dX\right] = (-\frac{EI}{2}Y_{XX}^2)\Big|_{X=0} + \frac{\rho A}{2}\{Y_t+\dot{L}Y_X\}^2\Big|_{X\ L(t)}. \tag{2.46}$$

This equation states that the rate of change of the component of the transverse momentum in the tangential direction is equal to the difference between the potential energy per unit length at the base of the protruding beam and the transverse complementary kinetic energy per unit length at the tip of the protruding beam.

The governing equation for the flexible extendible beam, Eq. (2.26), can also be obtained from any one of (2.27), (2.36), and (2.43), by simply carrying out the differentiations and simplifying the resulting expressions.

The correctness of Eqs. (2.35), (2.40), (2.41), (2.42), and (2.46) can be confirmed by direct differentiation of their left-hand sides. Since this differentiation is with respect to time and the upper limit of the integral is also a function of time, one must use the Leibniz rule to carry out the differentiation. For example, carrying out the differentiation of the left-hand side of Eq. (2.46) we have

$$\frac{d}{dt}\left[\int_0^{L(t)} \rho A \{Y_t + \dot{L} Y_X\} Y_X \, dX\right] =$$

$$\int_0^{L(t)} \rho A \left[ (Y_{tt} + \ddot{L} Y_X + 2\dot{L} Y_{Xt}) Y_X + (Y_t Y_{Xt}) \right] dX + \tag{2.47}$$

$$\rho A \dot{L} (Y_t + \dot{L} Y_X) Y_X \big|_{X = L(t)} .$$

Since the lower limit of the integral is fixed, the additional term of Leibniz integration vanishes at that limit. But from the governing equation (2.26) we have that

$$\rho A (Y_{tt} + \ddot{L} Y_X + 2\dot{L} Y_{tX}) = -EIY_{XXXX} - \rho A \dot{L}^2 Y_{XX} \quad , \tag{2.48}$$

which when substituted in Eq. (2.47) yields,

$$\frac{d}{dt}\left[\int_0^{L(t)} \rho A \{Y_t + \dot{L} Y_X\} Y_X \, dX\right] =$$

$$\int_0^{L(t)} (-EIY_{XXXX} Y_X - \rho A \dot{L}^2 Y_{XX} Y_X + \rho A Y_t Y_{Xt}) \, dX + \tag{2.49}$$

$$\rho A \dot{L} (Y_t + \dot{L} Y_X) Y_X \big|_{X = L(t)} .$$

Noting that

$$\rho A \dot{L}^2 Y_{XX} Y_X = \frac{\rho A}{2} \dot{L}^2 \frac{\partial}{\partial X} (Y_X^2) \qquad \text{and} \qquad \rho A Y_t Y_{Xt} = \frac{\rho A}{2} \frac{\partial}{\partial X} (Y_t^2) , \tag{2.50}$$

Eq. (2.49) can be simplified to

$$\frac{d}{dt}\left[\int_0^{L(t)} \rho A \{Y_t + \dot{L} Y_X\} Y_X dX\right] = \int_0^{L(t)} (-EIY_{XXXX} Y_X) \, dX + \tag{2.51}$$

$$\frac{\rho A}{2} (Y_t + \dot{L} Y_X)^2 \Big|_{X = L(t)} .$$

We now integrate the right-hand side integral by parts to get

$$\int_0^{L(t)} (-EIY_{XXXX}Y_X)\,dX = -\int_0^{L(t)} \frac{d}{dX}(EIY_{XXX}Y_X)\,dX + \int_0^{L(t)} (EIY_{XXX}Y_{XX})\,dX \quad , \tag{2.52}$$

or

$$\int_0^{L(t)} (-EIY_{XXXX}Y_X)\,dX = -(EIY_{XXX}Y_X)\Big|_0^{L(t)} + \int_0^{L(t)} (EIY_{XXX}Y_{XX})\,dX \tag{2.53}$$

Using the boundary conditions in Eqs. (2.34), the above expression simplifies to

$$\int_0^{L(t)} (-EIY_{XXXX}Y_X)\,dX = \int_0^{L(t)} (EIY_{XXX}Y_{XX})\,dX. \tag{2.54}$$

Finally, noting that

$$EIY_{XXX}Y_{XX} = \frac{EI}{2}\frac{d}{dX}(Y_{XX})^2, \tag{2.55}$$

Eq. (2.54) further simplifies to

$$\int_0^{L(t)} (-EIY_{XXXX}Y_X)\,dX = -\frac{EI}{2}Y_{XX}^2\Big|_{X=0}. \tag{2.56}$$

Substituting Eq. (2.56) into Eq. (2.51) we obtain

$$\frac{d}{dt}\left[\int_0^{L(t)} \rho A\{Y_t + \dot{L}Y_X\}Y_X dX\right] = \frac{\rho A}{2}\{Y_t + \dot{L}Y_X\}^2\Big|_{X=L(t)} - \frac{EI}{2}Y_{XX}^2\Big|_{X=0} \tag{2.57}$$

which is identical to Eq. (2.46).

## 2.2.3 Energy Considerations

The total energy of the flexible extendible beam for the special case of constant axial-velocity may be expressed as

$$E(t) = \int_0^{L(t)} \left[\frac{1}{2}\rho A(Y_t + \dot{L}Y_X)^2 + \frac{1}{2}EIY_{XX}^2\right]dX + \frac{1}{2}\rho A L_B \dot{L}^2. \tag{2.58}$$

This expression for total energy is in disagreement with the simpler expression for the total energy given by Wang and Wei (1987, Eq. (13)). These authors fail to take proper account of the time dependency of $X$ $(X_t = \dot{L})$ through the total time derivative of $Y$ in the complementary kinetic energy. Due to the time-dependent domain of the flexible extendible beam, the total energy of the system is time dependent. In fact, if the above differentiation is carried out, we get the following expression for the rate of change of total energy

$$\frac{d}{dt}E(t) = \rho A\dot{L}\left(\int_0^{L(t)} -2Y_t(Y_{Xt}+\dot{L}Y_{XX})\,dX + \int_0^{L(t)} Y_{tt}Y_X dX\right) + \rho A\dot{L}\left(\frac{1}{2}(Y_t+\dot{L}Y_X)^2 + \dot{L}(Y_tY_X)\right)\Big|_{X=L(t)} . \tag{2.59}$$

## 2.3 Concluding Remarks

We have derived the governing differential equation and the associated boundary conditions of the flexible extendible beam from Hamilton's principle. By not making a particular distinction between time and space variables we have developed other conservation statements and we have illustrated them for the flexible extendible beam problem. Such invariant forms are manifestations of inherent symmetries in the system being studied. They are therefore of intrinsic interest on physical grounds and they provide useful checks for soundness of numerical algorithms devised to solve the system equations as pointed out by Kane and Levinson (1988). The invariant statements will be used in subsequent sections for verification purposes.

If the differential equation and the boundary conditions of a physical problem are well posed, that is, if the problem is properly modelled, then one can expect to find solutions for the governing differential equation. The fact that the boundary conditions and the differential equation for the problem at hand emerge from a single variational statement ensures the consistency of these equations. However, these equations are reasonably complex and do not admit closed form solutions. Accordingly one must resort to a numerical procedure for solution. In the next chapter, we address this matter and devise finite-element procedures for solution of the problem at hand.

# Chapter 3

# Variable-Domain Beam Elements

In this work we use the finite-element method to obtain solutions for the axially-moving beam. Finite-element formulations are normally carried out for fixed-size domains. For time-dependent domains it is possible, in principle, to use fixed-size elements and to increase/decrease their number, in a step-wise fashion, as a function of time. Such an approach, though straightforward in concept, is difficult to implement in practice. It requires a very large number of small elements if reasonable smoothness in the results is to be obtained, and since the system's number of degrees of freedom changes continuously, special programing considerations are necessary. In this chapter, we follow a more elegant approach by developing elements with time-varying domains. In this case the number of elements remains fixed, but their sizes change in a prescribed fashion.

## 3.1 Element Lagrangian Function

In order to develop the finite element equations for the variable domain beam element, let us divide the protruding part of the beam of Fig. (2.1) into $n$ elements of equal length $l(t)$ as shown in Fig. (3.1). The Lagrangian for the $i^{th}$ element is then given by

$$L_i = \int_0^{l(t)} \left[ \frac{1}{2}\rho A \left(y_t + x_t y_x\right)^2 - \frac{1}{2} E I y_{xx}^2 + \frac{1}{2}\rho A \left(L - L_i - x\right) \ddot{L} y_x^2 \right] dx + \frac{1}{2}\rho A l \dot{L}^2, \quad (3.1)$$

where the lower case symbols $x$ and $y$ correspond to the element coordinate system (ECS), and $L_i$ locates the ECS as shown in Fig. (3.2). As time evolves, elements elongate (or contract). Let us consider a point $A$ along the neutral axis of the $i^{th}$ element as shown in Fig. (3.2). This point's location, with respect to the inertial frame $XY$, is given by

$$X = L_i + x. \quad (3.2)$$

Solving for the element coordinate $x$ and differentiating with respect to time, we obtain

$$x_t = X_t - \dot{L}_i. \quad (3.3)$$

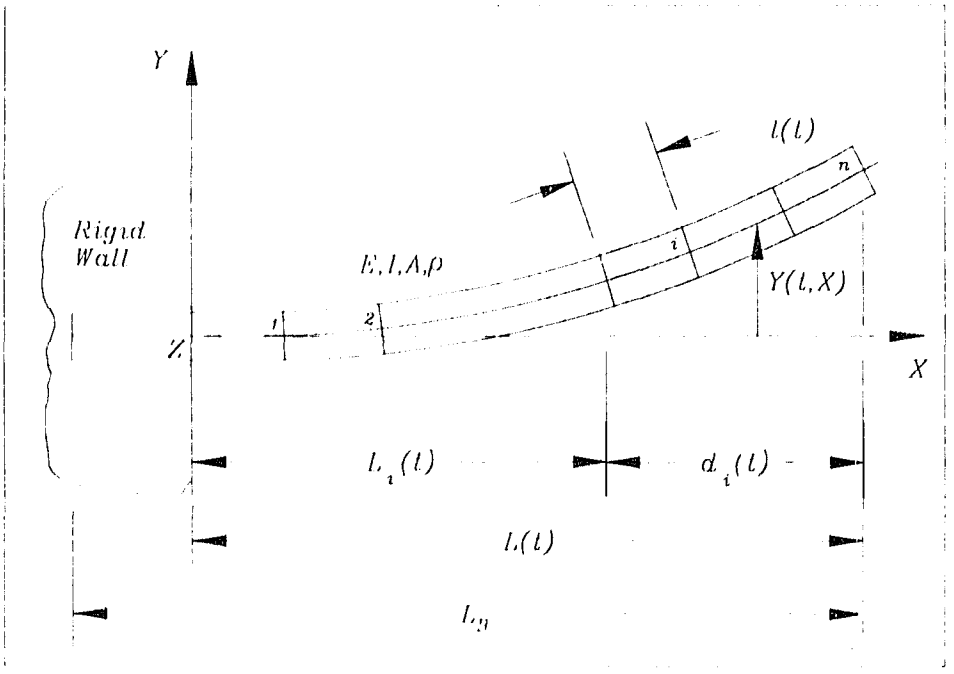


Figure 3.1: Variable-domain beam elements.

However, since $X_t = \dot{L}$, the rate of change with respect to time of the element coordinate $x$ is given by

$$x_t = \dot{L} - \dot{L}_i. \quad (3.4)$$

It is convenient at this point to introduce a new parameter $d_i$, shown in Fig. 3.1), defined for each element as follows

$$d_i = L - L_i = L\,(1 - (i-1)/n) \qquad i = 1, 2, \ldots n. \tag{3.5}$$

Using the above definition, the expression for the Lagrangian of the $i^{th}$ element (Eq. (3.1)) becomes

$$\mathcal{L}_i = \int_0^{l(t)} \left[\frac{1}{2}\rho A\,(y_t + \dot{d}_i y_x)^2 - \frac{1}{2}EIy_{xx}^2 + \frac{1}{2}\rho A\,(d_i - x)\,\dot{L}y_x^2\right]dx + \frac{1}{2}\rho A l\dot{L}^2. \tag{3.6}$$

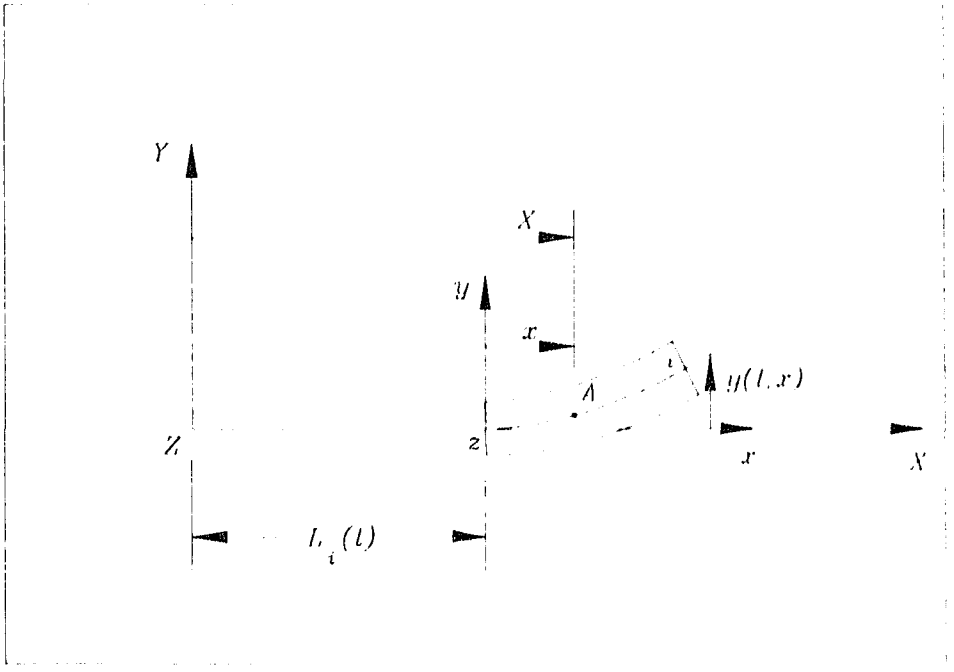


Figure 3.2: Element coordinate system (ECS).

## 3.2 Finite-Element Discretization

The transverse deflections of the flexible extendible beam are modelled by a cubic polynomial as follows

$$y\,(t,x) = c_0 + c_1 x + c_2 x^2 + c_3 x^3, \tag{3.7}$$

where the $c$'s are functions of time only and $x$ is the distance along the element as shown in Fig. (3.3). The slope distribution is given by

$$y_x(t,x) = c_1 + 2c_2x + 3c_3x^2. \tag{3.8}$$

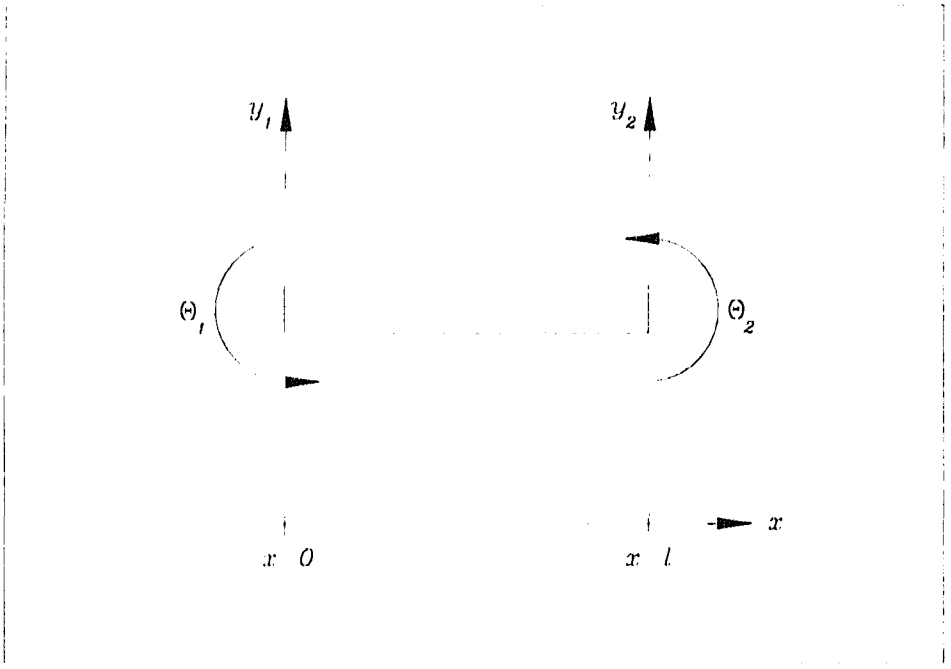


Figure 3.3: Nodal variables of a beam finite element.

Referring to Fig. (3.3), the nodal deflection and slope variables are:

$$\begin{aligned} y(t,0) &= y_1, \qquad y_x(t,0) = \Theta_1, \\ y(t,l) &= y_2, \qquad y_x(t,l) = \Theta_2, \end{aligned} \tag{3.9}$$

When Eqs. (3.9) are used in Eqs. (3.7) and (3.8), we can write the resulting system of equations as

$$[G]\{q\} = \{y\}, \tag{3.10}$$

where

$$\{q\}^T = \left[c_0, c_1, c_2, c_3\right], \tag{3.11}$$

$$\{y\}^T = \left[y_1 \ , \ \Theta_1 \ , \ y_2 \ , \ \Theta_2\right], \tag{3.12}$$

$$[G] = \begin{bmatrix} 1 & 0 & 0 & 0 \\ 0 & 1 & 0 & 0 \\ 1 & l & l^2 & l^3 \\ 0 & 1 & 2l & 3l^2 \end{bmatrix}. \tag{3.13}$$

Solving this system of equations, we obtain for the $c$'s

$$\begin{aligned} c_0 &= y_1 , \\ c_1 &= \Theta_1 , \\ c_2 &= (2l\Theta_1 + 3y_1 - 3y_2 + l\Theta_2)/l^2 , \\ c_3 &= (2y_1 + l\Theta_1 - 2y_2 + l\Theta_2)/l^3 . \end{aligned} \tag{3.14}$$

Substituting for the $c$'s from Eq. (3.14) into Eq. (3.7) we obtain

$$y = \lfloor N \rfloor_y \{y\} , \tag{3.15}$$

where the shape-functions vector is given by

$$\lfloor N \rfloor_y = \left[1 - \frac{3x^2}{l^2} + \frac{2x^3}{l^3} \ , \ x - \frac{2x^2}{l} + \frac{x^3}{l^2} \ , \ \frac{3x^2}{l^2} - \frac{2x^3}{l^3} \ , \ -\frac{x^2}{l} + \frac{x^3}{l^2}\right], \tag{3.16}$$

and the nodal-variables vector is given by

$$\{y\}^T = \left[y_1 \ , \ \Theta_1 \ , \ y_2 \ , \ \Theta_2\right]. \tag{3.17}$$

It is worth noting that in this case the shape-functions vector is time-dependent by virtue of the element length $l$ changing in time. In order to evaluate $y_t$, $y_x$, and $y_{xx}$ for use in the element Lagrangian, Eq. (3.6), we use Eq. (3.15) and perform the appropriate differentiations to obtain

$$\begin{aligned} y_x &= \lfloor N' \rfloor_y \{y\} , \\ y_{xx} &= \lfloor N'' \rfloor_y \{y\} , \\ y_t &= \lfloor \dot{N} \rfloor_y \{y\} + \lfloor N \rfloor_y \{\dot{y}\} , \end{aligned} \tag{3.18}$$

where primes and dots indicate partial differentiation with respect to $x$ and $t$, respectively. This implies that for calculation of $\lfloor N \rfloor$, $x$ is held fixed and $l(t)$ is differentiated with respect to time. Returning now to the expression for the element Lagrangian (Eq. (3.6)), and substituting Eqs. (3.15) and (3.18), we obtain

$$\begin{aligned} \mathcal{L}_i = & \frac{1}{2}\{\dot{y}\}^T[m]\{\dot{y}\} - \frac{1}{2}\{y\}^T[k]\{y\} + \\ & \frac{1}{2}\{y\}^T[k_1]\{y\} + \frac{1}{2}\{y\}^T[k_2]\{y\} + \\ & \frac{1}{2}\{y\}^T[c_1]\{\dot{y}\} + \frac{1}{2}\{\dot{y}\}^T[c_2]\{y\} + \frac{1}{2}\rho A l \dot{L}^2, \end{aligned} \tag{3.19}$$

where

$$[m] = \int_0^{l(t)} \rho A \lfloor N \rfloor_y^T \lfloor N \rfloor_y dx, \tag{3.20}$$

$$[k] = \int_0^{l(t)} EI \lfloor N'' \rfloor_y^T \lfloor N'' \rfloor_y dx, \tag{3.21}$$

$$\begin{aligned} [k_1] = \int_0^{l(t)} \rho A \Big[ & \lfloor \dot{N} \rfloor_y^T \lfloor \dot{N} \rfloor_y + \dot{d}_i \left( \lfloor \dot{N} \rfloor_y^T \lfloor N' \rfloor_y + \lfloor N' \rfloor_y^T \lfloor \dot{N} \rfloor_y \right) + \\ & \dot{d}_i^2 \left( \lfloor N' \rfloor_y^T \lfloor N' \rfloor_y \right) \Big] dx, \end{aligned} \tag{3.22}$$

$$[k_2] = \int_0^{l(t)} \rho A \ddot{L} (d_i - x) \lfloor N' \rfloor_y^T \lfloor N' \rfloor_y dx, \tag{3.23}$$

$$[c_1] = \int_0^{l(t)} \rho A \left[ \lfloor \dot{N} \rfloor_y^T \lfloor N \rfloor_y + \dot{d}_i \lfloor N' \rfloor_y^T \lfloor N \rfloor_y \right] dx, \tag{3.24}$$

$$[c_2] = \int_0^{l(t)} \rho A \left[ \lfloor N \rfloor_y^T \lfloor \dot{N} \rfloor_y + \dot{d}_i \lfloor N \rfloor_y^T \lfloor N' \rfloor_y \right] dx. \tag{3.25}$$

Matrices $[k]$ and $[m]$ are the well-known stiffness and consistent mass matrices of the beam element respectively. Their components may be found in many finite element books (e.g. Cook et al. (1989)). The components of matrices $[k_1]$, $[k_2]$, $[c_1]$, and $[c_2]$

have been determined explicitly using the symbolic-computation program Maple (Char et al. (1988)), and are given in Appendix B. It is important to note that matrix $[k_2]$ vanishes under two special cases. The first case has already been mentioned with regards to the Lagrangian of the flexible extendible beam (Section 2.1, Eq. (2.2)); namely, when the axial motion is caused by a uniform acceleration field. The second case occurs when the axial motion occurs at a constant velocity, i.e. $\ddot{L} = 0$.

## 3.3 Finite-Element Equations

The Lagrange equations for an element, considering it to be unconstrained and independent of other elements, are given by

$$\frac{\partial \mathcal{L}_i}{\partial \{y\}^T} - \frac{d}{dt}\left[\frac{\partial \mathcal{L}_i}{\partial \{\dot{y}\}^T}\right] = \{0\}. \tag{3.26}$$

Using the expression for the element Lagrangian (Eq. (3.19)), we can evaluate the required quantities by carrying out the indicated operations of Eq. (3.26). For the first term we obtain

$$\frac{\partial \mathcal{L}_i}{\partial \{y\}^T} = (-[k] + [k_1] + [k_2])\{y\} + [c_2]^T\{\dot{y}\}, \tag{3.27}$$

where we have used the identity $[c_1] = [c_2]^T$. The second term requires the total time derivative, that is,

$$\frac{d}{dt}\left[\frac{\partial \mathcal{L}_i}{\partial \{\dot{y}\}^T}\right] = [\dot{m}]\{\dot{y}\} + [m]\{\ddot{y}\} + [\dot{c}_2]\{y\} + [c_2]\{\dot{y}\}. \tag{3.28}$$

where the components of the $[\dot{m}]$ and $[\dot{c}_2]$ have been determined explicitly and are also given in Appendix B. Substituting Eqs. (3.27) and (3.28) into the Lagrange equations (3.26), we obtain the element governing equations as follows

$$[m]\{\ddot{y}\} + [c_{eq}]\{\dot{y}\} + [k_{eq}]\{y\} = \{0\}, \tag{3.29}$$

where the *equivalent*-damping and -stiffness matrices are given by

$$[c_{eq}] = [\dot{m}] + [c_2] - [c_2]^T, \tag{3.30}$$

$$[k_{eq}] = [k] + [\dot{c}_2] - [k_1] - [k_2]. \tag{3.31}$$

In Eq. (3.30), the first term is clearly symmetric. However, the combination of the second and third terms produces a skew-symmetric matrix. Thus $[c_{eq}]$ is in general not symmetric. In addition, since the second and third terms provide a skew-symmetric matrix, the definiteness of $[c_{eq}]$ depends only on $[\dot{m}]$. That is, if the mass is increasing (extrusion), then $[c_{eq}]$ is positive-definite, whereas if the mass is decreasing (retraction), then $[c_{eq}]$ is negative-definite. Likewise in Eq. (3.31), the first term is symmetric but by virtue of the other terms we can see that $[k_{eq}]$ is in general not symmetric.

The assembly of the element equations to develop the global equations takes the well known format, and the global equations emerge as

$$[M]\{\ddot{Y}\} + [C_{eq}]\{\dot{Y}\} + [K_{eq}]\{Y\} = \{0\}. \tag{3.32}$$

The above system of equations is a set of linear, second-order differential equations with variable coefficients. The flexible extendible beam problem is of the *gyroscopic instationary* type (Ziegler (1968)); in the course of lateral motion of the beam, beam elements are subjected to Coriolis acceleration – hence the term gyroscopic – and the system is clearly instationary due to the time dependence of the system matrices.

## 3.4 Concluding Remarks

In the foregoing we have developed the governing equations of motion for the flexible extendible beam through finite-element discretization. In doing so, we have developed a variable-domain beam element capable of describing the extendible beam in terms of a fixed number of elements. In the case of axial acceleration caused by a root-applied force, the element developed also accounts for the coupling of axial and transverse effects. The next two chapters are devoted to the verification of this element through a series of examples.

# Chapter 4

# Time Integration of System Equations

The governing system of equations derived in the last chapter (Eq. (3.32)) may be numerically integrated under specified initial and boundary conditions. It is important to validate the integration scheme used and hence, in Section 4.1, we first consider simple configurations for which results are available in the literature through either special closed-form solutions, simulations, and/or experiments. The remaining sections demonstrate the effectiveness of the variable-domain element through examples motivated from applications in the dynamic modeling of robotic manipulators. Section 4.2 deals with the effects of a tip mass on the time response of the system. In Section 4.3 we look at the case where the flexible extendible beam is nested within another beam. This problem was chosen to demonstrate the capability of modeling flexible links moving through prismatic joints. Finally, Section 4.4 investigates the effects of high-frequency axial-motion perturbations on the transverse oscillations of the extendible beam.

## 4.1 Verification Examples

### 4.1.1 Experiments and Simulations by Yuh and Young (1991)

Yuh and Young (1991) conducted experiments with a flexible extendible beam (both extruding and retracting). In these experiments, the tip deflection of the beam was observed and compared to the results of simulations using the assumed-mode method outlined by Tabarrok et al. (1974). The governing system of equations included the effects of physical damping in the first two modes (the modal-damping functions were obtained experimentally). In this section we integrate the finite-element governing system of equations (Eq. (3.32)) to obtain nodal deflections, velocities and accelerations, and we compare the tip-deflection histories to those found in Yuh and Young (1991 Figs. (4) through (8)). Since the actual data from Yuh and Young's experiments and simulations is not available (private communications), a detailed comparison is not possible. Accordingly, we are limited to a qualitative comparison[1]. In order to account for the damping effects, the system equivalent-damping matrix must be modified as follows

$$[C_{eq}] = [\dot{M}] + [C_2] - [C_2]^T + [C_p], \tag{4.1}$$

where $[C_p]$ is the physical system proportional-damping matrix (see for example Bathe (1982)) expressed as

$$[C_p] = \alpha_c [M] + \beta_c [K], \tag{4.2}$$

where $[M]$ and $[K]$ are the system mass and structural stiffness matrices, respectively. Parameters $\alpha_c$ and $\beta_c$ are calculated using the two experimental modal-damping functions described in the next chapter (Eqs. (5.13)). Our finite-element model used four elements (eight degrees of freedom), and the time integration of the governing system of equations (Eq. (3.32)) was performed using the Newmark direct-integration method with variable time-step size. Details of this integration approach are given in Appendix C. The results of our simulations (corresponding to Yuh and Young's four experiments) are shown in Figs. (4.1) through (4.4). Figures (4.1) and (4.2) show the results of linear retraction and extrusion, respectively. Figures (4.3) and (4.4) show the results of constant-acceleration retraction and extrusion, respectively, where the coupling of

1. Comparisons with Yuh and Young's results (1991) include: a) Qualitative visual comparisons of the complete tip-displacement history; b) Comparisons of amplitude and period of oscillations at various points in time.

axial effects and transverse oscillations is present. The length of the beam in all four experiments is given by

$$L(t) = L_o + vt + at^2/2, \tag{4.3}$$

where the values for the initial length $L_o$, velocity $v$, and acceleration $a$ are given in Table (4.1).

| Test case # | $L_o$ (m) | $v$ (m/s) | $a$ (m/s$^2$) | Figure # Appendix D |
|---|---|---|---|---|
| 1 | 0.5250 | -0.1145 | +0.0000 | 4.1 |
| 2 | 0.4255 | +0.0410 | +0.0000 | 4.2 |
| 3 | 0.5210 | -0.0300 | -0.0540 | 4.3 |
| 4 | 0.4400 | +0.0080 | +0.0150 | 4.4 |

Table 4.1: Parameters for experimental test cases, Yuh and Young (1991).

Our results were compared to the graphs of Yuh and Young (1991), which are shown in Figs. (4.1) through (4.4) in Appendix D. Good agreement was achieved in all four test cases.

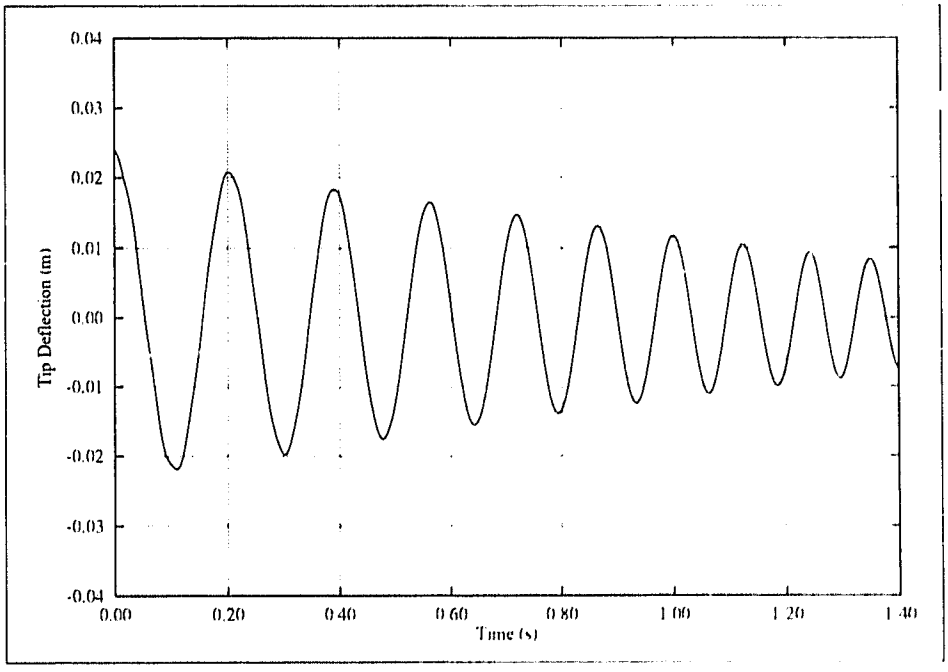


Figure 4.1: Test case # 1. Constant-velocity retraction.

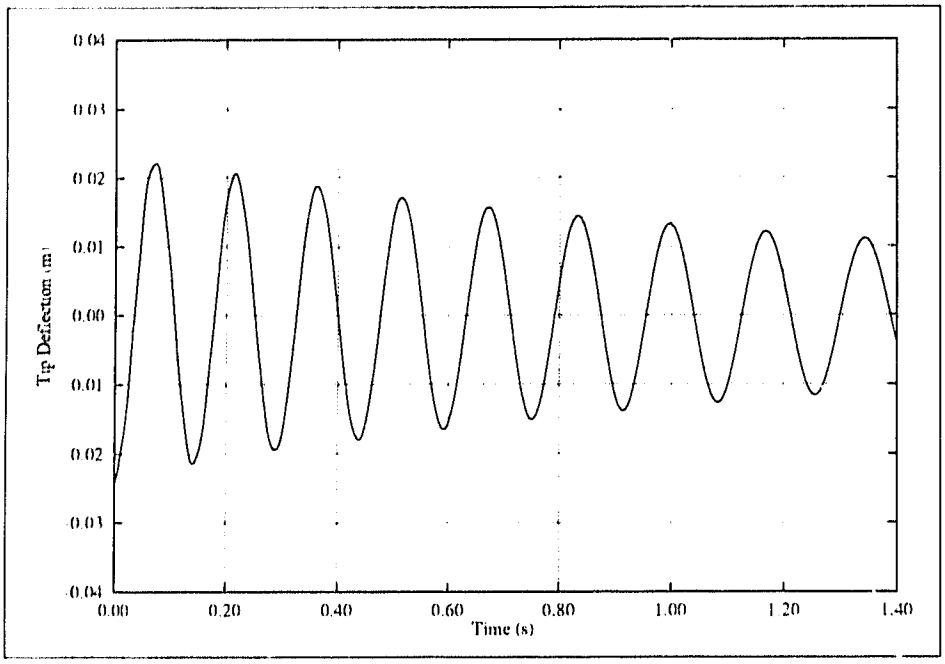


Figure 4.2: Test case # 2. Constant-velocity extrusion.

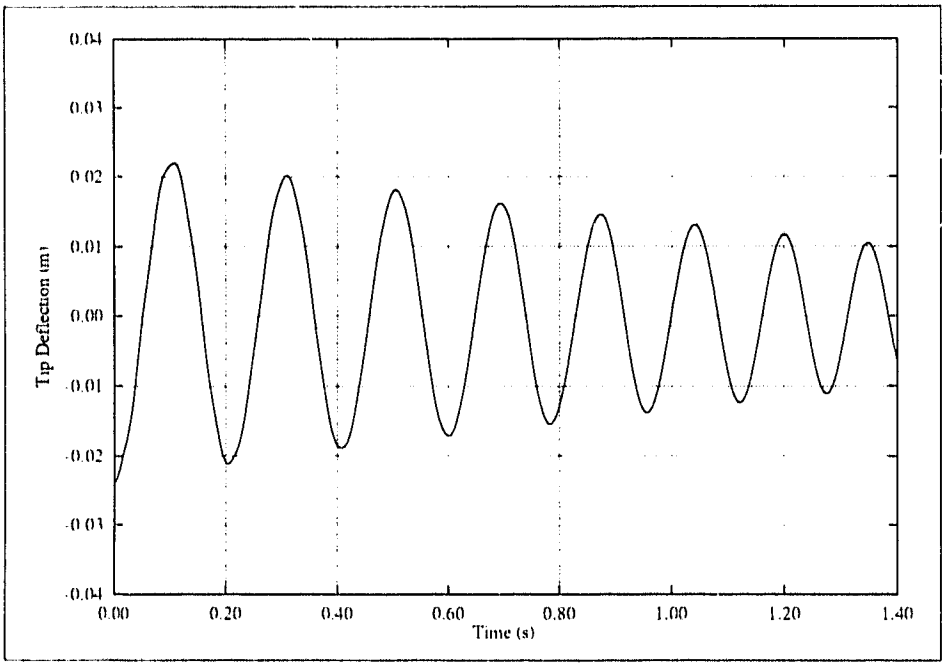


Figure 4.3: Test case # 3. Constant-acceleration retraction.

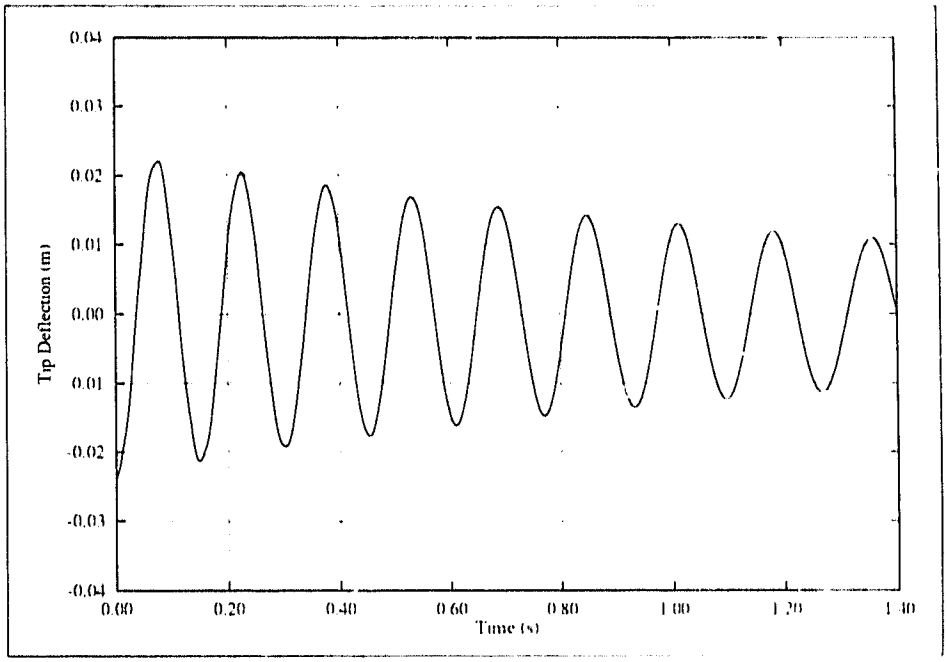


Figure 4.4: Test case # 4. Constant-acceleration extrusion.

Four additional simulations were performed that clearly demonstrate the change in frequency of oscillation due to the changing length of the beam. The beam's length for these simulations is given by

$$L(t) = L_o + \frac{c}{\tau}\left[ t - \frac{\tau}{2\pi} \sin(2\pi t/\tau) \right], \tag{4.4}$$

where values for $L_o$, $c$, and $\tau$ are given in Table (4.2).

| Simulation # | $L_o$ (m) | c (m) | $\tau$ (s) | Figure # Appendix |
|---|---|---|---|---|
| 1 | 0.3500 | +0.7000 | 1.2000 | 5 |
| 3 | 1.0500 | -0.7000 | 1.2000 | 6 |
| 5 | 0.3500 | +0.7000 | 0.2000 | 7 |
| 7 | 1.0500 | -0.7000 | 0.2000 | 8 |

Table 4.2: Parameters for simulation cases, Yuh and Young (1991).

The results of the integrations are shown in Figures (4.5) through (4.8). Our results are in fair agreement with the simulation results obtained by Yuh and Young (1991) using two modes (shown by the solid-line response in Figs. (5) through (8) in Appendix D).

Note that the high frequency content of the periodic part of the length function in Eq. (4.4) for simulation cases 5 and 7 can be expected to excite higher modes of beam vibration. In our view, modeling this behaviour would require more than the two modes used by Yuh and Young (1991). As a result, we believe that our eight-degree of-freedom model is more accurate than the two-degree-of-freedom model in the assumed-modes method.

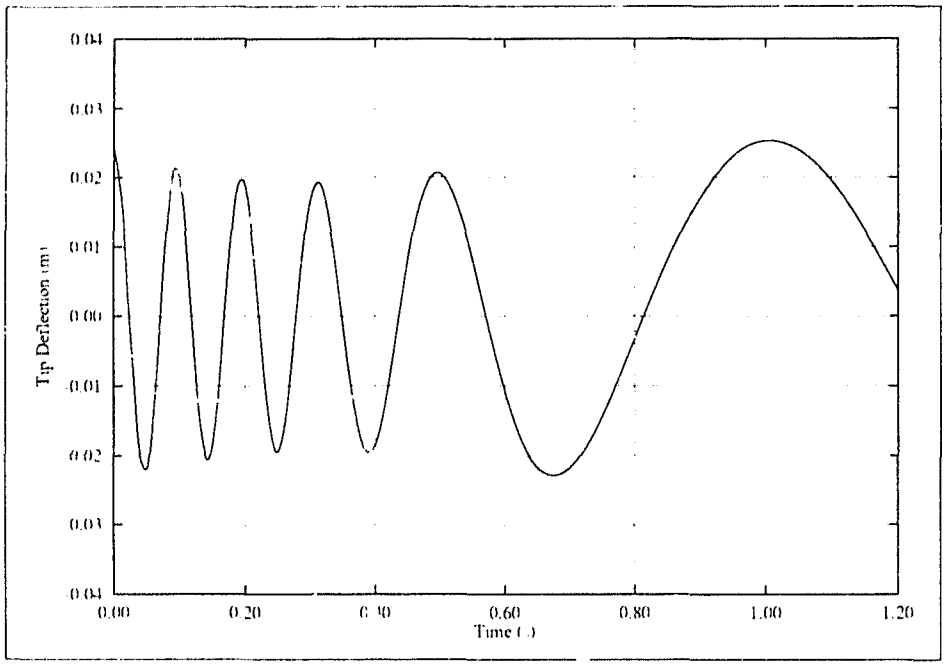


Figure 4.5: Simulation # 1. Low-frequency extrusion.

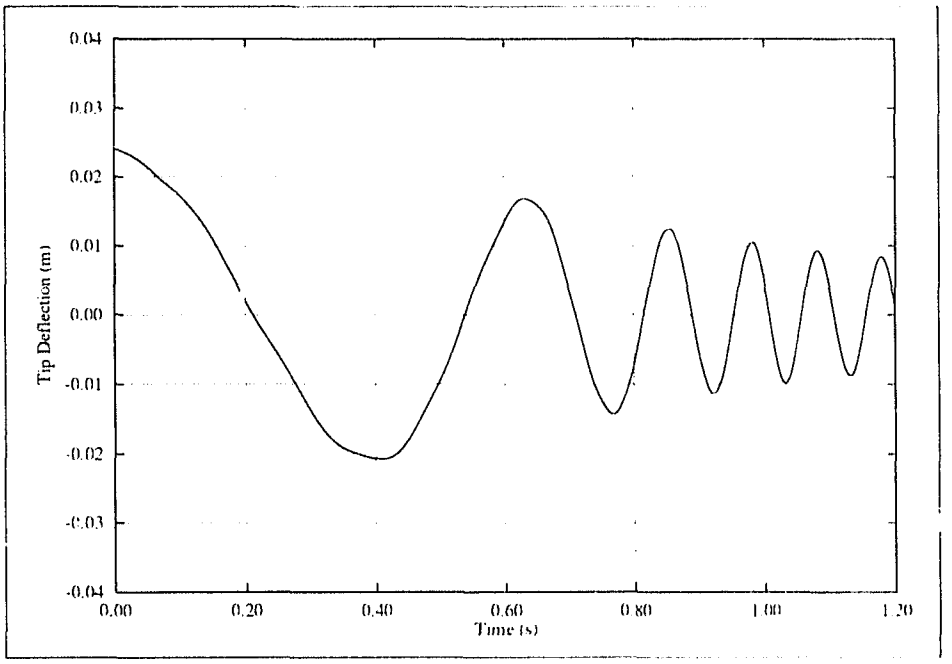


Figure 4.6: Simulation # 3. Low-frequency retraction.

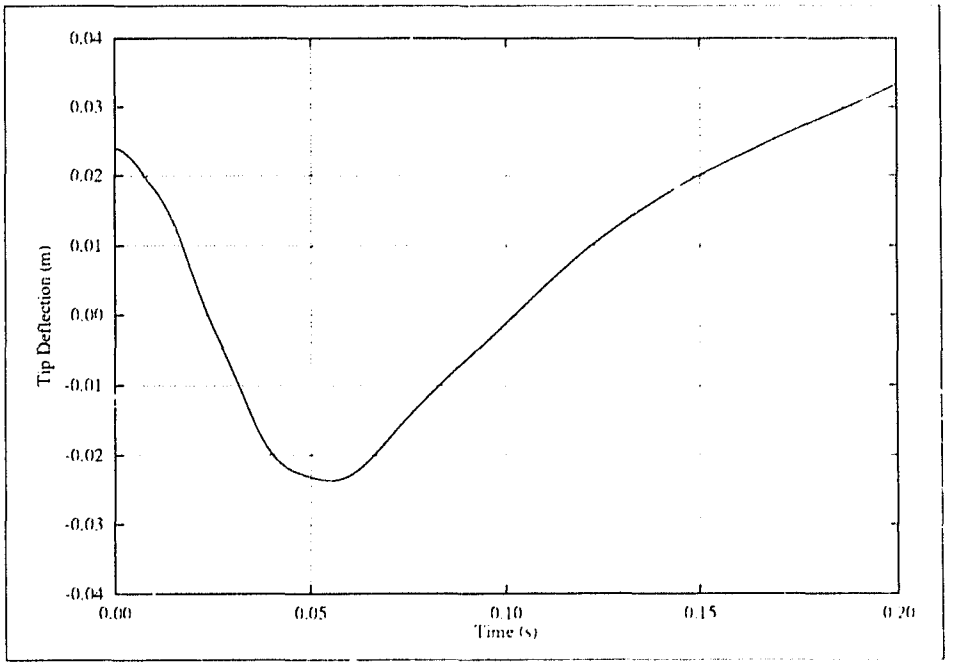


Figure 4.7: Simulation # 5. High-frequency extrusion.

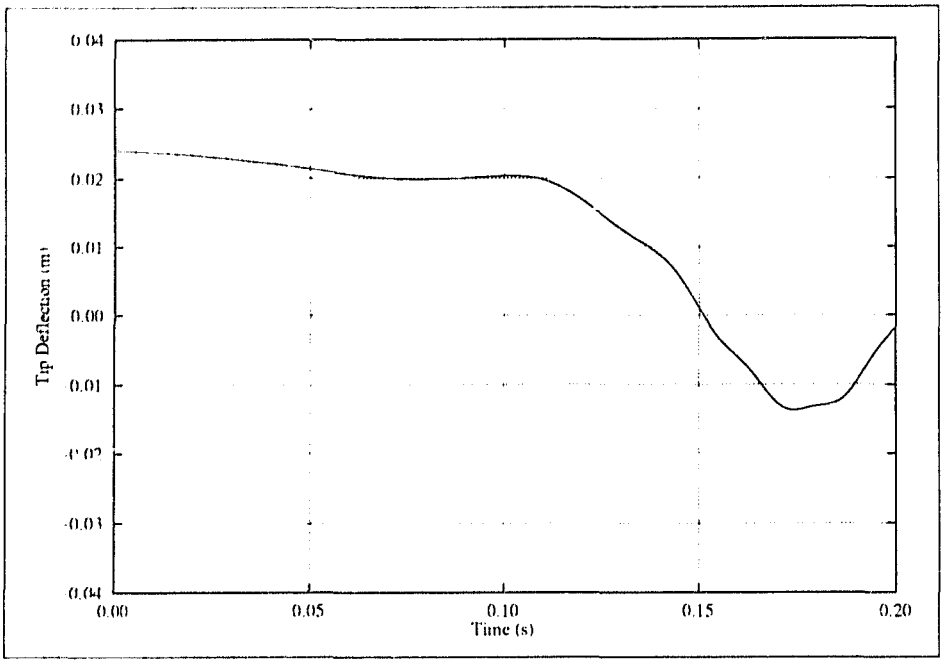


Figure 4.8: Simulation # 7. High-frequency retraction.

### 4.1.2 Energy Considerations

As mentioned in Section 3.3, the nature of the equivalent damping matrix $[C_{eq}]$ depends on the type of axial motion. In general, $[C_{eq}]$ is positive-definite (dissipative) for extrusion and negative-definite (energy generating) for retraction. The total energy of a flexible extendible beam protruding at a constant velocity is given by Eq. (2.58), which upon discretization via Eqs. (3.15) and (3.18) becomes

$$E(t) = \frac{1}{2}\{\dot{Y}\}^T[M]\{\dot{Y}\} + \frac{1}{2}\{Y\}^T[K_1]\{Y\} \\ \frac{1}{2}\{Y\}^T[C_1]\{\dot{Y}\} + \frac{1}{2}\{\dot{Y}\}^T[C_2]\{Y\} + \frac{1}{2}\{Y\}^T[K]\{Y\}, \tag{4.5}$$

where we have left out the prescribed (and in this case constant) contribution of the complementary kinetic energy due to the axial motion of the beam. Equation (4.5) was evaluated for the first two test cases considered in Section 4.1.1 In this case of zero physical damping, the resulting total energy, as a function of time, is shown in Figs. (4.9) and (4.10).

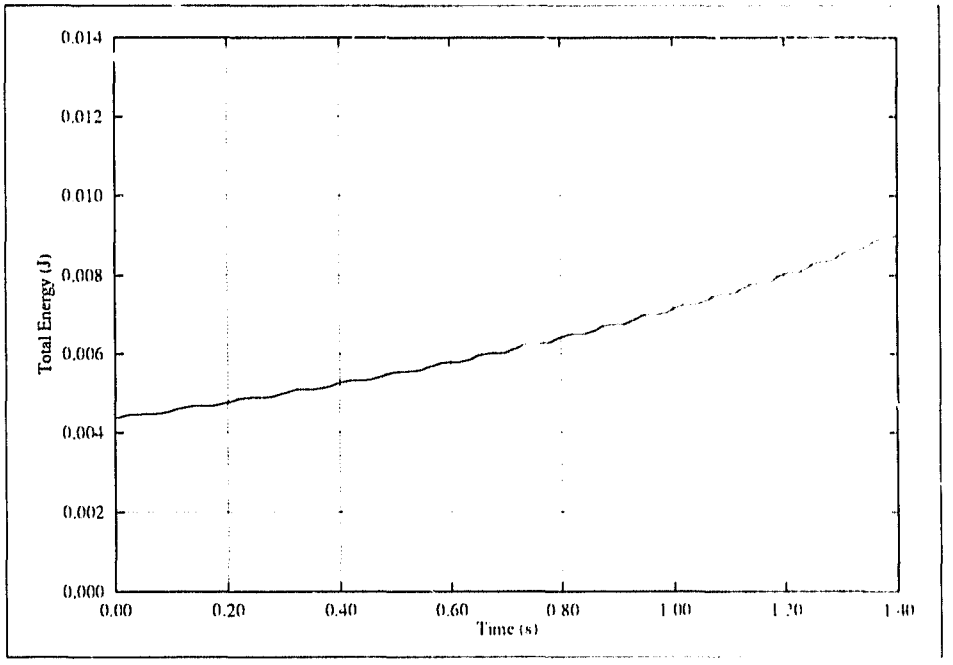


Figure 4.9: Test case #1. Total energy during constant-velocity retraction.

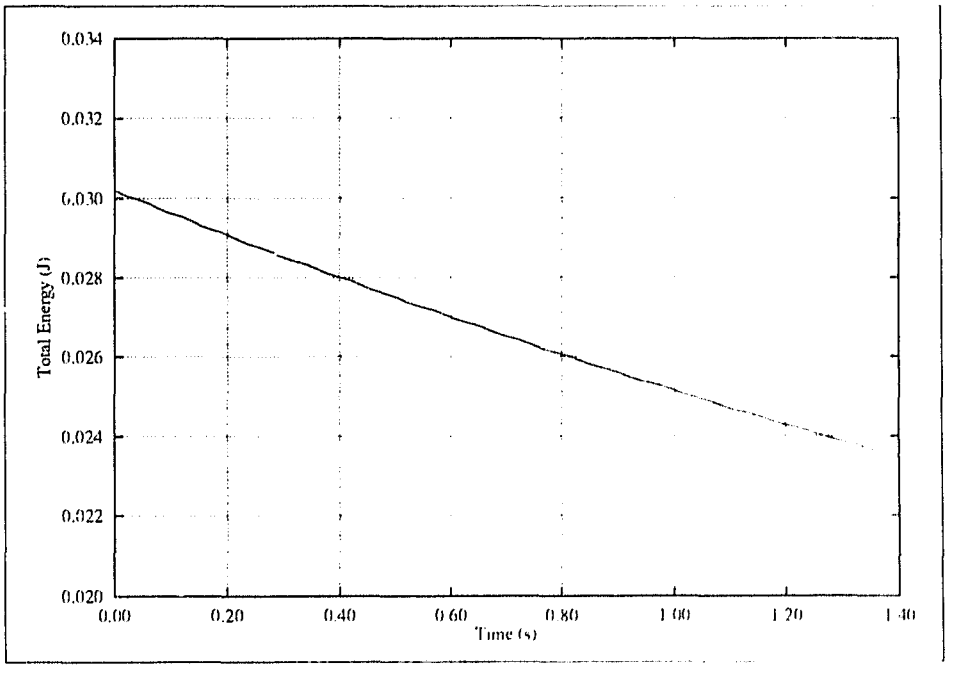


Figure 4.10: Test case # 2. Total energy during constant-velocity extrusion.

Our findings confirm that during retraction the flexible extendible beam gains energy, while during extrusion the flexible extendible beam dissipates energy. A possible physical interpretation of these results is as follows:

> During retraction (extrusion), positive (negative) external work is required to maintain the prescribed axial motion which in turn brings about a convection of mass out of (into) the domain of interest.

### 4.1.3 Conserved Quantities

In this section, we use the invariant expressions for the flexible extendible beam derived in Section 2.2.2 to verify the accuracy of the finite-element model and time-integration of the equations of motion. We begin by substituting Eqs. (3.15) and (3.18) into the invariant expressions, e.g. Eq. (2.46) and obtain

$$\begin{aligned} &\{\dot{Y}\}^T |A_1| \{Y\} + \{Y\}^T |\dot{A}_1| \{Y\} + \{Y\}^T (|A_1| + |\dot{A}_2|) \{\dot{Y}\} + \\ &\{\dot{Y}\}^T |A_2| \{\dot{Y}\} + \{Y\}^T |A_2| \{\ddot{Y}\} = \\ &\left[\frac{\rho A}{2} (Y_t + \dot{L} Y_X)^2\right]_{X = L(t)} - \left[\frac{EI}{2} \{b_1\} \{y\}\right]_{\text{element 1}}, \end{aligned} \tag{4.6}$$

where the element matrices $|a_i|$ and vector $\{b_i\}$ are given in Appendix E. The left-hand side (LHS) and right-hand side (RHS) of the above expression were evaluated for the solution history of the first test case in Section 4.1.1 using a four-element model with no physical damping, and are shown in Fig. (4.11). The agreement is such that the values of the RHS and LHS terms, superimposed in Fig. (4.11), are indistinguishable. These results show that the four-element model is more than adequate for the evaluation of all the derivatives in Eq. (2.46), up to second-order in space.

A similar procedure can be followed for the other two invariant expressions (Eqs. (2.35) and (2.41)). For example Eq. (2.35) becomes

$$\{\dot{b}_2\}^T \{Y\} + [\{b_2\} + \{\dot{b}_3\}]^T \{\dot{Y}\} + \{b_3\}^T \{\ddot{Y}\} = [EI \{b_4\}^T \{y\}]_{\text{element 1}} \tag{4.7}$$

where the vectors $\{b_i\}$ are given in Appendix E. Figure (4.12) shows the left- and right-hand sides of Eq. (4.7) for the solution history of the first test case in Section 4.1.1 using a four-element model with no physical damping. In this case, the values of the

RHS and LHS (superimposed in Fig. (4.12)) are in slight disagreement. It is apparent that the four-element model is not inadequate for the evaluation of all derivatives in Eq. (2.35). Since transverse deflections of the variable-domain beam element are modeled by a cubic polynomial (Eq. (3.7)), the shear force (which involves a third-order space derivative) is approximated as a constant along the element. This approximation yields exact shear-force calculations in static analysis under concentrated loads only. For dynamic analysis, where the flexible extendible beam is subject to inertial forces, it is expected that a coarse mesh will yield a poor approximation to the shear force at the base of the protruding part of the beam. However, if the number of elements is increased the results can be expected to improve. For comparison, Figs. (4.13) and (4.14) show the difference between the RHS and LHS using the four- and ten-element models, respectively. The ten-element model was also successfully used to evaluate Eqs. (4.6) and (4.7) under high axial-velocities (up to 10 *m/s*) and high axial accelerations (up to one *g*).

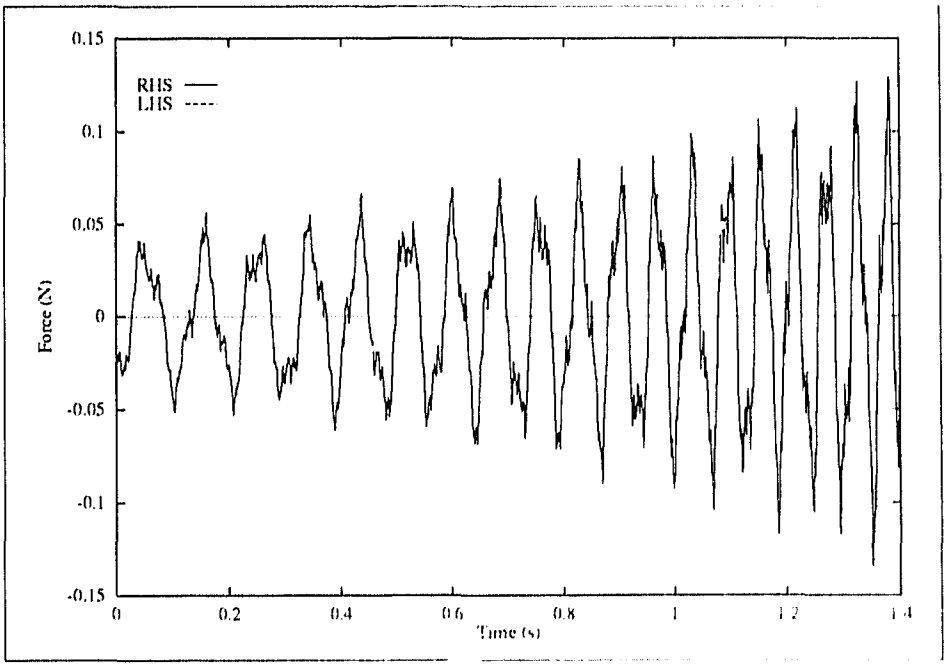


Figure 4.11: Right- and left-hand sides of Eq. (4.6) with a four-element model.

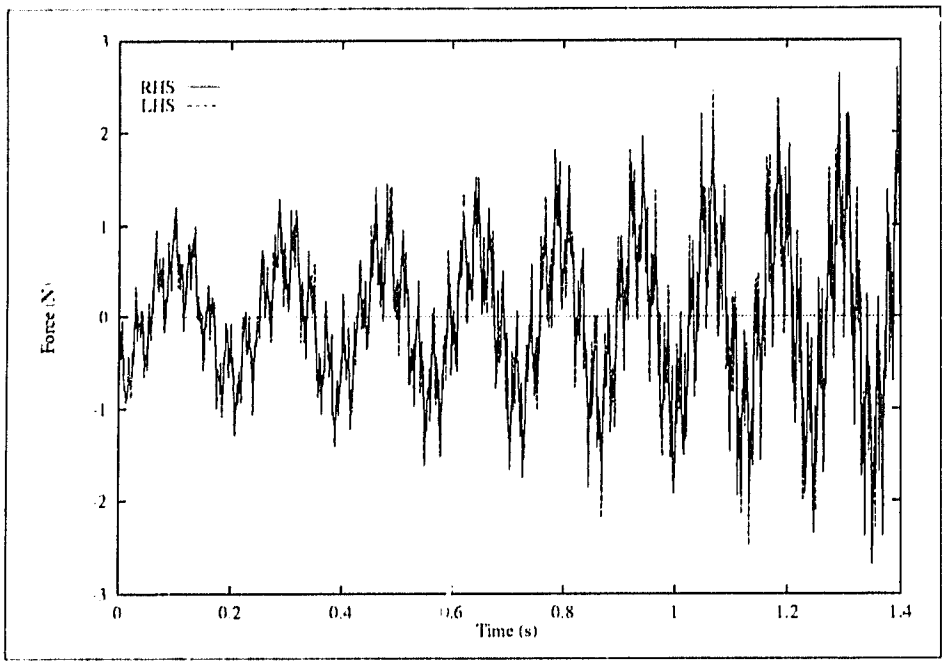


Figure 4.12: Right- and left-hand sides of Eq. (4.7) with a four-element model.

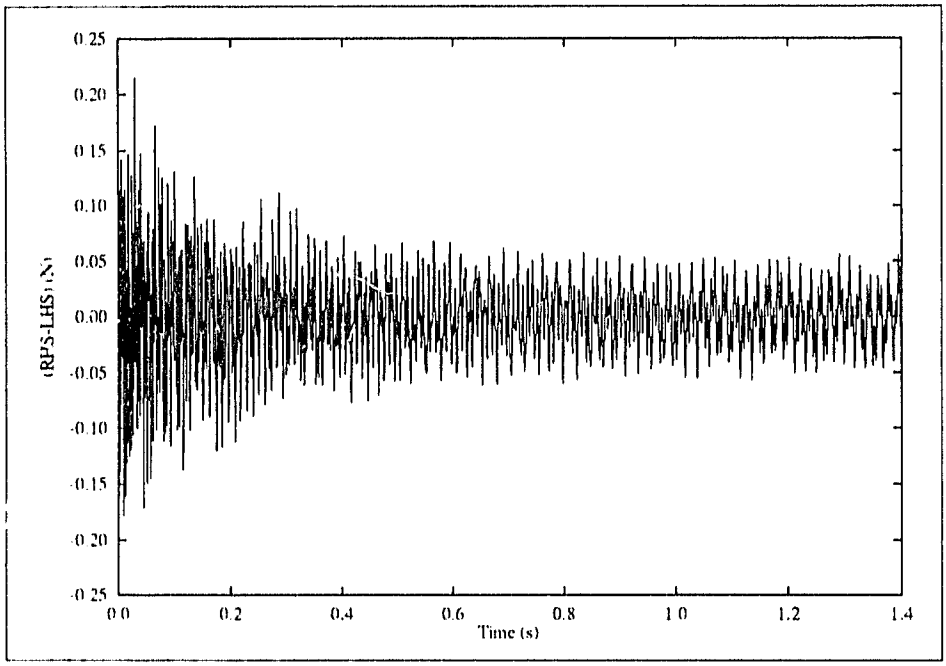


Figure 4.13: Error (RHS - LHS) for Eq. (4.7) with a four-element model.

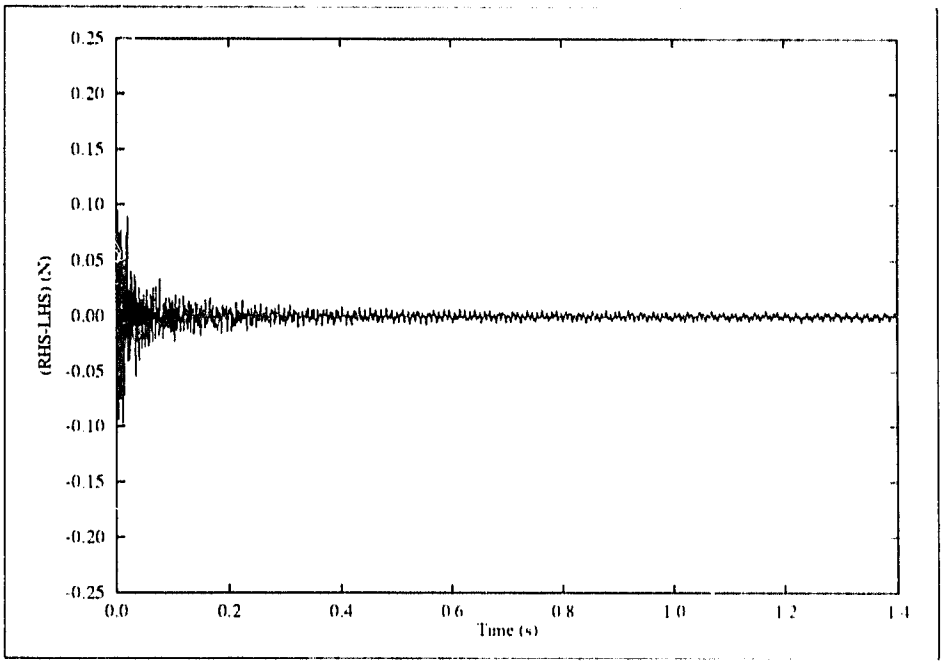


Figure 4.14: Error (RHS - LHS) for Eq. (4.7) with a ten-element model.

### 4.1.4 Parabolic Extrusion

As mentioned earlier, Tabarrok et al. (1974) obtained a similarity solution to the flexible extendible beam problem. In this special case, the beam extrudes from a rigid wall with a parabolic axial-motion profile given by

$$L(t) = \eta\sqrt{t}. \tag{4.8}$$

The parameter $\eta$ has units of $m/\sqrt{s}$. As will be discussed in Chapter 5, for such an axial motion history the problem reduces to an eigenvalue problem. For a finite-element model with $n$ degrees of freedom, the similarity solution corresponds to $n$ similarity pairs $[U_i,\{S_i\}]$ where

$$U_i = (\eta_i^2/2)\sqrt{\frac{\rho A}{EI}} = (2i-1)\pi \qquad i = 1,\ldots n, \tag{4.9}$$

and $\{S_i\}$ are vectors of order $n$. The first two analytical similarity modes (which appear in a Fresnel integral form) are plotted in Figs. (4.15) and (4.16).

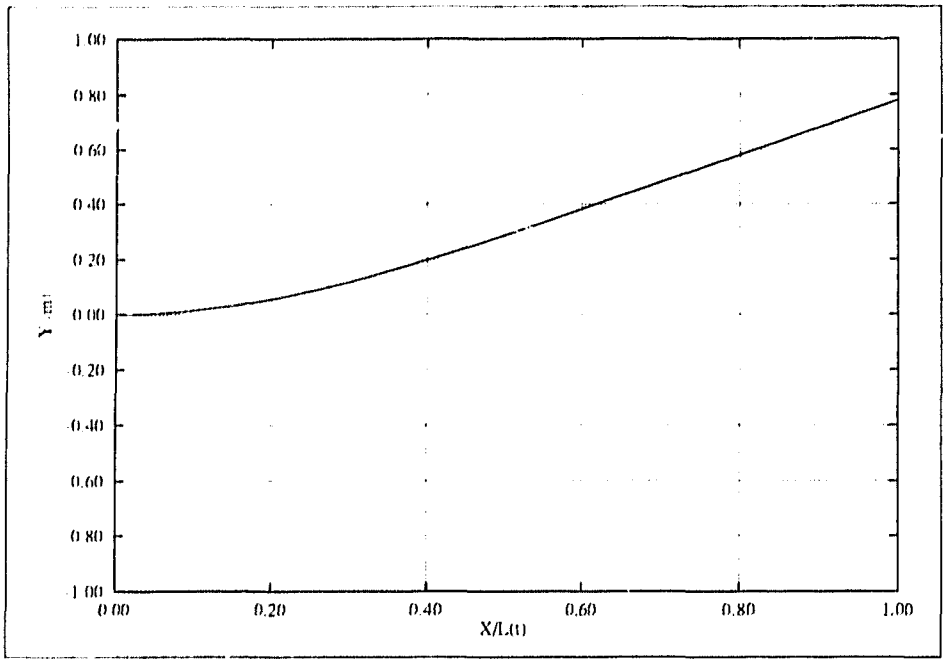


Figure 4.15: First similarity mode.

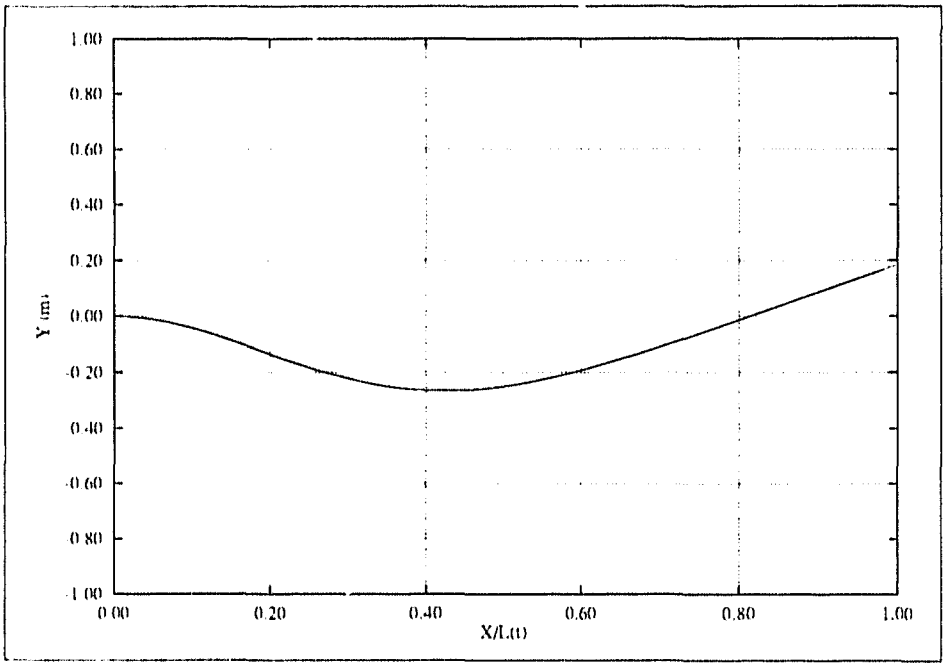


Figure 4.16: Second similarity mode.

The extrusion profile of Eq. (4.8) indicates the presence of acceleration. Hence, we need to specify whether the extrusion is due to an acceleration field or a root-applied force. For the purpose of the following examples, we assume that the extrusion is due to a uniform acceleration field (hence matrix $[k_2]$ in Eq. (3.31) vanishes).

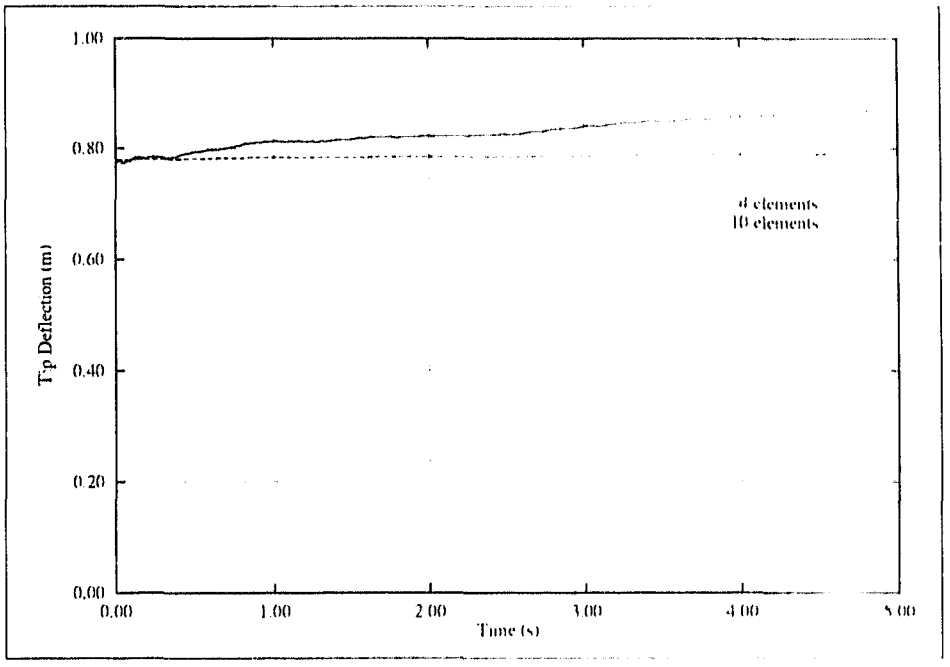


Figure 4.17: Tip-deflection history of the similarity simulation.

In Chapter 5 we discuss in detail the significance and physical interpretation of the similarity solution. For the purpose of this section, it suffices to say that the parabolically-extruding beam is expected to perform a non-oscillatory motion if the parameter $\eta$ of Eq. (4.8) and the beam's initial deflection are given by a similarity pair $[U_1,\{S_1\}]$. Figure (4.17) depicts the tip-deflection history of a simulation where the parameter $\eta$ and the beam's initial deflection are given by the first similarity pair $[U_1,\{S_1\}]$ computed from the finite-element model (described in Chapter 5). The initial length of the beam was taken as one metre. We used two finite-element models, one with four variable-domain beam elements and the other with ten. Due to the absence of physical damping and the extremely high axial velocity and axial acceleration at initial time, numerical-integration difficulties bring about small spurious oscillations at the beginning of the response history. The final length of the beam is $38.8\ m$, at which time the

maximum deviation of the tip from the initial deflection is *0.09 m* and *0.01 m* for the four- and ten-element models, respectively.

## 4.2 A Flexible Extendible Beam with a Tip Mass

It is an easy task to include a lumped mass at the tip of the beam in the finite-element model. A tip mass affects the mass matrix $[m]$ of the tip element only and the matrix $[k_2]$ of all elements. The definitions for these matrices become

$$[m]_{\text{element}} = \left( \int_0^{l(t)} \rho A \lfloor N \rfloor^T \lfloor N \rfloor dx \right) + \begin{bmatrix} 0 & 0 & 0 & 0 \\ 0 & 0 & 0 & 0 \\ 0 & 0 & \hat{m} & 0 \\ 0 & 0 & 0 & 0 \end{bmatrix}, \tag{4.10}$$

$$[k_2]_i = \int_0^{l(t)} \ddot{L} \left( \rho A \left( d_i - x \right) + \hat{m} \right) \lfloor N' \rfloor^T \lfloor N' \rfloor dx, \tag{4.11}$$

where $\hat{m}$ is the translational inertia of the tip mass.

The next two examples revisit the fourth experimental test case and the seventh simulation case of Section 4.1.1, with the addition of a tip mass. The results are shown in Figs. (4.18) and (4.19). In both cases, the tip mass is taken as 10% of the mass of the protruding part of the beam at time zero. The addition of the tip mass has the expected effect of lowering the frequency of oscillations. However, it is also noted that the amplitude of oscillations increases. This is due to the instationary nature of the problem. In Chapter 5, we study the effects of a tip mass on the stability characteristics of the system.

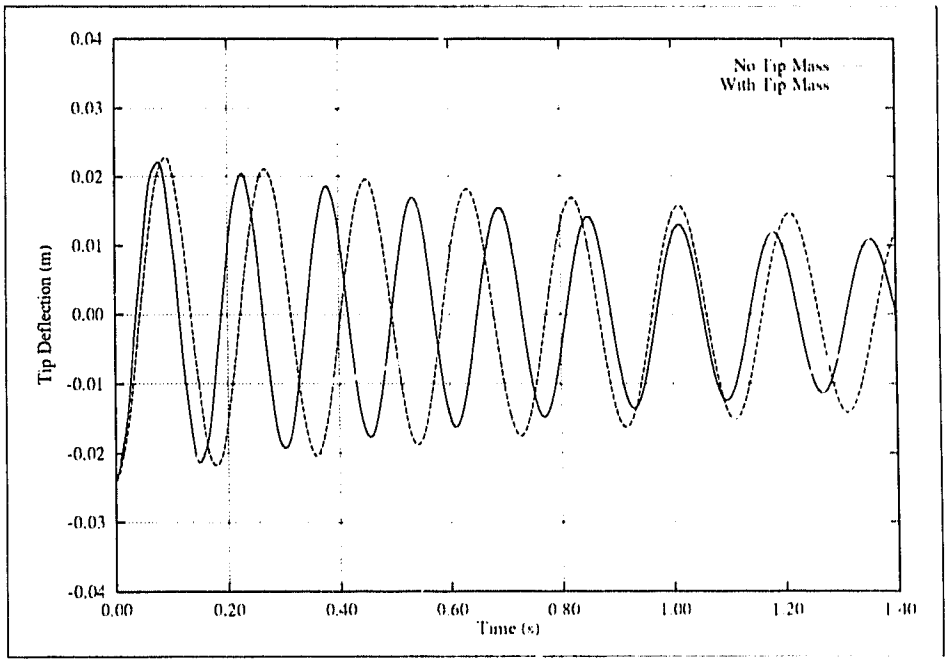


Figure 4.18: Test case # 4 with a tip mass. Constant-acceleration extrusion.

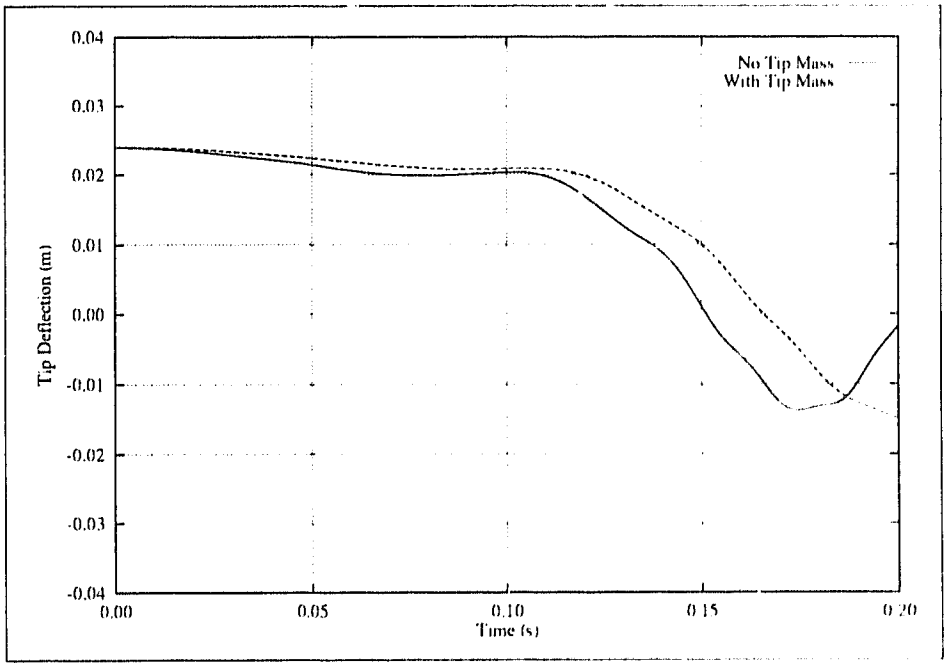


Figure 4.19: Simulation #7 with a tip mass. High-frequency retraction.

## 4.3 A Nested Axially-Moving Beam

This example deals with an axially-moving beam nested in part within a stationary, simply-supported envelope beam as shown in Fig. (4.20).

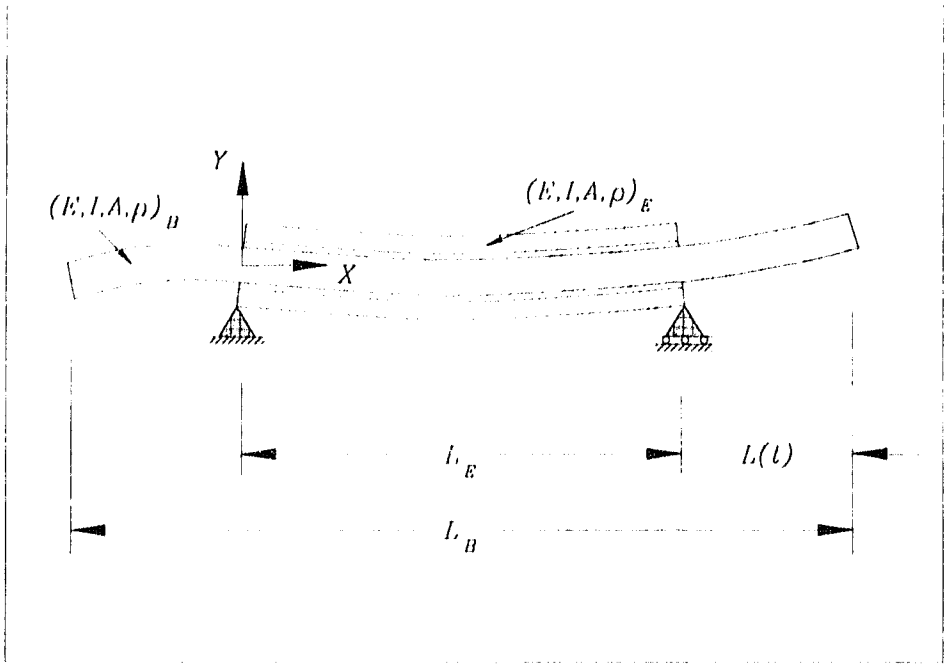


Figure 4.20: A nested axially-moving beam.

Our finite-element model has a total of twenty-four degrees of freedom, with four elements for each of the four regions described below. With $l_i$ as the length of the $i^{th}$ element and $d_i$ as defined in Eq. (3.5), we have the following modelling parameters:

1. Retracting left-hand side of axially-moving beam

$$l_i = (L_B - L(t) - L_E)/4, \qquad d_i = -(i-1)\,l_i, \qquad i = 1, \ldots 4. \tag{4.12}$$

2. Nested part of axially-moving beam

$$l_i = L_E/4, \qquad d_i = L(t) + L_E - (i-5)\,l_i, \qquad i = 5, \ldots 8. \tag{4.13}$$

3. Extruding right-hand side of axially-moving beam

$$l_i = L(t)/4, \qquad d_i = L(t) - (i-9)\,l_i, \qquad i = 9, \ldots 12. \tag{4.14}$$

4. Stationary envelope beam

$$l_i = L_E/4, \qquad d_i = \text{not applicable}, \qquad i = 12, \ldots 16. \tag{4.15}$$

Since the elements of the middle part of the axially-moving beam are of constant length, $\lfloor \dot{N} \rfloor_y$ vanishes in Eq. (3.18) for these elements. To illustrate the effect of the flexible envelope beam on the motion of the axially-moving beam, we examine two cases in which we vary the geometric and material properties of the envelope beam while keeping the properties of the axially-moving beam the same as the ones used in Yuh and Young's experiments and simulations.

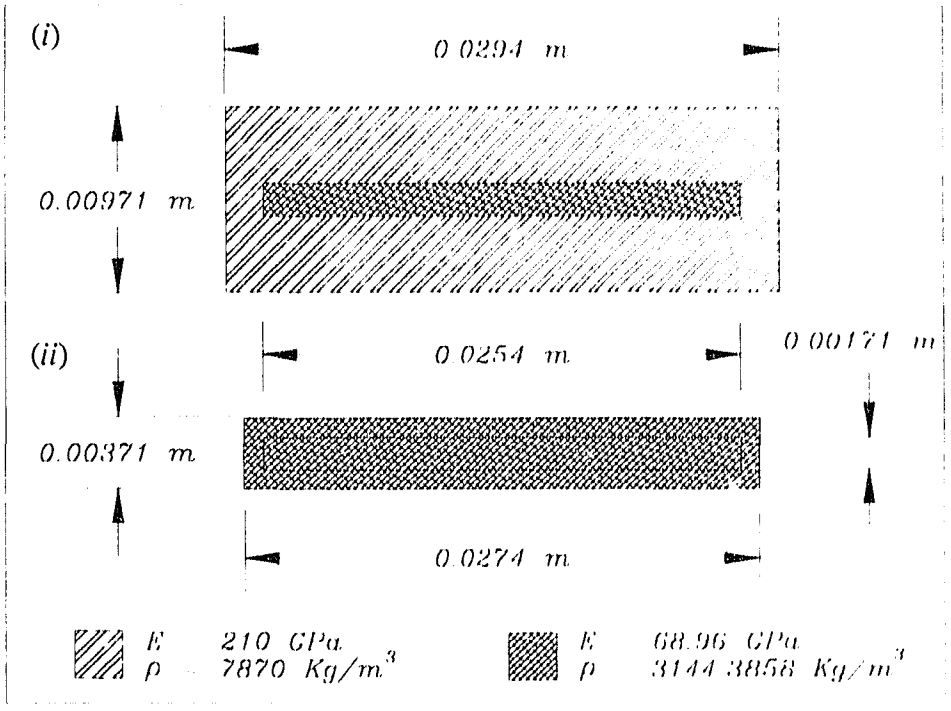


Figure 4.21: Geometric and material properties of the beams.

In the first case, we use the first cross-sectional geometry of Fig. (4.21) and take the material as steel. This combination makes the envelope beam considerably stiffer than the axially-moving beam. The axially-moving beam is made to move in the positive $X$ direction with the profile $L(t)$ used in the first simulation of Yuh and Young in Section 4.1.1. The length of the axially-moving beam is taken as $L_B$=1.7$m$ and that of the envelope beam as $L_E$=0.3$m$. We observe the motion of the right- and left-hand tips.

This configuration gives us Yuh and Young's first and third simulations of Section 4.1.1 simultaneously. The extruding right-hand side corresponds to the first simulation, and the retracting left-hand side corresponds to the third simulation. The same system configuration is also used in the second case where the axially-moving beam and the envelope beam have comparable stiffness and mass distributions. In this case, however, the envelope has the second cross-sectional geometry of Fig. (4.21) and the material is aluminium for both beams.

We also attach tip masses to the extruding right-hand and retracting left-hand tips (one at a time) with their mass taken as 10% of the mass of the corresponding protruding part of the axially-moving beam at time zero. The response obtained is shown in Fig. (4.22), where we show the time response of the extruding tip when the axially-moving beam is protruding from a rigid wall, and compare it with the results obtained from the two cases of the nested axially-moving beam of Fig. (4.20). A similar procedure is followed for the retracting left-hand tip with the results shown in Fig. (4.23).

From results depicted in Figs. (4.22) and (4.23), one may conclude the following:

1) As the stationary envelope beam is made stiffer, the responses of the retracting and extruding tips of the axially-moving beam approach the corresponding responses obtained when the axially-moving beam is protruding from a rigid wall.

2) The flexibility of the envelope beam reduces the frequency of oscillations, as evidenced by the period elongation in the time response of both tips.

3) The amplitude of the oscillations is not visibly affected in these two cases, and since the system is instationary, it is difficult to draw general conclusions as to the effect of the envelope flexibility on the amplitude of oscillations. However, through additional simulations we have found that the effect of the flexible envelope is to increase (decrease) the amplitude of oscillations for the extruding (retracting) part of the axially-moving beam.

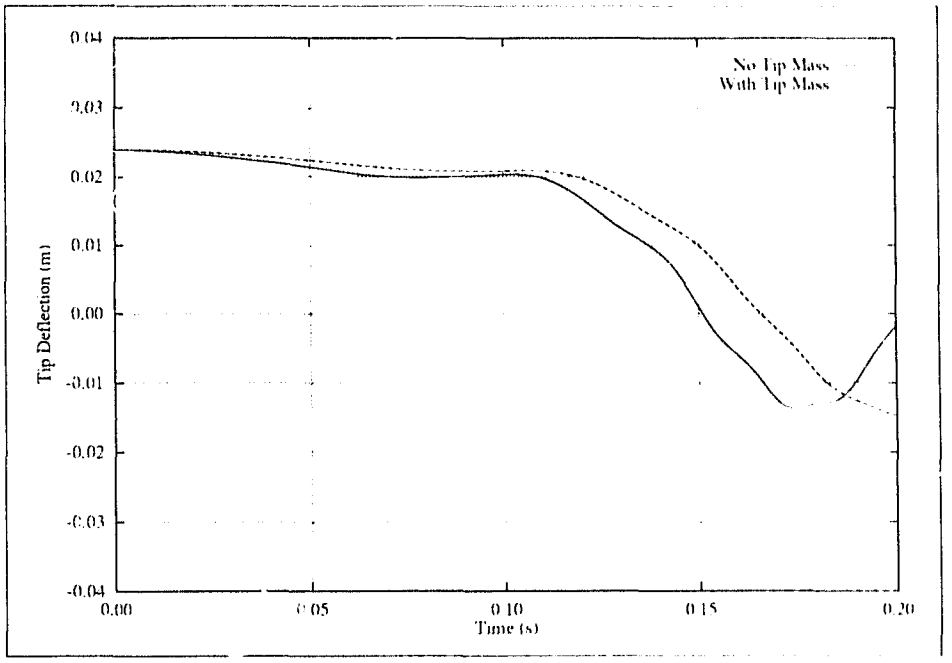


Figure 4.22: Nested extruding right-hand tip.

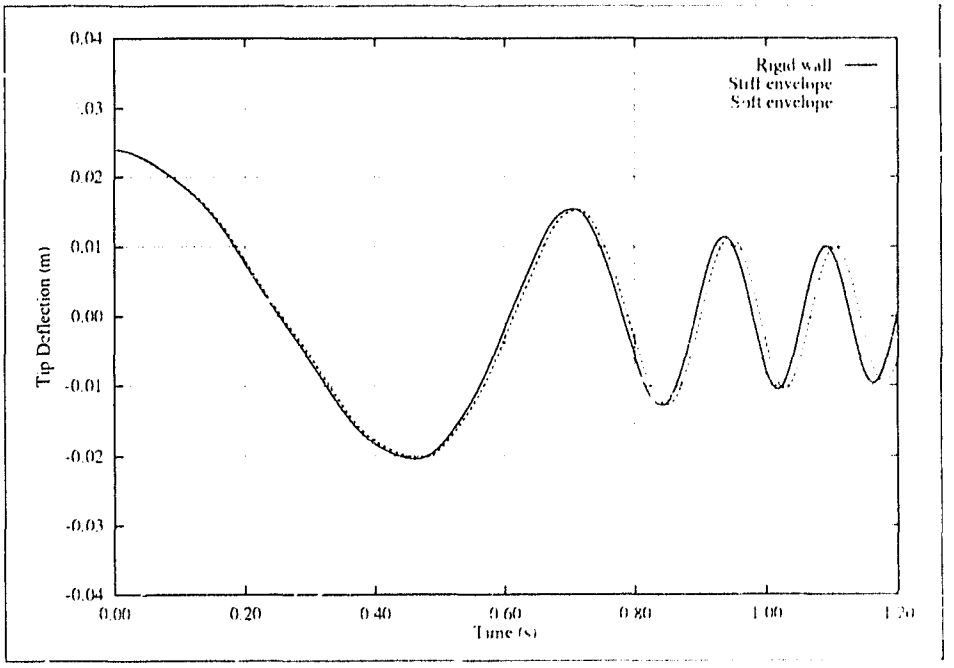


Figure 4.23: Nested retracting left-hand tip.

It should be noted here that the time integration of the first case (where the envelope was considerably stiffer than the axially-moving beam) was performed using the Newmark direct integration method with constant time-step. This was necessary since the relatively stiff envelope causes the variable time-step size algorithm to choose very conservative time-step sizes (many orders of magnitude smaller than necessary for accurate time-integration of the equations of motion of the axially-moving beam).

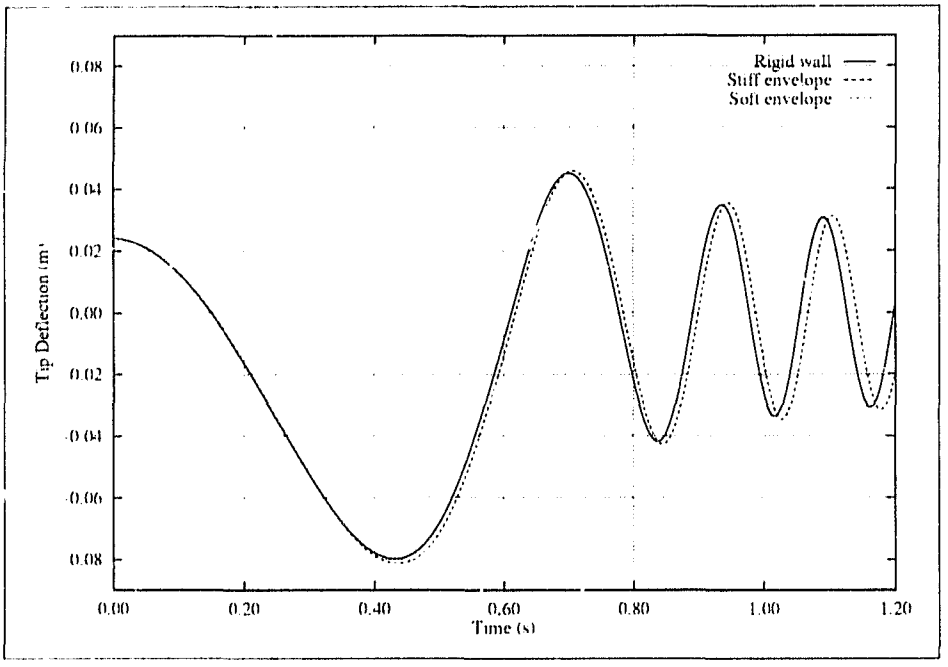


Figure 4.24: Retracting left-hand tip with active transverse acceleration.

Our finite-element analysis program can also model transverse loads (constant and time dependent) applied to any nodal point of the envelope and the axially-moving beam. In addition, it can model forces caused by transverse acceleration fields, such as the gravitational field. To demonstrate this capability, we solve again the two cases of the nested axially-moving beam, but this time with active transverse acceleration in the negative $Y$ direction (Fig. (4.20)) of magnitude $1.0\ m/s^2$, and we monitor only the response of the retracting left-hand tip.

The time response of the left-hand tip is shown in Fig. (4.24). As expected, the amplitude of the oscillations increases considerably beyond that obtained in the absence of the transverse acceleration field (Fig. (4.23)). The effects of the flexibility of the enve-

lope beam on the response of the retracting tip are in keeping with the observations made earlier in this section.

## 4.4 Active Vibration Suppression Using High Frequency Perturbations

Golnaraghi (1991) used a sliding mass-spring-dashpot mechanism placed at the free end of a stationary cantilever beam to passively reduce transverse oscillations. From some preliminary studies we have found that it is possible to reduce the transverse oscillations of flexible extendible beams by introducing a high-frequency, low-amplitude perturbation to the otherwise constant-velocity axial motion. We used the first two test cases of Section 4.1.1 with the modified axial-motion profile given by

$$L(t) = L_0(1 + \varepsilon \sin(\hat{\omega} t)) + vt. \tag{4.16}$$

The variables $L_0$, $v$ and $t$ have the same meaning as in Eq. (4.3) and their values are repeated in Table (4.3).Using an iterative procedure, we varied the size of the perturbation amplitude $\varepsilon L_0$ and frequency $\hat{\omega}$ and observed the effect on the transverse oscillations of the constant-velocity flexible extendible beam. Our preliminary study revealed that the same combination of values for $\varepsilon L_0$ and $\hat{\omega}$ has the same general effect on the transverse oscillations of the system regardless of whether the beam is retracting or extruding. For example, it was found that for the two test cases examined, the optimum values of the perturbation parameters for vibration suppression are as follows

$$\varepsilon L_0 \approx 7\ mm, \qquad \text{and} \qquad \hat{\omega} \approx 1/1\,\omega_1\ \text{rad/s}, \tag{4.17}$$

where $\omega_1$ is the instantaneous fundamental natural frequency of the flexible extendible beam.

| Test case # | $L_0$ (m) | $v$ (m/s) | $\varepsilon$ | $\omega_1 / 2\hat{\omega}$ |
|---|---|---|---|---|
| 1: Retraction | 0.5250 | -0.1145 | 0.0133 | 2.3452 |
| 2: Extrusion | 0.4255 | +0.0410 | 0.0165 | 2.3452 |

Table 4.3: Parameters for vibration suppression.

The resulting suppression of oscillations is clearly depicted in Figs. (4.25) and (4.26) where the tip response of both the unperturbed and perturbed systems are shown. During the final stages of the retracting and extruding test cases, the high-frequency perturbation reduces the amplitude of oscillations by 34% and 43%, respectively.

The problem of transverse oscillations of beams subjected to prescribed axial oscillatory motion has been studied theoretically by Zajaczkowski and Lipinski (1979) and Zajaczkowski and Yamada (1980). These authors show that the governing equations are of Mathew-Hill type giving rise to regions of stability and instability. Zajaczkowski and Lipinski (1979) investigated the parametric instability of the motion of a cantilever beam of periodically varying length $L(t) = L_o(1 - \varepsilon\cos\hat{\omega}t)$. Their results are presented in the form of stability charts in terms of $\varepsilon$ versus the parameter $\sqrt{\omega_1/2\hat{\omega}}$. It is of interest that the values for $\varepsilon$ and $\sqrt{\omega_1/2\hat{\omega}}$ listed in Table (4.3), found by trial and error in this study, fall within the extreme case of stable solutions found by Zajaczkowski and Lipinski (1979).

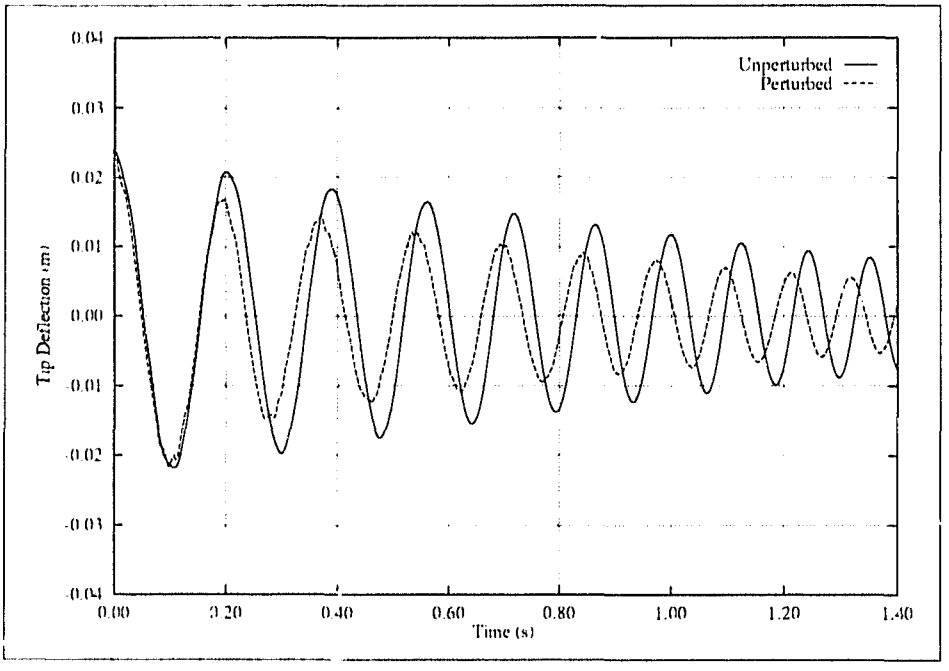


Figure 4.25: Test case # 1 with high-frequency perturbation (retraction).

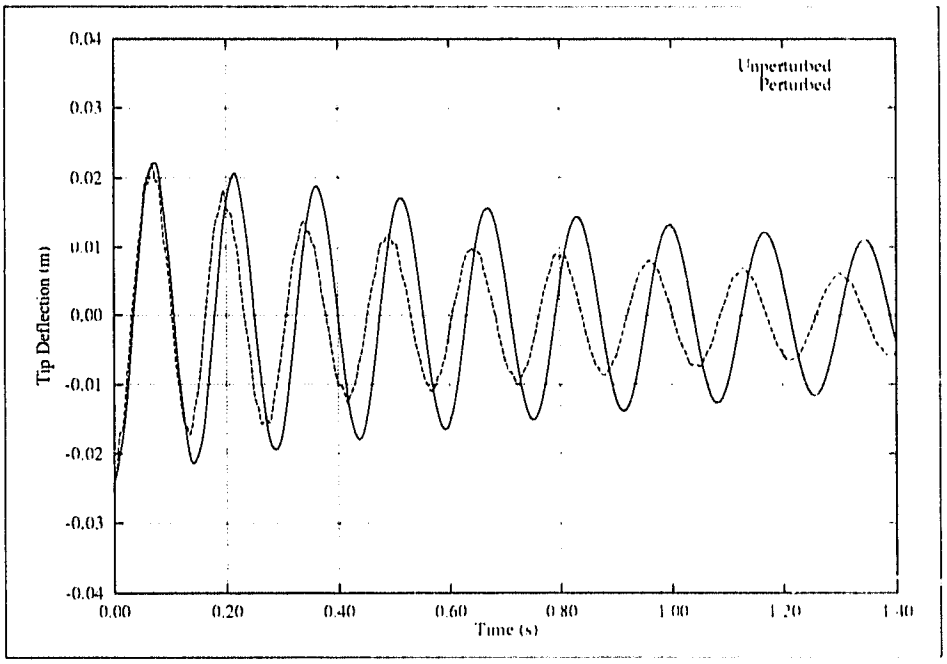


Figure 4.26: Test case # 2 with high-frequency perturbation (extrusion).

## 4.5 Concluding Remarks

In the foregoing, we have used various axial-motion profiles and integrated the finite-element equations. The time histories of the tip deflection were compared to the experimental and simulation results obtained by Yuh and Young (1991). Good agreement was achieved in all eight cases. Furthermore, we have reproduced the expected behaviour of the flexible extendible beam as predicted by the similarity solution. Specifically, we have shown that the flexible extendible beam undergoes a non-oscillatory motion if the axial-motion profile and initial deflection are given by a similarity pair $[U_i,\{S_i\}]$. The adequacy of the finite-element models and the accuracy of the solution procedure were also verified by computation of the invariant quantities derived in Section 2.2.2.

For the case of constant axial-velocity, it was shown that the total energy of the system changes in time. Specifically, it was demonstrated that during extrusion the system dissipates energy, while during retraction it gains energy.

The generality of the variable-domain element was demonstrated in examples which are not readily analysed by the assumed-modes approach. The addition of a tip mass is a trivial task in the case of the variable-domain element approach, whereas in the case of the assumed-modes approach, one set of mode-functions must be assumed in the absence of a tip mass and another set assumed when a tip mass is added. The assumed-modes also depend on the boundary conditions and, in many cases, the modal functions may not be available in closed form, making it necessary to generate the modal functions numerically at each time step, and then to numerically differentiate them to obtain their derivatives. The significant loss of accuracy associated with numerical differentiation of functions is well known; furthermore, when the functions are already approximate, one can anticipate considerable deterioration of accuracy as higher-order derivatives are computed.

The second example shows how the variable-domain element was successfully used to model a more complicated configuration, namely, the case of a flexible link moving through a flexible prismatic joint. In addition, this example demonstrated the effect of a transverse acceleration field on the response of the nested axially-moving beam. Finally, we briefly discussed how high-frequency axial-motion perturbations can be used to suppress transverse oscillations of flexible extendible beams.

# Chapter 5

# Stability Analysis

The illustrative examples of Chapter 4 were concerned exclusively with the numerical integration of the system equations with an emphasis on the time response of the tip of the flexible ex :ndible beam. However, to gain a deeper insight into the mechanics of the flexible extendible beam, it is beneficial to examine the stability characteristics of this system. In the following, we analyse the stability of the flexible extendible beam under changes of some of its pertinent parameters, such as the axial-motion profile, physical damping, mass distribution, tip support, wall flexibility, etc. We also demonstrate the versatility of the variable-domain be m element by analysing the stability of pipes conveying fluid.

## 5.1 Dynamic Stability

The flexible extendible beam, being an instationary system (as long as the boundary conditions are such that its length changes with time), may loose stability by either divergence (a static form of instability) or flutter (a dynamic form of instability). In addition, it may have multiple stable and unstable ranges which can be determined through the use of the dynamic method of stability analysis (see Herrmann (1967)). In

general, we seek values of a system-characteristic quantity for which the most general free motion of the perfect system – in the vicinity of the equilibrium configuration – ceases to be bounded. We begin by reducing the system of governing equations (Eq. (3.32)) to a set of first-order differential equations. The set of reduced equations takes the form:

$$[A]\,\{\dot{Z}\} + [B]\,\{Z\} = \{0\}, \tag{5.1}$$

where

$$[A] = \begin{bmatrix} [0] & [M] \\ [M] & [C_{eq}] \end{bmatrix}, \qquad [B] = \begin{bmatrix} -[M] & [0] \\ [0] & [K_{eq}] \end{bmatrix}, \qquad \{Z\} = \begin{bmatrix} \{\dot{Y}\} \\ \{Y\} \end{bmatrix}. \tag{5.2}$$

As discussed in Section 3.3, the equivalent-damping and equivalent-stiffness matrices are non-symmetric. Therefore, matrices $[A]$ and $[B]$ will, in general, be non-symmetric as well. Rearranging Eq. (5.1), we write

$$\{\dot{Z}\} - [D]\,\{Z\} = \{0\}, \tag{5.3}$$

where

$$-[D] = [A]^{-1}[B] = \begin{bmatrix} [M]^{-1}[C_{eq}] & [M]^{-1}[K_{eq}] \\ -[I] & [0] \end{bmatrix}. \tag{5.4}$$

We now assume that $\{Z\}$ is periodic, i.e.

$$\{Z\} = \{\Lambda\}\, e^{\lambda t}, \tag{5.5}$$

where $\lambda$ is generally complex. Then Eq. (5.3) takes the familiar form of an eigenvalue problem,

$$(\lambda [I] - [D])\,\{\Lambda\} = \{0\}. \tag{5.6}$$

In the eigenvalue problem of Eq. (5.6), the axial-motion profile must be prescribed for evaluation of the matrix $[D]$, and only then can we proceed with the solution of the conventional eigenvalue problem. For a system with $n$ degrees of freedom the eigen-problem of order $2n$ in Eq. (5.6) will, in general, yield $2n$ complex eigenvalues $\lambda_i$ with corresponding complex eigenvectors $\{\Lambda_i\}$. Each consecutive pair of eigensolutions

$[\lambda_i,\{\Lambda_i\}]$ and $[\lambda_{i+1},\{\Lambda_{i+1}\}]$ corresponds to a single physical oscillatory mode. That is, the first two eigensolutions $[\lambda_1,\{\Lambda_1\}]$ and $[\lambda_2,\{\Lambda_2\}]$ correspond to the fundamental oscillatory mode, $[\lambda_3,\{\Lambda_3\}]$ and $[\lambda_4,\{\Lambda_4\}]$ to the second oscillatory mode and so on. It should be noted that the real and imaginary parts of the eigenvalues are related to the modal damping coefficients and the oscillatory frequencies. Thus, if for the $i^{th}$ oscillatory mode we write the corresponding set of complex conjugate eigenvalues as

$$\lambda_1^i = -a+jb \qquad \lambda_2^i = -a-jb \tag{5.7}$$

and we let $\xi_i$ and $\omega_i$ correspond to the modal damping coefficient and oscillatory frequency, respectively, we can then write

$$\begin{aligned} a &= \omega_i \xi_i \\ b &= \omega_i \sqrt{1-\xi_i^2} \end{aligned} \tag{5.8}$$

The oscillatory mode-shapes are contained within the complex conjugate eigenvectors. They correspond to the lower part of $\{\Lambda_i\}$ which is purely real. The stability characteristics of the system may then be deduced from the nature of the complex eigenvalues $\lambda_i$ (see for example Thompson (1987)) and do not depend on the system eigenvectors. In the sequel, we perform a stability analysis of the flexible extendible beam under changes of some of its pertinent parameters. In particular, we investigate the effects of the following factors on the stability characteristics of the flexible extendible beam:

1. Type of axial-motion profile function $L(t)$.

2. Addition of physical damping.

3. Inclusion of wall flexibility (the flexible extendible beam protrudes from a flexible cantilevered beam).

4. Addition of a tip mass.

5. Change of tip support.

In this chapter we also use the variable-domain beam element to perform a stability analysis of pipes conveying fluid and compare our results with those obtained by Païdoussis

doussis (1991) who uses analytical methods as well as various numerical techniques including the assumed-modes approach.

Unless otherwise stated, we consider a flexible extendible beam with a finite-element model using ten variable-domain beam elements, with the beam's geometric and material properties as shown in Fig. (4.21).

## 5.2 Constant-Velocity Extrusion

The axial motion of the beam is described by a function of the general form

$$L(t) = L_0 + vt, \tag{5.9}$$

where $L_0$ is the initial length and $v$ the extruding velocity. The lateral motion of this system is governed by the partial differential equation (see Eq. (2.5))

$$\rho A\,(Y_{tt} + 2vY_{tX} + v^2 Y_{XX}) + EIY_{XXXX} = 0. \tag{5.10}$$

Comparing this with the equation for lateral motion of a beam subjected to a conservative axially-applied compressive load $p$, namely

$$\rho AY_{tt} + pY_{XX} + EIY_{XXXX} = 0, \tag{5.11}$$

we note that the centrifugal force $\rho Av^2$ plays a similar role to the compressive load $p$. Hence, we expect that the equivalent-stiffness of the system will diminish with increasing axial velocity $v$, and that for sufficiently high extruding velocities the centrifugal force may overcome the flexural restoring force. Likewise, we expect the system's oscillatory frequencies to decrease with increasing axial velocity $v$, to the point where the fundamental oscillatory frequency vanishes. The Coriolis force per unit length $2\rho AvY_{tX}$ being conservative, performs no work on the system, but as will be seen it will have an effect on the stability characteristics of the system.

Following Païdoussis, we define a non-dimensional axial velocity as follows

$$U = vL\sqrt{\frac{\rho A}{EI}}. \tag{5.12}$$

Païdoussis determines the changes in the eigenvalues of his system (pipes conveying fluid) as a function of his non-dimensional velocity. We intend to do likewise and in so

doing we will determine the stability characteristics of our problem. There is, however, a subtle but important difference between Païdoussis' non-dimensional velocity and our own. For the problem of pipes conveying fluid, the length $L$ is fixed and hence changes in $U$ are directly related to changes in the actual velocity $v$. In our case, the length changes and this provides us a choice for calculating and interpreting the relationship between the eigenvalues of the system and $U$. We may choose to

a) keep $L$ fixed, say *1.0 m*, and then relate $U$ to $v$ as in the problem of pipes conveying fluid, or

b) keep $v$ constant, say *10.0 m/s*, and relate $U$ to $L$.

The eigenvalues of the system, to be determined as a function of $U$, can then be interpreted in two different ways. Under option (a), the eigenvalues will refer to the configuration of the system at a fixed instant of time, when for instance $L$=*1.0 m* and $v$ takes different values. Under option (b), the eigenvalues can be viewed as those of the system at different instants of time, for a specified constant value of $v$. In order that we may make some comparisons with the problem of pipes conveying fluid, we adopt option (a) for the calculation and interpretation of our results. It is important to note, however, that the calculated critical values $U$ are independent of the option chosen.

### 5.2.1 The Simplest Case

The eigenvalue problem of Eq. (5.6) is solved for the flexible extendible beam with the extrusion profile in Eq. (5.9) for various values of $v$. The evolutions of the system's first six complex eigenvalues are shown in Figs. (5.1) through (5.3), where the real and imaginary parts of the eigenvalues are shown separately in the left and right plots respectively.

We will now give a detailed description of the evolution of the first two eigenvalues shown in Fig. (5.1), with an emphasis on the consequences to the stability characteristics of the constant-velocity extruding beam. The name in brackets at the end of each description refers to the type of phase portrait (see, for example, Thompson (1987)).

1. For zero axial velocity ($U=0$), all eigenvalues are complex conjugates with zero real parts. This case corresponds to an undamped stationary cantilever beam of length $L_0$ (in this case $L_0=1.0\ m$). Therefore, the imaginary parts of the first and second eigenvalues correspond to the beam's fundamental natural frequency. *(center)*

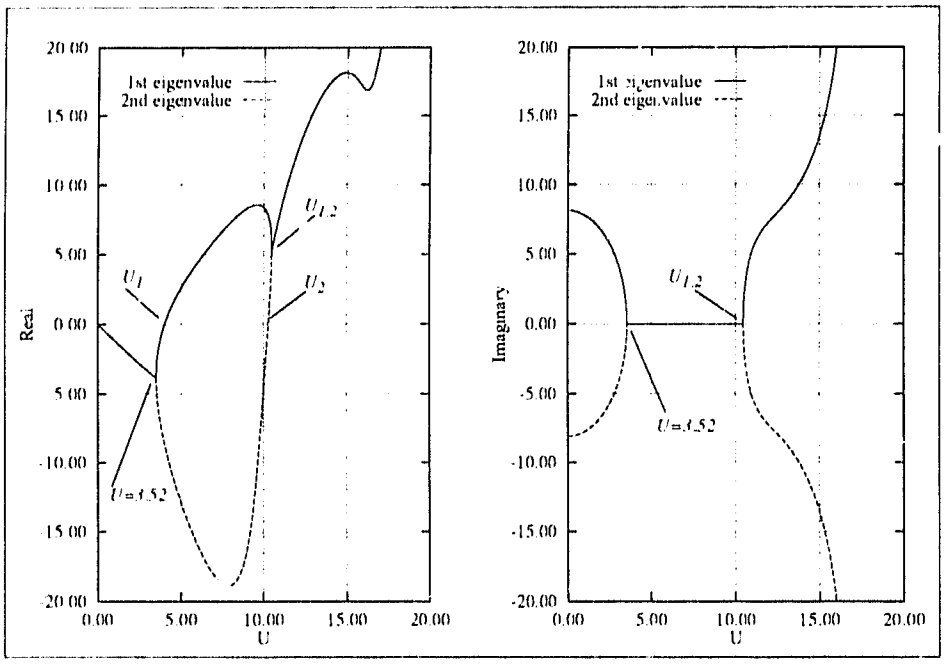


Figure 5.1: Real and imaginary components of the first and second eigenvalues.

2. For small values of $U$, all eigenvalues become complex conjugates with negative real parts, indicating the presence of dissipative forces. Under these conditions all oscillatory modes are stable. As noted in Section 3.3, for the case of extrusion where new mass elements enter the domain, the equivalent damping matrix $[C_{eq}]$ is positive-definite, implying that dissipative forces are generated. This finding is in direct contradiction with the conclusion of Wang and Wei (1987) that during extrusion the flexible extendible beam gains energy. *(stable focus)*

3. As $U$ is increased, the imaginary parts of all eigenvalues decrease and at $U \approx 3.52$ the imaginary parts of the first and second eigenvalues vanish. Up to this point, the real parts of the first and second eigenvalues are equal and negative, confirming that the first mode remains stable, albeit non-oscillatory. *(stable inflected node)*

4. As $U$ is further increased, the first and second eigenvalues move apart, but remain real and negative. *(stable node)*

5. When $U$ reaches the value of $U_f \approx 4.01$, the first eigenvalue vanishes altogether (i.e. $[K_{eq}]$ becomes singular) while the second eigenvalue remains real and negative. For conservative systems, a divergence instability (buckling) is characterised by the simultaneous vanishing of both eigenvalues, corresponding to an oscillatory mode. However, in the presence of dissipative forces, the onset of divergence is identified with the vanishing of only one of the eigenvalues. In order to distinguish between the two forms of instabilities, divergence in the case of dissipative systems will be referred to as *damped divergence*. Therefore, for the constant-velocity extruding beam, $U_f$ signals the onset of damped divergence where the undeformed configuration becomes unstable and all adjacent deformed states in the first mode become possible equilibria.

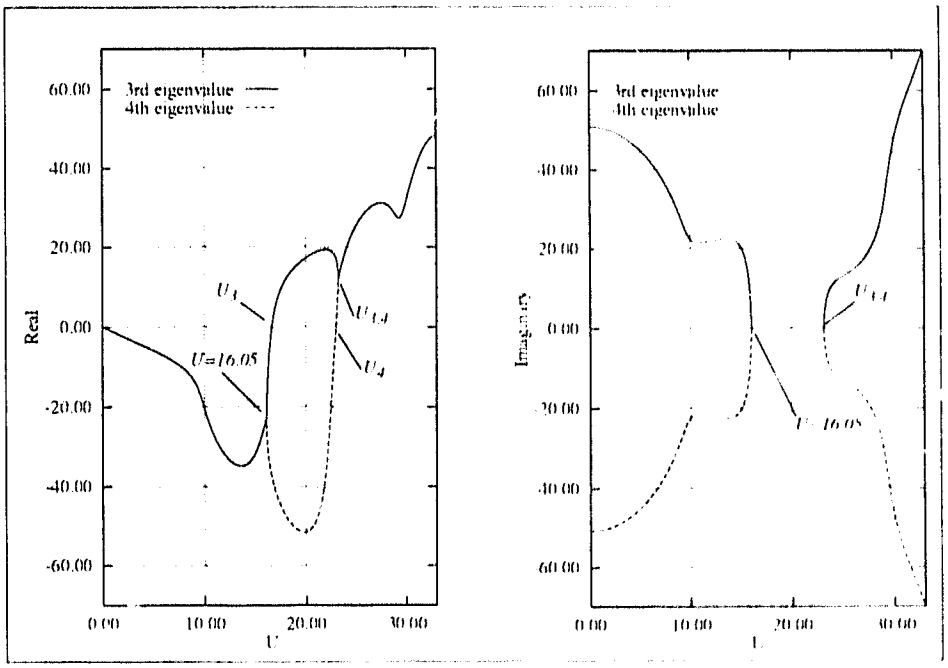


Figure 5.2: Real and imaginary components of the third and fourth eigenvalues.

6. Beyond $U_f$, the first eigenvalue becomes real and positive while the second eigenvalue remains real and negative. With one of its eigenvalues real and positive, the first mode is now unstable. *(saddle)*

7. If $U$ is increased further, it is seen that the second eigenvalue, still being real, vanishes at $U_2 \approx 10.28$, but the first eigenvalue remains real and positive, indicating that the first mode remains unstable.

8. Beyond $U_2$, the second eigenvalue also becomes real and positive. The first mode remains unstable since both eigenvalues are now real and positive. *(unstable node)*

9. At a slightly higher velocity than $U_2$, namely $U_{1,2} \approx 10.47$, the loci of the first and second eigenvalues coalesce with the imaginary parts remaining zero. The first mode remains unstable. *(unstable inflected node)*

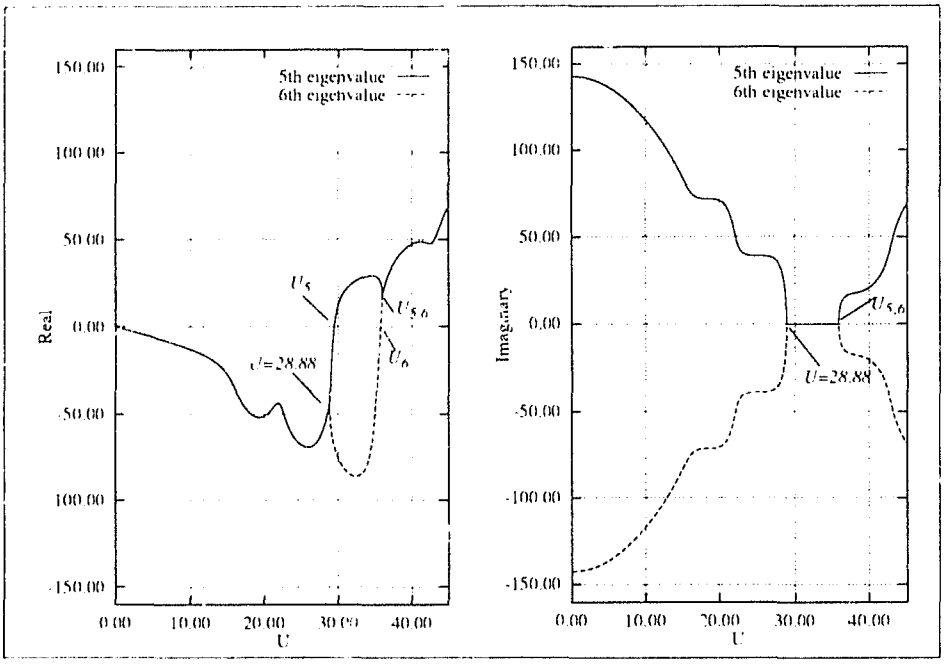


Figure 5.3: Real and imaginary components of the fifth and sixth eigenvalue.

10. At slightly higher velocities than $U_{1,2}$, the imaginary parts become non-zero and the first and second eigenvalues become, once again, complex conjugates, this time, however, with positive real parts. Therefore, $U_{1,2}$ is the critical axial velocity beyond which the constant-velocity extruding beam flutters. That is, any general free motion in the vicinity of the equilibrium configuration ceases to be bounded. It is important to note that at this point, flutter is due to the coalescence of the eigenvalue branches of a single oscillatory mode. Hence, it is of the one-degree-of-freedom type. Returning to Eqs. (5.10) and (5.11) and noting that a beam under

compressive conservative loading is not subject to oscillatory instabilities, we conclude that the existence of flutter in the case of the constant-velocity extruding beam is connected to the (conservative) Coriolis forces. *(unstable focus)*

The same general behavior (damped divergence followed by flutter) is also observed for the higher oscillatory modes, as can be seen from Figs. (5.2) and (5.3). Since linear theory cannot provide reliable information once the system motions leave the vicinity of the undeformed state, the physical existence of post-divergence flutter remains an open question. In the case of pipes supported at both ends and conveying fluid (a gyroscopic conservative system), linear theory's prediction of post-divergence flutter does not materialise physically. This was shown by experiments (Païdoussis, 1991) and by non-linear theory (Holmes, (1978)). However, the constant-velocity extruding beam is a gyroscopic instationary system, which can be subject to post-divergence flutter, and in fact this is what linear theory predicts.

| $U$ | Two elements | Four elements | Ten elements |
|---|---|---|---|
| $U_1$ | 4.08 | 4.02 | 4.01 |
| $U_2$ | 10.45 | 10.54 | 10.28 |
| $U_{1,2}$ | 10.56 | 10.73 | 10.47 |
| | | | |
| $U_3$ | 31.62 | 16.67 | 16.58 |
| $U_4$ | -- | 26.74 | 23.00 |
| $U_{3,4}$ | -- | 27.51 | 23.23 |
| | | | |
| $U_5$ | -- | 34.87 | 29.45 |
| $U_6$ | -- | -- | 35.74 |
| $U_{5,6}$ | -- | -- | 35.97 |

Table 5.1: Critical non-dimensional velocities versus number of elements.

The convergence of the computed values for the critical non-dimensional velocities with respect to the number of elements used is shown in Table (5.1). It is noted that the two- and four-element models are sufficiently accurate for the computation of up to the second and third critical axial velocities, respectively, and that due to the instationary

nature of the problem, convergence, in relation to the number of degrees of freedom, is non-monotonic.

The stability analysis of this section was also performed using option (b) as described in Section 5.2. The evolutions of the system's eigenvalues and a brief discussion may be found in Appendix F. A dynamic simulation during which the extruding beam loses stability by divergence may also be found in Appendix F.

### 5.2.2 Effect of Physical Damping

In order to account for damping effects, we introduced the physical proportional damping matrix $[C_p]$ discussed in Section 4.1. In this section, we study the effect of physical damping on the stability characteristics of the constant-velocity extruding beam. That is, we select values for the first two modal damping coefficients $\xi_1$ and $\xi_2$, form $[C_p]$ and $[C_{eq}]$ as defined in Eqs. (4.1) and (4.2), and perform a dynamic stability analysis. All examples in this section use the axial-motion profile in Eq. (5.9).

| $U$ | $\xi_1 = 0.0$<br>$\xi_2 = 0.0$<br>$L = 1$ m | $\xi_1 = 14.99\ 10^{-3}$<br>$\xi_2 = 15.33\ 10^{-3}$<br>$L = 1$ m | $\xi_1 = 14.99\ 10^{-3}$<br>$\xi_2 = 15.33\ 10^{-3}$<br>$L = 5$ m | $\xi_1 = 149.9\ 10^{-3}$<br>$\xi_2 = 153.3\ 10^{-3}$<br>$L = 1$ m |
|---|---|---|---|---|
| $U_1$ | 4.01 | 4.01 | 4.01 | 4.01 |
| $U_2$ | 10.28 | 10.28 | 10.28 | 10.28 |
| $U_{1,2}$ | 10.47 | 10.49 | 10.49 | 10.65 |
| | | | | |
| $U_3$ | 16.58 | 16.58 | 16.58 | 16.58 |
| $U_4$ | 23.00 | 23.00 | 23.00 | 23.00 |
| $U_{3,4}$ | 23.23 | 23.31 | 23.31 | 24.12 |

Table 5.2: Effect of physical damping on the critical velocities.

Table (5.2) lists the critical velocities of the system using various values of modal damping. The first column lists the critical velocities of the undamped extruding beam. The second and third columns list the critical velocities of a one metre long and a five metre long extruding beam, respectively, with the modal damping parameters as found experimentally by Yuh and Young (1991). Finally, the fourth column lists the critical velocities of an extruding beam with artificially high damping coefficients. As

expected, regardless of the amount of physical damping added, there is no effect on the onset of divergence instabilities.

Figures (5.4) and (5.5) show the evolutions of the system's first four complex eigenvalues for the case of heavy damping (fourth column in Table (5.2)). Using the same format as used in the previous section, the real and imaginary parts of the eigenvalues are shown separately in the left and right plots, respectively. As can be seen, the evolution of the eigenvalues of the damped constant-velocity extruding beam follows the same general pattern as the undamped system described in detail in the previous section. However, the addition of damping has the following effects on the stability characteristics of the constant-velocity extruding beam (for details refer to Table (5.2) and Figs. (5.4) and (5.5)):

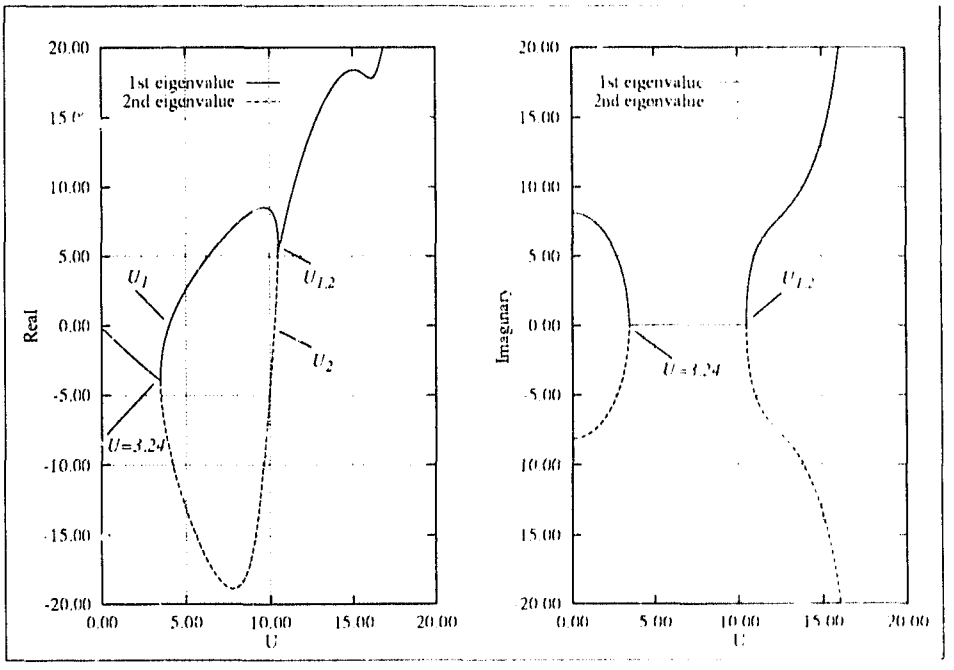


Figure 5.4: Effect of heavy damping on the first and second eigenvalues.

1. Since the system is now physically damped (by virtue of the presence of $[C_p]$), even for zero axial velocity ($U=0$), all eigenvalues are complex conjugates with negative real parts. This case corresponds to a damped stationary cantilever beam of length $L_0$ ($L_0$ = *1.0m*). Therefore, the imaginary parts of the first and second eigenvalues correspond to the beam's damped fundamental natural frequency.

2. As expected, the addition of $[C_p]$ results in the onset of non-oscillatory modes at lower axial velocities. For instance, the imaginary parts of the first and second eigenvalues vanish at $U \approx 3.24$, as opposed to $U \approx 3.52$ in the absence of physical damping.

3. The addition of $[C_p]$ postpones the onset of flutter. Specifically, the first and second eigenvalues coalesce at $U_{1,2} \approx 10.65$, as opposed to $U_{1,2} \approx 10.47$ in the absence of physical damping.

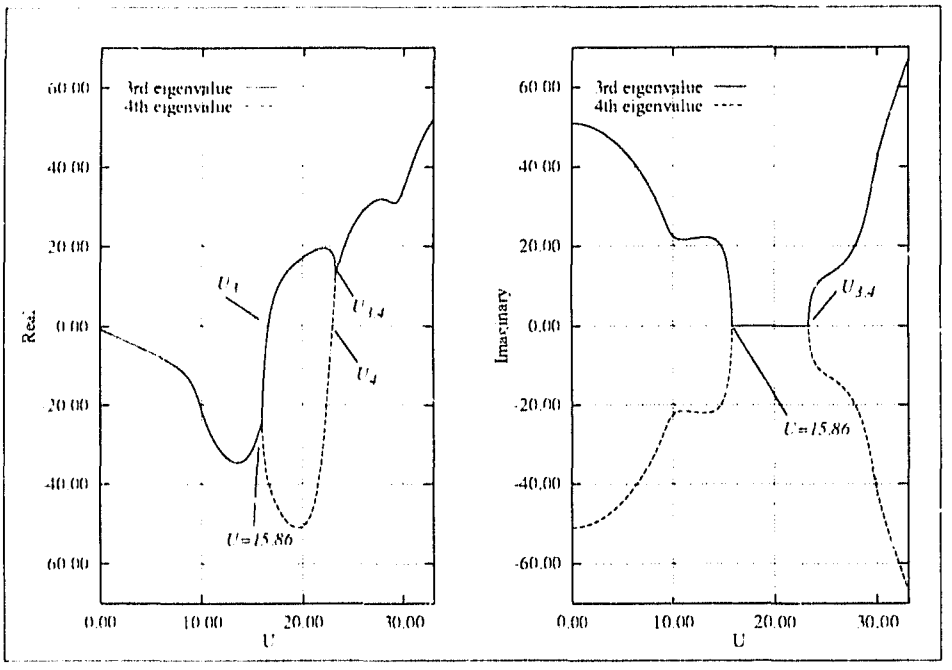


Figure 5.5: Effect of heavy damping on the third and fourth eigenvalues.

4. The final observation is related to the way we model damping through the use of the proportional damping matrix $[C_p]$. As can be seen from Table (5.2), by using the same damping coefficients for the first two oscillatory modes ($\xi_1$ and $\xi_2$), all critical velocities corresponding to all modes remain unchanged regardless of the beam's length. Therefore, the experimentally-obtained modal damping functions used by Yuh and Young (1991), namely

$$\xi_1 = \frac{0.4874}{4L^2\omega_1}$$
$$\xi_2 = \frac{3.124}{4L^2\omega_2} \tag{5.13}$$

where $\omega_1$ and $\omega_2$ are the instantaneous first and second natural frequencies of a cantilever beam of length $L(t)$, ensure that modal damping coefficients remain constant regardless of the length of the flexible extendible beam.

From the results presented in this section, one may conclude that structural damping has no appreciable effect (even at artificially high levels) on the overall stability characteristics of the constant-velocity extruding beam. Nevertheless, it was found that physical damping has the important effect of postponing the onset of flutter instabilities.

### 5.2.3 Effect of a Flexible Envelope Beam

Thus far our examples have dealt with flexible extendible beams protruding from an *infinitely rigid* wall. In this section we study the effect of flexibility at the root of the constant-velocity extruding beam. For this purpose, we use a flexible extendible beam nested in a cantilevered flexible envelope beam as shown in Fig. (5.6).

The rigidity of the cantilevered envelope beam is varied by appropriate selection of its cross-sectional geometric and material properties. In this section, *stiff* and *soft* envelopes refer to the cases where the cantilevered envelope and flexible extendible beams have the first and second cross-sectional geometric and material properties of Fig. (4.21), respectively. These geometric and material properties were chosen so as to ensure that the stiff envelope beam is considerably stiffer than the flexible extendible beam, whereas the soft envelope is of comparable stiffness and mass distribution to the flexible extendible beam.

The finite-element model for the nested configuration has a total of sixteen degrees of freedom, with four elements for each of the three regions described below. With $l_i$ the length of the $i^{th}$ element, and $d_i$ as defined in Eq. (3.5), we have the following modelling parameters:

1. Enveloped part of the flexible extendible beam

$$l_i = L_E/4, \qquad d_i = L(t) + L_E \quad (i-1)\, l_i, \qquad i = 1, \ldots 4. \tag{5.14}$$

2. Extruding right-hand side of the flexible extendible beam

$$l_i = L(t)/4, \qquad d_i = L(t) - (i-5)\, l_i, \qquad i = 5, \ldots 8. \tag{5.15}$$

3. Stationary envelope beam

$$l_i = L_E/4, \qquad d_i = \text{not applicable}, \qquad i = 9, \ldots 12. \tag{5.16}$$

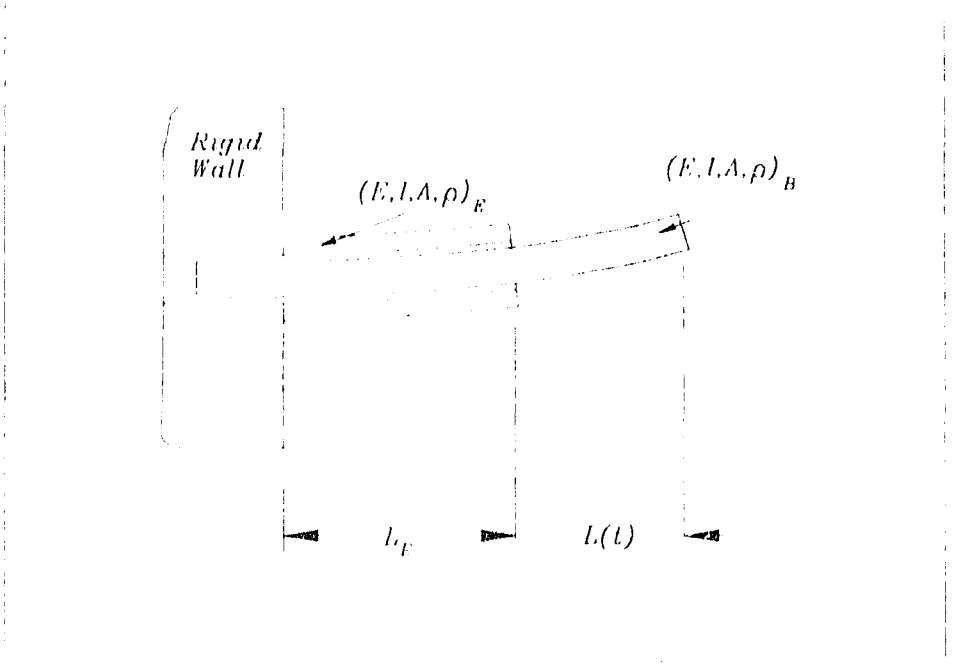


Figure 5 6: A nested flexible extendible beam.

Since the elements of the enveloped part of the flexible extendible beam are of constant length, $|\dot{N}|_i$ vanishes in Eq. (3.18) for these elements. The length of the envelope beam is taken as $L_E = 0.3\ m$ and the extrusion profile is, once again, given by Eq. (5.9) with $L_0 = 1.0\ m$.

The addition of the flexible envelope beam alters the system's rigidity and mass distribution and is expected to affect the onset of both static and dynamic instabilities. Figures (5.7) and (5.8) show the evolutions of the system's first four complex eigenvalues

for the case of the stiff envelope while Figs. (5.9) and (5.10) show the results for the case of the soft envelope. A comparison of these figures with the corresponding ones obtained for the undamped constant-velocity extruding beam (Figs. (5.1) and (5.2)) reveals that even in the case of the soft envelope, the evolution of the eigenvalues follows the same pattern. However, this study reveals the following effects of envelope flexibility on the stability characteristics of the system (for details refer to Table (5.3) and Figs. (5.7) through (5.10)):

1. The onset of non-oscillatory modes occurs at lower velocities. Specifically, the imaginary parts of the first and second eigenvalues vanish at $U \approx 3.33$ for the soft-envelope case ($U \approx 3.53$ for the stiff-envelope case) as opposed to $U \approx 3.53$ for the rigid-wall case.

2. Damped divergence occurs at lower velocities. For example, the first mode diverges at $U \approx 9.76$ for the soft-envelope case ($U \approx 10.53$ for the stiff-envelope case) as opposed to $U \approx 10.54$ for the rigid-wall case.

3. The onset of flutter also occurs at lower velocities. For instance, the first and second eigenvalues coalesce at $U_{1,2} \approx 9.88$ in the case of the soft envelope ($U_{1,2} \approx 10.72$ for the stiff-envelope case) as opposed to $U_{1,2} \approx 10.73$ for the rigid-wall case.

| $U$ | Rigid Wall | Stiff Envelope | Soft Envelope |
|---|---|---|---|
| $U_1$ | 4.02 | 4.02 | 3.80 |
| $U_2$ | 10.54 | 10.53 | 9.76 |
| $U_{1,2}$ | 10.73 | 10.72 | 9.88 |
| | | | |
| $U_3$ | 16.67 | 16.65 | 14.83 |
| $U_4$ | 26.74 | 26.73 | 19.73 |
| $U_{3,4}$ | 27.51 | 27.47 | 19.96 |

Table 5.3: Effect of the flexible envelope on the critical velocities.

In conclusion, the flexible envelope can have appreciable effect on the onset of both static and dynamic instabilities. The degree of influence depends on the envelope's dynamic stiffness relative to the flexible extendible beam. The onset of both damped divergence and flutter occurs at lower axial velocities as the stiffness of the envelope is decreased.

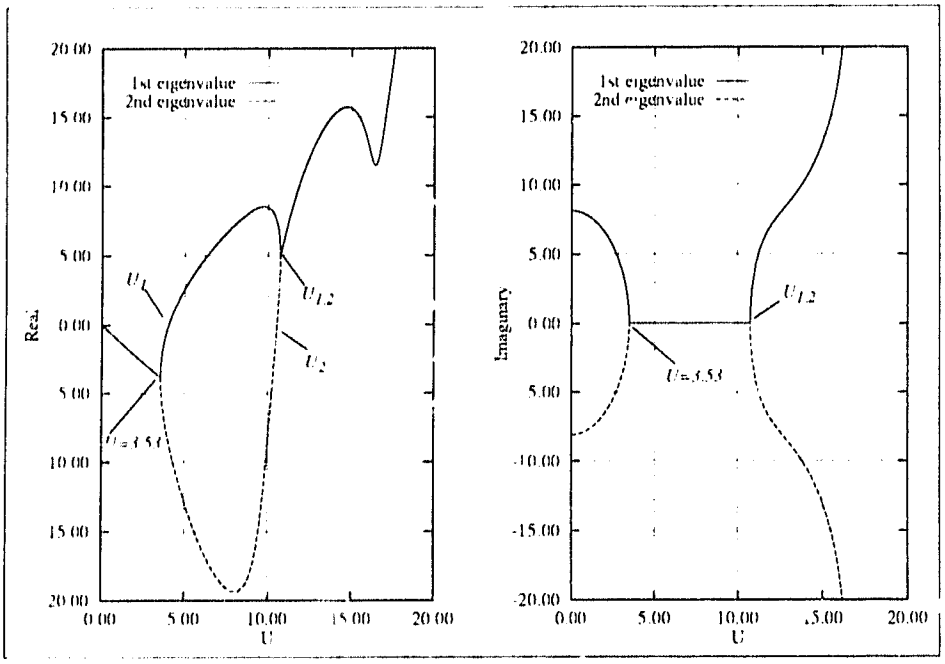


Figure 5.7: Effect of the stiff envelope on the first and second eigenvalues.

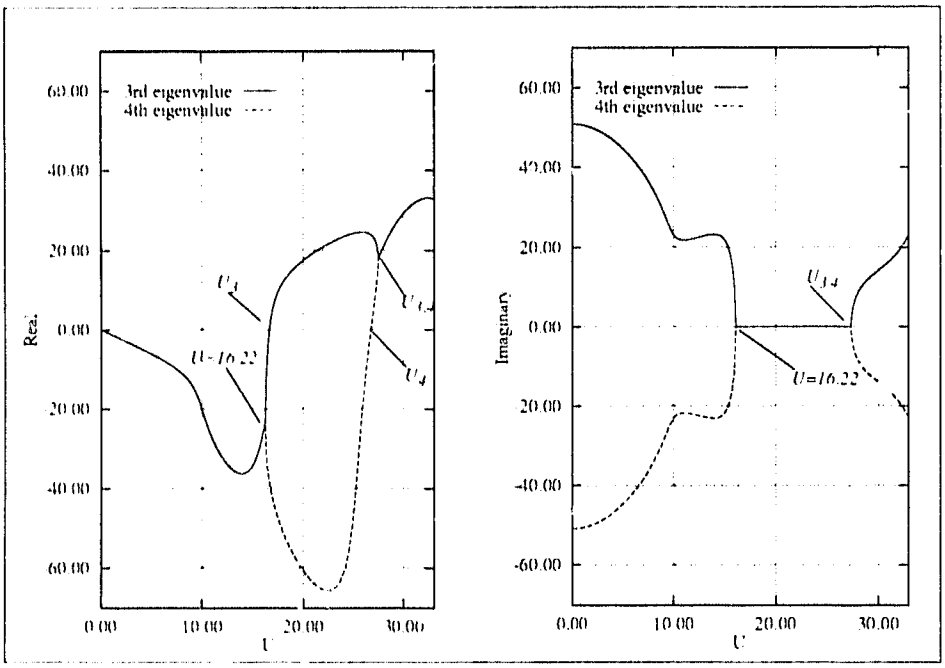


Figure 5.8: Effect of the stiff envelope on the third and fourth eigenvalues.

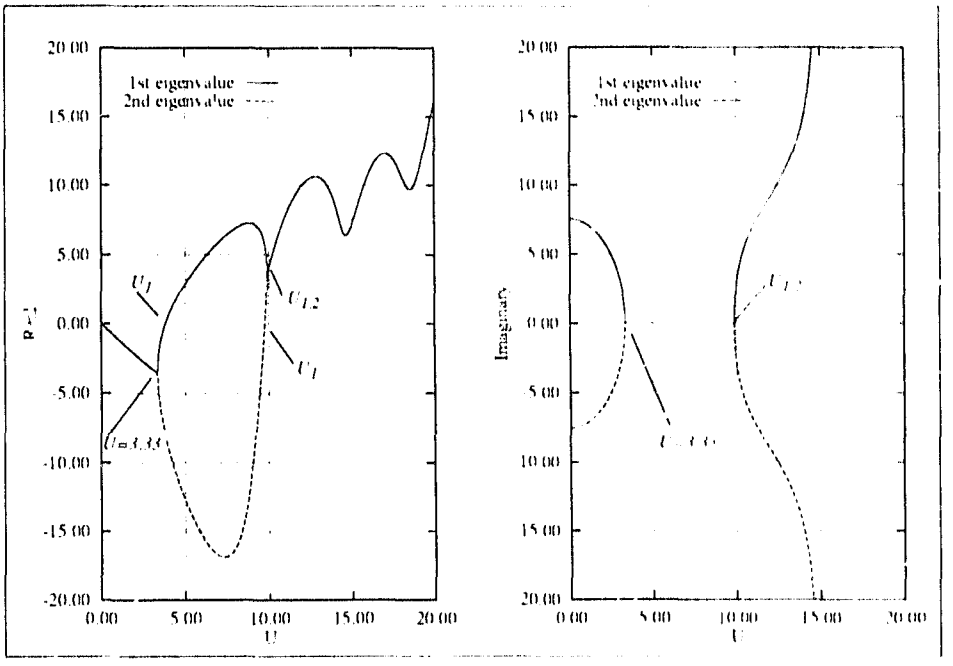


Figure 5.9: Effect of the soft envelope on the first and second eigenvalues.

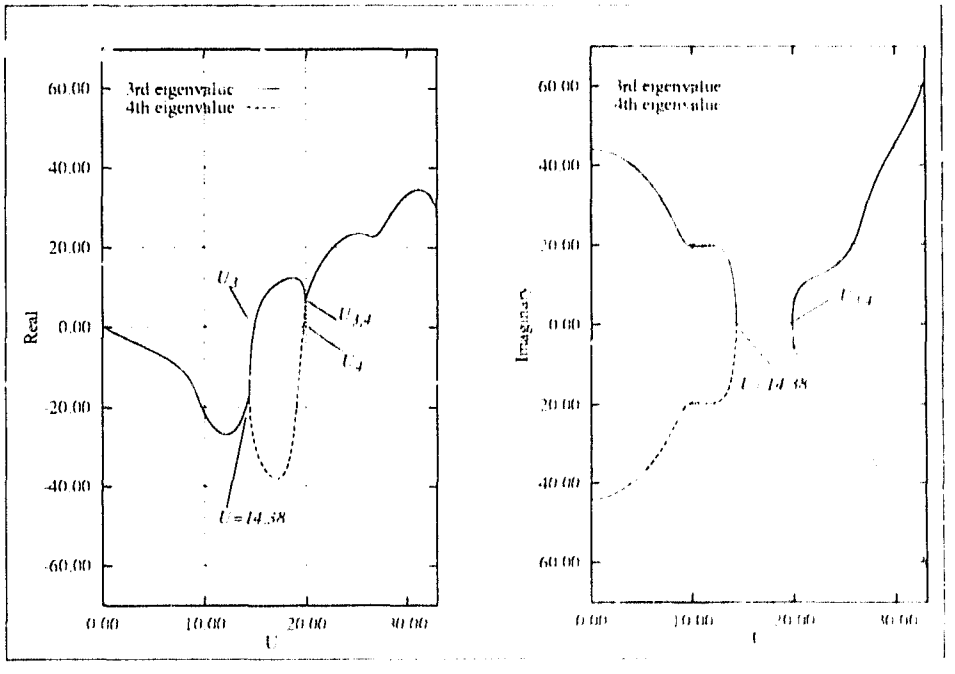


Figure 5.10: Effect of the soft envelope on the third and fourth eigenvalues.

### 5.2.4 Effect of a Tip Mass

In this section, we examine the effect of a tip mass on the stability characteristics of the constant-velocity extruding beam. For constant-velocity extrusion, the addition of a tip mass affects the inertial forces only. Hence, we do not expect it to have any effect on the divergence characteristics of the system. Several simulations were performed using various sizes of tip mass. The size of the tip mass was chosen as a percentage of the beam's total mass. That is, a 10% tip mass has a mass equal to 10% of the mass of the beam at time zero. Our simulations used the axial-motion profile in Eq. (5.9) with $L_0 = 1.0\ m$ and tip masses up to 100%.

| $U$ | No tip mass | 10% tip mass | 50% tip mass |
|---|---|---|---|
| $U_1$ | 4.01 | 4.01 | $U_1$ = 4.01 |
| $U_2$ | 10.28 | 10.28 | $U_3$ = 10.28 |
| $U_{1,2}$ | 10.47 | 10.53 | $U_{1,3}$ = 11.43 |
| | | | |
| $U_3$ | 16.58 | 16.58 | -- |
| $U_4$ | 23.00 | 23.00 | -- |
| $U_{3,4}$ | 23.23 | 23.35 | -- |
| | | | |
| $U_5$ | 29.57 | 29.57 | -- |
| $U_6$ | 35.75 | 35.75 | -- |
| $U_{5,6}$ | 35.98 | 36.11 | -- |

Table 5.4: Effect of a tip mass on the critical velocities.

Figures (5.11) and (5.12) show the evolutions of the system's first four complex eigenvalues for the case of the 50% tip mass. However, it should be noted that in this case we do not plot the evolution of consecutive eigenvalues as has been the practice thus far. Instead, Fig. (5.11) contains the evolution of the first and third eigenvalues, and Fig. (5.12) of the second and fourth. The reasons behind this change will soon become apparent. An examination of Figs. (5.11) and (5.12) will indicate that the general stability characteristics of the constant-velocity extruding beam have been drastically affected by the addition of the relatively large tip mass. This is also confirmed by the 50% tip mass column of Table (5.4) where we note that the velocity value 10.28, which

has thus far been associated with the vanishing of the second eigenvalue, now marks the vanishing of the third eigenvalue. In addition, we note that the velocity that signals the onset of flutter is no longer denoted by $U_{f,2}$, but by $U_{f,3}$ instead. This was necessary since, as we will see shortly, it is the coalescence of the first and third eigenvalues that leads to flutter in this case. Due to the many changes in the stability characteristics of the constant-velocity extruding beam brought about by the addition of a relatively large tip mass, a detailed description of the evolution of the first four eigenvalues is given below. Since eigenvalues belonging to the same mode are now drawn in separate figures, the reader will find it necessary to simultaneously refer to Figs. (5.11) and (5.12) throughout the following discussion. The emphasis, once again, is on the consequences to the system's stability characteristics:

1. For zero axial velocity ($U=0$), all eigenvalues are complex conjugates with zero real parts. This case corresponds to an undamped stationary cantilever beam with a mass attached at its tip. Therefore the imaginary parts of the eigenvalues correspond to its oscillatory frequencies. *(center)*

2. For small values of $U$, all eigenvalues become complex conjugates with negative real parts, indicating the presence of dissipative forces. Under these conditions all oscillatory modes are stable. *(stable focus)*

3. As $U$ is increased, the imaginary parts of all eigenvalues decrease and at $U \approx 3.81$ the imaginary parts of the first and second eigenvalues vanish. The real parts of the first and second eigenvalues are equal and negative, confirming that the first mode remains stable, albeit non-oscillatory. Hence, the addition of the 50% tip mass postpones the onset of non-oscillatory modes since in the absence of the tip mass the real parts of the first and second eigenvalue vanish at $U \approx 3.52$. *(stable inflected node)*

4. As $U$ is further increased, the first and second eigenvalues move apart, but remain real and negative. *(stable node)*

5. When the velocity reaches the value $U_f \approx 4.01$, the first eigenvalue vanishes altogether while the second eigenvalue remains real and negative. This signals the onset of damped divergence.

6. Beyond $U_f$, the first eigenvalue becomes real and positive while the second remains real and negative. With one of its eigenvalues real and positive, the first mode is now unstable. *(saddle)*

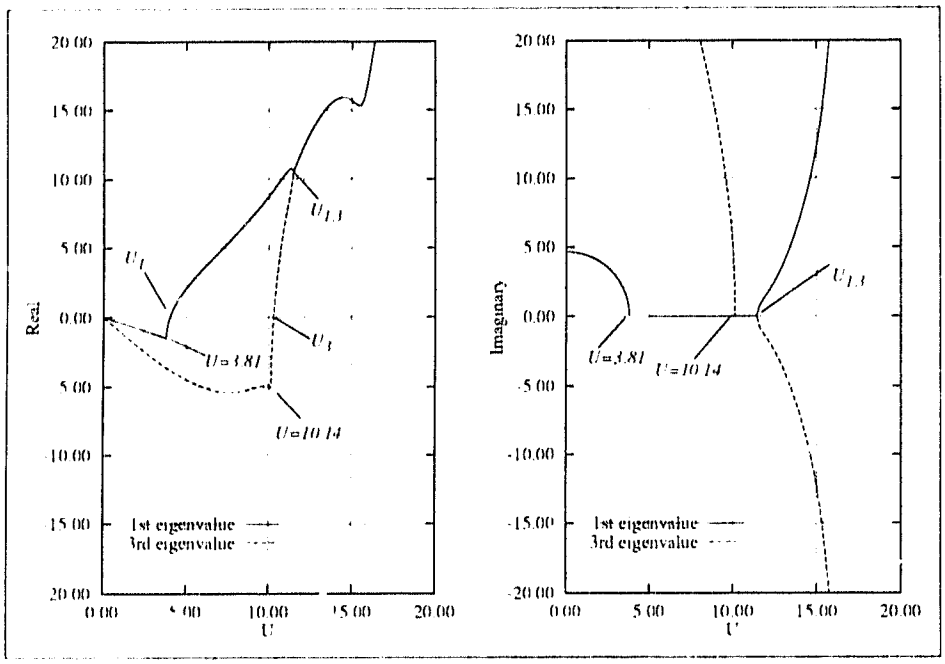


Figure 5.11: Effect of a 50% tip mass on the first and third eigenvalues.

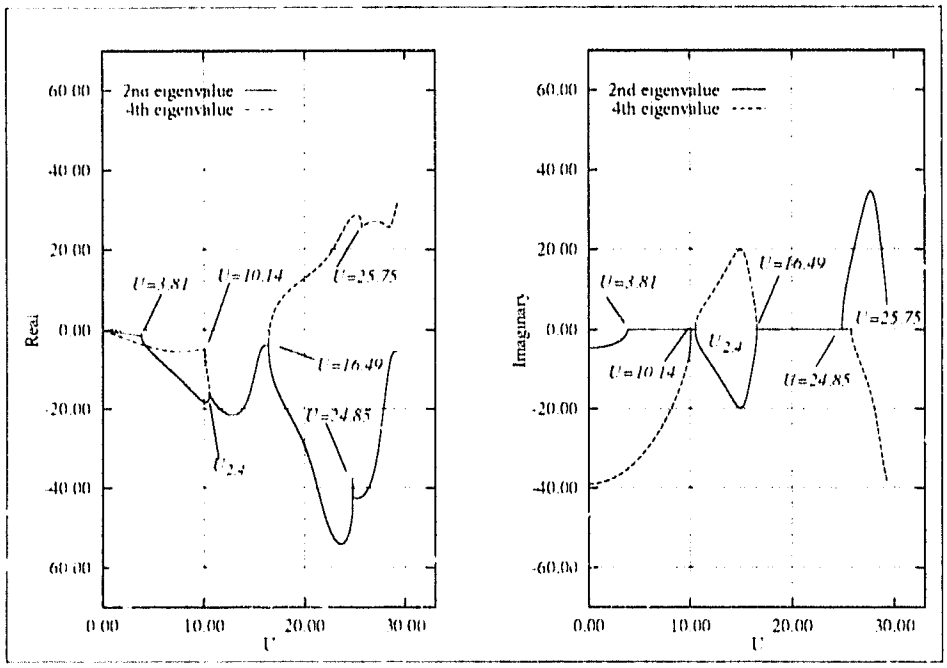


Figure 5.12: Effect of a 50% tip mass on the second and fourth eigenvalues.

7. If $U$ is increased further, it is seen that at $U = 10.14$ the imaginary parts of the third and fourth eigenvalues vanish. The real parts of the third and fourth eigenvalues are equal and negative, confirming that the second mode remains stable but non-oscillatory. *(stable inflected node)*

8. As $U$ is further increased, the third and fourth eigenvalues move apart, but remain real and negative. *(stable node)*

9. When the velocity reaches the value $U_3 = 10.28$, the third eigenvalue vanishes altogether while the fourth eigenvalue remains real and negative.

10. Beyond $U_3$, the third eigenvalue becomes real and positive while the fourth remains real and negative. With one of its eigenvalues real and positive, the second mode is now unstable. *(saddle)*

11. As $U$ is further increased, we note (Fig. (5.12)) that at $U_{2,4} = 10.53$, the loci of the second and fourth eigenvalues coalesce with negative real parts while their imaginary parts remain zero.

12. At slightly higher velocities than $U_{2,4}$ the imaginary parts become non-zero and the second and fourth eigenvalues become complex conjugates with negative real parts. Therefore, the constant-velocity extruding beam exhibits for the first time thus far, *coupled-mode stable* oscillations.

13. At $U_{1,3} = 11.43$, the loci of the first and third eigenvalues coalesce with the imaginary parts remaining zero. Hence, the addition of the tip mass postpones the coalescence of the first eigenvalue since in the absence of the tip mass it occurs at $U_{1,2} = 10.47$. For all cases examined thus far, the coalescence that led to flutter has always involved eigenvalue branches belonging to the same oscillatory mode. For instance, the first coalescence has always been between the branches of the first and second eigenvalues (which belong to the first oscillatory mode). The addition of the large tip mass has the additional effect of causing the coalescence to be between eigenvalues belonging to different modes.

14. At slightly higher velocities than $U_{1,3}$, when the imaginary parts of the first and third eigenvalues are non-zero, the eigenvalues become complex conjugates with positive real parts. Consequently, $U_{1,3}$ is the critical velocity beyond which flutter occurs. As mentioned earlier, flutter is due to the coalescence of the first and third eigenvalues. Hence in the case of the 50% tip mass, the oscillatory instability is of the *coupled-mode flutter* type.

15. As the velocity is further increased to $U \approx 16.49$, the imaginary parts of the second and fourth eigenvalues vanish once again with their real parts equal and negative. At higher velocities it was noted that the branches of the second and fourth eigenvalues coalesce again, but this time with branches of other higher eigenvalues. With large tip masses at high axial velocities, eigenvalue plots tend to cross in the complex plane, making it difficult to identify them. Nevertheless, it was possible to observe that at higher velocities (24.85 and 25.75), the second and fourth eigenvalues coalesce with other higher eigenvalues, leading to coupled-mode stable oscillations and coupled-mode flutter, respectively. Such major changes in stability characteristics of dynamic systems has been also reported by Païdoussis (1975) for simply-supported pipes conveying fluid. For this dynamic system, the changes are brought about by high values of the non-dimensional parameter $\beta$ (defined as $M/(M+m)$) where $M$ and $m$ are the mass per unit length of the fluid and pipe, respectively. An increase of the density of the flexible extendible beam alone (even by two orders of magnitude) failed to produce similar results.

The investigation of the effect of a tip mass on the constant-velocity extruding beam was originally performed using the static (Euler) stability analysis, a computationally simpler approach than the dynamic method described earlier. In the static approach, one seeks values of a system-characteristic that renders the equivalent stiffness matrix $[K_{eq}]$ singular. As expected, the static stability analysis showed that the onset of divergence instabilities is unaffected by the size of the tip mass. For instance, the first two static instabilities occur at $U \approx 4.01$ and $U \approx 10.28$, as shown in Table (5.4). As we have seen, however, depending on the relative size of the tip mass, they might not correspond to the expected eigenvalues (the first and second). This is a good demonstration of the limitations of the static approach to stability analysis

### 5.2.5 Effect of Tip Support

In this section we examine the effect of displacement constraints at the tip of the constant-velocity extruding beam on the system's stability characteristics. In particular, we examine the following two cases:

1. Simply-supported tip: $Y(L(t)) = Y_{XX}(L(t)) = 0.$

2. Clamped tip: $Y(L(t)) = Y_{X}(L(t)) = 0.$

In both cases, extrusion is assumed to be from a rigid wall. The addition of the tip constraints increases the rigidity of the flexible extendible beam, hence raising the critical velocities as shown in Table (5.5).

| $U$ | Free | Simply-supported | Clamped tip |
|---|---|---|---|
| $U_1$ | 4.01 | 8.92 | 10.41 |
| $U_2$ | 10.28 | 14.52 | 15.76 |
| $U_{1,2}$ | 10.47 | 14.59 | 15.80 |
| | | | |
| $U_3$ | 16.58 | 21.50 | 23.04 |
| $U_4$ | 23.00 | 27.53 | 28.89 |
| $U_{3,4}$ | 23.23 | 27.60 | 28.93 |

Table 5.5: Effect of tip constraints on the critical velocities.

The evolutions of the system's first four complex eigenvalues are shown in Figs. (5.13) and (5.14) for the case of the simply-supported tip, and in Figs. (5.15) and (5.16) for the case of the clamped tip.

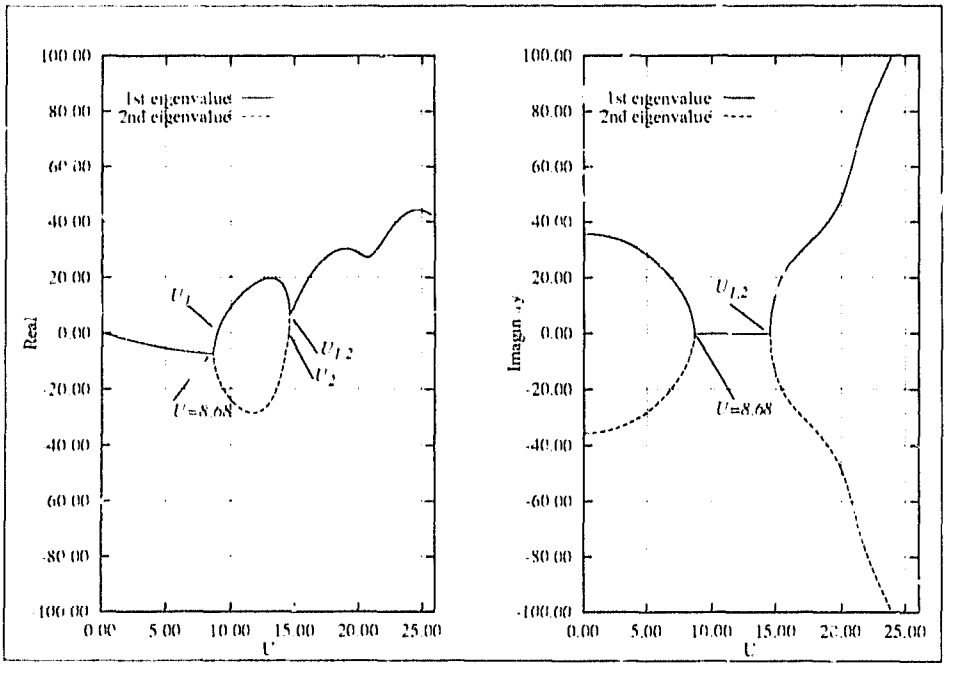


Figure 5.13: Simply-supported tip. First and second eigenvalues.

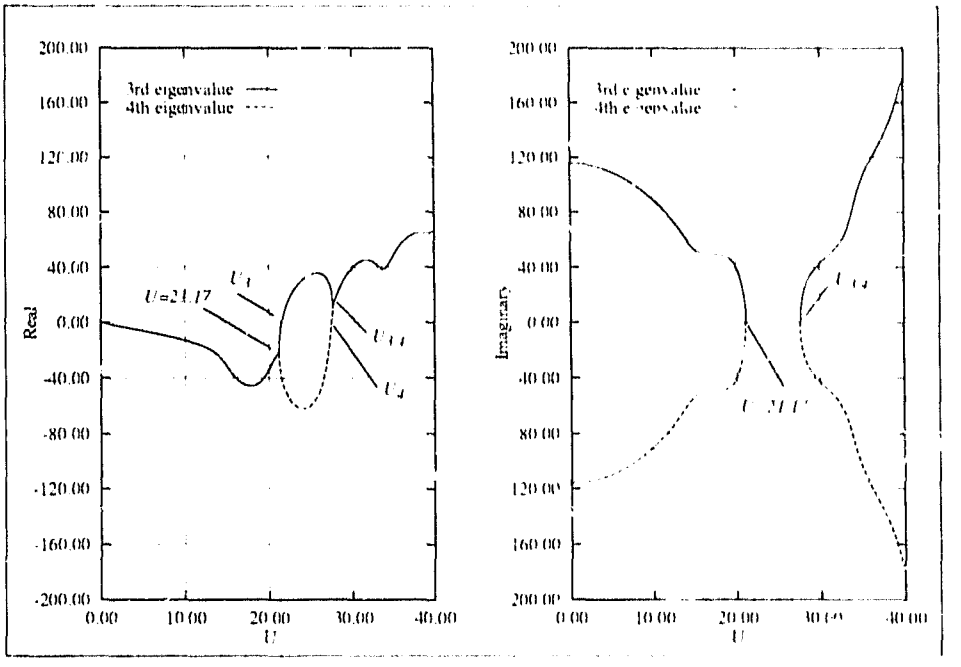


Figure 5.14: Simply-supported tip. Third and fourth eigenvalues.

As can be seen from Figs. (5.13) and (5.14) the eigenvalues of the constant-velocity extruding beam with the simply-supported tip follow the same general pattern as in the case of the cantilever constant-velocity extruding beam of Section 5.2.1.

Figures (5.15) and (5.16) show that the eigenvalues of the constant-velocity extruding beam with the clamped tip also follow a similar general pattern as that for the case of the cantilever constant-velocity extruding beam of Section 5.2.1. Hence, regardless of the tip constraints, the constant-velocity extruding beam has the same general stability characteristics: damped divergence followed by flutter due to the coalescence of eigenvalue branches of a single oscillatory mode. This is consistent with Zajaczkowski and Yamada's (1980) findings that the parametric stability characteristics of a cantilever beam of periodically varying length are not much altered by the change of tip boundary conditions. This is unlike the case of pipes conveying fluid, where the mere support of the pipe's tip changes not only the general stability characteristics of the problem, but also changes the system's classification from non-conservative gyroscopic (cantilever pipe) to conservative gyroscopic (pipes supported at both ends). In that case, however, the domain of the problem is of fixed size and mass is conserved.

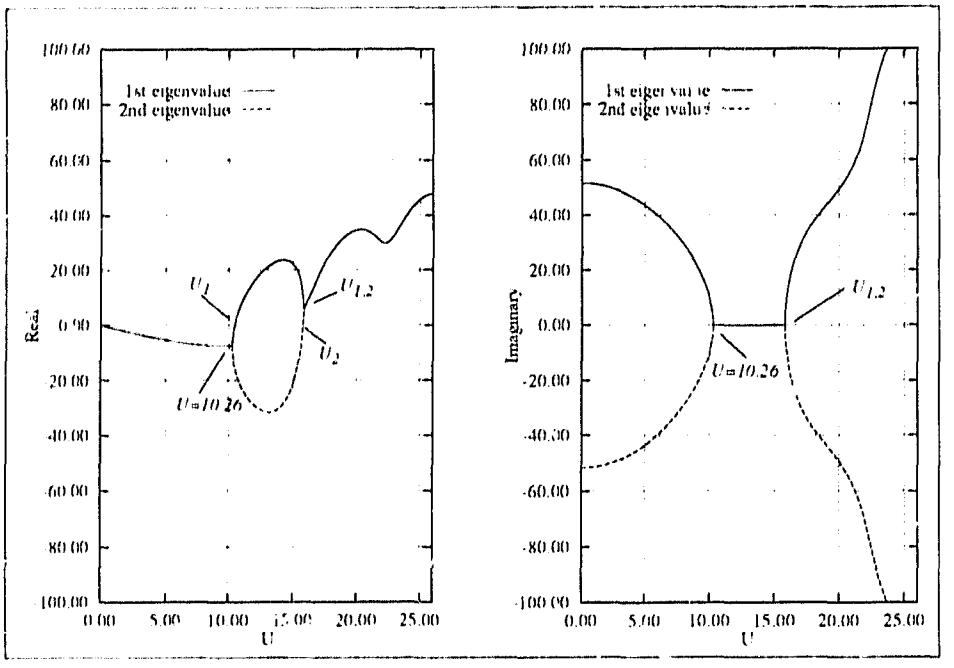


Figure 5.15: Clamped tip. First and second eigenvalues.

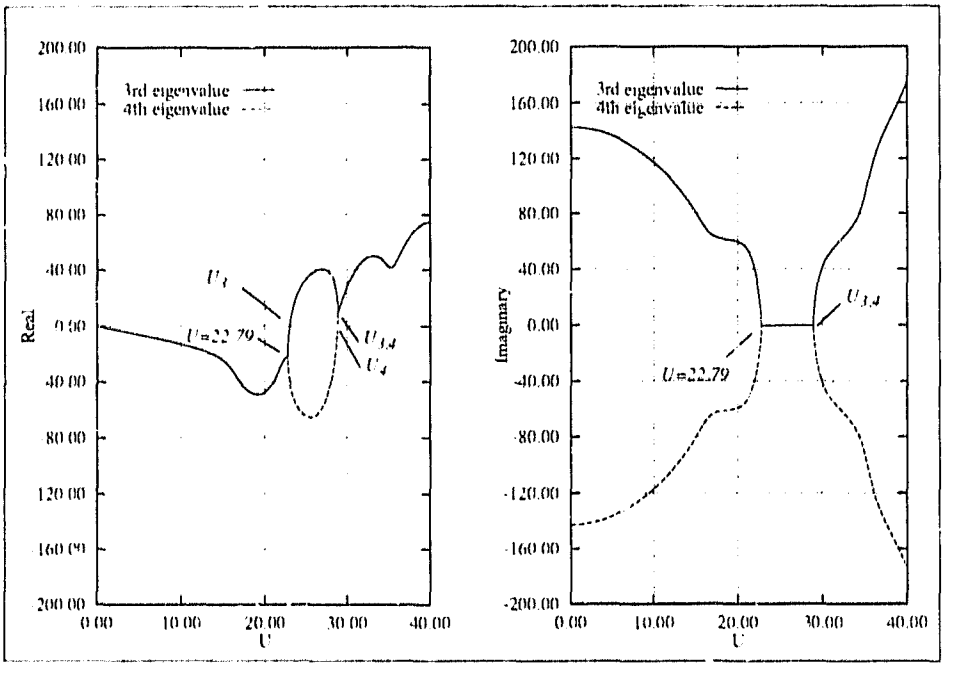


Figure 5.16: Clamped tip. Third and fourth eigenvalues.

## 5.3 Constant-Velocity Retraction

In this section we study the stability characteristics of flexible extendible beams with a retraction profile of the form

$$L(t) = L_0 - vt, \tag{5.17}$$

with initial length $L_0$, and retracting velocity $v$. We start with the case of an undamped beam retracting into a rigid wall, and then investigate the effect of physical damping, wall flexibility, tip mass and tip support.

### 5.3.1 The Simplest Case

Table (5.6) lists the values for the critical non-dimensional velocities $U$ for a flexible extendible beam retracting into a rigid wall. These values of $U$ are identical to those obtained for the extruding beam of Section 5.2.1 (third column of Table (5.1)), but as we will soon discuss, their interpretation is different.

| $U$ | Ten element model |
|---|---|
| $U_1$ | 4.01 |
| $U_2$ | 10.28 |
| $U_{1,2}$ | 10.47 |
| | |
| $U_3$ | 16.58 |
| $U_4$ | 23.00 |
| $U_{3,4}$ | 23.23 |
| | |
| $U_5$ | 29.45 |
| $U_6$ | 35.74 |
| $U_{5,6}$ | 35.97 |

Table 5.6: Critical non-dimensional velocities.

The evolutions of the system's first six complex eigenvalues are shown in Figs. (5.17) through (5.19), where once again the real and imaginary parts of the eigenvalues are

shown separately. Following is a detailed description of the evolution of the first two eigenvalues:

1. For zero axial velocity ($U=0$), all eigenvalues are complex conjugates with zero real parts. This case corresponds to an undamped stationary cantilever beam of length $L_0$ ($L_0$ is once again taken as $1.0m$). Therefore the imaginary parts of the first and second eigenvalues correspond to the beam's fundamental natural frequency. *(center)*

2. For small values of $U$, all eigenvalues become complex conjugates with *positive* real parts. Under these conditions, all oscillatory modes are unstable. As noted in Section 3.3, for the case of retraction where mass elements leave the domain, the equivalent damping matrix $[C_{eq}]$ is negative-definite, implying that energy is generated. This is contrary to Wang and Wei's (1987) conclusion that during retraction energy is dissipated. *(unstable focus)*

3. As $U$ is increased, the imaginary parts of all eigenvalues decrease, and at $U \approx 3.52$ the imaginary parts of the first and second eigenvalues vanish. The real parts of the first and second eigenvalues are equal and positive, confirming that the first mode remains unstable, albeit non-oscillatory. *(unstable inflected node)*

4. As $U$ is further increased, the first and second eigenvalues move apart, but remain real and positive. *(unstable node)*

5. When $U$ reaches the value of $U_1 \approx 4.01$, the first eigenvalue vanishes altogether while the second eigenvalue remains real and positive. Therefore, for the constant-velocity retracting beam, $U_1$ signals the onset of divergence.

6. Beyond $U_1$, the first eigenvalue becomes real and negative while the second eigenvalue remains real and positive. With one of its eigenvalues real and positive, the first mode remains unstable. *(saddle)*

7. If $U$ is increased further, it is seen that the second eigenvalue, still remaining real, vanishes at $U_2 \approx 10.28$. Since the first eigenvalue remains real and negative, the first mode now becomes stable.

8. Beyond $U_2$, the second eigenvalue also becomes real and negative. The first mode remains stable since both eigenvalues are now real and negative. *(stable node)*

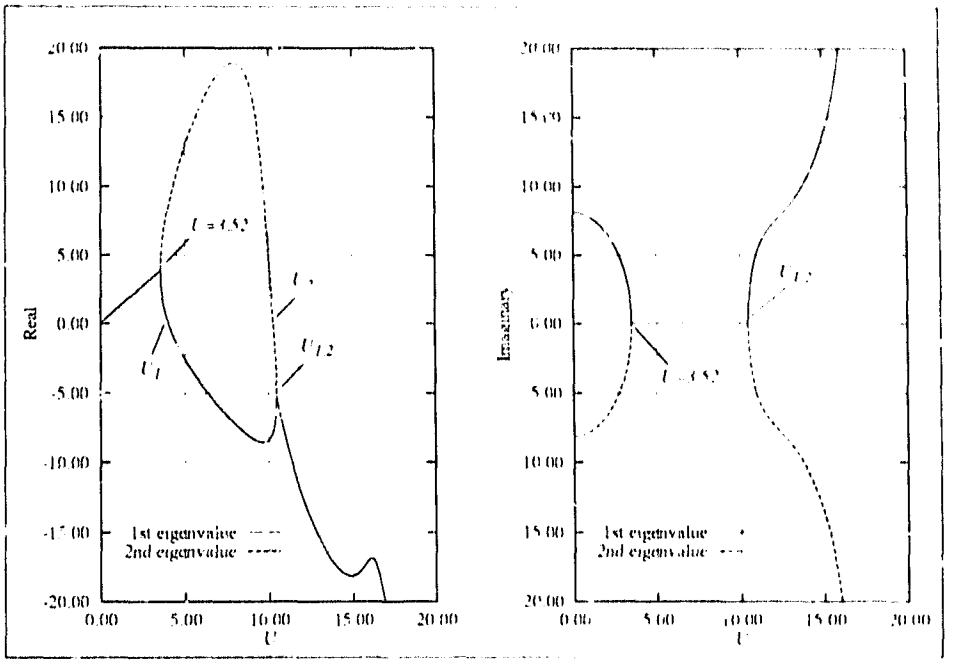


Figure 5.17: Real and imaginary components of the first and second eigenvalues.

9. At a slightly higher velocity than $U_2$, namely $U_{1,2} = 10.47$, the loci of the first and second eigenvalues coalesce with the imaginary parts remaining zero. The first mode remains stable. *(stable inflected node)*

10. At slightly higher velocities than $U_{1,2}$, the imaginary parts become non-zero and the first and second eigenvalues become, once again, complex conjugates, this time, however, with negative real parts. Therefore, $U_{1,2}$ is the critical axial velocity beyond which the first oscillatory mode exhibits stable oscillations. *(stable focus)*

The same general behaviour (divergence followed by stable oscillations) is also observed for the higher oscillatory modes, as can be seen from Figs. (5.18) and (5.19). It should be noted that the evolution of the eigenvalues of the constant-velocity retracting beam described above is essentially the reverse of that for the constant-velocity extruding beam. The real parts of Figs. (5.17) through (5.19) are the mirror images about the $U$ axis of Figs. (5.1) through (5.3), respectively. The modes of the extruding beam start out as stable-oscillatory, and as $U$ is increased they loose stability by divergence and finally flutter, whereas the modes of the retracting beam initially flutter and as $U$ is increased they diverge and finally become oscillatory and stable.

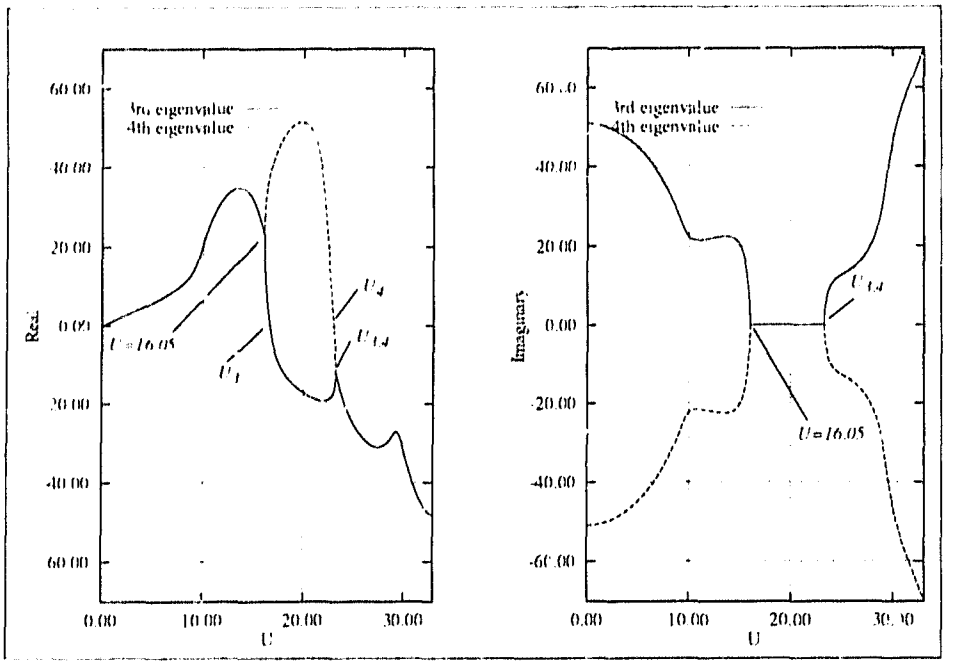


Figure 5.18: Real and imaginary components of the third and fourth eigenvalues.

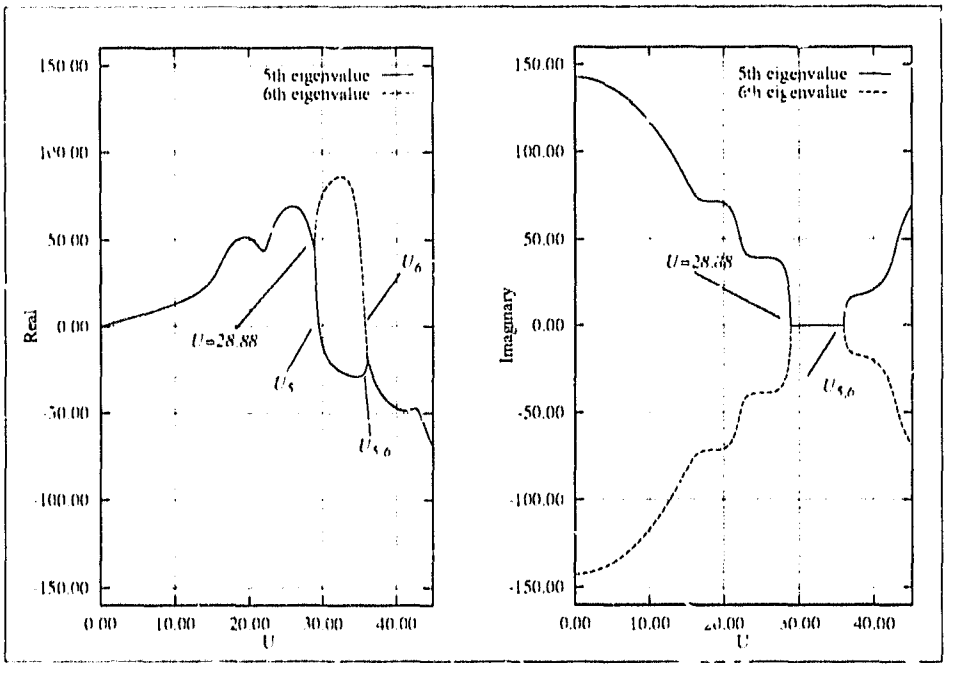


Figure 5.19: Real and imaginary components of the fifth and sixth eigenvalues.

## 5.3.2 Effect of Physical Damping

Table (5.7) lists the critical velocities of the system using various values of modal damping. The first column lists the critical velocities of the undamped retracting beam. The second column lists the critical velocities of the retracting beam with modal damping parameters as found by Yuh and Young (1991). Finally, the third column lists the critical velocities of a retracting beam with artificially high damping coefficients. As expected, regardless of the amount of physical damping added, there is no effect on the onset of divergence instabilities.

| $U$ | $\xi_1 = 0.0$<br>$\xi_2 = 0.0$<br>$L = 1$ m | $\xi_1 = 14.99\ 10^{-3}$<br>$\xi_2 = 15.33\ 10^{-3}$<br>$L = 1$ m | $\xi_1 = 149.9\ 10^{-3}$<br>$\xi_2 = 153.3\ 10^{-3}$<br>$L = 1$ m |
|---|---|---|---|
| $U_1$ | 4.01 | 4.01 | 4.01 |
| $U_2$ | 10.28 | 10.28 | 10.28 |
| $U_{1,2}$ | 10.47 | 10.45 | 10.33 |
| | | | |
| $U_3$ | 16.58 | 16.58 | -- |
| $U_4$ | 23.00 | 23.00 | -- |
| $U_{3,4}$ | 23.23 | 23.16 | -- |

Table 5.7: Effect of physical damping on the critical velocities.

As seen from Table (5.7), light structural damping has no appreciable effect (even at artificially high levels) on the critical velocities of the system. However, in contrast to the case of the extruding beam, heavy damping has considerable effect on the stability characteristics of the system. Figures (5.20) through (5.22) show the evolutions of the system's first six complex eigenvalues for the case of heavy damping (third column in Table (5.7)). Using the same format as used in the previous sections, the real and imaginary parts of the eigenvalues are shown separately. The changes in the stability characteristics of the constant-velocity retracting beam, brought about by the addition of the relatively heavy damping, are highlighted in the following:

1. Since the system is now damped by physical damping (by virtue of the presence of $[C_p]$), all eigenvalues are complex conjugates with negative real parts for zero axial velocity ($U=0$). This case corresponds to a damped stationary cantilever beam of length $L_0$ ($L_0=1.0m$). Therefore the imaginary parts of the eigenvalues correspond to the beam's damped natural frequencies. *(stable focus)*

2. For small values of $U$, due to the presence of physical damping, all eigenvalues remain complex conjugates with negative real parts. *(stable focus)*

3. As $U$ is increased, the real parts (still negative) of all eigenvalues decrease due to the energy-generating characteristic of the system. At $U \approx 1.04$ the real parts of the first and second eigenvalues vanish, indicating that, for the first mode, the energy dissipated by physical damping and the energy generated by the system in that mode balance out. *(center)*

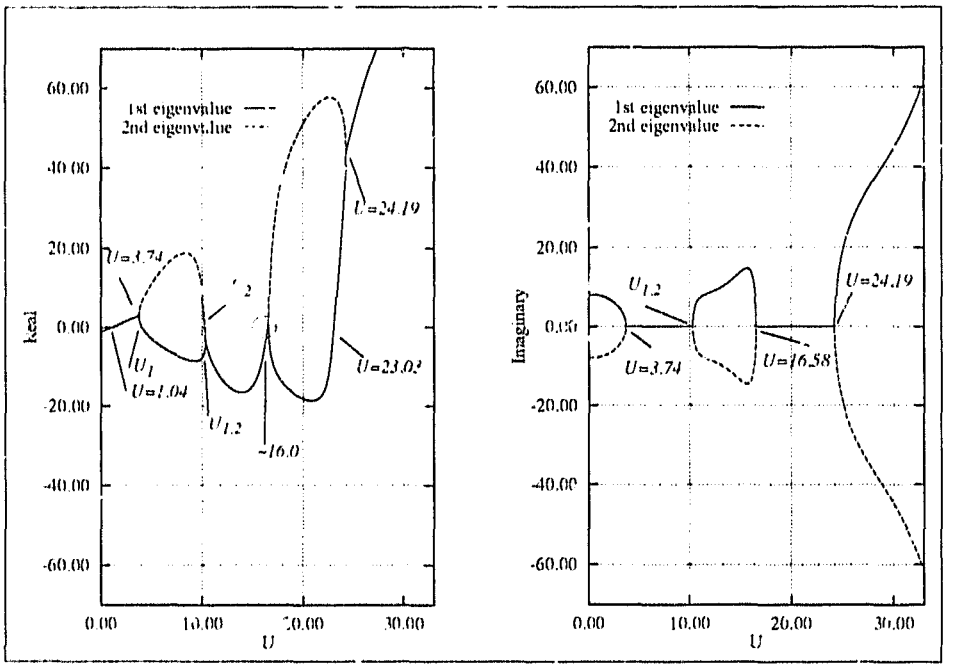


Figure 7.20: Effect of heavy damping on the first and second eigenvalues.

4. At slightly higher values of $U$ the real parts of the first and second eigenvalues become positive. This is a classic example of a Hopf bifurcation (see for example Thompson (1987)). The first two eigenvalues are now complex conjugates with positive real parts, indicating the onset of flutter. *(unstable focus)*

5. The addition of physical damping postpones the onset of non-oscillatory modes. For instance, the imaginary parts of the first and second eigenvalues vanish at $U \approx 3.74$ as opposed to $U \approx 3.52$ in the absence of physical damping. The real parts of the first and second eigenvalues are equal and positive, confirming that the first mode remains unstable. *(unstable inflected node)*

6. The addition of physical damping brings about the coalescence of the loci of the first and second eigenvalues (with the imaginary parts remaining zero) at lower axial velocities. Specifically, coalescence occurs at $U_{1,2} \approx 10.33$ as opposed to $U_{1,2} \approx 10.47$ in the absence of damping. This is consistent with Hermann's (1967) comments that the flutter system-characteristic parameter of the undamped system is an upper bound for that of the system with light damping.

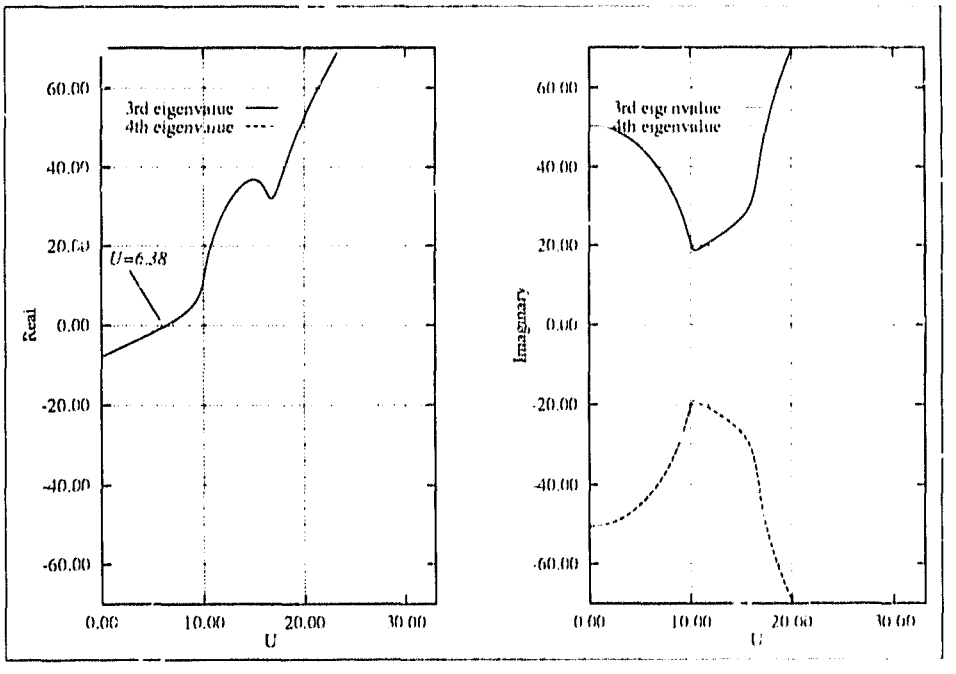


Figure 5.21: Effect of heavy damping on the third and fourth eigenvalues.

7. In the neighborhood of $U \approx 16.00$, a series of interesting events takes place that involve the first and second eigenvalues. At $U \approx 16.49$, their real parts vanish, indicating the balance between the dissipated and generated energy *(center)*. At slightly higher velocities they acquire small positive real parts. Hence the first mode becomes unstable *(unstable focus)*. At $U \approx 16.58$ their imaginary parts vanish. With their real parts still real and positive, the first mode remains unstable *(unstable*

*inflected node).* As $U$ is further increased, the first two eigenvalues move apart but remain real. The first eigenvalue becomes negative and the second remains positive. Therefore, the first mode remains unstable. *(saddle)*

8. When $U$ reaches the value of $U \approx 23.03$, the first eigenvalue vanishes while the second remains real and positive.

9. Beyond $U = 23.03$, the first eigenvalue also becomes real and positive. With both eigenvalues real and positive, the first mode remains unstable. *(unstable node)*

10. As $U$ is further increased, the loci of the first and second eigenvalues coalesce at $U \approx 24.19$ (for the second time) with the imaginary parts remaining zero. The first mode remains unstable. *(unstable inflected node)*

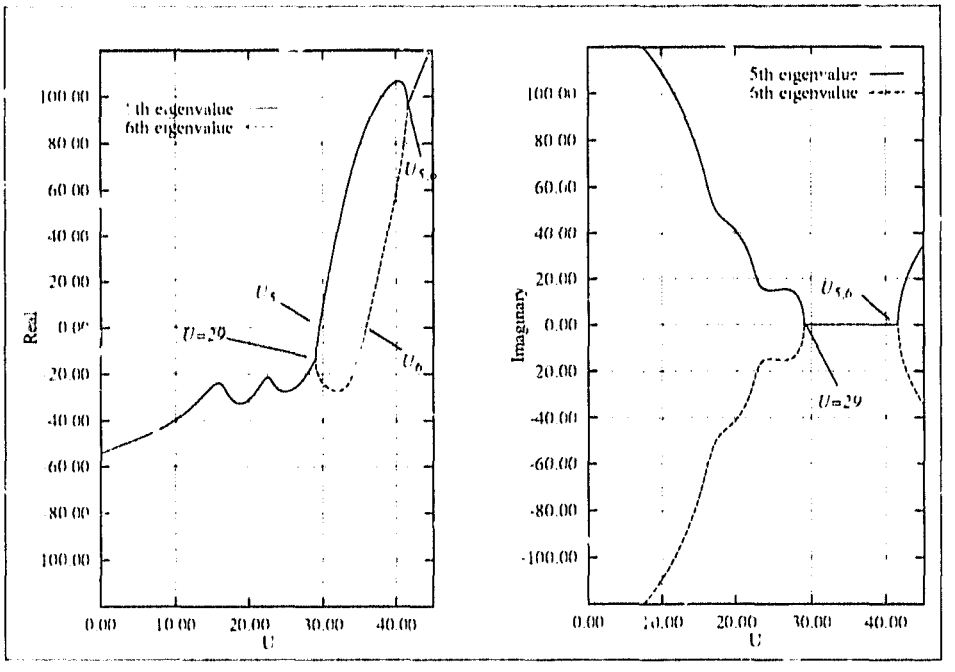


Figure 5.22: Effect of heavy damping on the fifth and sixth eigenvalues.

11. At velocities higher than $U \approx 24.19$, the imaginary parts become non-zero and the first and second eigenvalues become, once again, complex conjugates with positive real parts. *(unstable focus)*

12. As shown in Fig. (5.21), damping also affects the higher oscillatory modes. The second mode starts out as stable-oscillatory, but at $U = 6.38$ it becomes unstable oscillatory through a Hopf bifurcation. However, this is the first time we encounter a mode that neither diverges nor do the loci of the real part ever separate.

In practical situations, physical damping is always present. Therefore, in the case of the retracting beam, it is desirable to have retracting velocities for which the energy generated is less than the energy dissipated by the physical damping in the first oscillatory mode. This will ensure that all modes (hence the system itself) remain stable.

### 5.3.3 Effect of Wall Flexibility, Tip Mass, Tip support

We studied the effect of wall flexibility, tip mass, and change of tip support on the stability of the retracting beam. We found that the critical values for the non-dimensional velocity $U$ remain the same as in the corresponding cases of the extruding beam (Tables (5.3) through (5.5)). However, their interpretation follows the description of Section 5.3.1 for the retracting beam. Therefore, these cases will not be dealt with here in detail.

## 5.4 Constant-Acceleration Extrusion and Retraction

In this section, we examine the effect of axial acceleration on the stability characteristics of the flexible extendible beam. Constant axial acceleration due to both a uniform acceleration field and a root-applied force are considered.

The axial-motion profile for constant-acceleration extrusion is taken as

$$L(t) = L_0 + vt + \frac{1}{2}at^2, \tag{5.18}$$

with initial length $L_0 = 1.0\ m$, extruding velocity $v$, and acceleration $a$. The general stability characteristics of the flexible extendible beam are not affected by the addition of the axial acceleration. However, new values for the non-dimensional critical velocities are obtained and are listed in Table (5.8). The magnitude of the axial acceleration is always taken to be equal to the gravitational constant $g = 9.81\ m/s^2$.

| $U$ | $a = 0$ | $a = g$ (root force) | $a = -g$ (root force) | $a = g$ (accel. field) | $a = -g$ (accel. field) |
|---|---|---|---|---|---|
| $U_1$ | 4.01 | 3.69 | 4.31 | 4.16 | 3.87 |
| $U_2$ | 10.28 | 10.11 | 10.44 | 10.29 | 10.27 |
| $U_{1,2}$ | 10.47 | 10.28 | 10.66 | 10.47 | 10.47 |

Table 5.8: Effect of axial-acceleration on the critical extruding velocities.

The first column lists the results of a constant-velocity extrusion profile (Section 5.2.1). Depending on whether the acceleration is due to a uniform acceleration field or a root-applied force, the effect on the governing system of equations will be different because matrix $[c_2]$ (Eq. (3.31)) models the effect of the uniform acceleration field and matrix $[k_2]$ (Eq. (3.31)) models the effect of the root-applied force.

If the beam is accelerating due to a root-applied force, then a compressive axial load is expected to decrease the beam's stiffness and hence the system's critical velocities. This is verified by our results in the second column of Table (5.8). On the other hand, a root-applied force causing deceleration will have the opposite effect since, in this case, the beam is under a tensile axial load. Therefore, the critical velocities increase as shown in the third column of Table (5.8).

If the axial acceleration is due to a uniform acceleration field, the effect on the critical velocities is not evident. As shown in the last two columns of Table (5.8), the effect is to raise the critical velocities if the beam is accelerating and to lower them if the beam is decelerating. From the same results, one also notes that, unlike the root-applied force, the uniform acceleration field affects only the lower instabilities. It was confirmed that critical velocities higher than $U_{1,2}$ are not affected by the uniform acceleration field.

If the axial-motion profile for constant-acceleration retraction is taken as

$$L(t) = L_0 - vt + \frac{1}{2}at^2, \tag{5.19}$$

with the same value for $L_0$ as in the extruding case, then the new critical velocities of the system are as shown in Table (5.9). These values are identical to those obtained for the extruding case in Table (5.8).

| $U$ | $a = 0$ | $a = g$ (root force) | $a = -g$ (root force) | $a = g$ (accel. field) | $a = -g$ (accel. field) |
|---|---|---|---|---|---|
| $U_1$ | 4.01 | 3.69 | 4.31 | 4.16 | 3.87 |
| $U_2$ | 10.28 | 10.11 | 10.44 | 10.29 | 10.27 |
| $U_{1,2}$ | 10.47 | 10.28 | 10.66 | 10.47 | 10.47 |

Table 5.9: Effect of axial-acceleration on the critical retracting velocities.

## 5.5 Parabolic Extrusion

In this section we examine the stability characteristics of the flexible extendible beam when the beam's length is given by

$$L(t) = \eta\sqrt{t}, \tag{5.20}$$

with the parameter $\eta$ having units of $m/\sqrt{s}$. As discussed in Section 2.1, Tabarrok et al. (1974) obtained a similarity solution for parabolically-extruding beams. For a system of $n$ degrees of freedom, the similarity solution corresponds to $n$ similarity pairs $[U_i,\{S_i\}]$ where $U_i$ are given by Eq. (4.9) and $\{S_1\}$, $\{S_2\}$ are shown in Figs. (4.15) and (4.16) respectively.

The first column of Table (5.10), lists the analytical values for the first four similarity parameters $U_i$ $(i = 1,...4)$. The second column of Table (5.10) lists the critical values for the similarity parameter obtained through the assumed modes method using the first five mode-shapes obtained from a free-vibration analysis.

| $U$ | **Exact (Similarity Solution) Tabarrok (1974)** | **Assumed-Modes (Five first modes) Tabarrok (1974)** | **Four elements** | **Ten elements** |
|---|---|---|---|---|
| $U_1$ | 3.14 | 3.14 | 3.16 | 3.14 |
| $U_2$ | 9.43 | 9.42 | 9.65 | 9.44 |
| $U_{1,2}$ | Not applicable | Not available | Not available | 13.74 |
| | | | | |
| $U_3$ | 15.71 | 15.90 | 15.99 | 15.77 |
| $U_4$ | 21.99 | 44.50 | 25.13 | 22.17 |
| $U_{3,4}$ | Not applicable | Not available | Not available | 27.31 |

Table 5.10: Critical values for similarity parameter $U$.

Figures (5.23) and (5.24) show the evolution of the system's first four eigenvalues. As shown, the stability characteristics are similar to those for the constant-velocity extruding beam of Section 5.2.1 (divergence followed by flutter). The last two columns of Table (5.10) list the critical values for the similarity parameter obtained using four and ten variable-domain beam elements, respectively. As can be seen from Table (5.10), each critical value of the similarity parameter corresponds to the vanishing of an eigenvalue. That is, $U_1$ corresponds to the vanishing of the first eigenvalue, $U_2$ corresponds to the vanishing of the second eigenvalue, and so on. From the finite-element model one may also obtain the corresponding similarity-modes $\{S_i\}$. The similarity solution does not yield values corresponding to flutter.

At this point it should be noted that the similarity parameter $U$ (Eq. (4.9)) does not depend on the beam's length. This implies that a critical value of $U$ remains critical regardless of the length of the beam. This is unlike the cases we have examined thus far, where the critical velocities are always a function of the beam's length. The physical interpretation of the similarity solution can now be stated as follows: if the beam extrudes with the axial-motion profile of Eq. (5.20), where $\eta$ corresponds to a critical value of the similarity parameter $U_k$, and the initial deflection of the beam is given by the corresponding similarity-mode $\{S_k\}$, the beam will not oscillate throughout its extrusion history. This was indeed confirmed in Section 4.1.4 through a time-integration of the governing equations using the variable-domain beam element under the conditions just described.

The similarity solution represents the only analytical result that we have found in the literature concerning flexible extendible beams. Therefore, the validity of approximate models should be tested by the calculation of at least the critical values for the similarity parameter $U$ (Table (5.10)). In addition, a more rigorous test is the time integration of the equations of motion under the similarity conditions in order to verify the non-oscillatory response of the beam throughout the extrusion history.

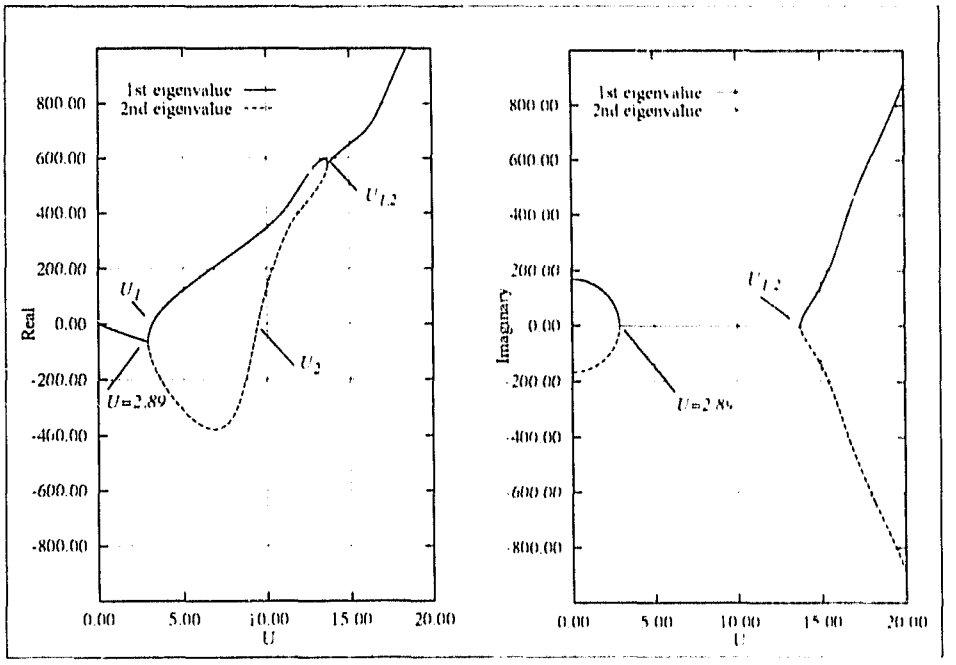


Figure 5.23: Real and imaginary components of the first and second eigenvalues.

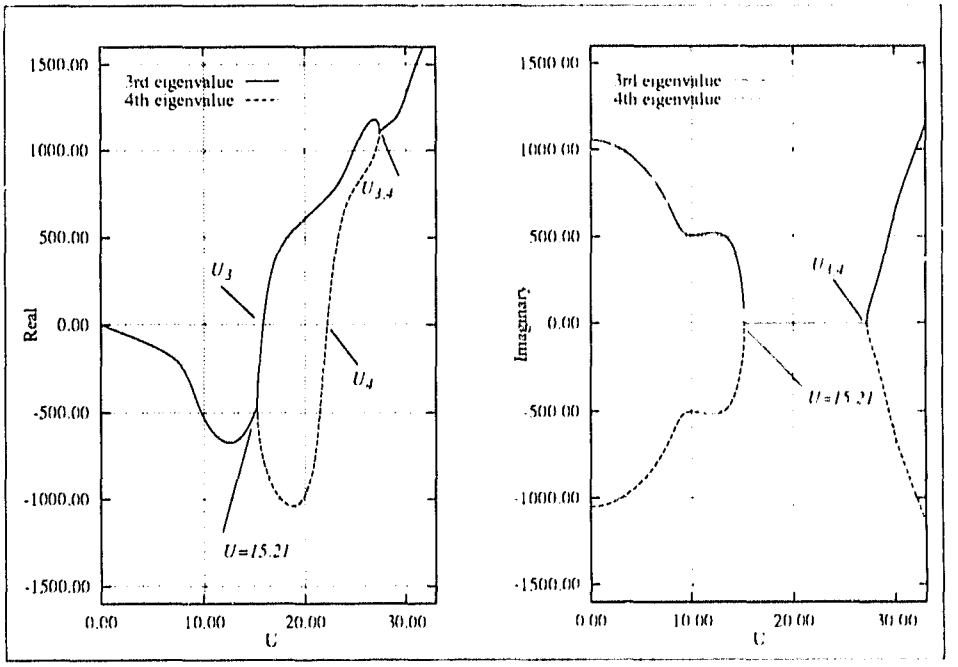


Figure 5.24: Real and imaginary components of the third and fourth eigenvalues.

## 5.6 Pipes Conveying Fluid

The variable-domain beam element may also be used for the analysis of a problem closely related to the nested axially-moving beam, namely that of pipes conveying fluid. In this section we describe how the variable-domain beam element may be used to model simply-supported and clamped-clamped pipes. In addition, we show the necessary modifications to the system equations to model cantilever pipes conveying fluid. The results of our stability analysis of pipes conveying fluid are compared with the results obtained by Païdoussis (1966,1974,1975,1991). This section is included primarily as a further verification of our modeling and solution procedures, and does not represent a detailed coverage of the topic. The reader is referred to Païdoussis and Workman (1991) for a detailed description of the problem of pipes conveying fluid.

A pipe conveying fluid at constant velocity $v$ is shown in Fig. (5.25). The pipe may be modeled with stationary Euler beam elements and the fluid with variable-domain beam elements with zero Young's modulus. That is, we have:

for the stationary pipe

$$l_i = L_P/4, \qquad d_i = \text{not applicable}, \qquad i = 1, \ldots 4, \tag{5.21}$$

and for the fluid

$$l_i = L_P/4, \qquad d_i = L_P - (i-5)\, l_i, \qquad i = 5, \ldots 8. \tag{5.22}$$

It should be noted that $[\dot{N}]_y$ vanishes in Eq. (3.18) for the fluid elements since these elements are also of constant length.

### 5.6.1 Pipes Supported at Both Ends

The examples in this section are those of simply-supported and clamped-clamped pipes conveying fluid. The global governing equations are given by Eqs. (3.32), where the mass matrix $[M]$ contains contributions from the pipe and the fluid, the equivalent-damping matrix becomes skew-symmetric (the problem of supported pipes conveying fluid is of the conservative gyroscopic type)

$$[C_{eq}] = [C_2] - [C_2]^T, \tag{5.23}$$

and the equivalent-stiffness matrix becomes

$$[K_{eq}] = [K] - [K_1], \tag{5.24}$$

where only the pipe contributes to the stiffness matrix $[K]$, and only the fluid contributes to the matrix $[K_f]$.

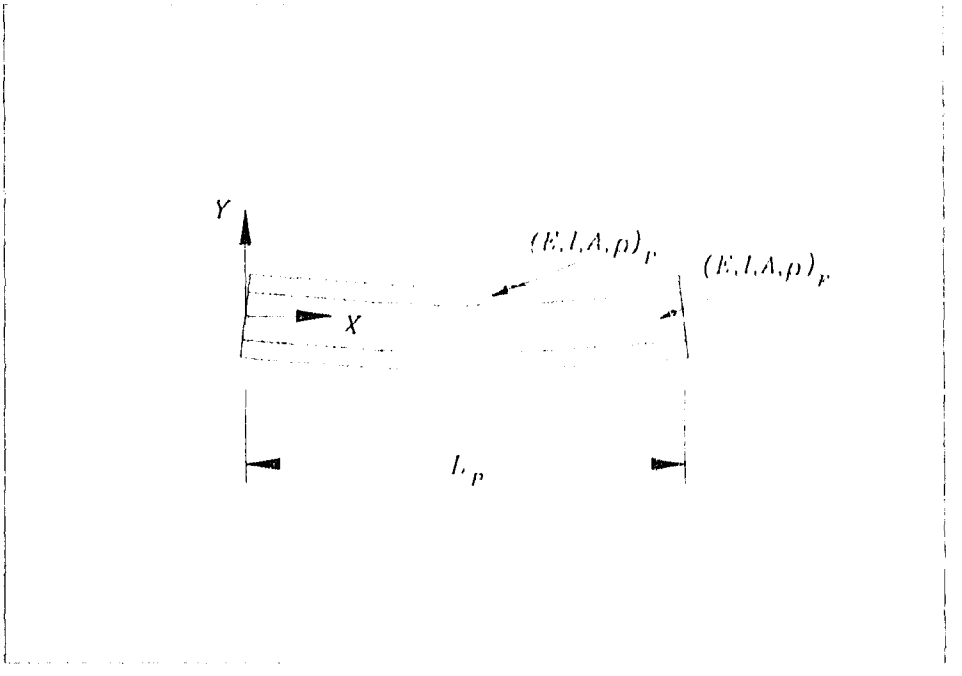


Figure 5.25: A pipe conveying fluid.

The results are shown in Tables (5.11) through (5.13) where the critical non-dimensional fluid velocity $U$ and the non-dimensional parameter $\beta$ are defined as

$$U = vL_P\sqrt{\frac{M}{EI}}, \qquad \beta = \frac{M}{(M+m)}, \tag{5.25}$$

with the velocity of the fluid $v$, the pipe length $L_P$, flexural rigidity of the pipe $EI$, the fluid mass per unit length $M$, and the pipe mass per unit length $m$. As the velocity of the fluid is increased, the natural frequencies of the system decrease, and since pipes supported at botn ends are conservative systems, divergence instabilities are characterised by the simultaneous vanishing of both eigenvalues corresponding to a particular natural frequency. Hence, in this section, $U_i$ is interpreted as the critical non-dimensional velocity at which the $i^{th}$ oscillatory mode diverges (as opposed o the $i^{th}$ eigen-

value). Similarly, $U_{i,j}$ denotes the critical non-dimensional velocity at which the $i^{th}$ and $j^{th}$ oscillatory modes coalesce.

In general, the four-element model is sufficiently accurate for determination of the critical velocities involving the first two oscillatory modes, while the ten-element model consistently yields near-exact results in all cases.

| $U$ | Païdoussis (1974) | Four elements | Ten elements |
|---|---|---|---|
| $U_1$ | 3.14 | 3.14 | 3.14 |
| $U_2$ | 6.28 | 6.31 | 6.28 |
| $U_{1,2}$ | 6.375 - 6.5[a] | 6.42 | 6.40 |

Table 5.11: Simply-supported pipe, $\beta = 0.1$.

a. The range 6.365 - 6.5 was obtained from a graph.

| $U$ | Païdoussis (1975) | Four elements | Ten elements |
|---|---|---|---|
| $U_1$ | 6.28 | 6.31 | 6.28 |
| $U_2$ | 8.99 | 9.10 | 8.99 |
| $U_{1,2}$ | $8.99^{+a}$ | 9.12 | 9.01 |

Table 5.12: Clamped-clamped pipe, $\beta = 0.1$.

a. $8.99^{+}$ is interpreted as a value slightly higher than $8.9^{9}$.

| $U$ | Païdoussis (1991) | Four elements | Ten elements |
|---|---|---|---|
| $U_1$ | 6.28 | 6.31 | 6.28 |
| $U_2$ | Not applicable | Not applicable | Not applicable |
| $U_{1,2}$ | 9.3 | 9.44 | 9.3 |

Table 5.13: Clamped-clamped pipe, $\beta = 0.5$.

It is interesting to note that by increasing the value of $\beta$ to 0.5, the second mode of the clamped-clamped beam never diverges. A similar effect was discussed in Section 5.2.4

for the case of the constant-velocity extruding beam carrying a large tip mass. In that case, however, it is the second eigenvalue that never vanishes.

### 5.6.2 Cantilever Pipes

The variable-domain beam element cannot be used without modification for the modeling of cantilever pipes conveying fluid. Specifically, it is necessary to introduce the effect of the equivalent-flow tip force (for an excellent discussion on the equivalent flow tip force, the reader is referred to Benjamin (1961)). This is accomplished by considering the virtual work of the equivalent-flow tip force (described in Appendix G). When this is done, the equivalent-damping and equivalent-stiffness matrices for the last element (the tip element) emerge as

$$[C_{eq}] = [T_1] + [C_2] - [C_2]^T, \tag{5.26}$$

$$[K_{eq}] = [K] + [T_2] - [K_1], \tag{5.27}$$

where the new matrices $[T_1]$ and $[T_2]$ model the effect of the equivalent-flow tip force on the last element. These matrices are given in Appendix G.

The cantilever pipe conveying fluid is a non-conservative system ($[C_{eq}]$ is no longer skew-symmetric as was the case for pipes supported at both ends) that loses stability by flutter through a Hopf bifurcation. As shown in Table (5.14), this problem requires more elements (particularly at the tip) than that used for the simply-supported (and clamped-clamped) pipes in order to accurately model the effect of the equivalent-flow tip force on the tip element. It is interesting to note that the flow of mass is responsible for the energy dissipation/generation for the axially-moving beam, whereas it is the equivalent-flow tip force that renders the cantilever pipe non-conservative.

| $U$ | Païdoussis (1966, 1991) | Two elements | Four elements | Ten elements |
|---|---|---|---|---|
| $U_{1,2}$ | 12.79 | 15.15 | 13.01 | 12.79 |

Table 5.14: Cantilever pipe, $\beta = 0.6$.

## 5.7 Concluding Remarks

In the foregoing, we have examined the stability of flexible extendible beams and the related problem of pipes conveying fluid. Results for the latter problem have been reported in the literature since the 1960's. For the former problem, however, we have presented some new results as summarised below:

<u>Constant-velocity Extrusion</u>

**Simplest Case**

1. The system is stable for low non-dimensional velocities $U$.

2. The first divergence instability occurs at $U_1 = 4.01$.

3. The system flutters at $U_{1,2} = 10.47$.

4. For all practical purposes, operating axial velocities must remain well below $U_1$.

**Effect of Physical Damping**

1. Physical damping has no appreciable effect on the stability characteristics of the system.

2. Physical damping has no effect on the onset of divergence instabilities.

3. In practical situations, where damping is almost always present, physical damping has the desirable effect of postponing the onset of flutter (as compared to the undamped case).

**Effect of a Flexible Envelope Beam**

1. The flexibility of the media from which the flexible extendible beam protrudes causes the onset of both divergence and flutter to occur at lower velocities than in the case of the rigid wall.

2. Modeling of the media from which the flexible-extendible beam protrudes as rigid is an idealisation. Therefore, in practical situations, divergence and flutter will occur at lower velocities than in the case of the rigid wall.

### Effect of a Tip Mass

1. The addition of a tip mass has no effect on the onset of divergence instabilities, although it postpones the onset of flutter.

2. For relatively large tip mass, the system may exhibit coupled-mode flutter.

### Effect of Tip Constraints

Supporting the tip of the flexible extendible beam postpones all the critical velocities (as compared to the cantilever flexible extendible beam).

## Constant Velocity Retraction

### Simplest Case:

1. The system is unstable for low non-dimensional velocities $U$.

2. The first divergence instability occurs at $U_1 = 4.01$.

3. The first oscillatory mode becomes stable at $U_{1,2} = 10.47$.

### Effect of Physical Damping

1. The addition of physical damping renders the system stable for low non-dimensional velocities.

2. Physical damping has no effect on the onset of divergence instabilities.

3. In practical situations, where physical damping is always present, operating velocities must remain well below the first occurrence of a Hopf bifurcation.

4. The stability characteristics of the system are greatly affected by the addition of heavy damping.

### Effects of a Flexible Envelope Beam, Tip Mass and Tip Constraints

The same effects were observed as in the case of the constant-velocity extruding beam.

## Constant-Acceleration Extrusion and Retraction

1. A constant acceleration due to a root-applied force has the expected effect during extrusion and retraction. Namely, it lowers the critical velocities if a compressive axial load is present, and it raises the critical velocities if a tensile axial load is present.

2. The effect of a constant acceleration due to a uniform acceleration field is to raise the critical extruding velocities if the beam is accelerating and to lower them if the beam is decelerating. The opposite is true for retracting beams under uniform acceleration field.

Our findings demonstrate that the conclusions reached by Wang and Wei (1987) regarding the total energy of the flexible extendible beam are incorrect. Namely, for velocities below the onset of instabilities, we have shown that extrusion causes energy dissipation whereas during retraction the system gains energy.

The similarity solution obtained by Tabarrok et al. (1974) was investigated through a dynamic stability analysis. It was found that it represents a very special case for which the flexible extendible beam remains buckled throughout the extrusion process. Numerical values for the similarity parameter from our finite-element formulation were found to be in agreement with the analytical similarity solution.

A stability analysis of pipes conveying fluid was also performed. We have shown that for pipes supported at both ends and conveying fluid, the variable-domain beam element can be used without modification. However, for cantilever pipes conveying fluid, the effect of the equivalent-flow tip force yields a modified set of equations. Numerical values for the critical fluid velocities from our finite-element formulation were found to be in agreement with the results found by Païdoussis (1966, 1974, 1975, 1991).

# Chapter 6

# A Spatial Flexible Extendible Beam

Chapters 2 to 5 have been concerned with one-dimensional flexible extendible beams. In this chapter, we derive the finite-element equations of a spatially translating and rotating flexible extendible beam, and perform two- and three-dimensional simulations. This formulation is of value for the analysis of flexible extendible spacecraft antennas, and flexible links traveling through prismatic joints of robotic manipulators.

## 6.1 Finite-Element Discretization

A spatially translating and rotating flexible extendible beam carrying a tip mass is shown in Fig. (6.1). For purposes of this work, this beam is subject only to transverse elastic deflections in two orthogonal planes, namely, the *XY*- and *XZ*-planes. These small deflections will be superimposed on the prescribed gross rigid-body translations and rotations.

Following the same procedure as that employed in Section 3.2, each of these deflections can be described using interpolation functions and nodal displacement values. That is, (with respect to the element coordinate system *xyz* (Fig. (3.2))

$xy$-plane ($y$-direction)

$$y(t,x) = \lfloor N \rfloor_y \{y\}, \tag{6.1}$$

$xz$-plane ($z$-direction)

$$z(t,x) = \lfloor N \rfloor_z \{z\}, \tag{6.2}$$

where the shape-functions vector $\lfloor N \rfloor_y$ was derived in Section 3.2 (Eq. (3.16)) and the nodal-variables vector $\{y\}$ is given by Eq. (3.17).

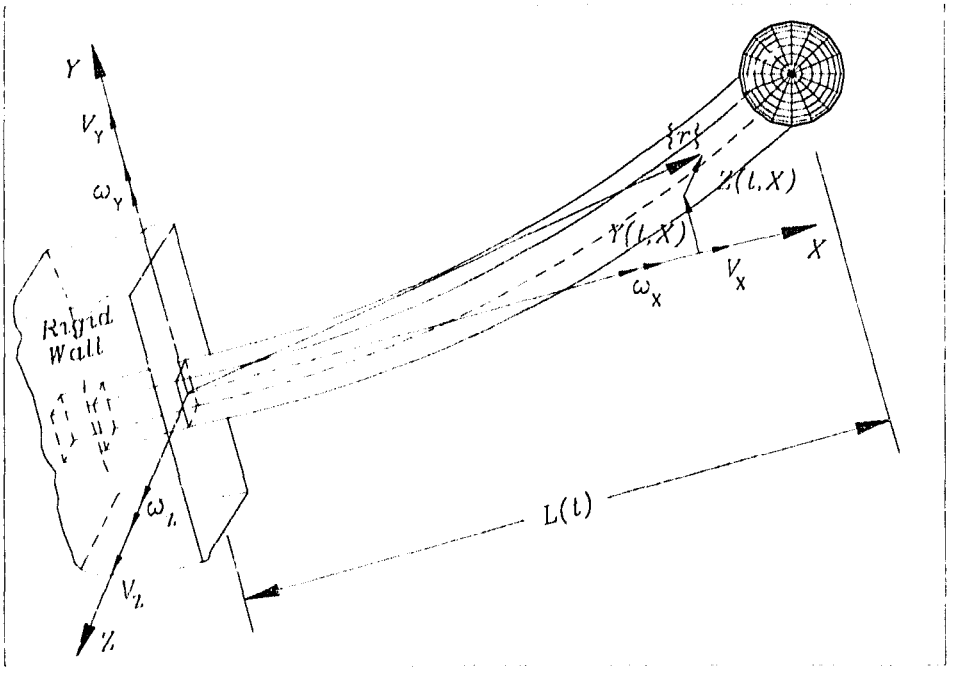


Figure 6.1: A spatial flexible extendible beam.

For the shape-functions and nodal-variables vectors in the $xz$-plane one obtains

$$\lfloor N \rfloor_z = \left[ 1 - \frac{3x^2}{l^2} + \frac{2x^3}{l^3} \;,\; -x + \frac{2x^2}{l} - \frac{x^3}{l^2} \;,\; \frac{3x^2}{l^2} - \frac{2x^3}{l^3} \;,\; \frac{x^2}{l} - \frac{x^3}{l^2} \right], \tag{6.3}$$

$$\{z\}^T = \left[ z_1 \;,\; \Phi_1 \;,\; z_2 \;,\; \Phi_2 \right], \tag{6.4}$$

where

$$
\begin{aligned}
z(t,0) &= z_1, \qquad z_x(t,0) = \Phi_1, \\
z(t,l) &= z_2, \qquad z_x(t,l) = \Phi_2,
\end{aligned}
\tag{6.5}
$$

with $z_i$ and $\Phi_i$ shown in Fig. (6.2). It is convenient at this time to define

$$
\{\chi\}^T = \left[y_1 \;,\; z_1 \;,\; \Theta_1 \;,\; \Phi_1 \;,\; y_2 \;\; z_2 \;,\; \Theta_2 \;,\; \Phi_2\right], \tag{6.6}
$$

$$
\lfloor \aleph \rfloor_y = \left[N_{y_1} \;,\; 0 \;,\; N_{y_2} \;,\; 0 \;,\; N_{y_3} \;,\; 0 \;,\; N_{y_4} \;,\; 0\right], \tag{6.7}
$$

$$
\lfloor \aleph \rfloor_z = \left[0 \;,\; N_{z_1} \;,\; 0 \;,\; N_{z_2} \;,\; 0 \;,\; N_{z_3} \;,\; 0 \;,\; N_{z_4}\right], \tag{6.8}
$$

where $N_{y_i}$ and $N_{z_i}$ are the $i^{th}$ components of the vectors $\lfloor N \rfloor_y$ and $\lfloor N \rfloor_z$ (Eqs. (3.16) and (6.3)), respectively. The finite-element discretization equations and their derivatives may now be written as

$$
\begin{aligned}
y &= \lfloor \aleph \rfloor_y \{\chi\}, & z &= \lfloor \aleph \rfloor_z \{\chi\}, \\
y_x &= \lfloor \aleph' \rfloor_y \{\chi\}, & z_x &= \lfloor \aleph' \rfloor_z \{\chi\}, \\
y_{xx} &= \lfloor \aleph'' \rfloor_y \{\chi\}, & z_{xx} &= \lfloor \aleph'' \rfloor_z \{\chi\}, \\
y_t &= \lfloor \dot{\aleph} \rfloor_y \{\chi\} + \lfloor \aleph \rfloor_y \{\dot{\chi}\}, & z_t &= \lfloor \dot{\aleph} \rfloor_z \{\chi\} + \lfloor \aleph \rfloor_z \{\dot{\chi}\}.
\end{aligned}
\tag{6.9}
$$

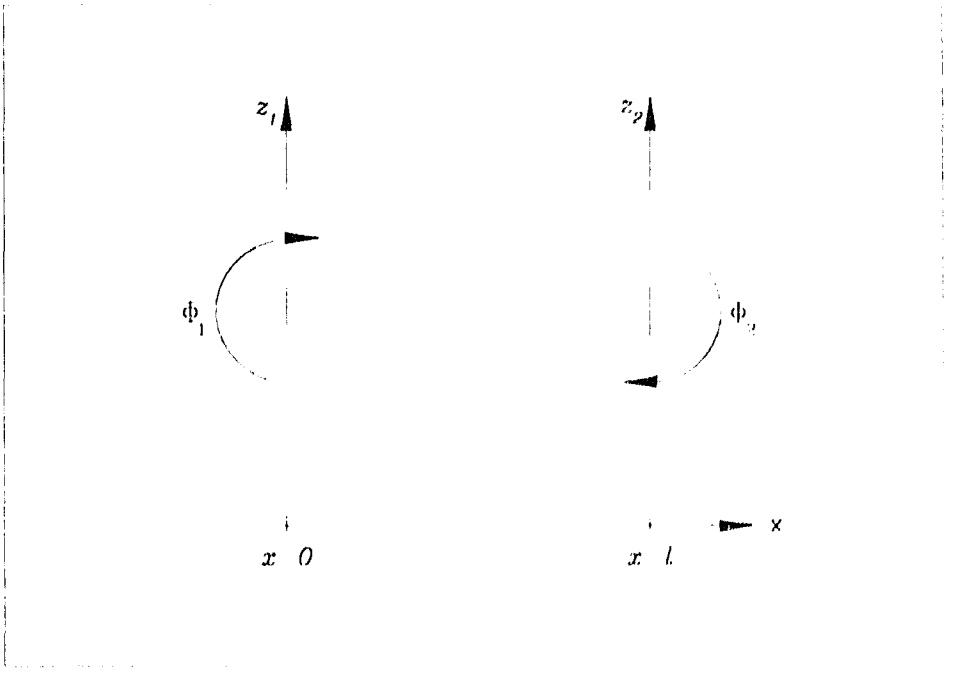


Figure 6.2 Nodal variables of a beam finite element in the $xz$-plane.

## 6.2 Velocity Distribution Along the Flexible Extendible Beam

The velocity distribution along a spatially translating and rotating flexible extendible beam is due to rigid-body translations, rotations, and extrusion/retraction, as well as elastic deformations. The flexible extendible beam of Fig. (6.1) has rigid-body translational velocities ($V_X$, $V_Y$, $V_Z$), rigid-body angular velocities ($\omega_X$, $\omega_Y$, $\omega_Z$) and the length of the protruding part of the beam is given by $L(t)$. These quantities are measured with respect to the system-fixed $XYZ$ coordinate system.

The position vector $\{r\}$ to an arbitrary point along the flexible extendible beam (Fig. (6.1)) may be expressed as a combination of a rigid-body vector $\{r_r\}$ and elastic vector $\{r_e\}$ as follows

$$\{r\} = \{r_r\} + \{r_e\}, \tag{6.10}$$

where

$$\{r_r\} = \begin{bmatrix} X \\ 0 \\ 0 \end{bmatrix}, \qquad \{r_e\} = \begin{bmatrix} 0 \\ Y(t,X) \\ Z(t,X) \end{bmatrix}. \tag{6.11}$$

Similarly, the angular-velocity vector $\{\omega\}$ of an arbitrary point along the flexible extendible beam (Fig. (6.1)) may be expressed as

$$\{\omega\} = \{\omega_r\} + \{\omega_e\}, \tag{6.12}$$

where

$$\{\omega_r\} = \begin{bmatrix} \omega_X \\ \omega_Y \\ \omega_Z \end{bmatrix}, \qquad \{\omega_e\} = \begin{bmatrix} 0 \\ Z_{Xt}(t,X) \\ Y_{Xt}(t,X) \end{bmatrix}. \tag{6.13}$$

The absolute linear velocity of an arbitrary point along the flexible extendible beam may then be expressed as

$$\{V\} = \{V_r\} + \frac{d}{dt}\{r\} + \{\omega_r\} \times \{r\}, \tag{6.14}$$

where

$$\{V_r\} = \begin{bmatrix} V_X \\ V_Y \\ V_Z \end{bmatrix}. \tag{6.15}$$

Substituting Eqs. (6.10) and (6.15) into Eq. (6.14) and carrying out the indicated total time differentiation and cross product, one obtains the absolute linear-velocity vector as

$$\{V\} = \begin{bmatrix} V_X + Z\omega_Y - Y\omega_Z + \dot{L} \\ V_Y - Z\omega_X + X\omega_Z + Y_t + \dot{L}Y_X \\ V_Z + Y\omega_X - X\omega_Y + Z_t + \dot{L}Z_X \end{bmatrix}. \tag{6.16}$$

## 6.3 Complementary Kinetic Energy

To be consistent with our work thus far, we neglect the rotary inertia of the slender spatial flexible extendible beam. Therefore, the expression for the complementary kinetic energy of the flexible extendible beam carrying a tip mass may be expressed as

$$T^* = T_b^* + T_m^*, \tag{6.17}$$

where $T_b^*$ and $T_m^*$ are the complementary kinetic energy expressions for the flexible extendible beam and tip mass, respectively. The expression for the complementary kinetic energy of the flexible extendible beam may be expressed as

$$T_b^* = \int_0^{L(t)} \frac{1}{2}\rho A \left( \{V\}^T \{V\} \right) dx, \tag{6.18}$$

which upon performing the inner product of the linear-velocity vector becomes

$$T_b^* = \int_0^{L(t)} \frac{1}{2}\rho A\Big[ (V_X + Z\omega_Y - Y\omega_Z + \dot{L})^2 + (V_Y - Z\omega_X + X\omega_Z + Y_t + \dot{L}Y_X)^2 + (V_Z + Y\omega_X - X\omega_Y + Z_t + \dot{L}Z_X)^2 \Big] dX. \tag{6.19}$$

Following a procedure similar to that employed in Section 3.1 (refer to Figs. (3.1) and (3.2) and Eqs. (3.2) and (3.5)), we write the complementary kinetic energy for the $i^{th}$ element as

$$T_{b_i}^* = \int_0^{l(t)} \frac{1}{2}\rho A\Big[ (v_x + z\omega_y - y\omega_z + \dot{d}_i)^2 + (v_y - z\omega_x + (L_i + x)\omega_z + y_t + \dot{d}_i y_x)^2 + (v_z + y\omega_x - (L_i + x)\omega_y + z_t + \dot{d}_i z_x)^2 \Big] dx \tag{6.20}$$

which after squaring the terms in the integrand becomes

$$\begin{aligned} T_{b_i}^* = \int_0^{l(t)} \frac{1}{2}\rho A\Big[ & (y_t + \dot{d}_i y_x)^2 + \omega_z^2((L_i + x)^2 + y^2) + 2v_y(y_t + \dot{d}_i y_x) + \\ & 2\omega_z((L_i + x)(y_t + \dot{d}_i y_x + v_y) - y(\dot{d}_i + v_x)) + \\ & \omega_x y(\omega_x y - 2\omega_y(L_i + x) + 2v_z) + \\ & (z_t + \dot{d}_i z_x)^2 + \omega_y^2((L_i + x)^2 + z^2) + 2v_z(z_t + \dot{d}_i z_x) - \\ & 2\omega_y((L_i + x)(z_t + \dot{d}_i z_x + v_z) - z(\dot{d}_i + v_x)) + \\ & \omega_x z(\omega_x z - 2\omega_z(L_i + x) - 2v_y) + \\ & 2\dot{d}_i\omega_x(z_x y - y_x z) + 2\omega_x(z_t y - y_t z) - \\ & 2\omega_y\omega_z yz + \{\dot{d}_i^2 + v_x^2 + v_y^2 + v_z^2 + 2\dot{d}_i v_x\}\Big] dx. \end{aligned} \tag{6.21}$$

Now substituting for the elastic deformations $y$, $y_x$, $z$, $z_x$ from Eqs. (6.9) in the above expression and ignoring the prescribed terms in braces (since they do not contribute to the equations of motion), the expression for the element complementary kinetic energy becomes

$$T_{b_i}^{*} = \frac{1}{2}\{\dot{\chi}\}^T[m]_b\{\dot{\chi}\} + \frac{1}{2}\{\chi\}^T[k_1]_b\{\chi\} + \frac{1}{2}\{\chi\}^T[c_1]_b\{\dot{\chi}\} + \frac{1}{2}\{\dot{\chi}\}^T[c_2]_b\{\chi\} + \frac{1}{2}\{\chi\}^T[k_3]_b\{\chi\} + \frac{1}{2}\{\chi\}^T[k_6]_b\{\chi\} + \frac{1}{2}\{\chi\}^T[k_7]_b\{\chi\} + \frac{1}{2}\{\dot{\chi}\}^T[c_3]_b\{\chi\} - \frac{1}{2}\{\chi\}^T[k_8]_b\{\chi\} + \{\chi\}^T\{r_1\}_b + \{\dot{\chi}\}^T\{r_2\}_b, \tag{6.22}$$

where

$$[m]_b = \int_0^{l(t)} \rho A\left[\lfloor \aleph \rfloor_y^T \lfloor \aleph \rfloor_y + \lfloor \aleph \rfloor_z^T \lfloor \aleph \rfloor_z\right] dx, \tag{6.23}$$

$$[k_1]_b = \int_0^{l(t)} \rho A\Big[\lfloor \dot{\aleph} \rfloor_y^T \lfloor \dot{\aleph} \rfloor_y + \lfloor \dot{\aleph} \rfloor_z^T \lfloor \dot{\aleph} \rfloor_z + \dot{d}_i^2\left[\lfloor \aleph' \rfloor_y^T \lfloor \aleph' \rfloor_y + \lfloor \aleph' \rfloor_z^T \lfloor \aleph' \rfloor_z\right] + \dot{d}_i\Big[\lfloor \dot{\aleph} \rfloor_y^T \lfloor \aleph' \rfloor_y + \lfloor \aleph' \rfloor_y^T \lfloor \dot{\aleph} \rfloor_y + \lfloor \dot{\aleph} \rfloor_z^T \lfloor \aleph' \rfloor_z + \lfloor \aleph' \rfloor_z^T \lfloor \dot{\aleph} \rfloor_z\Big]\Big] dx, \tag{6.24}$$

$$[c_1]_b = \int_0^{l(t)} \rho A\Big[\lfloor \dot{\aleph} \rfloor_y^T \lfloor \aleph \rfloor_y + \lfloor \dot{\aleph} \rfloor_z^T \lfloor \aleph \rfloor_z + \dot{d}_i\Big[\lfloor \aleph' \rfloor_y^T \lfloor \aleph \rfloor_y + \lfloor \aleph' \rfloor_z^T \lfloor \aleph \rfloor_z\Big]\Big] dx \tag{6.25}$$

$$[c_2]_b = \int_0^{l(t)} \rho A\Big[\lfloor \aleph \rfloor_y^T \lfloor \dot{\aleph} \rfloor_y + \lfloor \aleph \rfloor_z^T \lfloor \dot{\aleph} \rfloor_z + \dot{d}_i\Big[\lfloor \aleph \rfloor_y^T \lfloor \aleph' \rfloor_y + \lfloor \aleph \rfloor_z^T \lfloor \aleph' \rfloor_z\Big]\Big] dx \tag{6.26}$$

$$[k_3]_b = \int_0^{l(t)} \rho A\left[(\omega_x^2 + \omega_z^2)\lfloor \aleph \rfloor_y^T \lfloor \aleph \rfloor_y + (\omega_x^2 + \omega_y^2)\lfloor \aleph \rfloor_z^T \lfloor \aleph \rfloor_z\right] dx, \tag{6.27}$$

$$[k_6]_b = \int_0^{l(t)} 2\rho A \dot{d}_i \omega_x\left[\lfloor \aleph' \rfloor_z^T \lfloor \aleph \rfloor_y - \lfloor \aleph' \rfloor_y^T \lfloor \aleph \rfloor_z\right] dx, \tag{6.28}$$

$$[k_7]_b = \int_0^{l(t)} 2\rho A \omega_x\Big[\lfloor \dot{\aleph} \rfloor_z^T \lfloor \aleph \rfloor_y - \lfloor \dot{\aleph} \rfloor_y^T \lfloor \aleph \rfloor_z\Big] dx, \tag{6.29}$$

$$[c_3]_b = \int_0^{l(t)} 2\rho A \omega_x\left[\lfloor \aleph \rfloor_z^T \lfloor \aleph \rfloor_y - \lfloor \aleph \rfloor_y^T \lfloor \aleph \rfloor_z\right] dx, \tag{6.30}$$

$$[k_8]_b = \int_0^{l(t)} 2\rho A \omega_y \omega_z \lfloor \aleph \rfloor_y^T \lfloor \aleph \rfloor_z dx, \tag{6.31}$$

$$\begin{aligned}\{r_1\}_b = \int_0^{l(t)} \rho A \Big[ & (V_y + \omega_z (L_i + x)) \lfloor \aleph \rfloor_y^T + \dot{d}_i (V_y + \omega_z (L_i + x)) \lfloor \aleph' \rfloor_y^T + \\ & (\omega_x V_z - \omega_z (\dot{d}_i + V_x) - \omega_x \omega_y (L_i + x)) \lfloor \aleph \rfloor_y^T + \\ & (V_z - \omega_y (L_i + x)) \lfloor \dot{\aleph} \rfloor_z^T + \dot{d}_i (V_z - \omega_y (L_i + x)) \lfloor \aleph' \rfloor_z^T + \\ & (-\omega_x V_y + \omega_y (\dot{d}_i + V_x) - \omega_x \omega_z (L_i + x)) \lfloor \aleph \rfloor_y^T \Big] dx,\end{aligned} \tag{6.32}$$

$$\{r_2\}_b = \int_0^{l(t)} \rho A \left[ (V_y + \omega_z (L_i + x)) \lfloor \aleph \rfloor_y^T + (V_z - \omega_y (L_i + x)) \lfloor \aleph \rfloor_z^T \right] dx. \tag{6.33}$$

The $[m]_b$ matrix is the well-known consistent mass matrix of the beam element, and the skew-symmetric matrix $[c_3]_b$ is the beam gyroscopic matrix. The $\{r_1\}_b$ and $\{r_2\}_b$ vectors are dynamic loads acting on the flexible extendible beam due to the rigid-body motion.

### 6.3.1 Complementary Kinetic Energy of a Tip Mass

The complementary kinetic energy of the tip mass may be written as

$$T_m^* = \frac{1}{2} \hat{m} \left( \{V\}_{tip}^T \{V\}_{tip} \right), \tag{6.34}$$

where $\hat{m}$ is the translational inertia of the tip mass and $\{V\}_{tip}$ is the tip linear velocity given by Eq. (6.16) with $X = L$ as follows

$$\{V\}_{tip} = \begin{bmatrix} V_X + Z\omega_Y - Y\omega_Z + \dot{L} \\ V_Y - Z\omega_X + L\omega_Z + Y_t + \dot{L}Y_X \\ V_Z + Y\omega_X - L\omega_Y + Z_t + \dot{L}Z_X \end{bmatrix}_{X=L} . \tag{6.35}$$

Following a procedure similar to that employed in the previous section, the complementary kinetic energy of the tip mass may be written as

$$T_m^* = \frac{1}{2}\{\dot{\chi}\}^T[m]_m\{\dot{\chi}\} + \frac{1}{2}\{\chi\}^T[k_3]_m\{\chi\} + \frac{1}{2}\{\chi\}^T[k_6]_m\{\chi\} + \frac{1}{2}\{\chi\}^T[k_7]_m\{\chi\} + \frac{1}{2}\{\dot{\chi}\}^T[c_3]_m\{\chi\} - \frac{1}{2}\{\chi\}^T[k_8]_m\{\chi\} + \{\chi\}^T\{r_1\}_m + \{\dot{\chi}\}^T\{r_2\}_m, \tag{6.36}$$

where

$$[m]_m = \hat{m}\left[\lfloor \aleph \rfloor_y^T \lfloor \aleph \rfloor_y + \lfloor \aleph \rfloor_z^T \lfloor \aleph \rfloor_z\right]\Big|_{x=l}, \tag{6.37}$$

$$[k_3]_m = \hat{m}\left[(\omega_x^2+\omega_z^2)\lfloor \aleph \rfloor_y^T \lfloor \aleph \rfloor_y + (\omega_x^2+\omega_y^2)\lfloor \aleph \rfloor_z^T \lfloor \aleph \rfloor_z\right]\Big|_{x=l}, \tag{6.38}$$

$$[k_6]_m = 2\hat{m}\dot{d}_i\omega_x\left[\lfloor \aleph' \rfloor_z^T \lfloor \aleph \rfloor_y - \lfloor \aleph' \rfloor_y^T \lfloor \aleph \rfloor_z\right]\Big|_{x=l}, \tag{6.39}$$

$$[k_7]_m = 2\hat{m}\omega_x\left[\lfloor \dot{\aleph} \rfloor_z^T \lfloor \aleph \rfloor_y - \lfloor \dot{\aleph} \rfloor_y^T \lfloor \aleph \rfloor_z\right]\Big|_{x=l}, \tag{6.40}$$

$$[c_3]_m = 2\hat{m}\omega_x\left[\lfloor \aleph \rfloor_z^T \lfloor \aleph \rfloor_y - \lfloor \aleph \rfloor_y^T \lfloor \aleph \rfloor_z\right]\Big|_{x=l}, \tag{6.41}$$

$$[k_8]_m = 2\hat{m}\omega_y\omega_z\lfloor \aleph \rfloor_y^T \lfloor \aleph \rfloor_z\Big|_{x=l}, \tag{6.42}$$

$$\begin{aligned}\{r_1\}_m = \hat{m}\Big[&(V_y+\omega_z l)\lfloor \dot{\aleph} \rfloor_y^T + \dot{d}_i(V_y+\omega_z l)\lfloor \aleph' \rfloor_y^T + \\ &(\omega_x V_z - \omega_z(\dot{d}_i+V_x) - \omega_x\omega_y l)\lfloor \aleph \rfloor_y^T + \\ &(V_z-\omega_y l)\lfloor \dot{\aleph} \rfloor_z^T + \dot{d}_i(V_z-\omega_y l)\lfloor \aleph' \rfloor_z^T + \\ &(-\omega_x V_y + \omega_y(\dot{d}_i+V_x) - \omega_x\omega_z l)\lfloor \aleph \rfloor_y^T\Big]\Big|_{x=l},\end{aligned} \tag{6.43}$$

$$\{r_2\}_m = \hat{m}\left[(V_y+\omega_z l)\lfloor \aleph \rfloor_y^T + (V_z-\omega_y l)\lfloor \aleph \rfloor_z^T\right]\Big|_{x=l}, \tag{6.44}$$

The above matrices and vectors correspond to the contributions of the tip mass to the corresponding matrices and dynamic load vectors (Eqs. (6.23) through (6.33)) of the last element only (the tip element).

## 6.4 Flexural Strain Energy

The strain energy of the flexible extendible beam element (assuming it to be slender, hence described by Euler-Bernoulli beam theory), is due to bending in two transverse

planes, along with the effect of axial forces on the lateral displacement. The element lateral strain energy may be expressed as

$$V_{s_i} = \int_0^{l(t)} \frac{1}{2} (EI_z y_{xx}^2 + EI_y z_{xx}^2)\, dx. \tag{6.45}$$

Substituting for $y_{xx}$ and $z_{xx}$ from Eqs. (6.9) yields

$$V_{s_i} = \frac{1}{2} \{\chi\}^T [k] \{\chi\}, \tag{6.46}$$

where

$$[k] = \int_0^{l(t)} [EI_z [\aleph'']_y^T [\aleph'']_y + EI_y [\aleph'']_z^T [\aleph'']_z]\, dx, \tag{6.47}$$

which corresponds to the well-known element structural stiffness matrix.

## 6.5 Energy Due to Longitudinal Loads

The potential energy of the axial force in the flexible extendible beam undergoing transverse deflection may be expressed as

$$V_l = \int_0^{L(t)} \frac{1}{2} P(X, t)\, (Y_X^2 + Z_X^2)\, dX, \tag{6.48}$$

where $P(X, t)$ is the axial tensile load at a location $X$ along the beam at time $t$. For the flexible extendible beam carrying a tip mass, the above expression becomes

$$V_l = \int_0^{L(t)} \frac{1}{2} \left[ -\left\{ \int_X^{L(t)} \rho A \ddot{L}\, dX \right\} - \hat{m}\ddot{L} - \left\{ \int_X^{L(t)} \rho A \dot{V}_X dX \right\} - \hat{m}\dot{V}_X + \left\{ \int_X^{L(t)} \rho A X\, (\omega_Y^2 + \omega_Z^2)\, dX \right\} + \hat{m}\, (\omega_Y^2 + \omega_Z^2) \right] (Y_X^2 + Z_X^2)\, dX. \tag{6.49}$$

Upon carrying out the indicated integrations within braces, the expression for the potential energy of the axial force in the $i^{th}$ element becomes

$$V_{l_i} = \int_0^{l(t)} \frac{1}{2}\Big[-(\rho A\,(d_i - x) + \hat{m})\,\ddot{L} - (\rho A\,(d_i - x) + \hat{m})\,\dot{V}_x + (\omega_y^2 + \omega_z^2)\,(L\hat{m} + \rho A\,(d_i(L + x) - \frac{1}{2}(d_i^2 + x^2) - Lx))\Big](y_x^2 + z_x^2)\,dx. \tag{6.50}$$

Now, substituting for the elastic deformations $y_x$ and $z_x$ from Eqs. (6.9) we obtain

$$V_{l_i} = -\frac{1}{2}\{\chi\}^T[k_2]\{\chi\} - \frac{1}{2}\{\chi\}^T[k_4]\{\chi\} + \frac{1}{2}\{\chi\}^T[k_5]\{\chi\}, \tag{6.51}$$

where

$$[k_2] = \int_0^{l(t)} (\rho A\,(d_i - x) + \hat{m})\,\ddot{L}\,[\lfloor \aleph' \rfloor_y^T \lfloor \aleph' \rfloor_y + \lfloor \aleph' \rfloor_z^T \lfloor \aleph' \rfloor_z]\,dx, \tag{6.52}$$

$$[k_4] = \int_0^{l(t)} (\rho A\,(d_i - x) + \hat{m})\,\dot{V}_x\,[\lfloor \aleph' \rfloor_y^T \lfloor \aleph' \rfloor_y + \lfloor \aleph' \rfloor_z^T \lfloor \aleph' \rfloor_z]\,dx, \tag{6.53}$$

$$[k_5] = \int_0^{l(t)} (\omega_y^2 + \omega_z^2)\,(L\hat{m} + \rho A\,(d_i(L + x) - \frac{1}{2}(d_i^2 + x^2) - Lx))\,[\lfloor \aleph' \rfloor_y^T \lfloor \aleph' \rfloor_y + \lfloor \aleph' \rfloor_z^T \lfloor \aleph' \rfloor_z]\,dx. \tag{6.54}$$

It is interesting to note that the $[k_5]$ matrix has a stiffening effect only, whereas, the effect of $[k_2]$ and $[k_4]$ matrices depends on the corresponding signs of $\ddot{L}$ and $\dot{V}_x$, respectively.

## 6.6 Finite-Element Equations

In sections 6.3 through 6.5, we obtained expressions for the complementary kinetic energy and potential energy of the flexible extendible beam element. The Lagrangian for the $i^{th}$ element may now be expressed as

$$\mathcal{L}_i = T_{b_i}^* + T_{m_i}^* - (V_{s_i} + V_{l_i}), \tag{6.55}$$

where it is noted that the complementary kinetic energy of the tip mass is relevant for the tip element only (i.e. for the last element on which the tip mass is attached). Using Eqs. (6.22), (6.36), (6.46) and (6.51), the element Lagrangian becomes

$$
\begin{aligned}
\mathcal{L}_i = {} & \frac{1}{2}\{\dot{\chi}\}^T[m]\{\dot{\chi}\} + \frac{1}{2}\{\chi\}^T[k_1]\{\chi\} + \frac{1}{2}\{\chi\}^T[c_1]\{\dot{\chi}\} + \\
& \frac{1}{2}\{\dot{\chi}\}^T[c_2]\{\chi\} + \frac{1}{2}\{\chi\}^T[k_3]\{\chi\} + \frac{1}{2}\{\chi\}^T[k_6]\{\chi\} + \\
& \frac{1}{2}\{\chi\}^T[k_7]\{\chi\} + \frac{1}{2}\{\dot{\chi}\}^T[c_3]\{\chi\} - \frac{1}{2}\{\chi\}^T[k_8]\{\chi\} + \\
& \{\chi\}^T\{r_1\} + \{\dot{\chi}\}^T\{r_2\} - \frac{1}{2}\{\chi\}^T[k]\{\chi\} + \\
& \frac{1}{2}\{\chi\}^T[k_2]\{\chi\} + \frac{1}{2}\{\chi\}^T[k_4]\{\chi\} - \frac{1}{2}\{\chi\}^T[k_5]\{\chi\},
\end{aligned}
\tag{6.56}
$$

where

$$
\begin{aligned}
[m] &= [m]_b + [m]_m, \\
[k_1] &= [k_1]_b + [k_1]_m, \\
[c_1] &= [c_1]_b + [0], \\
[c_2] &= [c_2]_b + [0], \\
[k_3] &= [k_3]_b + [k_3]_m, \\
[k_6] &= [k_6]_b + [k_6]_m, \\
[k_7] &= [k_7]_b + [k_7]_m, \\
[c_3] &= [c_3]_b + [c_3]_m, \\
[k_8] &= [k_8]_b + [k_8]_m, \\
\{r_1\} &= \{r_1\}_b + \{r_1\}_m, \\
\{r_2\} &= \{r_2\}_b + \{r_2\}_m.
\end{aligned}
\tag{6.57}
$$

At this point, it should be noted that even though some of the element matrices used in this chapter share the same names and physical interpretation as their counterparts in Chapter 3, the matrices for the spatial flexible extendible beam are of order eight, whereas the corresponding matrices for the one-dimensional flexible extendible beam in earlier chapters are of order four.

The Lagrange equations for an element, considering it to be unconstrained and independent of other elements, are given by

$$\frac{\partial \mathcal{L}_i}{\partial \{\chi\}^T} - \frac{d}{dt}\left[\frac{\partial \mathcal{L}_i}{\partial \{\dot{\chi}\}^T}\right] = \{0\}. \tag{6.58}$$

Using the expression for the element Lagrangian (Eq. (6.56)), we obtain the element governing equations as

$$[m]\{\ddot{\chi}\} + [c_{eq}]\{\dot{\chi}\} + [k_{eq}]\{\chi\} = \{r_{eq}\}, \tag{6.59}$$

where the equivalent-damping and -stiffness matrices, and equivalent-load vector are given by

$$\begin{aligned}
[c_{eq}] &= [\dot{m}] + [c_2] - [c_2]^T + [c_3], \\
[k_{eq}] &= [\dot{c}] + [\dot{c}_2] - [k_1] - [k_2] + \\
&\quad [\dot{c}_3] - [k_3] - [k_4] + [k_5] - [k_6] - [k_7] + [k_8], \\
\{r_{eq}\} &= \{r_1\} - \{\dot{r}_2\}.
\end{aligned} \tag{6.60}$$

Finally, the assembly of the element equations yields the global equations as follows

$$[M]\{\ddot{\chi}\} + [C_{eq}]\{\dot{\chi}\} + [K_{eq}]\{\chi\} = \{R_{eq}\}. \tag{6.61}$$

Similar to the case of the stationary flexible extendible beam of earlier chapters, the governing equations (Eq. (6.61)) of the spatial flexible extendible beam is a set of linear, second-order differential equations with variable coefficients. However, in the case of the spatial flexible extendible beam, the right-hand side of the governing equations is non-zero, accounting for the transverse loads due to the prescribed rigid-body motion.

The next sections are devoted to the verification of the spatial variable-domain beam element through a series of examples.

## 6.7 Simulations

The governing system of equations derived in the last section will now be integrated under specified initial and boundary conditions. We begin, in Section 6.7.1, with a simple two-dimensional example of a constant-length beam in rotation. Sections 6.7.2 and 6.7.3 deal with two- and three-dimensional examples of flexible extendible beams, respectively.

### 6.7.1 A Constant-Length Beam in Rotation

In order to validate our finite-element formulation and time-integration of the flexible extendible beam undergoing two-dimensional rigid-body motion, we begin with a simple example. A single flexible-link manipulator has been considered by Tzou (1989) (using Timoshenko beam theory) and Gaultier (1990) (using Euler-Bernoulli beam theory). The constant-length link is subject to the rigid-body rotation described by

$$\Theta_z(t) = \begin{cases} \Theta_o\left(\frac{1}{\tau^2}\left(\frac{t^2}{2} + \left(\frac{\tau}{2\pi}\right)^2\left(\cos\left(\frac{2\pi t}{\tau}\right) - 1\right)\right)\right), & 0 \le t \le \tau, \\ \left(1 - \frac{1}{\tau^2}\left(\frac{(2\tau - t)^2}{2} + \left(\frac{\tau}{2\pi}\right)^2\left(\cos\left(\frac{2\pi t}{\tau}\right) - 1\right)\right)\right), & \tau < t \le 2\tau, \\ \Theta_o, & 2\tau < t, \end{cases} \tag{6.62}$$

where

$\tau$ is the period of oscillation (*0.3 s*)

$\Theta_o$ is the amplitude of rotation (*0.3 rad*).

The geometric and material properties of the constant-length link are given in Table (6.1).

| $E$ (*GPa*) | $\rho$ ($Kg/m^3$) | $I_z$ ($m^4$) | $L$ (*m*) |
|---|---|---|---|
| 207.0 | 7825.0 | $277.0\ 10^{-12}$ | 0.6096 |

Table 6.1: Geometric and material properties of constant-length link.

The tip-deflection history for this problem is shown in Fig. (6.3). The link was modeled using four elements. Our results are essentially identical to the results obtained by Tzou (1989), Gaultier (1990) and Sharf (1993). It is interesting to note that the work by Tzou (1989) showed that the axial elastic deformations of the rotating beam are one one-hundredth of the lateral elastic deformations, thus justifying the assumption of axial rigidity for slender beams like the one used in this example. In addition, it should be noted that since the beam in this example is slender, rotary inertia and shear deformations, accounted for by Tzou's Timoshenko-beam formulation, become negligibly

small. As mentioned by Gaultier (1990), this is the reason for the agreement between the results obtained by Tzou (1989) and the results obtained using Euler-Bernoulli theory.

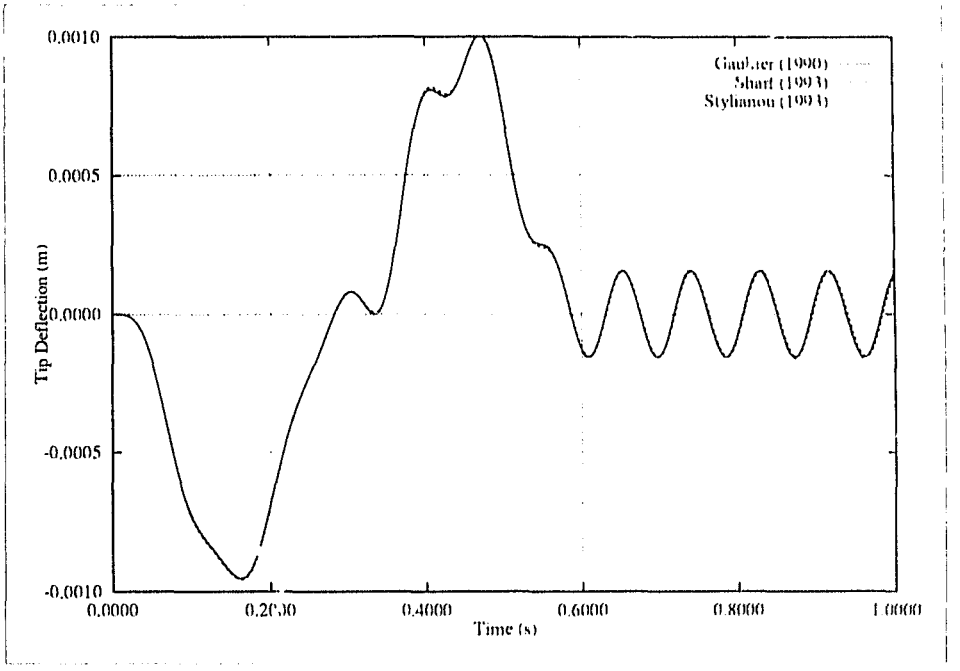


Figure 6.3: Tip response of a constant-length link in rotation.

### 6.7.2 Two-dimensional Experiments and Simulations by Yuh and Young

The next two examples correspond to Yuh and Young's (1991) experiments of axially-moving beams undergoing rigid-body rotation about the $z$-axis. The angular velocity of the beam is constant at $\omega_z = 2.6\ rad/s$ and the length of the beam is given by

$$L(t) = L_0 + vt, \tag{6.63}$$

where the values of the initial length $L_0$ and velocity $v$ are given in Table (6.2).

| Test case # | $L_0$ (m) | $v$ (m/s) | Figure # Appendix D |
|---|---|---|---|
| 5 | 0.5100 | -0.0720 | 4.5 |
| 6 | 0.4000 | +0.0350 | 4.6 |

Table 6.2: Parameters for experimental test cases, Yuh and Young (1991).

Our finite-element model used four variable-domain beam elements. Physical damping was modelled as discussed in Section 4.1. Our results for test case # 5 (Fig. (6.4)) were found to be in good agreement with the results of Yuh and Young (1991) (shown in Fig. (4.5) in Appendix D). However, a comparison of our results for test case # 6 (Fig. (6.5)) with the results of Yuh and Young (1991) (shown in Fig. (4.6) in Appendix D) was not feasible since we were unable to determine the time span depicted in their results.

Yuh and Young (1991) also performed four simulations of axially-moving beams in rotation. For these simulations, the length of the beam and the angle of rotation are given by

$$L(t) = L_o + \frac{c}{\tau}\left[ t - \frac{\tau}{2\pi}\sin(2\pi t/\tau) \right], \tag{6.64}$$

$$\Theta(t) = \Theta_o + \frac{d}{\tau}\left[ t - \frac{\tau}{2\pi}\sin(2\pi t/\tau) \right], \tag{6.65}$$

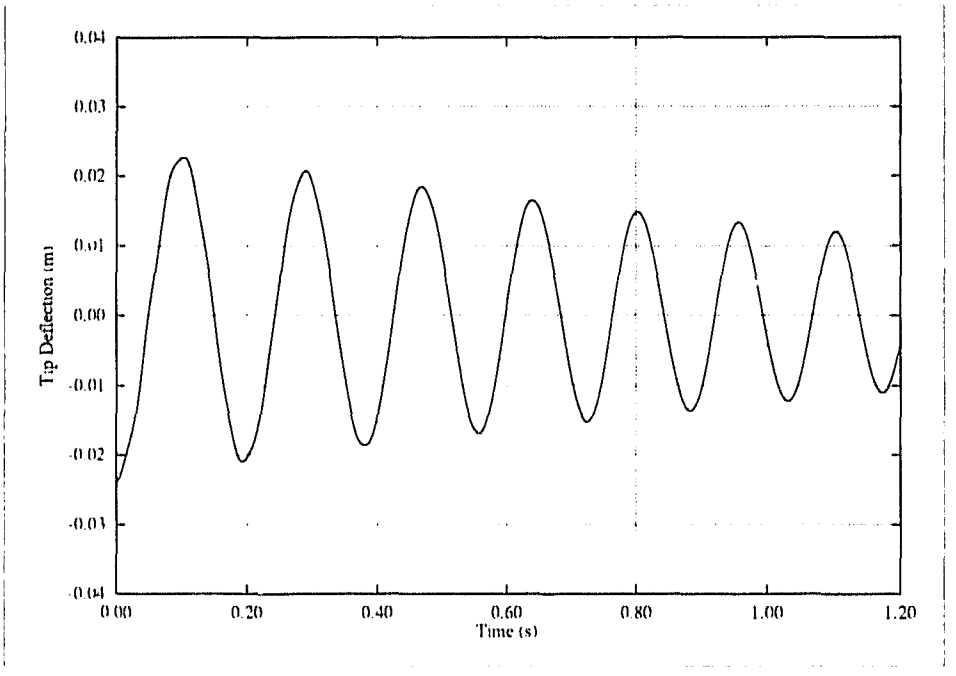


Figure 6.4: Test case # 5. Constant-velocity retraction and rotation.

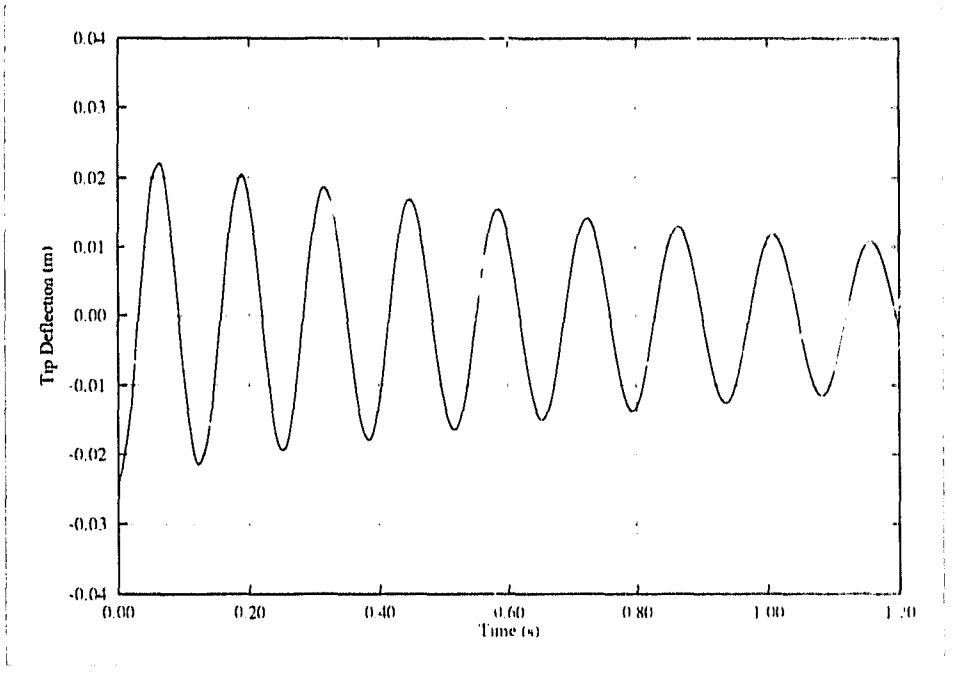


Figure 6.5: Test case # 6. Constant-velocity extrusion and rotation.

where values for $L_0$, $\Theta_0$, $c$, $d$, and $\tau$ are given in Table (6.3). These four simulations correspond to the four simulations considered in Section 4.1.1 (simulation numbers 1, 3, 5 and 7) with the addition of the rigid-body rotation.

| **Simulation #** | $L_0$ *(m)* | $\Theta_0$ *(rad)* | *c (m)* | *d (rad)* | $\tau$ *(s)* | **Figure # Appendix D** |
|---|---|---|---|---|---|---|
| 2 | 0.3500 | 0.0 | +0.7000 | 1.57 | 1.2000 | 5 |
| 4 | 1.0500 | 0.0 | -0.7000 | 1.57 | 1.2000 | 6 |
| 6 | 0.3500 | 0.0 | +0.7000 | 1.57 | 0.2000 | 7 |
| 8 | 1.0500 | 0.0 | -0.7000 | 0.50 | 0.2000 | 8 |

Table 6.3: Parameters for simulation cases, Yuh and Young (1991).

The results of our time-integrations are shown in Figs. (6.6) through (6.9) where the results of the simulations of Section 4.1.1 (Figs. (4.5) through (4.8)) are superimposed for easy reference (the solid lines). As can be seen from these results, the rigid-body rotation prescribed by Eq. (6.65) has an appreciable effect on the response of the flexible extendible beam, especially in the two retracting cases (simulations 4 and 8) where the beam starts out at its maximum length of $1.05m$.

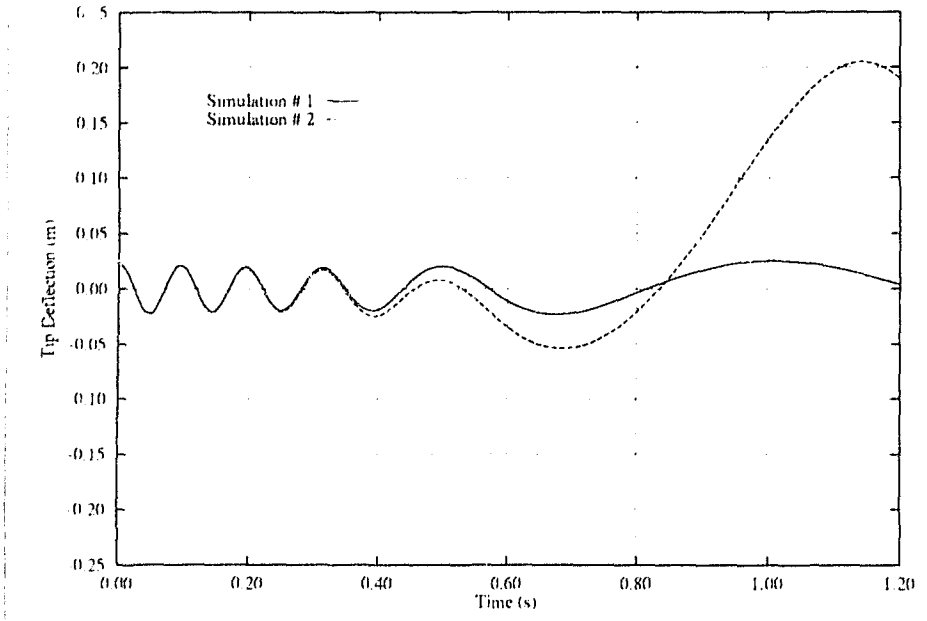


Figure 6.6: Simulation # 2. Low-frequency extrusion and rotation.

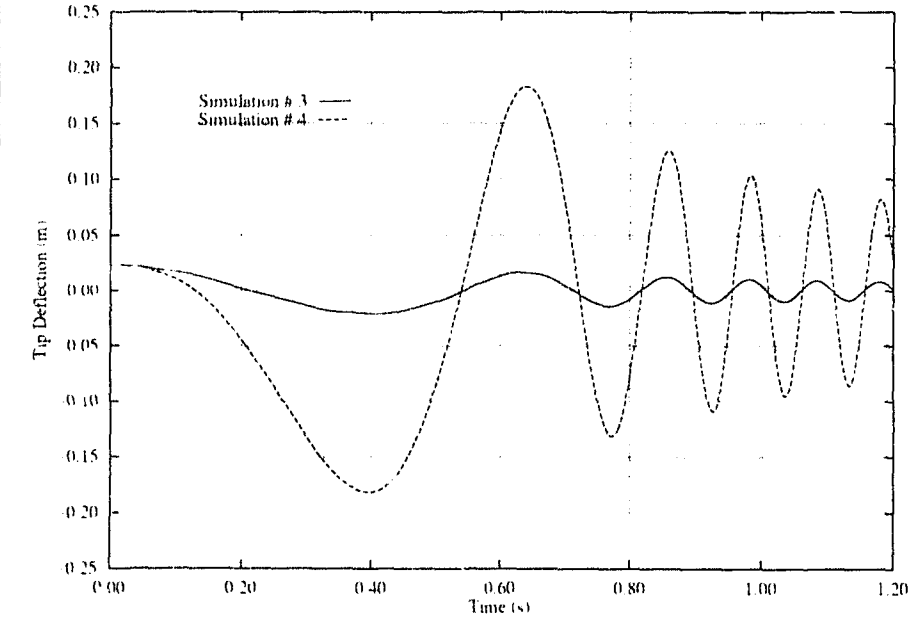


Figure 6.7: Simulation # 4. Low-frequency retraction and rotation.

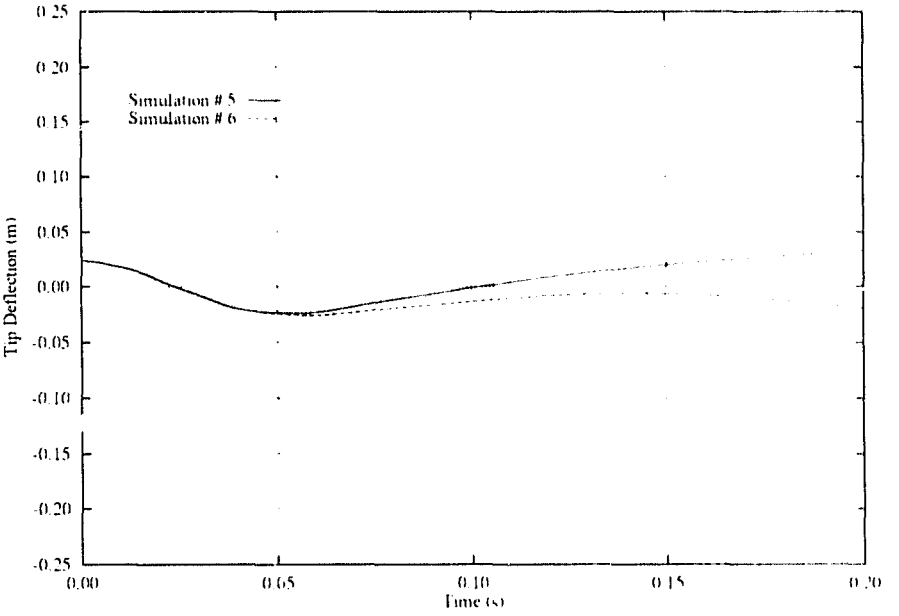


Figure 6.8: Simulation # 6. High-frequency extrusion and rotation.

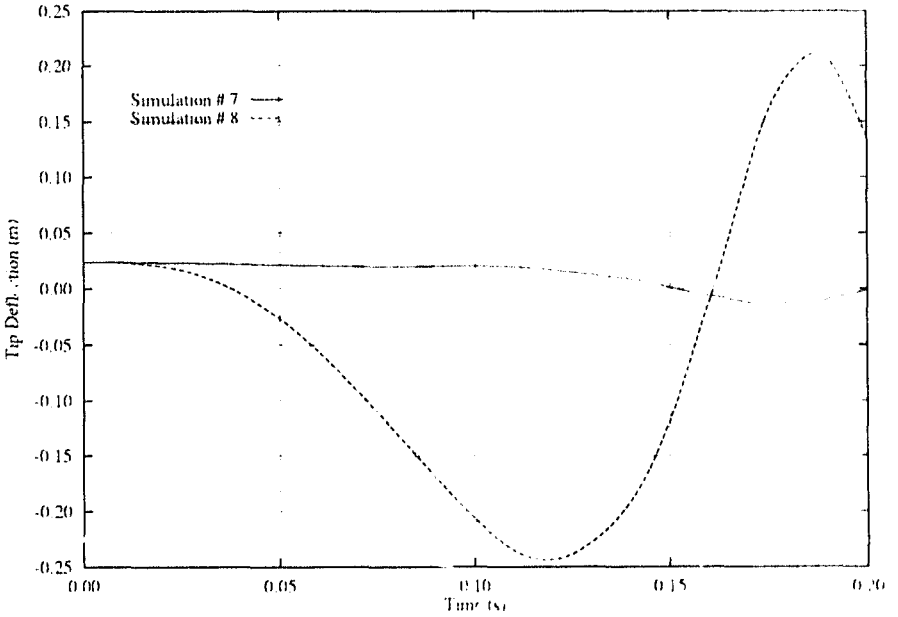


Figure 6.9: Simulation # 8. High-frequency retraction and rotation.

A comparison of our results to those of Yuh and Young (the dashed response in Figs. (5) through (8) of Appendix D) reveals that we are in disagreement. For instance, let us consider the eighth simulation in some detail. The beam is initially *1.05m* long and is deflected such that the tip displacement is *0.024m* in the positive *y*-direction, as shown in Fig. (6.10). At $t = 0$, the tip is released. According to the length and rotational motion profiles (Eqs. (6.64) and (6.65)), the beam will begin to retract and its base will accelerate counter-clockwise about the Z-axis. Under these conditions, one can anticipate on physical grounds, that the tip of the beam will move in the negative *y*-direction. This is indeed the behaviour predicted by our simulation results shown in Fig. (6.9). However, the simulation results of Yuh and Young (the dashed response in Fig. (8) of Appendix D) are in disagreement with this expected behaviour. Similar arguments based solely on physical considerations can be made with regards to the other three simulations (2, 4, and 6) that lead to the conclusion that the prescribed rigid-body rotation of Eq. (6.65) must have a much more profound effect on the transverse response of this slender axially-moving beam than predicted by Yuh and Young (1991). In fact, the deflections involved in simulation # 8 are too large (with the ratio $y_{tip}/L_i(t)$ reaching *0.6*) to be modelled by linear theory.

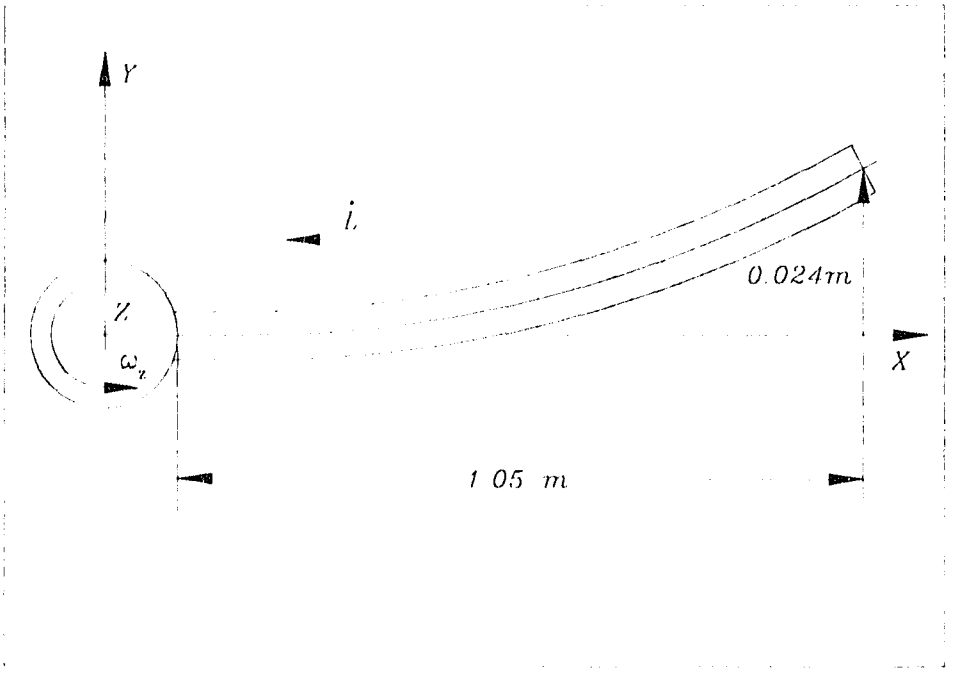


Figure 6.10: Simulation # 8. Initial system configuration.

Given that our formulation gives the correct results for the case of a constant-length beam undergoing two-dimensional rotation (as shown by the example in Section 6.7.1), we followed an alternative approach in verifying the correctness of our simulation results. In this approach, we set the extrusion velocity and acceleration to zero, and assign the beam's length according to Eq. (6.64). This approach is equivalent to integrating the governing equations of a constant-length beam in rotation at each time-step. The results of this *quasi-static* approach are superimposed in Fig. (6.11) with the results obtained using the complete dynamic model for the third and fourth simulations (Fig. (6.7)). As shown, the quasi-static and complete dynamic models initially yield identical results. However, as time progresses, the amplitude of the oscillations predicted by the complete dynamic model are larger than those predicted by the quasi-static model. This is consistent with our earlier findings that during retraction the system gains energy.

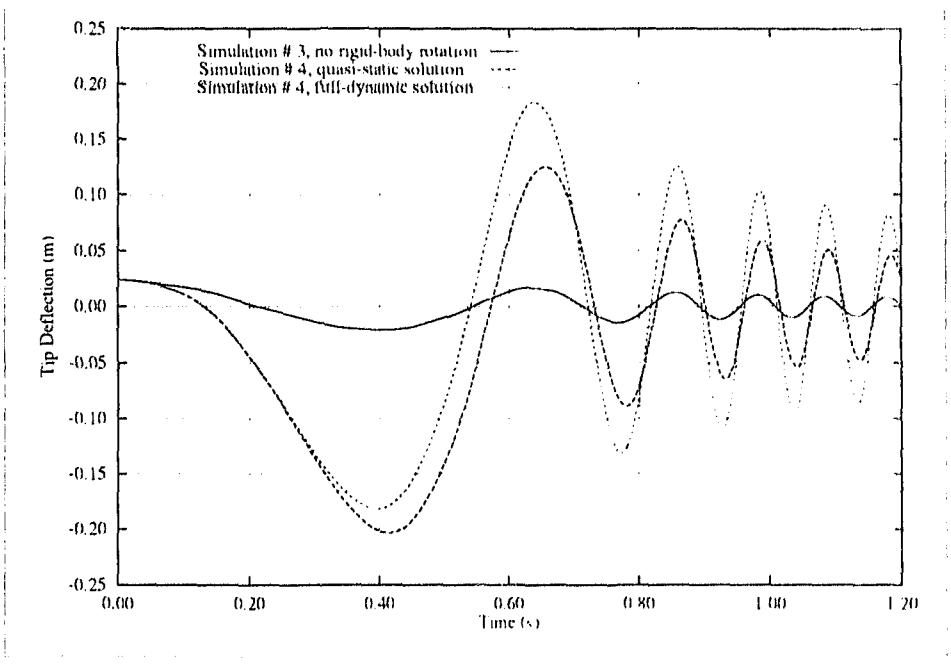


Figure 6.11: Simulation # 4. Comparison to a quasi-static formulation.

As mentioned in Chapter 1, the derivation of the governing equations of the flexible extendible beam by Wang and Wei (1987), Kim (1988), and Kim and Gibson (1991) left out certain terms. Specifically, their derivations fail to account for the time depen-

dency of $X$ in the expressions for the complementary kinetic energy. Ignoring these terms is equivalent to the quasi-static formulation just described. Therefore, Fig. (6.11) also shows, for the particular beam and motion profiles, the error incurred by ignoring the time dependency of $X$.

### 6.7.3 A Spatial Flexible Extendible Beam with a Tip Mass

As a final example, we consider the system configuration shown in Fig. (6.12). In this simulation the spatial flexible extendible beam carries a tip mass $\hat{m}$ and is partly nested in a flexible cantilever beam. The length of the protruding part of the beam and the rigid-body rotations are given by

$$L(t) = \begin{cases} L_0 + \frac{c}{\tau}\left[ t - \frac{\tau}{2\pi}\sin(2\pi t/\tau) \right], & 0 \le t \le \tau, \\ L_0 + c, & \tau < t, \end{cases} \tag{6.66}$$

$$\Theta_x = \begin{cases} t\,, & 0 \le t \le \tau, \\ \tau\,, & \tau < t, \end{cases} \tag{6.67}$$

$$\Theta_y(t) = \begin{cases} \Theta_0 + \frac{d}{\tau}\left[ t - \frac{\tau}{2\pi}\sin(2\pi t/\tau) \right], & 0 \le t \le \tau, \\ \Theta_0 + d, & \tau < t, \end{cases} \tag{6.68}$$

$$\Theta_z(t) = \begin{cases} \Theta_0 + \frac{d}{\tau}\left[ t - \frac{\tau}{2\pi}\sin(2\pi t/\tau) \right], & 0 \le t \le \tau, \\ \Theta_0 + d, & \tau < t, \end{cases} \tag{6.69}$$

where values for $L_0$, $\Theta_0$, $c$, $d$, and $\tau$ are given in Table (6.4).

| $L_0\,(m)$ | $\Theta_0\,(rad)$ | $c\,(m)$ | $d\,(rad)$ | $\tau\,(s)$ | $L_E\,(m)$ | $\hat{m}$ $(kg\ 10^{-6})$ |
|---|---|---|---|---|---|---|
| 0.3500 | 0.0 | +0.7000 | 1.57 | 2.4000 | 0.30 | 643.6149 |

Table 6.4: Parameters for spatial simulation.

The length $L_E$ of the envelope beam is taken as $0.3m$ and the tip mass $\hat{m}$ is taken as 10% of the mass of the protruding part of the beam at time zero. For the envelope and flexible extendible beams, we use the cross-sectional geometries of Fig. (6.13) and the material is taken as aluminum.

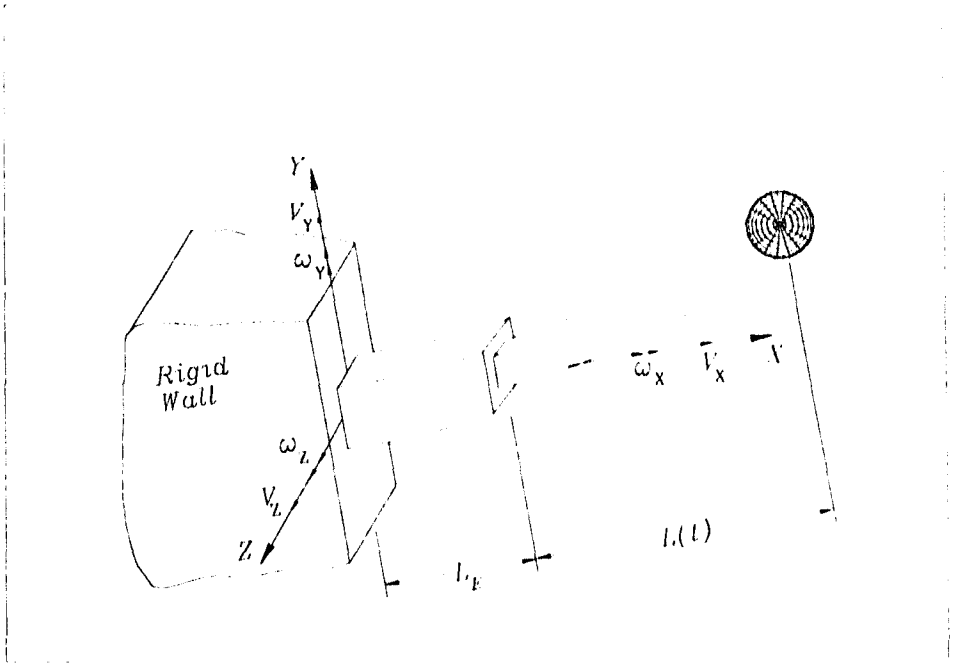


Figure 6.12: A nested spatial flexible extendible beam carrying a tip mass.

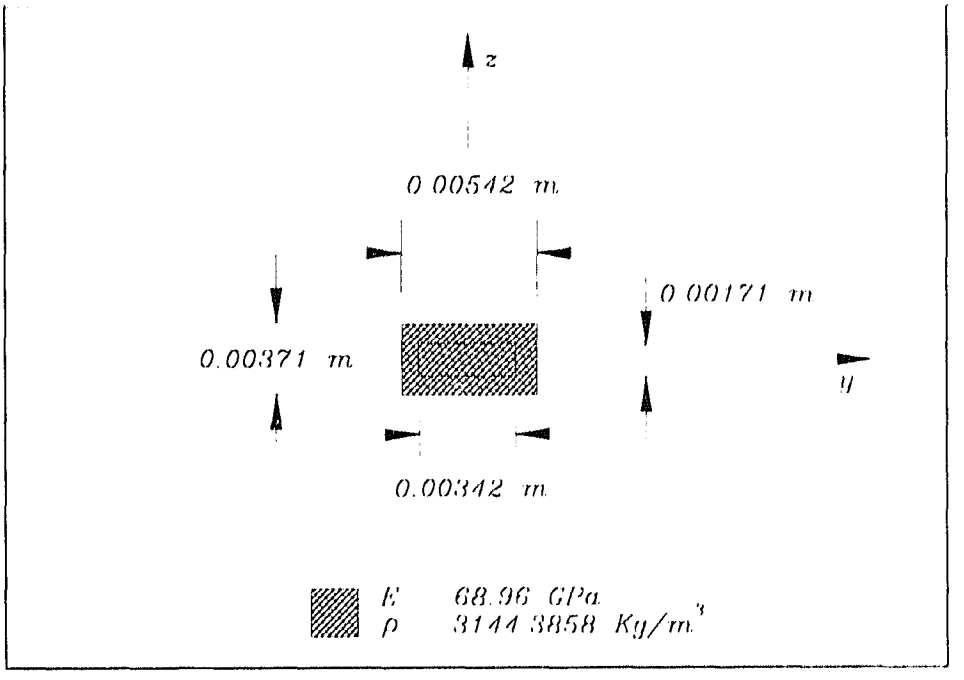


Figure 6.13: Geometric and material properties of the beams

The tip of the beam is given an initial deflection of $0.01m$ in the positive $y$- and $z$-directions, and is released at time $t = 0$. The extrusion and rotational motion profiles of Eqs. (6.66) to (6.69) are then prescribed starting at $t = 0$. The finite-element model for this configuration has a total of thirty-two degrees of freedom, with four elements for each of the three regions described below. With $l_i$ the length of the $i^{th}$ element and $d_i$ as defined in Eq. (3.5), we have the following modelling parameters:

1. Nested part of axially-moving beam

$$l_i = L_E/4, \qquad d_i = L(t) + L_E - (i-1)\,l_i, \qquad i = 1, \ldots 4. \tag{6.70}$$

2. Extruding part of axially-moving beam

$$l_i = L(t)/4, \qquad d_i = L(t) - (i-5)\,l_i, \qquad i = 5, \ldots 8. \tag{6.71}$$

3. Envelope beam

$$l_i = L_E/4, \qquad d_i = L_E - (i-9)\,l_i, \qquad i = 9, \ldots 12. \tag{6.72}$$

Physical damping was, once again, modelled as discussed in Section 4.1.1. The tip-deflection histories in the $y$- and $z$-directions (with and without a tip mass) are shown in Figs. (6.14) and (6.15), respectively.

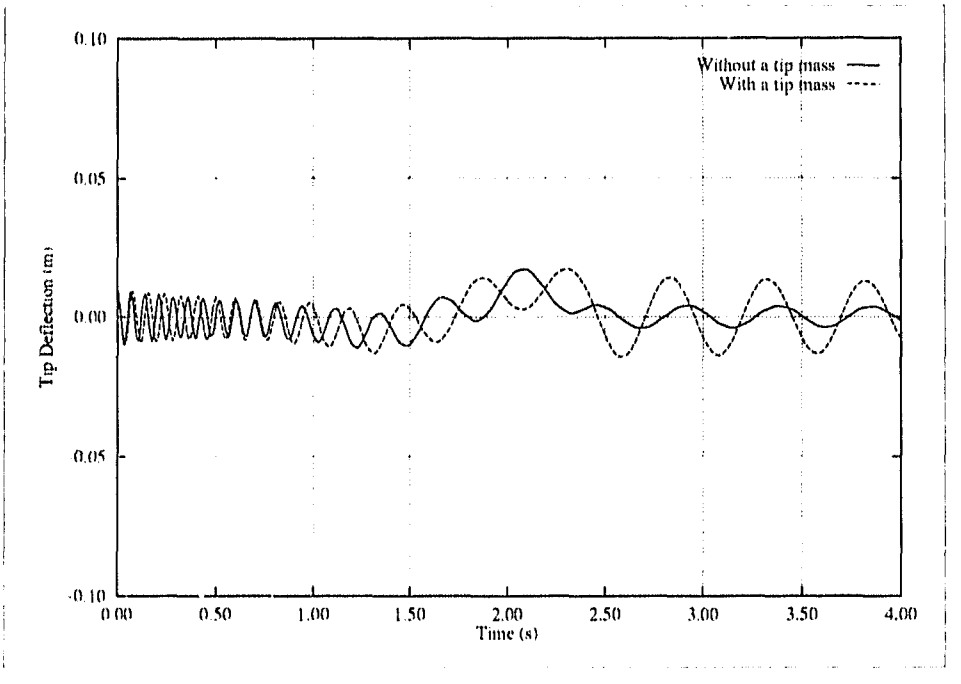


Figure 6.14: Tip-deflection in $y$-direction.

Since both the envelope and flexible extendible beams are less stiff in bending about the $y$-axis, the corresponding tip-deflections in the $z$-direction (Fig. (6.15)) are larger than the tip-deflections in the $y$-direction (Fig. (6.14)).

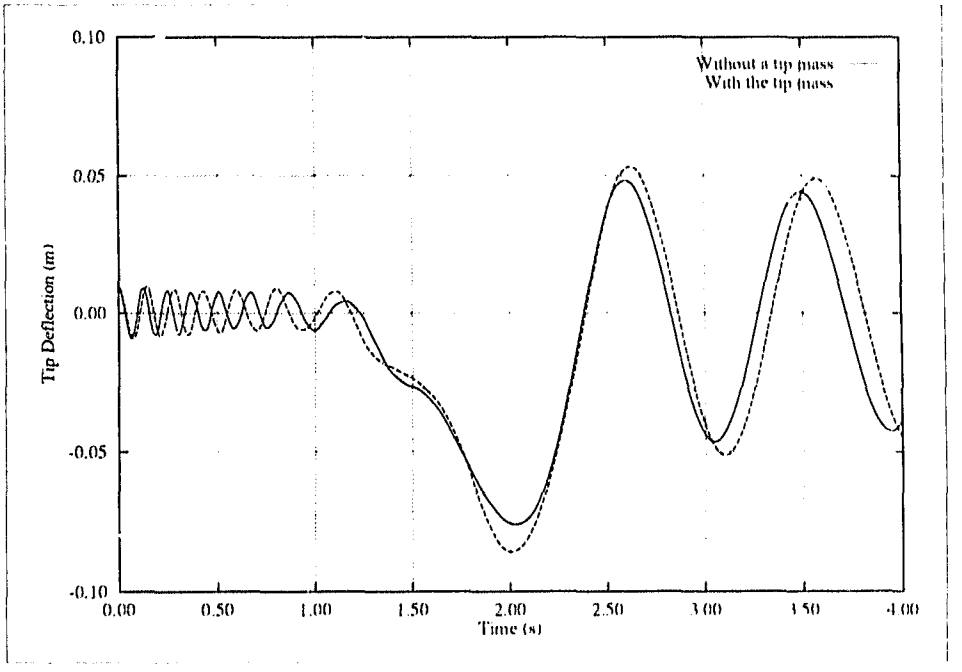


Figure 6.15: Tip-deflection in $z$-direction.

## 6.8 Concluding Remarks

In the foregoing we have developed the governing equations of motion for the spatial flexible extendible beam through finite-element discretization. Then, using various axial-motion profiles and two-dimensional rigid-body rotations, we integrated the finite-element equations. Good agreement was achieved with the simulation by Gaultier (1990) and the experimental results by Yuh and Young (1991). However, our findings are in disagreement with the simulation results given by Yuh and Young. Since Yuh and Young's results are not plausible on physical grounds, we believe them to be incorrect. Finally, the variable-domain beam element was used for a simulation involving spatial rigid-body rotations of a nested flexible extendible beam carrying a tip mass.

# Chapter 7

# Closing Comments

A necessary condition for the effective control of dynamical systems is a knowledge of the system's characteristics and properties. There is a duality between the concepts of system identification and control. Clearly, the better a system is identified, the more finely tuned a controller can be made, so that for a given amount of available control energy, the control is more efficient. On the other hand, the less knowledge we have about a system, the more robust a controller needs to be and, in general, the less efficient the control is. In this work, we developed a new variable-domain beam finite element that can be effectively used to model various dynamical systems. Its use was demonstrated through time-integration and stability analysis of numerous configurations of axially-moving beams, and through the stability analysis of pipes conveying fluid. The versatility of this finite-element formulation, was confirmed by the modelling of complex system configurations that can not be readily solved by other methods. The correctness of this new element and the soundness of the special solution techniques devised for the solution of these problems, were verified by comparing our results to results available in the literature through special closed-form solutions, simulations, and experiments. Further verification was performed by evaluation of the invariant quantities derived in Chapter 2.

Having formulated a variable-domain element and verified it through a series of examples, the way is now open to study other variable-domain problems not amenable to solution by other techniques.

Our preliminary findings with regards to our proposed engineering software certification approach are encouraging. The extra effort required by this approach was more than offset by not spending any time performing traditional "debugging". But perhaps of even more importance, is the high reliability and maintainability of the resulting program.

The following are suggestions for future work:

1) The technique we have used to arrive at the new invariant forms in Chapter 2, can be readily generalised to other higher order functionals. For instance, it would be relatively straight forward to derive corresponding results for problems of plate and shell dynamics.

2) For the modelling of prismatic joints, the Timoshenko beam theory will be more appropriate for relatively short envelope beams where shear and rotary effects become important.

3) A more detailed analysis of the effect of high-frequency axial motion perturbations on the transverse response of the axially-moving beam would be of significant practical importance.

4) A stability analysis using a non-linear formulation (Tabarrok et al. (1974)) will be a significant contribution towards a better understanding of this dynamically-rich system.

5) Problems of flow through curved pipes (as in condenser tubes) and over twisted beams (as in turbine blades) can be studied by modifying the variable-domain beam element developed in this work.

6) The improvement of the algorithm for the adaptive time-step size, so that it selects appropriate time-step sizes in problems with regions of incomparable dynamic stiffness.

7) Finally, the development of a variable-domain plate and shell elements would be a logical extension to this work.

# References

Bathe, K.J., 1982, "Finite Element Procedures in Engineering Analysis", Prentice-Hall, Inc., Toronto, pp. 527-532.

Benjamin, T.B., 1961, "Dynamics of a System of Articulated Pipes Conveying Fluid. I. Theory", Proceedings of the Royal Society (London), Series A, Vol. 261, pp. 457-486.

Buffinton, K.W., 1992, "Dynamics of Elastic Manipulators With Prismatic Joints", Transactions of the ASME, Journal of Dynamic Systems, Measurement, and Control, Vol. 114, pp. 41-49.

Char, B.W., Geddes, K.O., Gonnet, G.H., Monagan, M.B., Watt, S.M., 1988, "MAPLE Reference Manual", 5th edition, Canada Cataloguing in Publication Data, Waterloo.

Cherchas, D.B., Gossain, D.M., 1974, "Dynamics of a Flexible Solar Array During Deployment From a Spinning Spacecraft", C.A.S.I. Transactions, Vol. 7, No. 1, pp. 10-18.

Cook, R.D., Malkus, D.S., Plesha, M.E., 1989, "Concepts and Applications of Finite Element Analysis", 3rd Edition, John Wiley & Sons, Toronto, pp. 114, 371.

Dijkstra, E.W., 1976, "A Discipline of Programming", Prentice-Hall, Inc.

Dijkstra, E.W., 1969, "Structured Programming", In Conference Proceedings, NATO Science Committee.

Elmaraghy, R., Tabarrok, B., 1975, "On the Dynamic Stability of an Axially Oscillating Beam", Journal of the Franklin Institute, Vol. 300, No. 1, pp. 25-39.

Fagan, M.E., 1976, "Design and Code Inspections to Reduce Errors in Program Development", IBM Systems Journal, Vol. 15, No. 3, pp. 182-211.

Floyd, R.W., 1967, "Assigning Meanings to Programs", In Symposia in Applied Mathematics Proceedings, American Mathematical Society, Vol XIX, pp. 19-32.

Gaultier, P.E., 1990, "A Finite-Element Approach of Modelling Flexible Manipulators", M.A.Sc. dissertation, Department of Mechanical Engineering, University of Toronto.

Golnaraghi, M.F., 1991, "Vibration Suppression of Flexible Structures Using Internal Resonance", Mechanics Research Communications, Vol. 18, No. 2/3, pp. 135-143.

Gregory, R.W., Païdoussis, M.P., 1966, "Unstable Oscillation of Tubular Cantilevers Conveying Fluid. Part I - Theory", Proceedings of the Royal Society (London), Series A, Vol. 293, pp. 512-527.

Hoffman D.M., Snodgrass R., 1988, "Trace Specifications: Methodology and Models", IEEE Transactions in Software Engineering, Vol. 14, No. 9, pp. 1243-1252.

Hoffman, D.M., 1989, "A CASE Study in Module Testing", In Conference Proceedings, Software Maintenance, IEEE Computer Society, pp. 100-105.

Hoffman, D.M., 1990, Software Engineering, Lecture Notes, University of Victoria.

Herrmann, G., 1967, "Stability of Equilibrium of Elastic Systems Subjected to Nonconservative Forces", Applied Mechanics Reviews, Vol. 20, No. 2, pp. 103-107.

Holmes, P.J., 1978, "Pipes Supported at Both Ends Cannot Flutter", Journal of Applied Mechanics, Vol. 45, pp. 619-622.

Kane, T.R., Levinson, D.A., 1988, "A Method for Testing Numerical Integrations of Equations of Motion of Mechanical Systems", Journal of Applied Mechanics, Vol. 55, pp. 711-715.

Kim, Y.-K., 1988, "Adaptive Control of a Robotic Manipulator with a Sliding Flexible Link", Ph.D. dissertation, University of California, Los Angeles.

Kim, Y.-K., Gibson, J.S., 1991, "A Variable-order Adaptive Controller of a Manipulator with a Sliding Flexible Link", IEEE Transactions on Robotics and Automation, Vol. 7, No. 6, pp. 818-827.

Leech, C.M., 1970, "Dynamics of a Flexible Extendible Beam", Ph.D. dissertation, Department of Mechanical Engineering, University of Toronto, Ontario, Canada.

Mote, C.D., Jr., 1972, "Dynamic Stability of Axially Moving Materials", Shock and Vibration Digest, U.S. Naval Research Laboratory, Vol. 4, pp. 2-11.

NCC, 1989, "Verification, Validation and Testing", The National Centre for Information Technology, U.K.

Païdoussis, M.P., Issid, N.T., 1974, "Dynamic Stability of Pipes Conveying Fluid", Journal of Sound and Vibration, Vol. 33, No. 3, pp. 267-294.

Païdoussis, M.P., 1975, "Flutter of Conservative Systems of Pipes Conveying Incompressible Fluid", Journal of Mechanical Engineering Science, Vol. 17, No. 1, pp. 19-25.

Païdoussis, M.P., Workman, T., 1991, "Pipes Conveying Fluid: A Model Dynamical Problem", CANCAM Proceedings, pp. 1-33.

Parnas, D.L., 1972, "On the Criteria to be Used in Decomposing Systems Into Modules", Communications of ACM, Vol. 15, No. 12, pp. 1053-1058.

Parnas, D.L., Clements, P.C., 1986, "A Rational Design Process: How and Why to Fake it", IEEE Transactions in Software Engineering, Vol. SE-12, No. 2, pp. 251-257.

Richter, H.P., 1984, "Verifying the Reliability of Engineering Software", ASME Mechanical Engineering, January 1984, pp. 53-56.

Russell, G.W., 1991, "Experience With Inspections in Ultralarge-Scale Developments", IEEE Software, January 1991, pp. 25-31.

Sharf, I., 1993, Personal Communications, Department of Mechanical Engineering, University of Victoria, British Columbia, Canada.

Stylianou, M.C., Hoffman, D.M., 1991, "Upgrades for Software Engineering", ASME Computers in Engineering Conference, Vol. 1, pp. 197-203.

Tabarrok, B., Leech, C.M., Kim, Y.I., 1974, "On the Dynamics of an Axially Moving Beam", Journal of the Franklin Institute, Vol. 297, No. 3, pp. 201-220.

Tabarrok, B., 1990, "Wisdom Reference Manual", Version 4.0, Department of Mechanical Engineering, University of Victoria, BC.

Thompson, J.M.T., Stewart, H.B. 1987, "Nonlinear Dynamics and Chaos, Geometrical Methods for Engineers and Scientists", John Wiley and Sons, Toronto.

Wang, P.K.C., Wei, J., 1987, "Vibration in a Moving Flexible Robot Arm", Journal of Sound and Vibration, Vol. 116, No. 1, pp. 149-160.

Wheeler, M.J., 1986, "Reliability Issues in Finite Element Software", ASME International Computers in Engineering Conference and Exhibition. pp. 159, 163.

Wicker, J.A., Mote, C.D., Jr., 1988, "Current Research on the Vibration and Stability of Axially-Moving Materials", The Shock and Vibration Digest, Vol. 20, No. 5, pp. 3-13.

Yuh, J., Young, T., 1991, "Dynamic Modeling of an Axially Moving Beam in Rotation: Simulation and Experiment", Transactions of the ASME, Journal of Dynamic Systems, Measurement, and Control, Vol. 113, pp. 34-40.

Zajaczkowski, J., Lipinski, J., 1979, "Instability of the Motion of a Beam of Periodically Varying Length", Journal of Sound and Vibration, Vol. 63, pp. 9-18.

Zajaczkowski, J, Yamaki, G., 1980, "Further Results on Instability of the Motion of a Beam of Periodically Varying Length", Journal of Sound and Vibration, Vol. 68, pp. 173-180.

Zhou, H.S., 1989, "Distributed Controls of a Single-Link Flexible Arm using Distributed Viscoelastic Damper", The First International Applied Mechanical Systems Design Conference, Nashville, Tennessee, pp. p7.1-8.

Ziegler, H., 1968, "Principles of Structural Stability", Blessedly Publishing Company, Toronto.

# Appendices

## Appendix A:

### I. Second-Order Functionals with two Independent Variables

Consider the following general high-order functional with two independent variables

$$\delta \int_{\Omega} \mathcal{L}(t, X, Y, Y_t, Y_X, Y_{tX}, Y_{Xt}, Y_{tt}, Y_{XX})\, dtdX = 0. \tag{1}$$

where $t$ and $X$ are the independent variables and $Y(t,X)$ the dependent function. Carrying out the variation in Eq. (1) we obtain

$$\begin{aligned} &\int_{\Omega} \left(\frac{\partial \mathcal{L}}{\partial Y}\ \delta Y\right) dtdX + \int_{\Omega} \left(\frac{\partial \mathcal{L}}{\partial Y_t}\ \delta Y_t + \frac{\partial \mathcal{L}}{\partial Y_X}\ \delta Y_X\right) dtdX + \\ &\int_{\Omega} \left(\frac{\partial \mathcal{L}}{\partial Y_{tt}}\ \delta Y_{tt} + \frac{\partial \mathcal{L}}{\partial Y_{tX}}\ \delta Y_{tX} + \frac{\partial \mathcal{L}}{\partial Y_{Xt}}\ \delta Y_{Xt} + \frac{\partial \mathcal{L}}{\partial Y_{XX}}\ \delta Y_{XX}\right) dtdX. \end{aligned} \tag{2}$$

Integrating the second integral in Eq. (2) by parts

$$\begin{aligned} \int_{\Omega} \left(\frac{\partial \mathcal{L}}{\partial Y_t}\ \delta Y_t + \frac{\partial \mathcal{L}}{\partial Y_X}\ \delta Y_X\right) dtdX &= \int_{\Omega} \left[\left[\frac{\partial}{\partial t}\right] \quad \left[\frac{\partial}{\partial X}\right]\right] \begin{bmatrix} \dfrac{\partial \mathcal{L}}{\partial Y_t}\ \delta Y \\ \dfrac{\partial \mathcal{L}}{\partial Y_X}\ \delta Y \end{bmatrix} dtdX - \\ &\int_{\Omega} \left(\left[\frac{\partial}{\partial t}\right]\frac{\partial \mathcal{L}}{\partial Y_t} + \left[\frac{\partial}{\partial X}\right]\frac{\partial \mathcal{L}}{\partial Y_X}\right) \delta Y dtdX. \end{aligned} \tag{3}$$

The operators $\partial/\partial Y$, $\partial/\partial Y_X$, and $\partial/\partial Y_t$ are partial derivatives, that is, for these operations all variables, save those with respect to which the differentiation is being performed, are held fixed. On the other hand the operators $\partial/\partial t$ and $\partial/\partial X$, are for all intents and purposes, total derivatives except that for the former $X$ is held fixed and for the latter $t$ is fixed. To maintain clarity in the meaning of these operators we enclose them in brackets [ ] whenever a total derivative, in the sense just mentioned, is meant.

Using Green's theorem on the first integral of the right-hand side in Eq. (3)

$$\int_{\Omega}\begin{bmatrix}\left[\frac{\partial}{\partial t}\right] & \left[\frac{\partial}{\partial X}\right]\end{bmatrix}\begin{bmatrix}\frac{\partial \mathcal{L}}{\partial Y_t}\,\delta Y \\ \frac{\partial \mathcal{L}}{\partial Y_X}\,\delta Y\end{bmatrix} dt dX = \oint_S \begin{vmatrix} n_t & n_X \end{vmatrix}\begin{vmatrix}\frac{\partial \mathcal{L}}{\partial Y_t} \\ \frac{\partial \mathcal{L}}{\partial Y_X}\end{vmatrix}\delta Y dS, \tag{4}$$

where $\lfloor n_t \quad n_X \rfloor$ is the outward-normal unit-vector to the bounding curve $S$ of the region $\Omega$ shown in Fig. (2.2). Hence, the second integral in Eq. (2) becomes

$$\begin{aligned}\int_{\Omega}\left(\frac{\partial \mathcal{L}}{\partial Y_t}\,\delta Y_t + \frac{\partial \mathcal{L}}{\partial Y_X}\,\delta Y_X\right) dt dX = -\int_{\Omega}\left(\left[\frac{\partial}{\partial t}\right]\frac{\partial \mathcal{L}}{\partial Y_t} + \left[\frac{\partial}{\partial X}\right]\frac{\partial \mathcal{L}}{\partial Y_X}\right)\delta Y dt dX + \\ \oint_S \left(\frac{\partial \mathcal{L}}{\partial Y_t}\,n_t + \frac{\partial \mathcal{L}}{\partial Y_X}\,n_X\right)\delta Y dS,\end{aligned} \tag{5}$$

Now, integrating the third integral in Eq. (2) by parts we obtain

$$\begin{aligned}&\int_{\Omega}\left(\frac{\partial \mathcal{L}}{\partial Y_{tt}}\,\delta Y_{tt} + \frac{\partial \mathcal{L}}{\partial Y_{tX}}\,\delta Y_{tX} + \frac{\partial \mathcal{L}}{\partial Y_{Xt}}\,\delta Y_{Xt} + \frac{\partial \mathcal{L}}{\partial Y_{XX}}\,\delta Y_{XX}\right) dt dX = \\ &\int_{\Omega}\left(\left[\frac{\partial}{\partial t}\right]\left(\frac{\partial \mathcal{L}}{\partial Y_{tt}}\,\delta Y_t + \frac{\partial \mathcal{L}}{\partial Y_{Xt}}\,\delta Y_X\right) + \left[\frac{\partial}{\partial X}\right]\left(\frac{\partial \mathcal{L}}{\partial Y_{tX}}\,\delta Y_t + \frac{\partial \mathcal{L}}{\partial Y_{XX}}\,\delta Y_X\right)\right) dt dX - \\ &\int_{\Omega}\left(\left[\frac{\partial}{\partial t}\right]\frac{\partial \mathcal{L}}{\partial Y_{tt}}\,\delta Y_t + \left[\frac{\partial}{\partial t}\right]\frac{\partial \mathcal{L}}{\partial Y_{Xt}}\,\delta Y_X + \left[\frac{\partial}{\partial X}\right]\frac{\partial \mathcal{L}}{\partial Y_{tX}}\,\delta Y_t + \left[\frac{\partial}{\partial X}\right]\frac{\partial \mathcal{L}}{\partial Y_{XX}}\,\delta Y_X\right) dt dX.\end{aligned} \tag{6}$$

Using Green's theorem on the first integral of the right-hand side in Eq. (6) and integrating the second integral of the right-hand side in Eq. (6) by parts these two integrals become

$$\int_{\Omega} \left( \left[\frac{\partial}{\partial t}\right] \left( \frac{\partial \mathcal{L}}{\partial Y_{tt}} \delta Y_t + \frac{\partial \mathcal{L}}{\partial Y_{Xt}} \delta Y_X \right) + \left[\frac{\partial}{\partial X}\right] \left( \frac{\partial \mathcal{L}}{\partial Y_{tX}} \delta Y_t + \frac{\partial \mathcal{L}}{\partial Y_{XX}} \delta Y_X \right) \right) dt dX =$$

$$\oint_S \begin{bmatrix} n_t & n_X \end{bmatrix} \begin{bmatrix} \frac{\partial \mathcal{L}}{\partial Y_{tt}} \delta Y_t + \frac{\partial \mathcal{L}}{\partial Y_{Xt}} \delta Y_X \\ \frac{\partial \mathcal{L}}{\partial Y_{tX}} \delta Y_t + \frac{\partial \mathcal{L}}{\partial Y_{XX}} \delta Y_X \end{bmatrix} dS, \tag{7}$$

and

$$\begin{aligned} &\int_{\Omega} \left( \left[\frac{\partial}{\partial t}\right] \frac{\partial \mathcal{L}}{\partial Y_{tt}} \delta Y_t + \left[\frac{\partial}{\partial t}\right] \frac{\partial \mathcal{L}}{\partial Y_{Xt}} \delta Y_X + \left[\frac{\partial}{\partial X}\right] \frac{\partial \mathcal{L}}{\partial Y_{tX}} \delta Y_t + \left[\frac{\partial}{\partial X}\right] \frac{\partial \mathcal{L}}{\partial Y_{XX}} \delta Y_X \right) dt dX = \\ &-\int_{\Omega} \left[\frac{\partial}{\partial t}\right] \left( \left[\frac{\partial}{\partial t}\right] \frac{\partial \mathcal{L}}{\partial Y_{tt}} \delta Y + \left[\frac{\partial}{\partial X}\right] \frac{\partial \mathcal{L}}{\partial Y_{tX}} \delta Y \right) dt dX - \\ &\int_{\Omega} \left[\frac{\partial}{\partial X}\right] \left( \left[\frac{\partial}{\partial t}\right] \frac{\partial \mathcal{L}}{\partial Y_{Xt}} \delta Y + \left[\frac{\partial}{\partial X}\right] \frac{\partial \mathcal{L}}{\partial Y_{XX}} \delta Y \right) dt dX + \\ &\int_{\Omega} \left( \left[\frac{\partial}{\partial t}\right] \left( \left[\frac{\partial}{\partial t}\right] \frac{\partial \mathcal{L}}{\partial Y_{tt}} + \left[\frac{\partial}{\partial X}\right] \frac{\partial \mathcal{L}}{\partial Y_{tX}} \right) + \left[\frac{\partial}{\partial X}\right] \left( \left[\frac{\partial}{\partial t}\right] \frac{\partial \mathcal{L}}{\partial Y_{Xt}} + \left[\frac{\partial}{\partial X}\right] \frac{\partial \mathcal{L}}{\partial Y_{XX}} \right) \right) \delta Y \, dt dX. \end{aligned} \tag{8}$$

Using Green's theorem on the first integral on the right-hand side of Eq. (8) and using Eq. (7) the third integral of Eq. (2) becomes

$$\begin{aligned} &\int_{\Omega} \left( \frac{\partial \mathcal{L}}{\partial Y_{tt}} \delta Y_{tt} + \frac{\partial \mathcal{L}}{\partial Y_{tX}} \delta Y_{tX} + \frac{\partial \mathcal{L}}{\partial Y_{Xt}} \delta Y_{Xt} + \frac{\partial \mathcal{L}}{\partial Y_{XX}} \delta Y_{XX} \right) dt dX = \\ &-\oint_S \left( \left( \left[\frac{\partial}{\partial t}\right] \frac{\partial \mathcal{L}}{\partial Y_{tt}} + \left[\frac{\partial}{\partial X}\right] \frac{\partial \mathcal{L}}{\partial Y_{tX}} \right) n_t + \left( \left[\frac{\partial}{\partial t}\right] \frac{\partial \mathcal{L}}{\partial Y_{Xt}} + \left[\frac{\partial}{\partial X}\right] \frac{\partial \mathcal{L}}{\partial Y_{XX}} \right) n_X \right) \delta Y dS + \\ &\int_{\Omega} \left( \left[\frac{\partial^2}{\partial t^2}\right] \frac{\partial \mathcal{L}}{\partial Y_{tt}} + \left[\frac{\partial^2}{\partial t \partial X}\right] \frac{\partial \mathcal{L}}{\partial Y_{tX}} + \left[\frac{\partial^2}{\partial X \partial t}\right] \frac{\partial \mathcal{L}}{\partial Y_{Xt}} + \left[\frac{\partial^2}{\partial X^2}\right] \frac{\partial \mathcal{L}}{\partial Y_{XX}} \right) \delta Y dt dX + \\ &\oint_S \left( \left( \frac{\partial \mathcal{L}}{\partial Y_{tt}} n_t + \frac{\partial \mathcal{L}}{\partial Y_{tX}} n_X \right) \delta Y_t + \left( \frac{\partial \mathcal{L}}{\partial Y_{Xt}} n_t + \frac{\partial \mathcal{L}}{\partial Y_{XX}} n_X \right) \delta Y_X \right) dS. \end{aligned} \tag{9}$$

Finally, substituting Eqs. (5) and (9) into Eq. (2) yields

$$\int_{\Omega}\Big[\frac{\partial \mathcal{L}}{\partial Y}-\Big[\frac{\partial}{\partial t}\Big]\frac{\partial \mathcal{L}}{\partial Y_t}-\Big[\frac{\partial}{\partial X}\Big]\frac{\partial \mathcal{L}}{\partial Y_X}+\Big[\frac{\partial^2}{\partial t^2}\Big]\frac{\partial \mathcal{L}}{\partial Y_{tt}}+$$
$$2\Big[\frac{\partial^2}{\partial t\partial X}\Big]\frac{\partial \mathcal{L}}{\partial Y_{tX}}+\Big[\frac{\partial^2}{\partial X^2}\Big]\frac{\partial \mathcal{L}}{\partial Y_{XX}}\Big]\delta Y dt dX+$$
$$\oint_S\Big[\Big(\frac{\partial \mathcal{L}}{\partial Y_t}-\Big[\frac{\partial}{\partial t}\Big]\frac{\partial \mathcal{L}}{\partial Y_{tt}}-\Big[\frac{\partial}{\partial X}\Big]\frac{\partial \mathcal{L}}{\partial Y_{tX}}\Big)n_t+ \qquad (10)$$
$$\Big(\frac{\partial \mathcal{L}}{\partial Y_X}-\Big[\frac{\partial}{\partial t}\Big]\frac{\partial \mathcal{L}}{\partial Y_{Xt}}-\Big[\frac{\partial}{\partial X}\Big]\frac{\partial \mathcal{L}}{\partial Y_{XX}}\Big)n_X\Big]\delta Y dS+$$
$$\oint_S\Big[\frac{\partial \mathcal{L}}{\partial Y_{tt}}n_t+\frac{\partial \mathcal{L}}{\partial Y_{tX}}n_X\Big]\delta Y_t dS+\oint_S\Big[\frac{\partial \mathcal{L}}{\partial Y_{Xt}}n_t+\frac{\partial \mathcal{L}}{\partial Y_{XX}}n_X\Big]\delta Y_X dS=0.$$

The first integral is over the domain $\Omega$ whereas the other three integrals are along the boundary $S$. In order for the above expression to vanish identically for any function $Y(t,X)$, each integral term must vanish in (10). Therefore, the extremising function $Y(t,X)$ is governed by:

in the domain $\Omega$ by the Euler-Lagrange equation of this functional

$$\frac{\partial \mathcal{L}}{\partial Y}-\Big[\frac{\partial}{\partial t}\Big]\Big(\frac{\partial \mathcal{L}}{\partial Y_t}\Big)-\Big[\frac{\partial}{\partial X}\Big]\Big(\frac{\partial \mathcal{L}}{\partial Y_X}\Big)+\Big[\frac{\partial^2}{\partial t^2}\Big]\Big(\frac{\partial \mathcal{L}}{\partial Y_{tt}}\Big)+$$
$$\Big[\frac{\partial^2}{\partial X^2}\Big]\Big(\frac{\partial \mathcal{L}}{\partial Y_{XX}}\Big)+2\Big[\frac{\partial^2}{\partial t\partial X}\Big]\Big(\frac{\partial \mathcal{L}}{\partial Y_{tX}}\Big)=0. \qquad (11)$$

and along the boundary $S$

$$\Big[\Big(\frac{\partial \mathcal{L}}{\partial Y_t}-\Big[\frac{\partial}{\partial t}\Big]\frac{\partial \mathcal{L}}{\partial Y_{tt}}-\Big[\frac{\partial}{\partial X}\Big]\frac{\partial \mathcal{L}}{\partial Y_{tX}}\Big)n_t+$$
$$\Big(\frac{\partial \mathcal{L}}{\partial Y_X}-\Big[\frac{\partial}{\partial t}\Big]\frac{\partial \mathcal{L}}{\partial Y_{Xt}}-\Big[\frac{\partial}{\partial X}\Big]\frac{\partial \mathcal{L}}{\partial Y_{XX}}\Big)n_X\Big]\delta Y=0, \qquad (12)$$
$$\Big[\frac{\partial \mathcal{L}}{\partial Y_{tt}}n_t+\frac{\partial \mathcal{L}}{\partial Y_{tX}}n_X\Big]\delta Y_t=0,$$
$$\Big[\frac{\partial \mathcal{L}}{\partial Y_{Xt}}n_t+\frac{\partial \mathcal{L}}{\partial Y_{XX}}n_X\Big]\delta Y_X=0.$$

## II. The Flexible Extendible Beam

The variational statement for the flexible extendible beam is given by Eq. (2.4), namely

$$\delta \int_{t_1}^{t_2} \int_{0}^{L(t)} \left( \frac{1}{2}\rho A \left(Y_t + X_t Y_X\right)^2 - \frac{1}{2} EI Y_{XX}^2 + \frac{1}{2}\rho A a \left(L - X\right) Y_X^2 \right) dt = 0, \tag{13}$$

therefore the Lagrangian density function for the system is given by

$$\mathcal{L} = \frac{1}{2}\rho A \left(Y_t + X_t Y_X\right)^2 - \frac{1}{2} EI Y_{XX}^2 + \frac{1}{2}\rho A a \left(L - X\right) Y_X^2, \tag{14}$$

where $a$ is defined in Eq. (2.7). Substituting the following derivatives of $\mathcal{L}$

$$\begin{aligned}
&\frac{\partial \mathcal{L}}{\partial Y} = 0, && \frac{\partial \mathcal{L}}{\partial Y_t} = \rho A \left(Y_t + \dot{L} Y_X\right), \\
&\frac{\partial \mathcal{L}}{\partial Y_X} = \rho A \left(\dot{L} Y_t + \dot{L}^2 Y_X + a \left(L - X\right) Y_X\right), && \frac{\partial \mathcal{L}}{\partial Y_{tt}} = 0, \\
&\frac{\partial \mathcal{L}}{\partial Y_{tX}} = 0, && \frac{\partial \mathcal{L}}{\partial Y_{XX}} = -EI Y_{XX},
\end{aligned} \tag{15}$$

in Eq. (11), we obtain within the domain $\Omega$

$$\rho A \left(Y_{tt} + 2\dot{L} Y_{tX} + \dot{L}^2 Y_{XX} + \ddot{L} Y_X\right) + EI Y_{XXXX} + \rho A a \frac{\partial}{\partial X}\left[ \left(L - X\right) Y_X \right] = 0. \tag{16}$$

The above equation is recognised as the governing partial differential equation for the flexible extendible beam. Similarly, substituting the derivatives of $\mathcal{L}$ (Eqs. (15)) in Eq. (12) we obtain along the boundary $S$

$$\begin{aligned}
&\left[ \rho A \left(Y_t + \dot{L} Y_X\right) n_t + \right. \\
&\qquad \left. \left( \rho A \left(\dot{L} Y_t + \dot{L}^2 Y_X + a \left(L - X\right) Y_X\right) + EI Y_{XX} \right) n_X \right] \delta Y = 0, \\
&EI Y_{XX} n_X \delta Y_X = 0.
\end{aligned} \tag{17}$$

Using the outward-normal unit-vectors $\left[ n_t \quad n_X \right]$ as shown in Fig. (2.2) we may expand the above expressions. For example, the second of Eqs. (17) becomes

$$\int_{0}^{L(t_2)} EIY_{XX}(0)\,\delta Y_X dX\big|_{t=t_2} + \int_{t_2}^{t_1} EIY_{XX}\frac{1}{\sqrt{(1+\dot{L}^2)}}\delta Y_X(-\sqrt{(1+\dot{L}^2)}\,dt)\Big|_{X=L(t)} + \int_{L(t_1)}^{0} EIY_{XX}(0)\,\delta Y_X(-dX)\big|_{t=t_1} + \int_{t_1}^{t_2} EIY_{XX}(-1)\,\delta Y_X dt\big|_{X=0} = 0. \tag{18}$$

Removing the vanishing terms and simplifying, yields

$$\int_{t_2}^{t_1} [-EIY_{XX}\delta Y_X]\big|_{X=L(t)} dt + \int_{t_1}^{t_2} [-EIY_{XX}\delta Y_X]\big|_{X=0} dt = 0, \tag{19}$$

or

$$\int_{t_1}^{t_2} [EIY_{XX}\delta Y_X]\big|_{X=0}^{X=L(t)} dt = 0. \tag{20}$$

The above equation implies that the integrand must vanish, therefore

$$[EIY_{XX}]\,\delta Y_X = 0, \qquad \text{at} \qquad X = 0 \qquad \text{and} \qquad X = L. \tag{21}$$

Following a similar procedure for the first of Eqs. (17) yields

$$\begin{aligned} &[\rho Aa(L-X)Y_X + EIY_{XXX}]\,\delta Y\big|_{X=L(t)} = 0, \\ &-[\rho A\dot{L}(Y_t + \dot{L}Y_X) + \rho Aa(L-X)Y_X + EIY_{XXX}]\,\delta Y\big|_{X=0} = 0. \end{aligned} \tag{22}$$

Therefore, for the flexible extendible beam protruding from an infinitely rigid wall, we may write

$$[\rho Aa(L-X)Y_X + EIY_{XXX}]\,\delta Y = 0, \qquad \text{at} \qquad X = 0 \qquad \text{and} \qquad X = L. \tag{23}$$

# Appendix B: Components of System Matrices

## I. The $[k_1]$ Matrix

The components of the upper part of the $[k_1]$ matrix are given by:

$$
\begin{aligned}
k_1(1,1) &= C_1 \frac{\rho A}{l}(2.0l^2 + 7.0\dot{d}_i^2 - 7.0l\dot{d}_i) \\
k_1(1,2) &= \rho A(0.1\dot{d}_i^2 - 0.3l\dot{d}_i + C_2 l^2), \\
k_1(1,3) &= -C_1 \frac{\rho A}{l}(2.0l^2 + 7.0\dot{d}_i^2 - 7.0l\dot{d}_i), \\
k_1(1,4) &= -\rho A(C_3 l^2 - 0.1\dot{d}_i^2 - 0.1l\dot{d}_i), \\
k_1(2,2) &= C_4 \rho A l(14.0\dot{d}_i^2 - 7.0l\dot{d}_i + 4.0l^2), \\
k_1(2,3) &= -\rho A(0.1\dot{d}_i^2 - 0.3l\dot{d}_i + C_2 l^2), \\
k_1(2,4) &= -C_5 \rho A l(7.0\dot{d}_i^2 - 7.0l\dot{d}_i + 6.0l^2), \\
k_1(3,3) &= C_1 \frac{\rho A}{l}(2.0l^2 + 7.0\dot{d}_i^2 - 7.0l\dot{d}_i), \\
k_1(3,4) &= \rho A(C_3 l^2 - 0.1\dot{d}_i^2 - 0.1l\dot{d}_i), \\
k_1(4,4) &= C_4 \rho A l(14.0\dot{d}_i^2 - 21.0l\dot{d}_i + 11.0l^2),
\end{aligned}
\tag{24}
$$

where

$$
\begin{aligned}
C_1 &= 0.1714285714285714, \\
C_2 &= 0.1142857142857143, \\
C_3 &= 0.0857142857142857, \\
C_4 &= 0.0095238095238095, \\
C_5 &= 0.0047619047619047,
\end{aligned}
\tag{25}
$$

and density $\rho$, cross-sectional area $A$, element length $l$, and parameter $d_i$ as defined in Eq. (3.5).

## II. The $[k_2]$ Matrix

The components of the upper part of the $[k_2]$ matrix are given by:

$$
\begin{aligned}
k_2(1,1) &= -0.6\frac{\ddot{L}}{l}(-2.0\hat{m}-2.0\rho A d_i+\rho A l),\\
k_2(1,2) &= -0.1\ddot{L}(-\hat{m}-\rho A d_i+\rho A l),\\
k_2(1,3) &= 0.6\frac{\ddot{L}}{l}(-2.0\hat{m}-2.0\rho A d_i+\rho A l),\\
k_2(1,4) &= 0.1\ddot{L}(\hat{m}+\rho A d_i),\\
k_2(2,2) &= -C_1\ddot{L}l(-4.0\hat{m}-4.0\rho A d_i+\rho A l),\\
k_2(2,3) &= 0.1\ddot{L}(-m-\rho A d_i+\rho A l),\\
k_2(2,4) &= C_2\ddot{L}l(-2.0\hat{m}-2.0\rho A d_i+\rho A l),\\
k_2(3,3) &= -0.6\frac{\ddot{L}}{l}(-2.0\hat{m}-2.0\rho A d_i+\rho A l),\\
k_2(3,4) &= -0.1\ddot{L}(\hat{m}+\rho A d_i),\\
k_2(4,4) &= -C_1\ddot{L}l(-4.0\hat{m}-4.0\rho A d_i+3.0\rho A l),
\end{aligned}
\tag{26}
$$

where

$$
\begin{aligned}
C_1 &= 0.0333333333333333,\\
C_2 &= 0.0166666666666667,
\end{aligned}
\tag{27}
$$

and density $\rho$, cross-sectional area $A$, element length $l$, length of protruded beam $L$, mass of tip mass $\hat{m}$, and parameter $d_i$ as defined in Eq. (3.5).

## III. The $[c_2]$ Matrix

The components of the $[c_2]$ matrix ($[c_2]^T = [c_1]$) are given by:

$$
\begin{aligned}
c_2(1,1) &= \rho A\,(C_4\dot{l} - 0.5\dot{d}_i)\,,\\
c_2(1,2) &= C_1\rho A l\,(13.0\dot{l} + 21.0\dot{d}_i)\,,\\
c_2(1,3) &= -\rho A\,(C_4\dot{l} - 0.5\dot{d}_i)\,,\\
c_2(1,4) &= -C_1\rho A l\,(\dot{l} + 21.0\dot{d}_i)\,,\\
c_2(2,1) &= C_2\rho A l\,(3.0\dot{l} - 7.0\dot{d}_i)\,,\\
c_2(2,2) &= C_2\rho A l^2\dot{l},\\
c_2(2,3) &= -C_2\rho A l\,(3.0\dot{l} - 7.0\dot{d}_i)\,,\\
c_2(2,4) &= -C_3\rho A l^2\,(\dot{l} + 7.0\dot{d}_i)\,,\\
c_2(3,1) &= \rho A\,(C_5\dot{l} - 0.5\dot{d}_i)\,,\\
c_2(3,2) &= -C_1\rho A l\,(-22.0\dot{l} + 21.0\dot{d}_i)\,,\\
c_2(3,3) &= -\rho A\,(C_5\dot{l} - 0.5\dot{d}_i)\,,\\
c_2(3,4) &= C_1\rho A l\,(-34.0\dot{l} + 21.0\dot{d}_i)\,,\\
c_2(4,1) &= C_2\rho A l\,(-4.0\dot{l} + 7.0\dot{d}_i)\,,\\
c_2(4,2) &= C_3\rho A l^2\,(-8.0\dot{l} + 7.0\dot{d}_i)\,,\\
c_2(4,3) &= -C_2\rho A l\,(-4.0\dot{l} + 7.0\dot{d}_i)\,,\\
c_2(4,4) &= C_2\rho A l^2\dot{l},
\end{aligned}
\tag{28}
$$

where

$$
\begin{aligned}
C_1 &= 0.0047619047619048 \qquad C_2 = 0.0142857142857143\\
C_3 &= 0.0023809523809524 \qquad C_4 = 0.1857142857142857\\
C_5 &= 0.3142857142857143
\end{aligned}
\tag{29}
$$

and density $\rho$, cross-sectional area $A$, element length $l$, and parameter $d_i$ as defined in Eq. (3.5).

## IV. The $[\dot{m}]$ Matrix

The components of the upper part of the $[\dot{m}]$ matrix are given by:

$$\begin{aligned}
\dot{m}(1,1) &= C_1 \rho A \dot{l}, \\
\dot{m}(1,2) &= C_2 \rho A l \dot{l}, \\
\dot{m}(1,3) &= C_3 \rho A \dot{l}, \\
\dot{m}(1,4) &= -C_4 \rho A l \dot{l}, \\
\dot{m}(2,2) &= C_5 \rho A l^2 \dot{l}, \\
\dot{m}(2,3) &= C_4 \rho A l \dot{l}, \\
\dot{m}(2,4) &= -C_6 \rho A l^2 \dot{l}, \\
\dot{m}(3,3) &= C_1 \rho A \dot{l}, \\
\dot{m}(3,4) &= -C_2 \rho A l \dot{l}, \\
\dot{m}(4,4) &= C_5 \rho A l^2 \dot{l},
\end{aligned} \tag{30}$$

where

$$\begin{aligned}
C_1 &= 0.3714285714285714 & C_2 &= 0.1047619048000000 \\
C_3 &= 0.1285714285714286 & C_4 &= 0.0619047619000000 \\
C_5 &= 0.0285714285700000 & C_6 &= 0.0214285714300000
\end{aligned} \tag{31}$$

and density $\rho$, cross-sectional area $A$, and element length $l$.

## V. The $[\dot{c}_2]$ Matrix

The components of the $[\dot{c}_2]$ matrix are given by:

$$
\begin{aligned}
\dot{c}_2(1,1) &= \rho A\,(C_4\ddot{l} - 0.5\ddot{d}_i)\,,\\
\dot{c}_2(1,2) &= C_1\,(\rho A\dot{l}\,(13.0\dot{l} + 21.0\dot{d}_i) + \rho A l\,(13.0\ddot{l} + 21.0\ddot{d}_i))\,,\\
\dot{c}_2(1,3) &= -\rho A\,(C_4\ddot{l} - 0.5\ddot{d}_i)\,,\\
\dot{c}_2(1,4) &= -C_1\,(\rho A\dot{l}\,(\dot{l} + 21.0\dot{d}_i) + \rho A l\,(\ddot{l} + 21.0\ddot{d}_i))\,,\\
\dot{c}_2(2,1) &= C_2\,(\rho A l\,(3.0\dot{l} - 7.0\dot{d}_i) + \rho A l\,(3.0\ddot{l} - 7.0\ddot{d}_i))\,,\\
\dot{c}_2(2,2) &= C_2\rho A l^2\ddot{l} + C_6\rho A l\dot{l}^2\,,\\
\dot{c}_2(2,3) &= -C_2\,(\rho A l\,(3.0\dot{l} - 7.0\dot{d}_i) + \rho A l\,(3.0\ddot{l} - 7.0\ddot{d}_i))\,,\\
\dot{c}_2(2,4) &= -C_3\rho A l^2\,(\ddot{l} + 7.0\ddot{d}_i) - C_1\rho A l\dot{l}\,(\dot{l} + 7.0\dot{d}_i)\,,\\
\dot{c}_2(3,1) &= \rho A\,(C_5\ddot{l} - 0.5\ddot{d}_i)\,,\\
\dot{c}_2(3,2) &= -C_1\,(\rho A\dot{l}\,(-22.0\dot{l} + 21.0\dot{d}_i) + \rho A l\,(-22.0\ddot{l} + 21.0\ddot{d}_i))\,,\\
\dot{c}_2(3,3) &= -\rho A\,(C_5\ddot{l} - 0.5\ddot{d}_i)\,,\\
\dot{c}_2(3,4) &= C_1\,(\rho A\dot{l}\,(-34.0\dot{l} + 21.0\dot{d}_i) + \rho A l\,(-34.0\ddot{l} + 21.0\ddot{d}_i))\,,\\
\dot{c}_2(4,1) &= C_2\,(\rho A\dot{l}\,(-4.0\dot{l} + 7.0\dot{d}_i) + \rho A l\,(-4.0\ddot{l} + 7.0\ddot{d}_i))\,,\\
\dot{c}_2(4,2) &= C_3\rho A l^2\,(-8.0\ddot{l} + 7.0\ddot{d}_i) + C_1\rho A l\dot{l}\,(-8.0\dot{l} + 7.0\dot{d}_i)\,,\\
\dot{c}_2(4,3) &= -C_2\,(\rho A\dot{l}\,(-4.0\dot{l} + 7.0\dot{d}_i) + \rho A l\,(-4.0\ddot{l} + 7.0\ddot{d}_i))\,,\\
\dot{c}_2(4,4) &= C_2\rho A l^2\ddot{l} + C_6\rho A l\dot{l}^2\,,
\end{aligned}
\tag{32}
$$

where

$$
\begin{aligned}
C_1 &= 0.0047619047619048 & C_2 &= 0.0142857142857143\\
C_3 &= 0.0023809523809524 & C_4 &= 0.1857142857142857\\
C_5 &= 0.3142857142857143 & C_6 &= 0.02857142857
\end{aligned}
\tag{33}
$$

and density $\rho$, cross-sectional area $A$, element length $l$, and parameter $d_i$ as defined in Eq. (3.5).

# Appendix C:

## I. Newmark Method

The difference equations suggested by Newmark are

$$\{\dot{Y}\}_{t+\Delta t} = \{Y\}_t + \Delta t\,((1-\delta)\,\{\ddot{Y}\}_t + \delta\,\{\ddot{Y}\}_{t+\Delta t}), \tag{34}$$

and

$$\{Y\}_{t+\Delta t} = \{Y\}_t + \Delta t\,\{\dot{Y}\}_t + \Delta t^2((\frac{1}{2}-\alpha)\,\{\ddot{Y}\}_t + \alpha\,\{\ddot{Y}\}_{t+\Delta t}) \tag{35}$$

If the values of 1/2 and 1/6 are used for $\delta$ and $\alpha$, respectively, then above equations reduce to the equations used in the linear-acceleration method. First we consider the system of second-order differential equations at time $t = t+\Delta t$

$$[M]\,\{\dot{Y}\}_{t+\Delta t} + [C]\,\{\dot{Y}\}_{t+\Delta t} + [K]\,\{Y\}_{t+\Delta t} = \{F\}_{t+\Delta t}, \tag{36}$$

from wnich we intent to solve for the displacement $\{Y\}_{t+\Delta t}$. To do so, we must first obtain expressions for $\{\ddot{Y}\}_{t+\Delta t}$ and $\{\dot{Y}\}_{t+\Delta t}$ in terms of quantities at time $t$ and $\{Y\}_{t+\Delta t}$ only. From Eq. (35) we obtain

$$\{\ddot{Y}\}_{t+\Delta t} = \frac{1}{\alpha\Delta t^2}(\{Y\}_{t+\Delta t} - \{Y\}_t) - \frac{1}{\alpha\Delta t}\{\dot{Y}\}_t - (\frac{1}{2\alpha} - 1)\,\{\ddot{Y}\}_t, \tag{37}$$

which upon substitution in Eq. (34) yields

$$\{\dot{Y}\}_{t+\Delta t} = \{\dot{Y}\}_t + \Delta t\,((1-\delta)\,\{\ddot{Y}\}_t + \delta\,\{\ddot{Y}\}_{t+\Delta t}) \tag{38}$$

Substituting Eqs. (37) and (38) into the system of equations (36) and rearranging, we obtain

$$[\hat{K}]\,\{Y\}_{t+\Delta t} = \{F\}_{t+\Delta t} + \{R\}_t, \tag{39}$$

where

$$[\hat{K}] = \frac{1}{\alpha\Delta t^2}[M] + \frac{\delta}{\alpha\Delta t}[C] + [K], \tag{40}$$

and

$$\{\hat{R}\}_t = [M]\left(\frac{1}{\alpha\Delta t^2}\{Y\}_t + \frac{1}{\alpha\Delta t}\{\dot{Y}\}_t + (\frac{1}{2\alpha} - 1)\{\ddot{Y}_t\}\right) + [C](\frac{\delta}{\alpha\Delta t}\{Y\}_t + (\frac{\delta}{\alpha} - 1)\{\dot{Y}\}_t + \Delta t(\frac{\delta}{2\alpha} - 1)\{\ddot{Y}\}_t). \quad (41)$$

The system of equations in (39) can then be solved to obtain the displacements at $t = t+\Delta t$. Having done that, Eqs. (37) and (38) may be used to obtain the velocities and accelerations at time $t = t+\Delta t$.

Since equilibrium is considered at $t = t+\Delta t$, the Newmark method is an implicit time-integration method. The description of the algorithm for the Newmark method (as adapted for the solution of the time-dependent set of equations of the flexible extendible beam) is given below:

**Preliminary calculations**

1. Select values for $\alpha$ and $\delta$. In general the values *0.25* and *0.50* are used respectively.

2. Select a small time-step $\Delta t$. In general the value *0.000001 s* is used.

3. Select a value for the $J_{cr}$ parameter. A description of this parameter is given in the second part of this appendix.

4. Form the initial system matrices $[M]$, $[C]$ and $[K]$ at time $t$.

5. Using the initial displacement and velocity vectors, determine the initial accelerations using equilibrium at time $t$

$$[M]_t\{\ddot{Y}\}_t = \{F\}_t - [K]_t\{Y\}_t - [C]_t\{\dot{Y}\}_t. \quad (42)$$

**For each time-step**

1. Form $[\hat{K}]_{t+\Delta t}$

$$[\hat{K}]_{t+\Delta t} = \frac{1}{\alpha\Delta t^2}[M]_{t+\Delta t} + \frac{\delta}{\alpha\Delta t}[C]_{t+\Delta t} + [K]_{t+\Delta t}. \quad (43)$$

2. Form $\{\hat{R}\}_t$

$$\{\hat{R}\}_t = [M]_{t+\Delta t}\left(\frac{1}{\alpha\Delta t^2}\{Y\}_t + \frac{1}{\alpha\Delta t}\{\dot{Y}\}_t + \left(\frac{1}{2\alpha} - 1\right)\{\ddot{Y}_t\}\right) + [C]_{t+\Delta t}\left(\frac{\delta}{\alpha\Delta t}\{Y\}_t + \left(\frac{\delta}{\alpha} - 1\right)\{\dot{Y}\}_t + \Delta t\left(\frac{\delta}{2\alpha} - 1\right)\{\ddot{Y}\}_t\right). \tag{44}$$

3. Solve for the displacements at $t = t+\Delta t$

$$[\hat{K}]_{t+\Delta t}\{Y\}_{t+\Delta t} = \{F\}_{t+\Delta t} + \{\hat{R}\}_t. \tag{45}$$

4. Solve for the velocities and accelerations at $t = t+\Delta t$ through Eqs (37) and (38).

5. Adapt the time-step size according to the procedure described in the second part of this appendix.

## II. Procedure for Adaptive Time-Step Size

The criterion used for the selection of a time-step size is the magnitude of the rate of change of acceleration, known as jerk. Jerk is approximated by

$$\{J\}_n = \frac{\{\ddot{Y}\}_n - \{\ddot{Y}\}_{n-1}}{\Delta t_n}, \tag{46}$$

where the most recent results available are via the $n^{th}$ integration step using a time-step size of $\Delta t_n$. Next we determine the maximum component of the jerk vector, which we denote by $\hat{J}_n$. The maximum jerk is then normalised as follows

$$J_n = \hat{J}_n \Delta t_n^3. \tag{47}$$

The user of this procedure selects a value for the critical normalised jerk, denoted by $J_{cr}$, which corresponds to the largest value of normalised jerk allowed at the $n+1$ integration step, that is

$$J_{cr} = J_{n+1} = \hat{J}_{n+1} \Delta t_{n+1}^3. \tag{48}$$

For small time-step sizes, above expression may be approximated by

$$J_{cr} = \hat{J}_n \Delta t_{n+1}^3 \tag{49}$$

Now substituting for $\hat{J}_n$ from Eq. (47) and solving for $\Delta t_{n+1}$, Eq. (49) yields an expression for the estimation of the next time-step size, namely

$$\Delta t_{n+1} = \Delta t_n \left( \frac{J_{cr}}{J_n} \right)^{1/3}. \tag{50}$$

For structural dynamics problems, the user-specified value of $J_{cr}$ should be in the neighborhood of $0.001$. From a number of tests we have performed, we found that a 30% reduction in the number of time steps is normal in structural dynamics.

The flexible extendible beam problem necessitates the use of an adaptive time-step size algorithm for accurate and efficient integration of its time-dependent equations of motion. When the beam's length is small and the frequencies of oscillation high, this adaptive procedure ensures accurate integration by selecting appropriately small time-step sizes. However, as the beam becomes longer this procedure takes advantage of the

lower frequencies of oscillation and decreases the time-step size without any loss of accuracy. For this problem we found that a value of $J_{cr}$=0.000001 was adequate for all simulations. Even with such a conservative value for $J_{cr}$, the computational savings were significant. These savings were highly dependent on the specifics of the problem solved, especially the axial-motion profile and overall time of integration. One, even two orders of magnitude of reduction in the number of time steps was usual for most flexible extendible beam problems solved (see Table (1) below).

The computer implementation of this adaptive procedure takes certain additional measures to avoid artificially excited transients while adapting the time-step size. For instance, it does not allow a step-size increase after a decrease and visa versa. Also, it does not allow an increase or decrease of the time-step size by more than a factor of four.

| | $\Delta t_{min}\ 10^{+3}$ (s) | $\Delta t_{max}\ 10^{+3}$ (s) | $\Delta t_{avg}\ 10^{+3}$ (s) | **Number of Steps (Variable Time-Step Size)** | **Number of Steps (Constant Time-Step Size)** |
|---|---|---|---|---|---|
| Test Case # 1 | 0.0475 | 2.589 | 1.052 | 1,331 | 29,474 |
| Test Case # 2 | 0.0294 | 5.181 | 1.053 | 1,333 | 47,619 |
| Test Case # 3 | 0.0468 | 4.312 | 1.173 | 1,194 | 29,915 |
| Test Case # 4 | 0.0317 | 4.546 | 1.050 | 1,333 | 44,164 |
| Test Case # 5 | 0.0020 | 3.346 | 1.003 | 1,197 | 611,933 |
| Test Case # 6 | 0.0016 | 3.445 | 0.835 | 1,437 | 752,823 |
| Simulation # 1 | 0.0188 | 12.394 | 1.133 | 1,059 | 63,830 |
| Simulation # 2 | 0.0188 | 7.806 | 1.114 | 1,077 | 63,830 |
| Simulation # 3 | 0.2410 | 4.829 | 1.435 | 836 | 4,979 |
| Simulation # 4 | 0.2410 | 4.981 | 1.127 | 1,065 | 4,979 |
| Simulation # 5 | 0.0188 | 2.987 | 0.604 | 331 | 10,639 |
| Simulation # 6 | 0.0188 | 4.454 | 0.610 | 328 | 10,639 |
| Simulation # 7 | 0.2410 | 2.633 | 0.673 | 297 | 830 |
| Simulation # 8 | 0.2410 | 1.668 | 0.459 | 435 | 830 |
| Total | -- | -- | -- | 13,250 | 1,676,484 |

Table 1: Constant-time-step VS Variable-time-step algorithms.

# Appendix D:

## I. Experimental Results by Yuh and Young (1991)

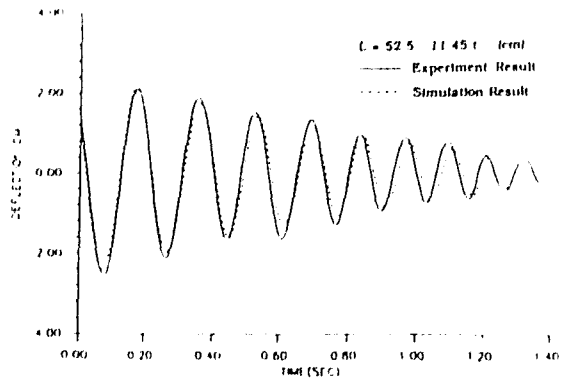


Fig. 4 Test 1

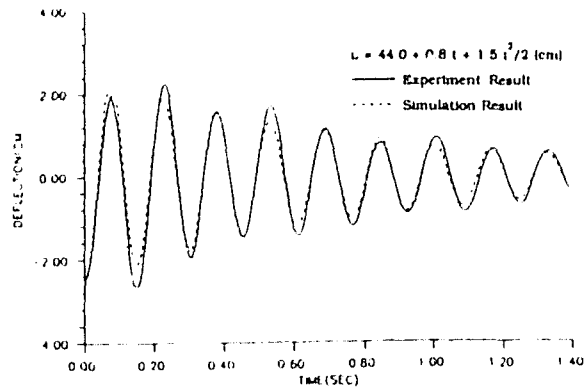


Fig. 4 Test 4

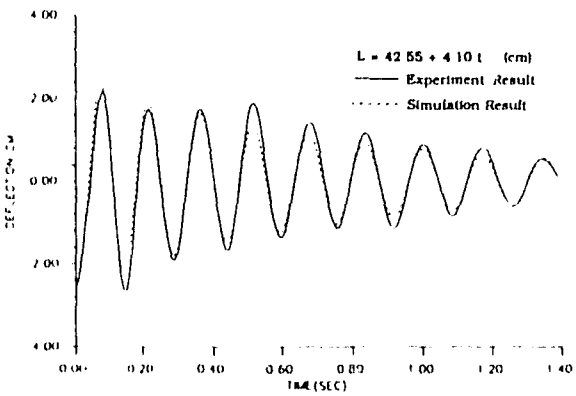


Fig. 4 Test 2

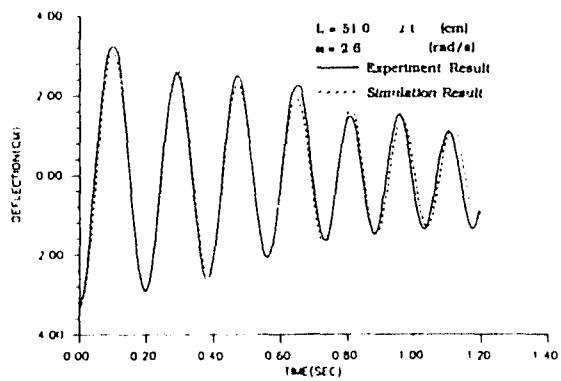


Fig. 4 Test 5

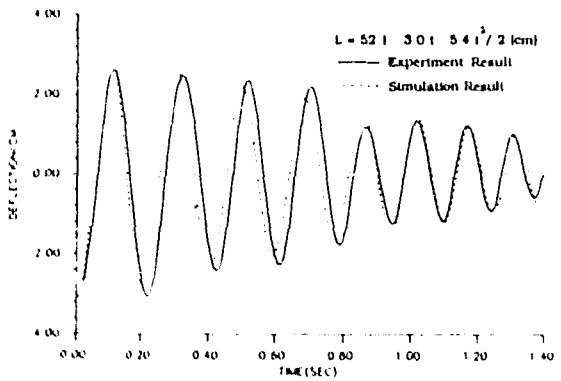


Fig. 4 Test 3

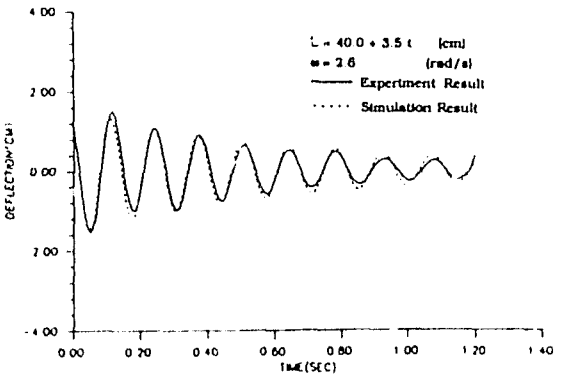


Fig. 4 Test 6

Fig. 4 Tip-deflections of experiment tests [ _ experimental result; .... simulation result]

# II. Simulation Results by Yuh and Young (1991)

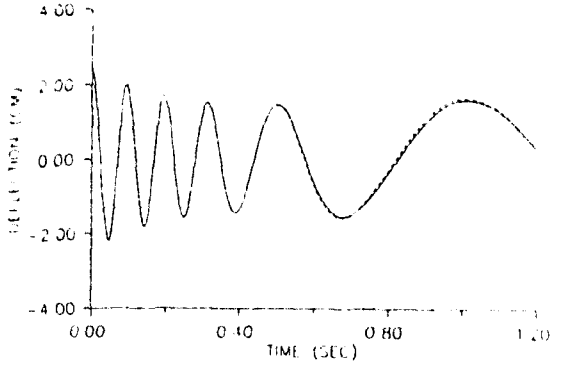


Fig. 5 Tip-deflection for the slow extention (case 1 __ ) and for the slow extention and rotation (case 2 ... )

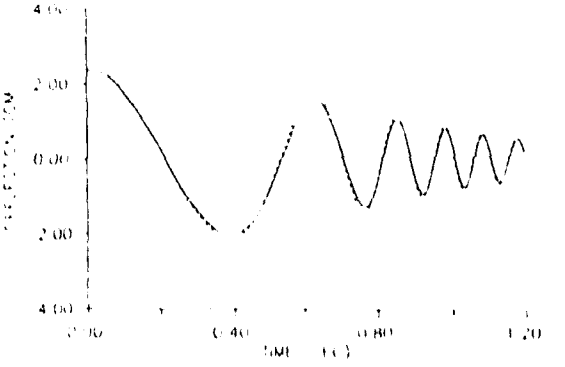


Fig. 6 Tip-deflection for the slow retraction (case 3 ) and for the slow retraction and rotation (case 4 ....)

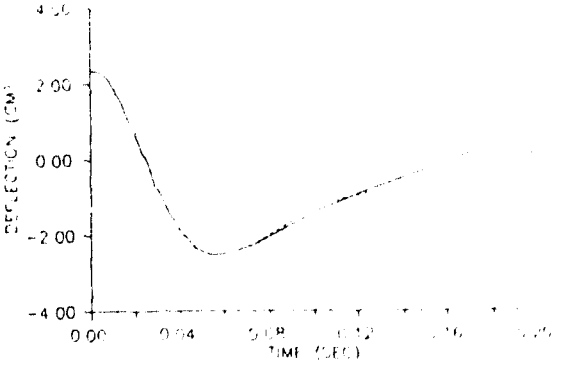


Fig. 7 Tip-deflection for the fast extention (case 5 _ ) and for the fast extention and rotation (case 6 ....)

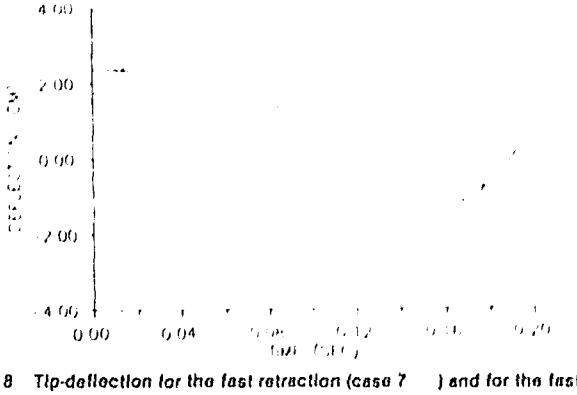


Fig. 8 Tip-deflection for the fast retraction (case 7 ) and for the fast retraction and rotation (case 8 ....)

# Appendix E: Components of Invariant Matrices and Vectors

## I. The $[a_1]$ Matrix

The components of the $[a_1]$ matrix are given by:

$$
\begin{aligned}
a_1(1,1) &= 0.6\frac{\rho A}{l}(-\dot{l}+2.0\dot{d}_i),\\
a_1(1,2) &= \rho A(-0.2\dot{l}+0.1\dot{d}_i),\\
a_1(1,3) &= -0.6\frac{\rho A}{l}(-\dot{l}+2.0\dot{d}_i),\\
a_1(1,4) &= 0.1\rho A(\dot{l}+\dot{d}_i),\\
a_1(2,1) &= 0.1\rho A(-\dot{l}+\dot{d}_i),\\
a_1(2,2) &= -C_1\rho A l(\dot{l}-4.0\dot{d}_i),\\
a_1(2,3) &= 0.1\rho A(\dot{l}\ \dot{d}_i),\\
a_1(2,4) &= C_1\rho A l(\dot{l}-\dot{d}_i),\\
a_1(3,1) &= -0.6\frac{\rho A}{l}(-\dot{l}+2.0\dot{d}_i),\\
a_1(3,2) &= \rho A(0.2\dot{l}-0.1\dot{d}_i),\\
a_1(3,3) &= 0.6\frac{\rho A}{l}(-\dot{l}+2.0\dot{d}_i),\\
a_1(3,4) &= 0.1\rho A(-\dot{l}\ \dot{d}_i),\\
a_1(4,1) &= 0.1\rho A\dot{d}_i,\\
a_1(4,2) &= -C_1\rho A l\dot{d}_i,\\
a_1(4,3) &= -0.1\rho A\dot{d}_i,\\
a_1(4,4) &= -C_1\rho A l(3.0\dot{l}-4.0\dot{d}_i),
\end{aligned}
\tag{51}
$$

where

$$C_1 = 0.0333333333333333 \tag{52}$$

and density $\rho$, cross-sectional area $A$, element length $l$, and parameter $d_i$ as defined in Eq. (3.5).

## II. The $[\dot{a}_1]$ Matrix

The components of the $[\dot{a}_1]$ matrix are given by:

$$
\begin{aligned}
\dot{a}_1(1,1) &= 0.6\left(\frac{\rho A}{l}(-\ddot{l}+2.0\ddot{d}_i)-\frac{\rho A\dot{l}}{l^2}(-\dot{l}+2.0\dot{d}_i)\right),\\
\dot{a}_1(1,2) &= \rho A(-0.2\ddot{l}+0.1\ddot{d}_i),\\
\dot{a}_1(1,3) &= -0.6\left(\frac{\rho A}{l}(-\ddot{l}+2.0\ddot{d}_i)-\frac{\rho A\dot{l}}{l^2}(-\dot{l}+2.0\dot{d}_i)\right),\\
\dot{a}_1(1,4) &= 0.1\rho A(\ddot{l}+\ddot{d}_i),\\
\dot{a}_1(2,1) &= 0.1\rho A(-\ddot{l}+\ddot{d}_i),\\
\dot{a}_1(2,2) &= -C_1(\rho A l(\ddot{l}-4.0\ddot{d}_i)+\rho A\dot{l}(\dot{l}-4.0\dot{d}_i)),\\
\dot{a}_1(2,3) &= 0.1\rho A(\ddot{l}-\ddot{d}_i),\\
\dot{a}_1(2,4) &= C_1(\rho A l(\ddot{l}-\ddot{d}_i)+\rho A\dot{l}(\dot{l}-\dot{d}_i)),\\
\dot{a}_1(3,1) &= -0.6\left(\frac{\rho A}{l}(-\ddot{l}+2.0\ddot{d}_i)-\frac{\rho A\dot{l}}{l^2}(-\dot{l}+2.0\dot{d}_i)\right),\\
\dot{a}_1(3,2) &= -\rho A(-0.2\ddot{l}+0.1\ddot{d}_i),\\
\dot{a}_1(3,3) &= 0.6\left(\frac{\rho A}{l}(-\ddot{l}+2.0\ddot{d}_i)-\frac{\rho A\dot{l}}{l^2}(-\dot{l}+2.0\dot{d}_i)\right),\\
\dot{a}_1(3,4) &= 0.1\rho A(-\ddot{l}\ \ddot{d}_i),\\
\dot{a}_1(4,1) &= 0.1\rho A\ddot{d}_i,\\
\dot{a}_1(4,2) &= -C_1(\rho A\dot{l}\dot{d}_i+\rho A l\ddot{d}_i),\\
\dot{a}_1(4,3) &= -0.1\rho A\ddot{d}_i,\\
\dot{a}_1(4,4) &= -C_1(\rho A l(3.0\ddot{l}-4.0\ddot{d}_i)+\rho A\dot{l}(3.0\ddot{l}-4.0\ddot{d}_i)),
\end{aligned}
\tag{53}
$$

where

$$C_1 = 0.0333333333333333 \tag{54}$$

and density $\rho$, cross-sectional area $A$, element length $l$, and parameter $d_i$ as defined in Eq. (3.5).

## III. The $[a_2]$ Matrix

The components of the $[a_2]$ matrix are given by:

$$
\begin{aligned}
a_2(1,1) &= -0.5\rho A, \\
a_2(1,2) &= -0.1\rho Al, \\
a_2(1,3) &= -0.5\rho A, \\
a_2(1,4) &= 0.1\rho Al, \\
a_2(2,1) &= 0.1\rho Al, \\
a_2(2,2) &= 0, \\
a_2(2,3) &= -0.1\rho Al, \\
a_2(2,4) &= C_1\rho Al^2, \\
a_2(3,1) &= 0.5\rho A, \\
a_2(3,2) &= 0.1\rho Al, \\
a_2(3,3) &= 0.5\rho A, \\
a_2(3,4) &= -0.1\rho Al, \\
a_2(4,1) &= -0.1\rho Al, \\
a_2(4,2) &= -C_1\rho Al^2, \\
a_2(4,3) &= 0.1\rho Al, \\
a_2(4,4) &= 0,
\end{aligned}
\tag{55}
$$

where

$$
C_1 = 0.016666667\ldots \tag{56}
$$

and density $\rho$, cross-sectional area $A$, and element length $l$.

## IV. The $[\dot{a}_2]$ Matrix

The components of the $[\dot{a}_2]$ matrix are given by:

$$\begin{aligned}
\dot{a}_2(1,1) &= 0, \\
\dot{a}_2(1,2) &= -0.1\rho A\dot{l}, \\
\dot{a}_2(1,3) &= 0, \\
\dot{a}_2(1,4) &= 0.1\rho A\dot{l}, \\
\dot{a}_2(2,1) &= 0.1\rho A\dot{l}, \\
\dot{a}_2(2,2) &= 0, \\
\dot{a}_2(2,3) &= -0.1\rho A\dot{l}, \\
\dot{a}_2(2,4) &= C_1\rho Al\dot{l}, \\
\dot{a}_2(3,1) &= 0, \\
\dot{a}_2(3,2) &= 0.1\rho A\dot{l}, \\
\dot{a}_2(3,3) &= 0, \\
\dot{a}_2(3,4) &= -0.1\rho A\dot{l}, \\
\dot{a}_2(4,1) &= -0.1\rho A\dot{l}, \\
\dot{a}_2(4,2) &= -C_1\rho Al\dot{l}, \\
\dot{a}_2(4,3) &= 0.1\rho A\dot{l}, \\
\dot{a}_2(4,4) &= 0,
\end{aligned} \tag{57}$$

where

$$C_1 = 0.3333333333333333 \tag{58}$$

and density $\rho$, cross-sectional area $A$, and element length $l$.

## V. The $[b_1]$ Vector

The components of the $\{b_1\}$ vector are given by:

$$\{b_1\} = \begin{bmatrix} -\dfrac{6.0}{l^2} \\ -\dfrac{4.0}{l} \\ \dfrac{6.0}{l^2} \\ -\dfrac{2.0}{l} \end{bmatrix}, \tag{59}$$

with element length $l$.

## VI. The $[b_2]$ and $[\dot{b}_2]$ Vectors

The components of the $\{b_2\}$ and $\{\dot{b}_2\}$ vectors are given by:

$$\{\dot{b}_2\} = \begin{bmatrix} \rho A\,(0.5\dot{l} - \dot{d}_i) \\ C_1 \rho A l \dot{l} \\ -\rho A\,(0.5\dot{l} - \dot{d}_i) \\ -C_1 \rho A l \dot{l} \end{bmatrix}, \qquad \{\dot{b}_2\} = \begin{bmatrix} \rho A\,(0.5\ddot{l} - \ddot{d}_i) \\ C_1 \rho A\,(l\ \ddot{l} + \dot{l}^2) \\ -\rho A\,(0.5\ddot{l} - \ddot{d}_i) \\ -C_1 \rho A\,(l\ \ddot{l} + \dot{l}^2) \end{bmatrix}, \tag{60}$$

with

$$C_1 = 0.1666666666666667, \tag{61}$$

and density $\rho$, cross-sectional area $A$, element length $l$, and parameter $d_i$ as defined in Eq. (3.5).

## VII. The $[b_3]$ and $[\dot{b}_3]$ Vectors

The components of the $\{b_3\}$ and $\{\dot{b}_3\}$ vectors are given by:

$$\{b_3\} = \begin{bmatrix} 0.5\rho Al \\ C_1\rho Al^2 \\ 0.5\rho Al \\ -C_1\rho Al^2 \end{bmatrix}, \qquad \{\dot{b}_3\} = \begin{bmatrix} 0.5\rho A\dot{l} \\ C_1\rho Al\dot{l} \\ 0.5\rho A\dot{l} \\ -C_1\rho Al\dot{l} \end{bmatrix}, \tag{62}$$

with

$$C_1 = 0.08333333333333333, \tag{63}$$

and density $\rho$, cross-sectional area $A$, element length $l$, and parameter $d_i$ as defined in Eq. (3.5).

## VIII. The $[b_4]$ Vector

The components of the $\{b_4\}$ vector are given by:

$$\{\dot{b}_4\} = \begin{bmatrix} \frac{12.0}{l^3} \\ \frac{6.0}{l^2} \\ -\frac{12.0}{l^3} \\ \frac{6.0}{l^2} \end{bmatrix}, \tag{64}$$

with element length $l$.

# Appendix F:

## Stability Analysis by Option (b) of Section 5.2

Under this option, the axial velocity is held fixed and the eigenvalues that emerge from the stability analysis can be viewed as those of the system at different instants of time. The axial motion of the beam is described by the linear extrusion profile of Eq. (5.9), with initial length $L_0 = 0.5m$, and constant axial velocity $v = 10.0\ m/s$. Therefore, the instantaneous length of the protruding part of the beam in metres is given by

$$L(t) = 0.5 + 10t. \tag{65}$$

The evolutions of the system's first four complex eigenvalues are shown in Figs. (1) and (2). The general characteristics of the evolutions of the eigenvalues are similar to those obtained using option (a) in Section 5.2 (Figs. (5.1) and (5.2)). The change in appearance is due to the change of the beam's length under option (b). However, as mentioned in Section 5.2, the critical values for the non-dimensional velocity $U$ are identical to those obtained under option (a) in Section 5.2 (third column in Table (5.1)).

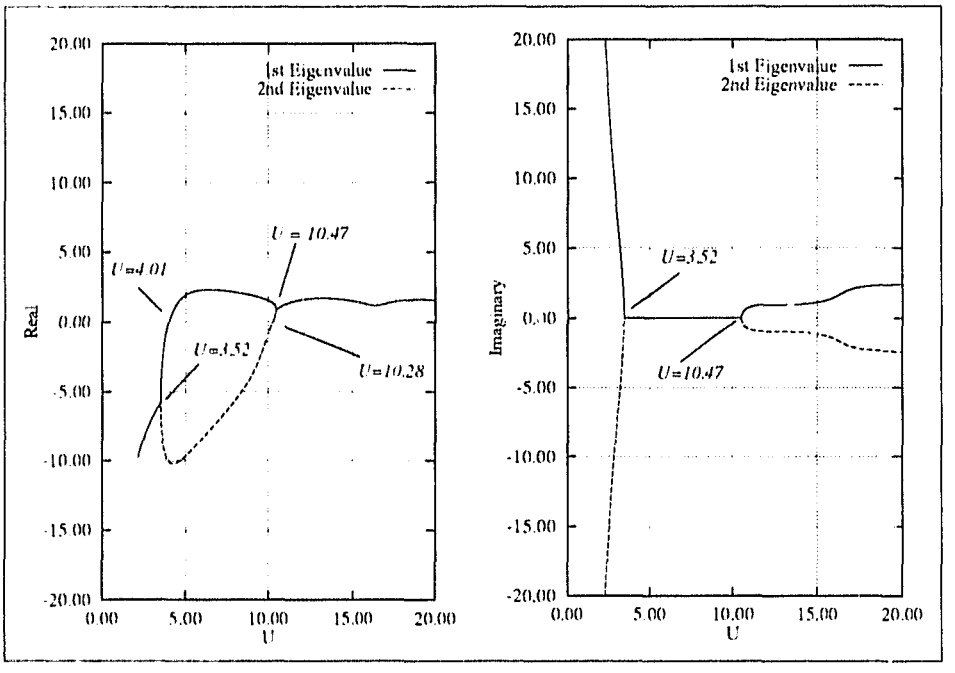


Figure 1: Real and imaginary components of first and second eigenvalues.

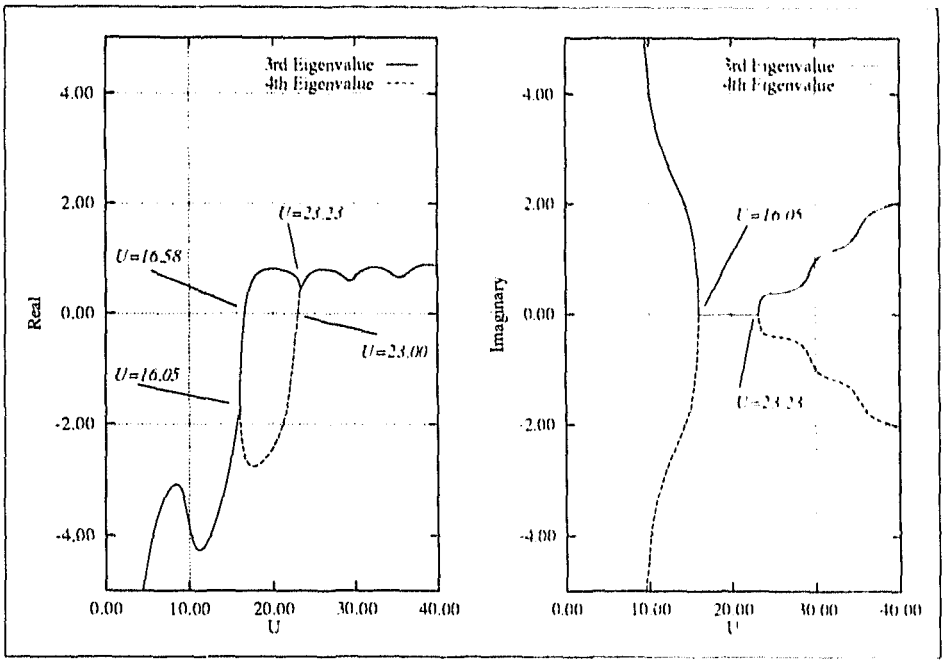


Figure 2: Real and imaginary components of third and fourth eigenvalues.

It is also instructive to perform a dynamic simulation during which the flexible extendible beam loses stability. The procedure is similar to the one used in Chapter 4. In this case, however, we make sure that during the time-integration the non-dimensional velocity $U$ attains a value at least equal to the lowest critical velocity found in Section 5.2.1. This procedure ensures that the flexible extendible beam loses stability by divergence during the dynamic simulation.

Fig. (3) shows the tip-deflection history for an extruding beam in the absence of physical damping with an axial-motion profile given by

$$L = 0.2 + t. \tag{66}$$

This specific simulation covers values of $U$ between $0.087$ and $6.141$. According to the results of Section 5.2.1, the first mode becomes non-oscillatory at $U = 3.52$ (which occurs at $t = 8\ s$) and the system diverges at $U = 4.01$ ($t = 9\ s$). As expected, Fig. (3) shows that the amplitude of oscillations, after the onset of divergence, grows without bound. This was further confirmed by carrying out the simulation for up to $t = 100\ s$.

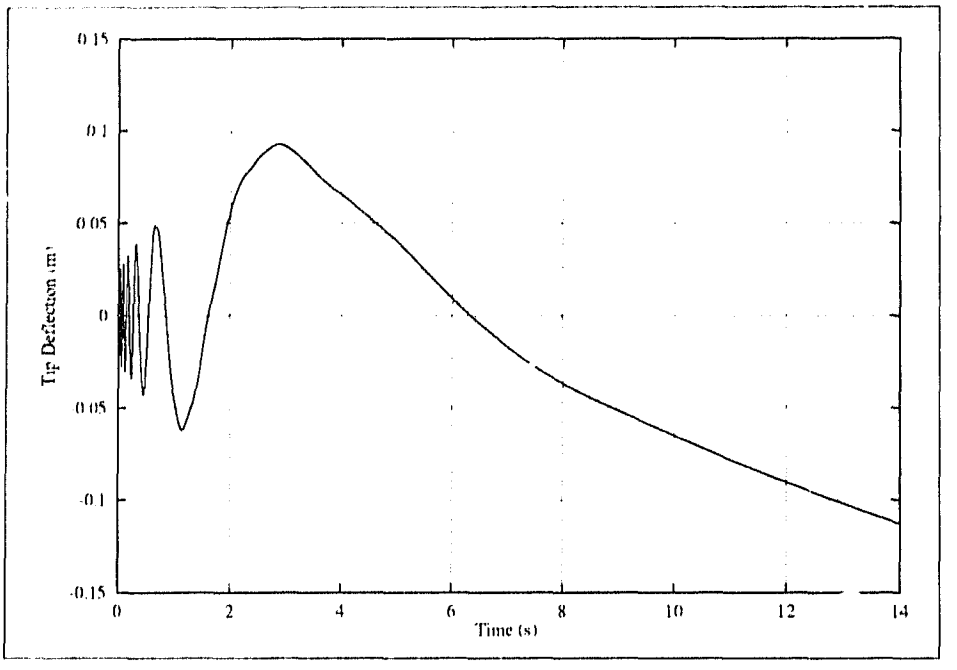


Figure 3: Time response through a divergence instability.

# Appendix G: Cantilever Pipes

Consider the pipe conveying fluid shown in Fig. (4). $M$ is the fluid density per unit length, $m$ is the pipe density per unit length, $EI$ is the flexural rigidity of the pipe, $v$ is the velocity of the fluid, and $Y(t,X)$ is the transverse displacement of the pipe as a function of time $t$ and position X. The parameter $\chi$ represents the axial motion of points along the pipe due to the pipe's transverse motion (a second-order effect) and is defined as

$$\chi = \int_0^X \frac{1}{2} Y_X^2 dX, \tag{67}$$

where partial derivatives of $Y$ with respect to $X$ and $t$ are denoted by corresponding subscripts on $Y$.

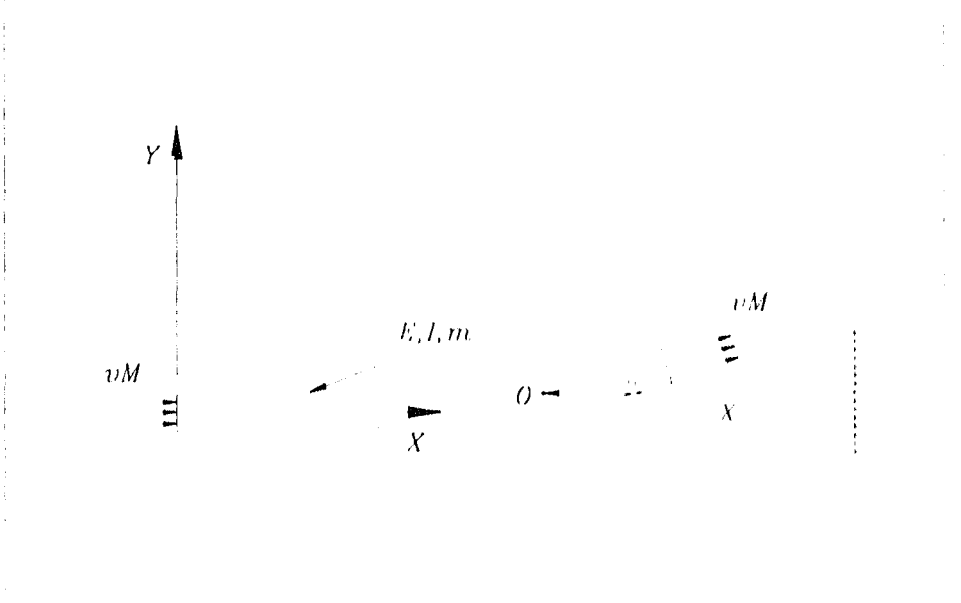


Figure 4: A pipe conveying fluid.

If the cross sectional area is constant along the pipe and the fluid is incompressible, the tangential velocity of the fluid with respect to the pipe is $v$. The horizontal and vertical

components of the fluid velocity with respect to point $O$ (which is fixed on the pipe) are given by

$$\begin{aligned} v_X &= v\cos\Theta = v\,(1 - Y_X^2/2)\,, \\ v_Y &= v\sin\Theta = vY_X, \end{aligned} \tag{68}$$

where we have retained up to the second-order terms in the Taylor series expansion. This will be the case throughout the derivation of the governing equations.

Since point $O$ on the pipe is also moving with horizontal and vertical velocity components given by $\dot{\chi}$ and $Y_t$ respectively, the absolute components of the fluid's velocity are given by

$$\begin{aligned} v_X &= v\,(1 - Y_X^2/2) - \dot{\chi}, \\ v_Y &= Y_t + vY_X. \end{aligned} \tag{69}$$

Now, we are ready to write the Lagrangian density function for this problem as

$$\mathcal{L} = \left(\frac{1}{2}M\,(Y_t^2 + 2vY_tY_X + v^2 - 2v\dot{\chi}) + \frac{1}{2}mY_t^2 - \frac{EI}{2}Y_{XX}^2\right), \tag{70}$$

where only up to the second-order terms have been retained.

We now need to consider the set of forces which the fluid exerts on the pipe at the tip. The components of the flux of absolute momentum out of the pipe are given by

$$\begin{aligned} P_X &= Mv\,(v\,(1 - Y_X^2/2) - \dot{\chi})\,\big|_{X=L}, \\ P_Y &= Mv\,(Y_t + vY_X)\,\big|_{X=L}. \end{aligned} \tag{71}$$

The work done by the horizontal component may be expressed as

$$-\left(Mv^2 - \frac{Mv^2Y_X^2}{2} - Mv\dot{\chi}\right)\frac{\partial\chi}{\partial X}\bigg|_{X=L}, \tag{72}$$

which upon retaining up to second-order terms only, becomes

$$-\frac{\partial}{\partial X}(Mv^2\chi)\,\big|_{X=L}. \tag{73}$$

Therefore, the horizontal component can be derived from a potential and hence allows us to add it to the Lagrangian density function. However, the vertical component can not be derived from a potential (it is a non- onservative force), hence we need to consider its virtual work. The variational statement for the pipes conveying fluid problem (originally given by Benjamin (1961)) may now be written as

$$\delta \int_{t_1}^{t_2} \int_{0}^{L} (\mathcal{L} + Mv^2 \chi|_{X=L})\, dX dt - \int_{t_1}^{t_2} Mv\,(Y_t + vY_X)\,\delta Y|_{X=L} dt = 0. \tag{74}$$

Noting that

$$\chi|_{X=L} = \int_{0}^{L} \frac{1}{2} Y_X^2, \tag{75}$$

the variational statement may be expressed as

$$\delta \int_{t_1}^{t_2} \int_{0}^{L} (\frac{1}{2}(M+m)\,Y_t^2 + Mv\,(Y_t Y_X + \frac{1}{2} v Y_X^2 - \dot{\chi}) - \frac{EI}{2} Y_{XX}^2)\, dX dt - \int_{t_1}^{t_2} Mv\,(Y_t + vY_X)\,\delta Y|_{X=L} dt = 0. \tag{76}$$

Using the same procedure as the one employed in Chapter 3, we first need to write the element variational statements. For all elements except the last, at the tip of the pipe, the element variational statement becomes

$$\delta \int_{t_1}^{t_2} \int_{0}^{l} (\frac{1}{2}((M+m)\,y_t^2) + Mv\,(y_t y_x + \frac{1}{2} v y_x^2 - \dot{\chi}) - \frac{EI}{2} y_x^2)\, dx dt = 0, \tag{77}$$

where $l$ is the length of the elements, and $y(t,x)$ is the transverse displacement of the pipe as a function of time $t$ and local position $x$. For the last element at the tip of the pipe, we need to include the virtual work of the non-conservative equivalent flow tip-force. Therefore, the element variational statement for the last element becomes

$$\int_{t_1}^{t_2}\int_{0}^{l}\left(\frac{1}{2}\left((M+m)\,y_t^2\right)+Mv\left(y_t y_x+\frac{1}{2}vy_x^2-\dot{\chi}\right)-\frac{EI}{2}y_x^2\right)dx\,dt-$$
$$\int_{t_1}^{t_2} Mv\left(y_t+vy_x\right)\delta Y\big|_{x=l}\,dt=0. \tag{78}$$

The discretization will be performed using the shape-functions vector of Eq. (3.16) and corresponding nodal-variables vector of Eq. (3.17). For this system, the length of the pipe remains constant, hence, the shape-functions vector is independent of time. The local transverse displacement and its derivatives may then be expressed as

$$\begin{aligned} y &= \lfloor N\rfloor_y\{y\},\\ y_t &= \lfloor N\rfloor_y\{\dot{y}\},\\ y_x &= \lfloor N'\rfloor_y\{y\},\\ y_{xx} &= \lfloor N''\rfloor_y\{y\}, \end{aligned} \tag{79}$$

where primes and dots indicate partial differentiation with respect to $x$ and $t$ respectively. Returning now to the variational statement of the tip element (Eq. (78)) and substituting Eqs. (75) and (79), we obtain

$$\begin{aligned} \delta\int_{t_1}^{t_2}\int_{0}^{l}\Big[&\frac{1}{2}(M+m)\,\{\dot{y}\}^T\lfloor N\rfloor_y^T\lfloor N\rfloor_y\{\dot{y}\}+Mv\,\{\dot{y}\}^T\lfloor N\rfloor_y^T\lfloor N'\rfloor_y\{y\}+\\ &\frac{1}{2}Mv^2\,\{y\}^T\lfloor N'\rfloor_y^T\lfloor N'\rfloor_y\{y\}-\frac{\partial}{\partial t}\int_0^x\frac{1}{2}\,\{y\}^T\lfloor N'\rfloor_y^T\lfloor N'\rfloor_y\{y\}\,dx-\\ &\frac{1}{2}EI\,\{y\}^T\lfloor N''\rfloor_y^T\lfloor N''\rfloor_y\{y\}\Big]dx\,dt-\\ &\int_{t_1}^{t_2}Mv\left[\delta\{y\}^T\lfloor N\rfloor_y^T\lfloor N\rfloor_y\{\dot{y}\}-v\delta\{y\}^T\lfloor N\rfloor_y^T\lfloor N'\rfloor_y\{y\}\right]\Big|_{x=l}dt=0. \end{aligned} \tag{80}$$

Carrying out the variation and using integration by parts, the various terms in Eq. (80) become

$$\delta\int_{t_1}^{t_2}\int_{0}^{l}\frac{1}{2}(M+m)\,\{\dot{y}\}^T\lfloor N\rfloor_y^T\lfloor N\rfloor_y\{\dot{y}\}\,dx\,dt=-\int_{t_1}^{t_2}\delta\{y\}^T\lfloor m\rfloor\{\ddot{y}\}\,dt, \tag{81}$$

$$\delta\int_{t_1}^{t_2}\int_0^l Mv\{\dot{y}\}^T\lfloor N\rfloor_y^T\lfloor N'\rfloor_y\{y\}\,dx\,dt = \int_{t_1}^{t_2}\delta\{y\}^T(\lfloor c_2\rfloor - \lfloor c_2\rfloor^T)\{\dot{y}\}\,dt, \tag{82}$$

$$\delta\int_{t_1}^{t_2}\int_0^l \frac{1}{2}Mv^2\{y\}^T\lfloor N'\rfloor_y^T\lfloor N'\rfloor_y\{y\}\,dx\,dt = \int_{t_1}^{t_2}\delta\{y\}^T\lfloor k_1\rfloor\{y\}\,dt, \tag{83}$$

$$-\delta\int_{t_1}^{t_2}\int_0^l\left(\frac{\partial}{\partial t}\int_0^x\frac{1}{2}\{y\}^T\lfloor N'\rfloor_y^T\lfloor N'\rfloor_y\{y\}\,dx\right)dx\,dt = 0, \tag{84}$$

$$-\delta\int_{t_1}^{t_2}\int_0^l\frac{1}{2}EI\{y\}^T\lfloor N''\rfloor_y^T\lfloor N''\rfloor_y\{y\}\,dx\,dt = -\int_{t_1}^{t_2}\delta\{y\}^T\lfloor k\rfloor\{y\}\,dt. \tag{85}$$

Substituting Eqs. (81) to (85) in Eq. (80) and grouping terms, we obtain

$$\int_{t_1}^{t_2}\delta\{y\}^T[\lfloor m\rfloor\{\ddot{y}\} + (\lfloor c_2\rfloor - \lfloor c_2\rfloor^T + \lfloor T_1\rfloor)\{\dot{y}\} + (\lfloor k\rfloor - \lfloor k_1\rfloor + \lfloor T_2\rfloor)\{y\}]\,dt = 0, \tag{86}$$

where

$$\lfloor m\rfloor = \int_0^l (M+m)\lfloor N\rfloor_y^T\lfloor N\rfloor_y dx, \tag{87}$$

$$\lfloor k\rfloor = \int_0^l EI\lfloor N''\rfloor_y^T\lfloor N''\rfloor_y dx, \tag{88}$$

$$\lfloor k_1\rfloor = \int_0^l Mv^2\lfloor N'\rfloor_y^T\lfloor N'\rfloor_y dx, \tag{89}$$

$$\lfloor c_2\rfloor = \int_0^l Mv\lfloor N\rfloor_y^T\lfloor N'\rfloor_y dx. \tag{90}$$

$$\lfloor T_1\rfloor = Mv\lfloor N\rfloor_y^T\lfloor N\rfloor_y\Big|_{x=l} \tag{91}$$

$$\lfloor T_2\rfloor = Mv^2\lfloor N\rfloor_y^T\lfloor N'\rfloor_y\Big|_{x=l} \tag{92}$$

Matrices $[m]$, $[k]$, $[k_1]$, $[c_2]$ for the pipe (Eqs. (87) through (90)) are equivalent to the corresponding matrices for the flexible extendible beam (Eqs. (3.20), (3.21), (3.22) and (3.25) respectively) if $\dot{l}$, $\dot{L}_i$ are set to zero, since the length of the elements remains constant, and $\dot{d}_i$ is set equal to the velocity of the fluid $v$. Matrices $[T_1]$ and $[T_2]$ are unique to the cantilever pipe conveying fluid and are relevant for the last element at the tip of the pipe only. These matrices are given by

$$[T_1] = \begin{bmatrix} 0 & 0 & 0 & 0 \\ 0 & 0 & 0 & 0 \\ 0 & 0 & Mv & 0 \\ 0 & 0 & 0 & 0 \end{bmatrix} \qquad [T_2] = \begin{bmatrix} 0 & 0 & 0 & 0 \\ 0 & 0 & 0 & 0 \\ 0 & 0 & 0 & Mv^2 \\ 0 & 0 & 0 & 0 \end{bmatrix}. \tag{93}$$

In order for Eq. (86) to vanish identically for any $\{y\}$, the integrand must vanish identically. However, due to the arbitrariness of the virtual displacement vector $\delta \{y\}^T$ the following must hold

$$[m] \{\ddot{y}\} + [c_{eq}] \{\dot{y}\} + [k_{eq}] \{y\} = \{0\}, \tag{94}$$

where the equivalent-damping and -stiffness matrices are given by

$$[c_{eq}] = [T_1] + [c_2] - [c_2]^T, \tag{95}$$

$$[k_{eq}] = [k] + [T_2] - [k_1]. \tag{96}$$

The assembly of the element equations to develop the global equations takes the well known format, and the global equations emerge as

$$[M] \{\ddot{Y}\} + [C_{eq}] \{\dot{Y}\} + [K_{eq}] \{Y\} = \{0\}, \tag{97}$$

# Appendix H: Towards Certification of Engineering Software

An important quality attribute of computer systems is the reliability with which they perform their intended functions. Engineers need to be concerned about the reliability of the programs they use (Richter (1984)):

1) Inadequate software can cause overruns in costs and scheduling and, in some cases, disasters.

2) Every engineer must answer for the accuracy of results he or she presents for subsequent use in the design and production of engineering systems.

3) In many cases, the actual results are not known. For instance, if the finite-element analysis solution is incorrect, it is unlikely that the user will know it.

4) The individual engineer is not expected to know all the inner details of the program used.

Despite its maturity, program verification research has had disturbingly little impact on industrial practice. It is still believed that program testing has been and will continue to be the primary method of demonstrating the absence of errors. In addition, there is little evidence of module testing, and code verification is conceived to be too costly to be of any practical importance (Richter (1984), Wheeler (1986)).

Results of various studies, including Russell (1991) and NCC (1989), indicate that code inspections can locate up to 80% of the faults present in a code (compared to a maximum of 60% for testing), and that they are also up to twenty times more cost effective than testing in finding faults. Due to the quality and cost implications, software developers should have a strong incentive to evaluate the effectiveness of various verification methods. We believe that a more practical approach to program certification of engineering software can be achieved without the necessity of using completely formal proofs.

Parnas and Clements (1986) present a sequence of software development phases, based on sound principles and demonstrated on substantial examples. The key themes are the use of precise specifications of observable behaviour (Hoffman and Snodgrass

(1988)), and the reduction of maintenance costs through information hiding (Parnas (1972)). This software development approach is characterized by six work products:

1) The *Requirements Specification* describes the complete observable behaviour of the system, including both normal and exceptional behaviour, and the changes expected during the lifetime of the system.

2) The *Module Guide* describes the decomposition of the system into modules and the motivation for the decomposition, in information-hiding terms.

3) There is one *Interface Specification* per module, specifying the assumptions that users of the module are permitted to make about the service it offers.

4) There is one, possibly more, *Implementation* per module, consisting of code intended to satisfy the interface specification.

5) The *Test Plan* describes the strategy used for selecting test inputs, and the scheme for applying the test, including stubs, drivers and test case files.

6) The *Test Implementation* consists of the code, data and procedures used to implement the test plan.

The works of Floyd (1967), Dijkstra (1976) and many others, have provided a fundamental understanding of programming and the programming process, and methods for performing formal program verification. Furthermore, the argument that correctness can only be demonstrated through proofs is convincing, given Dijkstra's Law of Testing (1969): "Program testing can be used to show the presence of bugs, but never their absence".

According to Fagan (1976), software inspection is an effective and economical method for improving software quality. Fagan's approach requires that the software development process be broken into a sequence of steps, with explicitly and precisely defined criteria for the product of each step. In inspection meetings, the participants examine the product in detail, attempting to find faults – deviations from the criteria.

Our proposed Engineering Software Certification approach used for the development of FLEXB, the FLexible EXtendible Beam program, combines the above techniques in a practical way:

1. We worked primarily within the framework developed by Parnas (Hoffman, (1990)). We developed criteria describing the purpose and evaluation criteria for each of the work products. These criteria must be precise enough to make faults identifiable, and concise enough to be practical. The criteria for specifications emphasise precision and completeness, including both normal and exceptional behaviour. Specification documents were written according to standard formats, to make application of the criteria simpler.

2. We performed code inspections. These are formal and explicit examinations with a primary objective to detect faults in the code. The inspection team paraphrases the code, line by line, to express source code functionality and ensure correctness.

3. We used systematic testing of both individual modules (Hoffman (1989)) and of the complete system to demonstrate the conformance of implementations to specifications. This process was automated by the use of custom-made tools.

4. Finally, we performed a disciplined exception analysis for proving that blocks of code are exception free.

Statistical data regarding the various work products of FLEXB are summarised in Table 1, where all numbers refer to the number of lines in the corresponding work product. There are thirteen modules in total, all of which, with the exception of two, have been developed specifically for FLEXB. The majority of the source code that makes up the linear algebra and linear solvers modules existed in the WISDOM program (Tabarrok, (1990)). However, according to our upgrade plan (Stylianou and Hoffman (1990)) it was modified to meet our Code Format Rules and Code Verification Rules. This upgrade also required the preparation of an Interface Specification, Test Plan, and Test Implementation. The success of this upgrade was confirmed when other members of the Computational Mechanics Group in our department were able to successfully use these modules with only the Interface Specifications as guides.

| Module name | Interface Specification | Module Implementation | Test Plan | Test Implementation |
|---|---|---|---|---|
| coordinate transformation | 124 | 476 | 50 | 339+275[a] |
| data base system | 582 | 1,585 | 169 | 910+450 |
| dynamic equations | 234 | 1,071 | 93 | 1,368+(20,105)[b] |
| element matrices | 147 | 4,880 | 33 | 715+680 |
| geometric properties | 85 | 237 | 46 | 87+37 |
| kinematic parameters | 133 | 426 | 52 | 112+31 |
| linear algebra | 286 | 583 | 28 | 388+247 |
| linear solvers | 197 | 747 | 26 | 1,283+743 |
| material properties | 61 | 144 | 41 | 72+27 |
| order reduction | 84 | 326 | 46 | 122+61 |
| payload properties | 105 | 301 | 51 | 124+45 |
| problem [illegible] | 109 | 438 | 57 | 865+193 |
| rayleigh damping | 89 | 312 | 50 | 374+216 |
| Main Program | - | 1,630 | - | 0+23,845[c] |
| TOTALS | 2,187 | 11,526 | 742 | 6,759+3,005 |

a. The first number refers to the number of lines of code in the driver program, and the second number to the lines in the expected results file that was initially inspected manually.

b. Expected results were graphically verified.

c. Expected results were graphically verified.

Table 2: The FLEXB system.

It is interesting to note that for each line of code in the Module Implementation, there corresponds almost one line in the Test Implementation. The combined effect of formal inspections and systematic module testing resulted in the development of a highly reliable program. Almost no time was spent on traditional "debugging" of the modules, which in turn gave us confidence and a feeling of being in control of the program development process.